RADIO PULSAR SEARCHING AND TIMING FOLLOW-UP

by

Alexander E. McEwen

A Dissertation Submitted in

Partial Fulfillment of the

Requirements for the Degree of

Doctor of Philosophy

in Physics

at

The University of Wisconsin-Milwaukee

August 2023

ABSTRACT

RADIO PULSAR SEARCHING AND TIMING FOLLOW-UP

by

Alexander E. McEwen

University of Wisconsin-Milwaukee, 2023
Under the Supervision of Professor David Kaplan, PhD

Pulsars provide some of the richest laboratories for studying the behavior of ultra-dense matter. As such, they have been utilized for decades to place stringent limits on gravitation and as probes of the material that fills our Galaxy. These tests benefit greatly from a catalog of pulsars that is as complete as possible, which in turn requires thorough searches of the Galaxy and precise timing of discoveries. These searches are informed by the continued characterization of the pulsar population, and so searching techniques develop in tandem with the analysis of their discoveries. Large scale pulsar surveys find pulsars; small scale follow-up on those discoveries uncover the pulsars' potential for continued science. In this way, both techniques are crucial to the future of pulsar experimentation.

In this dissertation, I discuss the continued analysis of two pulsar surveys utilizing the Green Bank Telescope and subsequent follow-up on the sources from them. In Chapter 1, I provide an overview on the behavior and evolution of pulsars. Aside from the pulsars themselves, I discuss modern pulsar searching techniques and some of the complexities inherent in pulsar timing. In Chapter 2, discussion focuses on the largest radio survey conducted to date: the Green Bank North Celestial Cap survey. This survey has discovered many pulsars that have led to seminal papers in gravitation and neutron star equations of state, but also provides an unprecedented snapshot of the pulsar population

at 350 MHz. I utilize these data to assess the survey's sensitivity to pulsars, an analysis that impacts Galactic population models. In Chapter 3, I shift focus to the GBT 820 MHz Cygnus survey, which covers a much smaller region of the Galactic plane that hosts an abundance of active stellar formation. Deep scans of this dense region uncovered several new pulsars, including a source in a relativistic orbit with a massive white dwarf companion. I discuss this source and its follow-up in detail, and utilize the survey results to highlight deficiencies in Galactic models commonly used for pulsar searching. In Chapter 4, I return to the GBNCC survey, but in the context of long-term timing follow-up of its discoveries. Through the use of a pipeline developed to maintain pulsar solutions as high-cadence data are continually collected from observatories like CHIME, I have updated timing solutions for 128 pulsars. This procedure has given rise to many newly measured parameters and updates to those that were previously published; it also provides a framework for iterative pulsar timing that will be essential in the era of dedicated, regular observations of large groups of pulsars. In Chapter 5, I provide an overview of the results from these studies and briefly discuss the future in pulsar searching and timing.

Publications Connected to this Dissertation

The work presented in **Chapter 2** has been published in the following papers:

McEwen, A. et al (2020). *The Green Bank North Celestial Cap Pulsar Survey. V. Pulsar Census and Survey Sensitivity*. The Astrophysical Journal.

→ https://iopscience.iop.org/article/10.3847/1538-4357/ab75e2/pdf

At the time of finishing and submitting this dissertation, the work in **Chapters 3 and 4** were being prepared to submit for publication.

TABLE OF CONTENTS

LIST OF FIGURES

LIST OF TABLES

LIST OF ABBREVIATIONS

DM	dispersion measure
EOS	equation of state
GBNCC	Green Bank North Celestial Cap survey
GBT820	Green Bank 820 MHz survey
GR	general relativity
ISM	interstellar medium
$\mathrm{M}_\odot$	solar mass
MSP	millisecond pulsar
PK	Post-Keplerian
PSR	pulsar
PTA	pulsar timing array
$\mathrm{R}_\odot$	solar radius
SN	supernova

ACKNOWLEDGMENTS

I cannot thank my family enough for all of the love and support throughout my graduate school career (and before). I have been impossibly lucky to have such a wonderful group of people to lean on - a fact that has been made continuously clear as time has passed. Dad, you have been one of my best friends since I was a kid; thank you for encouraging me with your excitement about my life and work, and for always providing us with love and fun. Mom, I wish you could be here for this part. I miss you terribly, but your love continues to fill my sails, and I will bring you wherever I go. Rob and Michael, you have both given me unending support and friendship and I can't imagine going through life without you both. Emily and Annika, thank you for enriching my life dramatically; I'm excited for the future we'll all share. Nick, thanks for all of the horror movies and music-making, and for being my best friend despite my continual home-buddiness and work exhaustion. Thanks to you all for all of the phone calls, texts, love, and laughs.

Kara, I have said for years that you are the single nail that keeps me together. I wouldn't be here without you. Thank you for always supporting me, for all of our experimentation in cooking and baking, for the thousands (I checked) of miles of walks we've taken, for the many hobbies we have both undertaken together and alongside one another, for Turnip, for discussing all of my problems with me, and for everything else. I love you.

The pandemic certainly complicated my graduate school social life. Lucky for me, I got to work with those driven grad students in Coffee Shop Astrophysics, who always managed to keep things running and have fun doing it. Thanks to you all for being my friends and co-presenters, in particular Allie and Gabe. Logan and Casey, thanks for all

the gaming - maybe someday we will conquer Valheim.

To my advisor David, thank you for your endless patience during the most difficult parts of my life. Thanks for repeating yourself, and repeating yourself again - it's the only thing that works. Your attention to detail and precision has helped me make progress even when I was sure I couldn't. To Joe, you have given me so much important information about science, pulsars, and life. Thanks for all you have done for me; here's to the next zoo visit with you, Sarah, and Finley.

To all the members of the department that have provided me with help and knowledge along the way, thank you. In particular, thanks to Sarah Vigeland, Tonia Klein, and Heidi Matera. Your kindness has not gone unnoticed, nor has your tireless work.

This work was supported by the NANOGrav PFC award numbers 1430284 and 2020265.

CHAPTER 1

Pulsar Astronomy Overview

1.1 PULSAR FUNDAMENTALS

Since their discovery in 1967 (Hewish et al., 1968), pulsars have proven themselves to be some of the best natural laboratories for examining the behavior of ultra-dense matter (Özel & Freire, 2016; Cromartie et al., 2020; Raaijmakers et al., 2021), for probing the material filling the Galaxy (Turner et al., 2021; Ocker et al., 2021; Wahl et al., 2022), and even the detection of the gravitational wave background emanating from the Universal ensemble of merging supermassive black holes (Agazie et al., 2023; Antoniadis et al., 2023; Reardon et al., 2023). Their immense moments of inertia serve to stabilize their rotation down to the microsecond level, even reaching nanosecond precision for the oldest and most rapidly rotating sources (Agazie et al., 2023). Observations of these faint radio pulses track the passage of time (and the acceleration of matter) in the Galaxy and beyond.

Pulsars are formed following the collapse of massive stars ($\geq 8\,\mathrm{M}_\odot$) when iron forms an incredibly dense core. As the outer layers cool and rapidly collapse inward, they rebound off of the proto-neutron star. The resulting shockwave blasts away the outer layers of the star in a violent supernova. This explosion sends most of the star's mass into the surrounding interstellar medium to form a nebula, leaving behind the much smaller ($\simeq 1.4\,\mathrm{M}_\odot$, $\simeq 15\,\mathrm{km}$ diameter) neutron star (Phillips, 1999). The angular momentum of the progenitor is conserved, and the reduction in radius (and an off-center SN kick, e.g. Spruit & Phinney 1998; Fragione & Loeb 2023) confers a large increase in the neutron star's rotation rate – typically 0.1-10 Hz at birth (Coleman & Burrows, 2022).

Similarly, the magnetic flux of the progenitor is conserved in the neutron star, though the reduced radius drives the strength of this flux from $\approx 100\,\mathrm{gauss}$ to $\geq 10^{12}\,\mathrm{gauss}$ (pos-

sibly supplemented with the help of a dynamo, e.g. Thompson & Duncan 1993). The rotation of the pulsar drags this field along with it, dredging plasma from the surface of the star into the surrounding medium. This plasma is bound to the magnetic field lines that encircle the pulsar and spins with it out to the "light cylinder" – an imaginary boundary at $r_c = c/\Omega$ where the tangential rotation velocity reaches that of light. This region is called the magnetosphere, and it is here where the observable radiation is generated.

Charged particles pulled from the surface spiral around the magnetic field lines and emit synchrotron radiation; only those particles that have reached the magnetic pole of the star can follow the magnetic field lines that extend to infinity there and escape the magnetosphere. The emission of light from the acceleration of these particles forms a beam of radiation at both poles, and as the pulsar rotates, these beams sweep through a cone described by the angle between the pulsar's rotation and magnetic axes. This beam contains particles each emitting curvature radiation that is observed in pulsar data. As the pulsar ages, its rotational energy is slowly converted into this radiation, which serves to energize the surrounding nebular material. In this way, energetic particles leaving the pulsar power much of the luminosity of nebulae.

As the rotational energy is converted to radiation, the pulsar gradually slows. Given that the pulsar acts as a rotating magnetic dipole, the change in rotational energy can be compared to the power emitted along the Poynting vector. Measurements of pulsar rotation and its derivative can be used to make an estimate of the overall magnetic field strength. This field will decrease with the pulsar's rotation, and so the emission from pulsars will fade as they age. At some point, the pulsar will no longer be detectable.

However, a sizeable fraction of pulsars evolve with a binary companion, which can greatly extend their lives as radio sources. In this scenario, two progenitor stars in orbit around one another will undergo supernovae at different times, with the more massive

star evolving first. Long after it has collapsed to a pulsar and shed its outer layers, the second star will enter its own giant phase. As it begins to overflow its Roche lobe, the neutron star will sweep up the excess matter and convert it into angular momentum. In this way, the pulsar can attain rotation periods much smaller than those it was born with – reaching a minimum around 1 ms (for this reason, they are dubbed "millisecond pulsars," of MSPs). The accreted material will also dampen the pulsar's magnetic field by a factor of 100 or so. This process of spinning-up (or recycling) the pulsar continues until the second star undergoes its own supernova and may collapse into another pulsar or slightly less massive white dwarf star, depending on its initial mass. This mass will dictate how long the two stars remain in the recycling phase, which in turn dictates the final spin period of the first star (as well as the final eccentricity of the system).

Studies of pulsars in binaries have laid out many possible evolutionary pathways that impact their final state (Tauris, 2011; Özel & Freire, 2016). When a pulsar's companion is sufficiently large, the recycling phase can be cut short by the onset of supernova in the companion. This leads to an intermediate period - faster than the typical birth rotation rate ($\simeq 1\,\mathrm{Hz}$), but not quite as fast as a standard MSP (generally taken to be $\geq 50\,\mathrm{Hz}$ or so). So, pulsars that are discovered with periods in this intermediate range are good candidates for high mass binaries, which provide the greatest scientific potential for studies of gravity (Stairs, 2003; Fonseca et al., 2014; Swiggum et al., 2015).

While pulsars are hailed for their amazing stability, there are various short- and long-term effects (other than dipole radiation) that impact the evolution of their rotation rate. Many young pulsars' periods will drift stochastically with time – an effect called "timing noise" (Lower et al., 2020; Antonelli et al., 2023). This is believed to be due to coupling and uncoupling of the neutron star's interior material and its crust (Parthasarathy et al., 2019). The characteristics of neutron star interiors are actively debated, though most mod-

els incorporate a superconducting fluid beneath a (mostly iron) crystalline crust. A small fraction of electrons and protons exist within this fluid, and their charges react strongly to the magnetic field of the star, therefore coupling the fluid to the star's rotation (Lyne & Graham-Smith, 2012). However, the coupling in the crust is different, and the difference between the two can result in variable observed rotation. Some of these sources also experience abrupt changes in period, known as glitches. Such glitches have been observed to correlate with pulse shape changes, though generally both the period and pulse profile exponentially return to their initial states. Their origins are most likely to be due to the unpinning of vortices within their superfluid interior, leading to differential rotation (Alpar, 1977; Link et al., 1992; Haskell et al., 2020; Melatos & Millhouse, 2023; Layek et al., 2023), though another common explanation is through crustal fractures ("starquakes," Alpar et al., 1994; Lai et al., 2018; Lu et al., 2023). Both suggest that measurements of glitches can shed some light on the strange material that fills neutron stars.

1.2 OBSERVING PULSARS

The first pulsar discovered by Jocelyn Bell was found serendipitously – a faint but clearly regular pulse train was identified in continuum data she had taken (Hewish et al., 1968). A few days of observations showed that the signal appeared at the same position, ruling out a terrestrial origin. And a month later, a second repeating signal found at a different sky location cemented that these were indeed a new astrophysical source.

As a pulsar rotates and its magnetic field beams radiation from its poles, that beam may cross the line of sight to Earth. If it does, each rotation produces a radio pulse when observed with a radio telescope of sufficient sensitivity. Individual pulses are generally too faint to be detected; instead, many pulses can be averaged together to produce a stable average profile. These pulses must be stacked together in both time and frequency

space: this requires accuracy in the pulsar's spin period and dispersion measure (DM). The former assures that each pulse is added in phase such that the peaks align and sum coherently, separating them from noise. The latter accounts for the broadband nature of pulsar emission, which will interact with charged particles in the interstellar medium (ISM) in a frequency-dependent way. This introduces a delay across the observing band $\Delta\nu$ (Lorimer & Kramer, 2004):

$$t_{\mathrm{DM}} \simeq 8.3 \times 10^{6}\mathrm{ms} \times \mathrm{DM} \times \Delta\nu \times \nu^{-3} \tag{1.1}$$

where ν is the central observing frequency.

If the DM used to sum the data is incorrect, the higher frequency part of the signal will be offset in time from the lower frequency part, and the resulting pulse will be spread across multiple bins in pulse phase. This smearing reduces the S/N of a pulsar detection dramatically. Mitigation of this effect is called dedispersion, and can be either incoherent or coherent. The former case, which is employed when the DM of a pulsar is not known a priori (i.e. when searching), involves splitting the observing bandwidth into multiple subbands and adding a small phase shift (calculated via Eqn. 1.1) to each. This recovers much of the S/N of the pulse, though smearing within each of these finite subbands can still widen (and diminish) the pulse. Correcting for this requires manipulation of the input voltages to recover the intrinsic pulse shape and mitigate smearing, which is the coherent form of dedispersion. This procedure incorporates the DM of the pulsar, and so it is only suitable for follow-up observations.

Aside from dispersion, the ISM alters the pulse along its path from the pulsar to Earth in a few ways. One significant alteration is from pulse scattering (Bhat et al., 2004; Young & Lam, 2023). As the pulse travels through the inhomogeneous ISM, the photons will be deflected by charged particles, and will follow slightly differing paths to Earth. These

minute path differences alter the arrival time at Earth and exponentially broaden an otherwise sharp pulse. The resulting scattered profile can be characterized by a scattering timescale τ_s, which scales with the distance to the pulsar d and observing frequency ν as (Lorimer & Kramer, 2004):

$$\tau_s = \frac{e^4}{4\pi^2 m_e^2} \frac{\Delta n_e^2}{a} d^2 \nu^{-4}, \tag{1.2}$$

where e and m_e are the electron charge and mass, Δn_e is the difference in number of electrons along two scattered lines of sight, and a is the characteristic length scale of this inhomogeneity. As timing precision for a given pulse scales with the S/N, scattering will limit timing capabilities for distant pulsars. This can be mitigated by observing with a higher frequency – though, since pulsars have generally steep spectra (flux density $S_\nu \propto \nu^\alpha$ with typical spectral index $\alpha = -1.4$, Bates et al., 2014), a balance must be struck.

The other deleterious effect imposed by the ISM is scintillation (Cordes & Rickett, 1998; Wu et al., 2023). In this process, the photons from the pulsar accumulate phase offsets that interfere at Earth. Subsequently, pulses show variable intensities in both frequency and time, and this variability can impact whether a pulsar is detectable in a given observation. Generally, this scintillation affects all observations; the pulse amplitude will only be significantly modulated when the number of peaks (due to coherent photons) and troughs (due to incoherent photons) is close to one. This is typically true for nearby (low-DM) sources (for some examples, see Wu et al., 2023; Main et al., 2023; Askew et al., 2023, etc.). In other cases, the individual fluctuations will average to zero, and the overall pulse shape will be maintained.

1.3 SEARCHING FOR NEW PULSARS

Pulsars are faint; only a few emit single pulses bright enough to stand above the background noise (one example is the Crab pulsar, Lewandowska et al., 2023). Even then,

these pulses will be smeared out if the data processing has not accounted for the pulsar's DM - which is only known after discovery. So, finding pulsars requires careful sampling in both DM and spin period space. The limits of these searches depend on the observing setup; short scans are obviously less sensitive to long period pulsars, and low frequency observations must utilize small steps in DM to avoid smearing. Pulsars are typically steep spectrum sources, a characteristic that becomes a problem when they are suspended in front of a radio-loud background (like the Galactic plane).

For a typical search, grid points on the sky are chosen such that the telescope's observing half-width-half-max (HWHM) for neighboring points will overlap. This way, the odds of detecting a pulsar in more than one observation (and thereby confirming its existence without additional observations) is made possible. The HWHM of the beam depends on the collecting area of the telescope as well as the observing wavelength (i.e $\sim \lambda/D$). For this reason, low frequency is generally chosen for rapid sky coverage, and high frequency is chosen for deep, scatter-mitigating searches. Both are necessary, and complement one another.

When a pulsar is observed, the time series data is recorded over a bandwidth $\Delta\nu$ at some sampling time $t_{\rm samp}$. The latter must be small enough to sample the pulse efficiently, which can be challenging for the most rapidly spinning pulsars (millisecond periods, with sub-ms pulse widths). The first search is over DM. Choosing step size is important, as pulsar searching pipelines are time/resource-demanding. Too small a step will greatly increase the time required to complete such a search. On the other hand, too large a step in DM can miss pulsars in the gap, as they will be smeared out below the S/N threshold for the next step. This smearing can be quantified by the effective pulse width $W_{\rm eff}$, which combines the pulsar's intrinsic pulse shape with the timescales for scattering and dispersion delays ($\tau_{\rm sc}$ and $\tau_{\rm DM}$, respectively) (Lorimer & Kramer, 2004):

$$W_{\rm eff} = \sqrt{W_{\rm int}^2 + \tau_{\rm DM}^2 + \tau_{\rm sc}^2}. \tag{1.3}$$

This is the observed width, which will impact the overall S/N of the detection. The dependence on observing frequency (see Eqns. 1.1 and 1.2) sets the maximum DM to include in a search, as scattered pulses with $W_{\rm eff} \geq$ spin period P are undetectable. At the heart of this measured S/N is the radiometer equation, which describes how the fluctuations in system temperature of a radio telescope due to an astrophysical source $\Delta T_{\rm sys}$ relate to the observation bandwidth $\Delta\nu$ and integration time $t_{\rm int}$ (Dicke, 1946):

$$\Delta T_{\rm sys} = \frac{T_{\rm sys}}{\sqrt{n_{\rm p}\Delta\nu t_{\rm int}}}. \tag{1.4}$$

Here, $n_{\rm p}$ is the number of summed polarizations in the receiver. Eqn. 1.4 must be modified to account for the pulsed emission from pulsars; the resulting fluctuations in temperature during such an observation is

$$\Delta T_{\rm obs} = \frac{T_{\rm sys}}{\sqrt{n_{\rm p}\Delta\nu t_{\rm int}}} \left(\frac{P}{\sqrt{W(P-W)}} \right), \tag{1.5}$$

where P is the pulse period and W comes from Eqn 1.3. Finally, we can connect the equations to the S/N (the ratio of peak antenna temperature $T_{\rm peak}$ and the temperature fluctuations) using

$$\mathrm{S/N} = \sqrt{n_{\rm p} t_{\rm int} \Delta\nu} \left(\frac{T_{\rm peak}}{T_{\rm sys}} \right) \frac{\sqrt{W(P-W)}}{P}. \tag{1.6}$$

This gives a measure of how bright a pulsar will appear in terms of the observing system's temperature. Characterizing the pulsar's brightness in terms of its flux density S makes use of the telescope's gain $G = A_{\rm e}/(2k_{\rm b})$, which depends on the telescope's ef-

fective collecting area $A_{\rm e}$. These measurements can then be directly compared to other pulsars, regardless of observing setup. A source with flux density S will confer a change in system temperature equal to $T_{\rm source} = GS$. It is important to note, though, that the observed source temperature will actually be a hidden sum of several noise sources. For radio observations, the main contributors include receiver noise ($T_{rec} \simeq 10-50\,{\rm K}$ depending on the telescope from thermal fluctuations in the telescope system); "spillover" noise ($T_{\rm spill} \leq 10\,{\rm K}$ from the ground near the telescope which enters the receiver), atmospheric noise ($T_{\rm atm}$, generally negligible for the lower radio frequencies observed in this dissertation), CMB noise ($T_{\rm CMB} \simeq 3\,{\rm K}$), and background sky noise ($T_{\rm sky}$). This last term varies the most widely, especially at lower radio frequencies. It is usually estimated using results from Haslam et al. (1982) which reports a power-law model with frequency scaling index of -2.6, and ranges from a few Kelvin toward the Galactic poles to $\geq 1000\,{\rm K}$ in the plane at 350 MHz.

Equation 1.6 is integral to pulsar searches. Initially, it can be used to predict the idealized sensitivity of a survey from the observing parameters. This is useful for estimating the survey's yield and generally motivating observations, and can be revisited after a survey's completion to tune pulsar population models. The S/N also provides a simple metric for sifting candidate sources.

For each of the trial DMs, the data are dedispersed and subsequently Fourier transformed. The resulting power spectrum contains peaks at candidate periods, which are used to "fold" the data. This process entails splitting the time series data into many small pieces, each of duration equal to the pulse period P. Summing all of these pieces together in pulse phase will average out the (off-pulse) noise while coherently adding each of the faint pulses together. The resulting average profile is quite stable, and is a kind of "fingerprint" of a pulsar. It is from this profile that the S/N of a detection is measured.

This procedure is generally sufficient for isolated pulsars. Pulsars in binary orbits may be significantly accelerated during an observation, and so a simple fold will not coherently sum pulses. Instead, searches for accelerated pulsars include additional processing to approximate the sinusoidal signature as a quadratic, which can then be applied to the folding step (Ransom et al., 2003). This does a much better job of finding those pulsars at the expense of additional computing time. The framework for acceleration (and even jerk) searches is built into the `PRESTO`[1] package (Ransom, 2011), which has been used extensively in this dissertation.

1.4 TIMING PULSARS

Timing a pulsar is iterative. Processes that impact the arrival time of a pulse work on many timescales, and so a solution that incorporates them all must be built over many observations. Simple pulsar models include terms that are quadratic (i.e. spin and spin-down), sinusoidal (position and proper motion), and frequency dependent (dispersion). More complex models include binary motion, time-varying DMs, parallax, and so on. Coupled with datasets that are often episodic, landing on a unique solution to describe a pulsar is difficult.

To properly time a pulsar, several effects that impact a pulse's arrival time on Earth must be accounted for. The first significant correction is the transformation to the Solar system barycenter (SSB). Because of the Earth's rotation and orbital motion, telescopes on its surface are not in an inertial reference frame, and this complicates the interpretation of the measured pulse arrival times. By using previous mass and position measurements of the members of the Solar system (Park et al., 2021), conversion to the SSB will relieve these

[1] https://github.com/scottransom/presto

complexities. In full, the transformation can be written as (Lorimer & Kramer, 2004):

$$t_{\rm SSB} = t_{\rm topo} + t_{\rm corr} - \Delta D/\nu^2 + \Delta_{\rm R\odot} + \Delta_{\rm S\odot} + \Delta_{\rm E\odot}. \tag{1.7}$$

The first term in the above expression, $t_{\rm topo}$, indicates the arrival time of the pulse as measured on Earth (the topocentric arrival time). This arrival time is referenced to a standard (telescope-independent) clock on Earth, adding the $t_{\rm corr}$ factor. The third term accounts for dispersion of the pulse by moving to the "infinite frequency" arrival time (see Eqn 1.1). The remaining three terms are the Römer delay, the Shapiro delay, and the Einstein delay. The first is the time difference between the pulse's arrival at Earth compared to the SSB (the light travel time between the two). The second arises from space-time curvature due to the gravitational potential of the bodies in the Solar system, and the final term is a combination of gravitational redshift and time dilation from those bodies.

A typical timing campaign begins with a group of short (typically <30 minutes) observations over the course of a week or so. Specifics for observing frequency, cadence, and duration are dependent on the source in question; if there is reason to believe it is in a binary, estimates for the binary motion can aid in determining times for optimal binary phases. But the primary objective for these sessions is to constrain the spin frequency by "phase-connecting" each observation. Phase-connection is the process of accounting for every rotation of the pulsar in order to reduce the uncertainty in the pulsar's rotational phase at the beginning of the next observation, optimally to ≤ 1 rotation.

To begin constructing a model, the first timing observation must be cleaned of radio frequency interference and "folded" at the pulsar's period. The time series data are split into pieces that each correspond to a single rotation and these pieces are summed together. Assuming the initial rotation model is within some margin of error, the folding

will coherently stack the individually recorded pulses and simultaneously minimize the noise in the off-pulse region. The summed profile is far more stable than any individual pulse and can achieve a much higher S/N ratio.

This profile can then be used as a template pulse to measure the fundamental pulsar timing datum: the time of arrival (TOA) of a pulse. This quantity, typically measured in modified Julian date (MJD), is determined by folding portions of the observation (sub-integrations) coherently and fitting the template pulse to each sub-integration. From this, the arrival time of the first pulse can be ascertained with much better precision than a fit to individual pulses, which are (generally) too faint. The number of sub-integrations used will ultimately depend on the S/N of the pulsar in the observation, which depends on the pulsar's intrinsic brightness, its spin frequency, and the accuracy of the timing model.

When the TOAs have sufficiently small uncertainty, typical timing software like TEMPO[2], TEMPO2[3] (Hobbs et al., 2006), or PINT (Luo et al., 2021) can be implemented to adjust timing parameters. These software packages use a model for the pulsar to predict the arrival time of a pulse at the MJD of the measured TOA and subtract the two. The difference (called the timing residual) contains information about the accuracy of the model. Given a sufficiently accurate model, the residuals will be normally distributed around zero. For an isolated pulsar, the only parameter that can be reasonably constrained by a single observation is the pulsar spin frequency. When plotted in pulsar phase against MJD (typical for timing residuals), an error in frequency produces an offset in phase that grows linearly with time. This offset can become statistically significant within an observation containing only a few hundred pulses – easily achievable for spin periods from 1 - 1e3 ms – so the model can be tuned to first order to predict the pulse phase at the start of the next observation. With the improved model in hand, the process can be repeated to

[2] http://www.atnf.csiro.au/research/pulsar/tempo
[3] http://www.atnf.csiro.au/research/pulsar/tempo2

produce a better profile and more precise TOAs. Ultimately, an uncertainty floor will be reached until more data are taken.

As the timing observations continue, the goal is to retain phase connection. Sufficiently high S/N and the improved timing models can permit larger gaps between subsequent observations, at least until additional parameters become measurable. The time scales for these measurements are variable, and many of them are covariant in early models. For example, position measurements from timing are the result of sinusoidally varying timing residuals from Earth's annual motion in the Solar system. The period of these oscillations is therefore well-known, but the amplitude is not. To complicate matters, the derivative of the pulsar's rotation frequency (predicted by magnetic dipole radiation/braking) is a second-order quadratic. This makes it difficult to disentangle from the position, especially when the data span less than a year.

1.4.1 Binary Pulsars

Orbital motion in pulsars results in additional timing complexities. In general, five parameters must be measured to fully describe the orbit:

- the orbital period, $P_{\rm B}$;
- the projection of the pulsar's semi-major axis in the plane of the sky, $a_{\rm p}{\rm sin}i$;
- the eccentricity of the orbit, e;
- the angle between the plane of the sky and periastron in the plane of the orbit (called the argument of periastron), ω; and
- a reference epoch of periastron passage, T_0.

Binary motion introduces Doppler shifting of pulse TOAs as the pulsar moves along its orbit: as it moves toward Earth, pulses will arrive earlier than predicted, and vice

versa. For tight orbits where a single observation can span ≥ 1 orbit (i.e. $P_{\rm B} \ll t_{\rm obs}$), this shifting operates on a timescale much shorter than most of the pulsar timing parameters. In this case, constraints on the binary motion can be placed by directly fitting for three parameters of a sinusoid (angular frequency, amplitude, and initial phase). The frequency of the oscillations is inversely proportional to the orbital period, and so the first Keplerian parameter is determined. The amplitude is proportional to the light travel time along the line of sight in the orbit, which is in turn proportional to the relative semi-major axis of the orbit, $a_{\rm R}$. Using Kepler's third law

$$\left(\frac{2\pi}{P_{\rm B}}\right)^2 \left(\frac{a_{\rm R}}{c}\right)^3 = \frac{GM_\odot}{c^3}(m_{\rm p} + m_{\rm c}) \tag{1.8}$$

and the transformation from the center-of-mass frame to the pulsar's semi-major axis

$$a_{\rm p} = a_{\rm R}\frac{m_{\rm c}}{m_{\rm p} + m_{\rm c}}, \tag{1.9}$$

these observables place constraints on the so-called mass function of the binary

$$f(m_{\rm p}, m_{\rm c}) = \frac{(m_{\rm c}{\rm sin}i)^3}{(m_{\rm c} + m_{\rm p})^2} = \frac{4\pi^2}{G}\frac{(a_{\rm p}{\rm sin}i)^3}{P_{\rm B}^2}. \tag{1.10}$$

This sets a bound on the companion mass $m_{\rm c}$, typically under the assumption that the pulsar has mass $m_{\rm p} \simeq 1.4\,{\rm M}_\odot$. The inclination term ${\rm sin}i$ is only measurable in special cases, though its implicit $[0, 1]$ bounds fix the minimum mass of the companion.

For binaries in which the pulsar's velocity approaches c, measurement of additional perturbations to the Keplerian orbit can constrain the two masses independently. Such measurements are necessary for constraining the evolutionary scenario for the binary, and for probing the interior of neutron stars (Özel & Freire, 2016). Specifically, measurement

of two Post-Keplerian (PK) parameters uniquely determines both masses in the orbit. These measurements will depend on the theory of gravity used, and so additional PK measurements provide a consistency check of the theory. In pulsar timing residuals, the measurable PK parameters (as described in Damour & Deruelle 1986) include:

- the relativistic Römer delay, which encapsulates deformations to the orbit;
- the Einstein delay, a combination of time dilation and redshift effects from the pulsar's motion through different points in the gravitational potential of its companion;
- the Shapiro delay, which accounts for the additional light travel time of an emitted pulse that passes into and out of the companion's gravitational field; and
- aberration delay due to the pulsar's motion during pulse emission.

Additionally to these orbital effects are several secular effects that are observable with a sufficiently long baseline:

- the change in orbital period $\dot{P}_{\rm B}$, due primarily to the emission of gravitational waves (GW) and a change in the observed Doppler shift from the pulsar's proper motion and location in the Galaxy relative to Earth;
- the corresponding change in projected semi-major axis $\dot{a}_{\rm p}{\rm sin}i$, also due to GW damping and proper motion but also annual orbital parallax as the system is observed at different points of Earth's orbit;
- changes to the argument of periastron $\dot{\omega}$, which are dominated by relativistic effects (from the geometry of spacetime in the presence of gravitational potentials), but apparent changes can arise from proper motion; and
- changes in the eccentricity of the orbit $\dot{e}$, again due to GW emission.

These parameters can also be influenced by spin-orbit coupling from the pulsar and/or its companion, mass loss from the system, and precession of the pulsar (measured via profile changes), though these effects are much less significant than those listed above.

All of these parameters are theoretically measurable in pulsar timing (though the aberration delay is only measurable in very special circumstances, with the only measurement in PSR B1534+12, Stairs et al. 2004), but feasibility of making such a measurement depends on the details of the system. For example, the significance of Shapiro delays depends strongly on the projected separation of the two orbiting stars when the pulsar passes behind its companion (i.e. the inclination of the orbit). So, finding new binary sources is well-motivated, and each binary system must be timed to sufficient precision to assess their suitability for such tests.

CHAPTER 2

The Green Bank North Celestial Cap Pulsar Survey. V. Pulsar Census and Survey Sensitivity

2.1 INTRODUCTION

The Green Bank North Celestial Cap (GBNCC; Stovall et al. 2014) pulsar survey began in 2009 and, when complete, will cover the entire sky accessible to the 100 m Robert C. Byrd Green Bank Telescope (GBT; $\delta \geq -40^\circ$, or 85% of the celestial sphere) at 350 MHz. As of mid-2019, the survey is 85% complete and 161 pulsars have been discovered, including 25 millisecond pulsars (MSPs) and 16 rotating radio transients (RRATs; McLaughlin et al., 2006). Timing solutions for these discoveries have been published in Stovall et al. (2014), Karako-Argaman et al. (2015), Kawash et al. (2018), Lynch et al. (2018b), and Aloisi et al. (2019), and more are forthcoming. As such, this constitutes one of the largest and most uniform pulsar surveys to date.

In addition to the newly discovered pulsars, the uniform coverage of GBNCC allows a robust re-assessment of the known pulsar population with reliable flux density measurements. Here we present a detailed search for all known pulsars in the GBNCC footprint. We find that 572 previously published pulsars and 98 unpublished pulsars have been re-detected by the survey pipeline and visually confirmed, comprising 670 detections in total, the largest low-frequency, single-survey sample. Similar to previous efforts based on results from the Parkes Multibeam Pulsar Survey (PMPS) and the Pulsar Arecibo L-band Feed Array (PALFA) survey (e.g., see Lorimer et al., 2006; Swiggum et al., 2014; Lazarus et al., 2015), we conduct a detailed analysis of the GBNCC pulsar survey and compare its sensitivity with that of other surveys in overlapping regions of sky. Flux densities at

350 MHz (S_{350}) are presented for all detections, as well as pulse widths and profiles, all of which are given in Appendix A.

In §2.2, we outline the process used to generate a comprehensive list of pulsars as well as predicting and measuring signal-to-noise ratios (S/N) of detections in the survey. In §2.3, we present the recovered S/N and flux density measurements for all detected pulsars as well as measurements of pulse width, dispersion measure (DM), and spectral index. We also present the profiles for all of these pulsars. In §2.4, we discuss how the GBNCC survey is performing compared to expectations and RFI characteristics of the survey, and remark on interesting detections and notable non-detections. We also discuss the implications of our results for the Galactic pulsar population. Finally, in §2.5, we summarize the main conclusions of this analysis.

2.2 SAMPLE ASSEMBLY AND DATA REDUCTION

The GBNCC data set as of late fall 2018 included ∼108,000 120 s pointings, each tagged with a unique beam number. Each dual-polarization observation was taken with the GBT over the past ≃10 years. The survey utilizes the GUPPI backend, with a sampling time of 82 μs and 100 MHz of bandwidth centered at 350 MHz (for more information on the observing setup for the GBNCC survey, see Stovall et al., 2014). We began by organizing a comprehensive list of all known pulsars with parameters that were available for use, whether they were published or not. By utilizing the Australia Telescope National Facility (ATNF) pulsar catalog[1] (v1.59, Manchester et al., 2005a), we amassed the bulk of the sources from the list of all published pulsars and their positions on the sky as well as their spin parameters and other relevant quantities (dispersion measure, etc.). Discovery parameters are also available for additional pulsars that have not been published but were

[1] http://www.atnf.csiro.au/research/pulsar/psrcat

detected in a number of other recent or ongoing surveys. Many of these surveys, including AODrift (Deneva et al., 2013), SUPERB (Keane et al., 2018, Spiewak et al., 2019, in prep.), GBT 350 MHz Drift (Boyles et al., 2013), PALFA (Cordes et al., 2006; Lazarus et al., 2015), LOTAAS (Sanidas et al., 2019), and HTRU-South (Keith et al., 2010a) include pulsars that are in GBNCC survey area, and so were included in the list. More information on these surveys is included in Table 2.1. Furthermore, we included the list of pulsars that had been discovered in the search pipeline for the GBNCC survey. We then limited this list to pulsars within the range of the survey, i.e., pulsars with $\delta > -40°$. In total, this list contained 2299 pulsars. We determined which pulsars were within 30′ (FWHM of GBT at 350 MHZ) of completed GBNCC pointings, adjusting when necessary to compensate for large (>30′) uncertainties in pulsar position. This reduced the total number of pulsar candidates to 1413. We could then match each pulsar with the GBNCC beams closest to its position before beginning to process the data.

Radio frequency interference (RFI) excision is the first step of GBNCC data analysis, and is done primarily with the `rfifind` tool from the `PRESTO`[2] pulsar data analysis software package (Ransom, 2001) as described in §3.1 of Stovall et al. (2014). We also performed an analysis of the `rfifind` output files spanning the lifetime of the GBNCC survey up to late 2018 (roughly 83% of the total survey) to characterize the effects of RFI over the course of the survey. These files contain information about which frequency channels were masked due to RFI for every 120 second scan in the survey. For a particular scan, the effective bandwidth $\Delta\nu$ is the total 100 MHz bandwidth of the GBT 350 MHz receiver multiplied by the ratio of unmasked to total channels for that scan, minus an additional 20 MHz for rolloff.

In some cases, the `rfifind` masks were insufficient to remove additional RFI that

[2] http://www.cv.nrao.edu/~sransom/presto/

was either narrow in frequency space or brief in time. The latter often appears as a very bright burst at $\sim$0 DM for portions of the observation. To mitigate this, we employed some additional narrowband flagging in the `PRESTO` `prepfold` command as well as removing corrupted portions of the scan in the time-domain. Note that these changes also alter the values for $\tau_{\rm obs}$ and $\Delta\nu$ which consequently change the measured S/N for a given observation. For this reason, we calculate the fraction of data points from the observations that were not omitted in processing and multiply the total bandwidth by this fraction.

After removal of RFI, we dedispersed and folded the observations at each pulsar's rotational period and integrated the profiles to obtain a single average profile for each observation. For the vast majority of sources included in this analysis, a precise ephemeris from the ATNF catalog was used to perform the folding. In all other cases, only the discovery parameters (period, DM and, if known, period derivative) were used. We also repeated this process while allowing dispersion measure to vary and, in some cases, also allowing variations in period and period derivative. This second iteration allows for fine-tuning previously published parameters at the cost of potentially finding bright RFI, which will often occur when attempting to detect low-DM pulsars as sources of RFI have DM = $0\,{\rm pc\,cm^{-3}}$. The 120 second observation times utilized in the GBNCC survey limit sensitivity to period refinement, so fitting for period was only used to increase the S/N of detections of pulsars for which only discovery parameters were used, and no further timing analysis was done as a part of this study. All folded data were visually inspected to determine likelihood of an actual detection. In cases where RFI still existed in the data, we removed high order (>5) polynomials from the off-pulse regions of the profile. With folded profiles, we calculated a measured signal-to-noise ratio (S/N) (Lorimer & Kramer,

2004),

$$\mathrm{S/N}_{\mathrm{meas}} = \sum_{i=0}^{N_{\mathrm{bin}}} \frac{p_i - \bar{p}_{\mathrm{off}}}{\sigma_{\mathrm{off}} \sqrt{W N_{\mathrm{bin}}/P}} \, \gamma, \tag{2.1}$$

where N_{bin} is the number of bins across the pulse profile, p_i is the value of bin i, $\bar{p}_{\mathrm{off}}$ is the mean of the off-pulse bins, σ_{off} is the standard deviation of the off-pulse bins, W is the on-pulse width in seconds, P is the pulsar spin period in seconds, and γ is a correction factor. When continuous signals are assigned to a finite number of bins in the profile during the folding process in `PRESTO`, their intensity is "smeared" over the neighboring bins, resulting in correlations in the bins' intensities. This correction, dubbed γ, depends on the sampling time and the number of bins in the profile, which (for this study) is dependent on the pulsar spin period. Typical values are close to 0.95. The number of bins N_{bin} was determined by the pulsar period as follows: profiles for pulsars with periods shorter than 1.7 ms had 28 bins, periods shorter than 10 ms had 50 bins, periods shorter than 50 ms had 128 bins, and all others had 200 bins. This prescription retains sensitivity to long-period pulsars but avoids bin widths corresponding to time intervals smaller than the sampling time of 82 μs. Pulse widths were determined with a standard process. First, sigma-clipping was used to find the off-pulse region. Then, the peak value above the noise floor was identified, and bins on either side of the peak were added to the on-pulse width. This process was repeated, adding bins on the sides of the peak until we reached bins within 2σ of the mean of the noise. The edges of the pulse were found by fitting lines to the two bins on either side of the pulse and finding the fraction of the outermost bins that were above the noise floor. At this point, we consider the full on-pulse width to be determined. Each profile was then checked by eye, and corrections to the on-pulse region were made. Any components of the pulse width that were distinct from the main pulse were determined using the same algorithm. To determine the sensitivity of uncertainties in S/N from the choice of the number of on-pulse bins, noisy Gaussian

pulses were simulated and various width choices were used to measure the fractional error on S/N. From this test, it was found that on-pulse widths that exceed at least one σ beyond the Gaussian mean were sufficient to greatly reduce the fractional uncertainty on S/N. Beyond this, adding bins had little effect on this fractional uncertainty - so, pulse widths were chosen to encompass all of the pulse visible above the noise. In some cases, additional RFI features were removed prior to the determination of W to minimize errors in W and S/N (see §2.4.2).

Characteristic measurements of pulse width include measurements at both 50% and 10% of the pulse profile's maximum amplitude (hereafter W_{50} and W_{10}, respectively). These widths are dependent on both pulse period and observing frequency, so measurements at 350 MHz help to fill out the low-frequency regime for a wide range of pulse periods. However, the noise floor in some pulsars limits the ability to determine W_{10} robustly. Note also that W_{50} and W_{10} are distinct from W, which includes all bins that contain the pulse signal, and so W is generally slightly larger than W_{10}.

The expected S/N of a pulsar can be estimated as (Dewey et al., 1985a; Lorimer & Kramer, 2004)

$$\mathrm{S/N}_{\mathrm{exp}} = \frac{S_{350} G \sqrt{N_{\mathrm{pol}} \tau_{\mathrm{obs}} \Delta\nu}}{T_{\mathrm{sys}} \beta} \sqrt{\frac{P - W}{W}} f(\theta), \tag{2.2}$$

where S_{350} is the flux density at 350 MHz, $G = 2\,\mathrm{K/Jy}$ is the gain of the Green Bank Telescope (Stovall et al., 2014), $N_{\mathrm{pol}} = 2$ is the number of polarizations recorded, $\tau_{\mathrm{obs}} = 120\,\mathrm{s}$ is the length of the observation, $\Delta\nu$ is the bandwidth in MHz after removing RFI (see §2.4.2), T_{sys} is the system temperature (including the sky temperature at the source position, receiver temperature $\simeq 20\,\mathrm{K}$, and CMB temperature $\simeq 3\,\mathrm{K}$), $\beta \simeq 1.1$ is an instrument-dependent correction factor due to downsampling the data to 2 bits (Lorimer & Kramer, 2004), and $f(\theta)$ is a radial Gaussian factor accounting for sensitivity degradation as a function of angular offset from the center of the circular beam θ. The sky temperature in the

direction of each pulsar was determined by using the measurements made by Haslam et al. (1981) for the beam positions, scaled to 350 MHz with the spectral index therein, -2.6.

Where possible we use flux densities at other frequencies and previous measurements of spectral index (α, with $S_\nu \propto \nu^\alpha$) from the ATNF catalog to determine an expected flux density at 350 MHz and the expected S/N (Manchester et al., 2005a). In cases where there was no published value for α but flux densities at both 400 MHz and 1400 MHz were published, we determine a spectral index using a simple power law. In all other cases, we assume a spectral index of -1.4 (Bates et al., 2014) to estimate the flux density at 350 MHz. We also calculate the measured flux density of each pulsar by inverting Equation 2.2 and using measured values for S/N (determined from Equation 2.1) and pulse width. Comparing the expected flux density to our measurements can both roughly confirm our current models for pulsar emission as well as aid in explaining non-detections.

2.3 PULSAR FLUX DENSITY CENSUS AT 350 MHZ

We detected 670 pulsars out of a total of 1413 in the survey area, and these detections are listed in Table A.1 in Appendix 1. For all following analysis, the beams corresponding to the brightest detections (highest S/N) were used, as these are most likely to represent the pulsars' flux density. Along with pulsar names, we provide several relevant quantities: dispersion measure from searching with `PRESTO` (Ransom, 2001), MJD of the brightest detection, angular offset from the center of the beam, W_{50}, W_{10} (when S/N was large enough), detection S/N, 350 MHz flux density measured from the GBNCC data, and measured spectral index α (see §2.3.2). Uncertainties on the S/N and flux densities were calculated using standard error propagation from equations 2.1 and 2.2 and uncertainties on bandwidth, temperature, and θ of 5 MHz, 10 K, and 0.5 degrees, respectively. Among

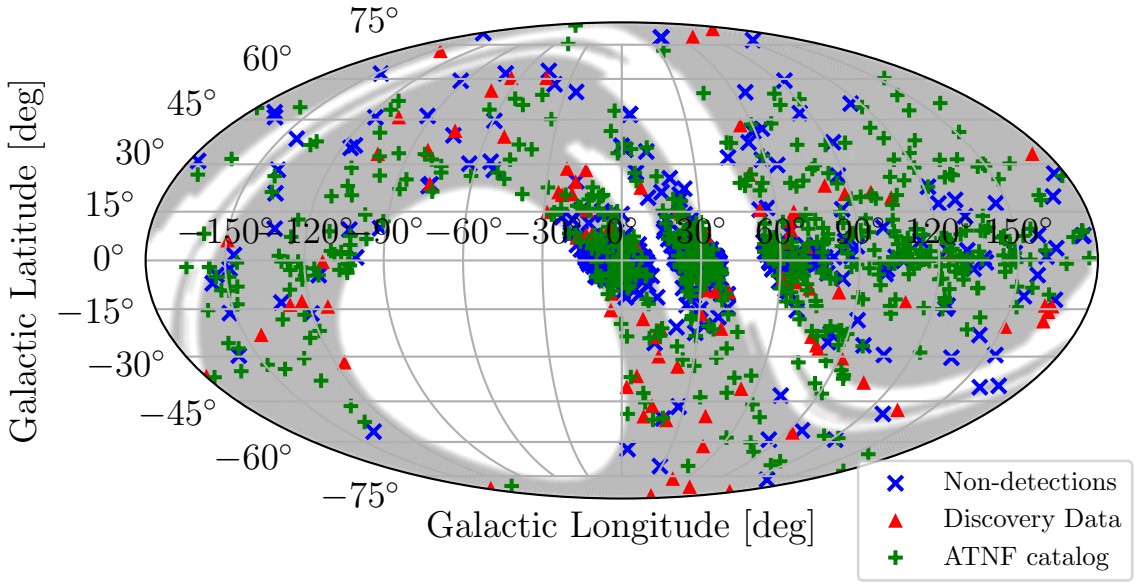

Figure 2.1 Sky map with pulsars from overlapping surveys, plotted in Galactic coordinates as a Mollweide projection. The shaded regions indicate completed GBNCC observations. Detected pulsars from the ATNF catalog and pulsars that were detected using discovery parameters from overlapping surveys are differentiated by marker type, with green plus symbols indicating pulsars from the catalog and red triangles indicating pulsars from the surveys listed in Table 2.1. Pulsars that were not detected are plotted as blue "x" symbols.

these are 66 millisecond pulsars (MSP), defined here as pulsars with spin periods shorter than 30 ms. The integrated pulse profiles for all of the brightest detections are shown in Figures A.1 – A.12 along with pulsar names, dispersion measure, and flux density. Figure 2.1 shows all detected pulsars plotted by their Galactic positions, and different markers indicate whether or not the pulsars were from the ATNF catalog or were a part of one of the other survey lists mentioned above.

Table 2.1. Pulsar Survey Comparison

Survey	Central Frequency (MHz)	Limiting Flux Density[a] (mJy)	Detections[b]	Reference
AODrift	327	0.59	7/13	Deneva et al. (2013)
HTRU−S (low-lat)	1352	0.40	0/9	Keith et al. (2010a)
HTRU−S (med-lat)	1352	0.95	3/27	Keith et al. (2010a)
HTRU−S (high-lat)	1352	1.2	1/8	Keith et al. (2010a)
SUPERB	1352	0.4	2/15	Keane et al. (2018)
LOTAAS	134	0.63	10/39	Sanidas et al. (2019)
PALFA	1400	0.23	0/29	Lazarus et al. (2015)
GBT350	350	0.59	3/6	Boyles et al. (2013)
GBNCC	350	0.70	72/72	Stovall et al. (2014)

[a]Averaged over the survey area and scaled to 350 MHz.

[b]Number of detections of pulsars from this survey by GBNCC/number of pulsars from this survey within the GBNCC survey area.

Note. — Information about individual detections is reported in Table A.1.

2.3.1 Comparison Between the GBNCC and Overlapping Pulsar Surveys

Out of the 210 pulsars with discovery parameters that are not currently listed in the ATNF catalog, 98 were detected. Names, central frequencies, scaled limiting flux densities, and the ratio of detected to processed pulsars are given for each survey in Table 2.1. It should be noted that there are many pulsars from these surveys (excluding GBNCC) in regions of the sky where the GBNCC survey has yet to observe, and so they may be detected in the future; these pulsars are not included in the counts listed in Table 2.1. Three of these surveys (SUPERB, HTRU-S, PALFA) were conducted at higher frequencies,, where average sky temperature (especially near the Galactic plane) is much lower. This reason and the increased sensitivity to high DM pulsars at high frequency is useful for diagnosing missed detections. Because these pulsars have neither published flux densities nor spectral indices, reasons for missed detections cannot be determined more robustly than

those due to sky temperature, position relative to the survey, extreme nulling/intensity variation, and high DM/short periods. It is also possible that for some of these pulsars, the discovery parameters may not be precise enough to be found in this analysis.

The most surprising missed detections come from the GBT350, AODrift, and LOTAAS surveys, which all have comparable sensitivities and frequencies. In an effort to explain why these pulsars were missed, all of the discovery plots were checked against our results, and acceleration searches were run. Three pulsars (J0100+69 and J0121+14 from LOTAAS, and J1854+36 from AODrift) that were originally missed were found on the second trial, as the DM used in the first run was not close enough to the DM at which the pulsar was discovered. For the majority of pulsars that were not detected after re-running the pipeline, the discoveries were quite dim. The LOTAAS survey also has much longer integration times (60 minutes), which significantly improves the chances of the survey detecting pulsars which may be faint and/or nulling. When checking the discovery plots, it became clear that both of these effects were common to many of the missed pulsars. Some pulsars even appeared to exhibit nulling with 'off' times as large as 100 seconds. Nulling behavior was also seen in many cases for the AODrift survey. For the GBT350 missed pulsars, all three of those that were missed were faint, and several GBNCC beams in which the pulsars were most likely to be found had RFI that spanned the entire 100 MHz band.

Eight binary pulsars that were originally discovered in the GBNCC survey were not detected in the first pass of this pipeline. These pulsars required acceleration searches, which are automatically performed as a part of the search pipeline, but not here. As a part of the missed pulsar analysis, we ran an additional acceleration search using `ACCELSEARCH` from within the `PRESTO` package, and they were all detected. We also reprocessed data for 15 binary pulsars from the ATNF catalog with short ($\leq$ 0.5 day) orbital periods that were not detected in the first pass using acceleration searches; none of these were de-

Table 2.2. Broken Powerlaw Spectral Indices.

PSR	α_l[a]	α_h[a]	Break Frequency (MHz)
J0034−0534	0.6(3)	−3.1(2)	181
J0218+4232	1.15(7)	−2.7(4)	149
J1900−2600	0.2(4)	−1.89(15)	204
J2002+4050	0.2(16)	−1.51(18)	378

[a]Spectral indices below (α_l) and above (α_h) the break.

Note. — Quantities in parentheses are uncertainties in the last digit. See Figure 2.2 for the corresponding plots.

tected.

Pulsars with long periods (greater than 2.5 s) were also followed up with a search for single pulses. Because these pulsars would only be observed for at most 48 pulses, non-detections are more common. To address this, we implemented `single_pulse_search.py` from the `PRESTO` package, which searches a range of dispersion measures to find bright single pulses in the data and characterize them by their S/N. In this way, a pulsar that is not detected via a periodicity search may be found by individual pulses. However, we were still unable to find these pulsars using this method.

2.3.2 Spectral Indices

Many previously published spectral indices were determined from flux measurements from high-frequency surveys (e.g., see Jankowski et al., 2018a). Therefore, low frequency surveys like the GBNCC survey provide more stringent constraints on these calculations.

Results from this analysis are listed in Table A.1. The majority of the pulsars in this data set follow a single power law, or do not have enough (>2) flux density measurements to fit multiple power law functions. However, there are a small number of cases where the emission is better fit by a broken power law, defined instead as a piecewise function composed of two power laws. All 339 pulsars for which we measured spectral index had three or more flux measurements (including our 350 MHz measurements) and were checked by eye to determine whether or not a broken line fit was appropriate. Four pulsars fit these criteria. For these pulsars, we fit two lines, one for high frequency flux density measurements and one for low frequency. The breaking point for the power law was determined by finding the maximum change in the derivative of flux density with respect to frequency. A similar analysis was done in Murphy et al. (2017). Plots of these cases are provided in Figure 2.2 with both indices included. These plots also display the best-fit line to all measured flux densities. The measured values of α_l and α_h are reported in Table 2.2.

2.3.3 Comparison of Dispersion Measure with Catalog Values

The relatively low frequency of the GBNCC survey allows much higher precision DM measurements than typical 1400-MHz surveys, as dispersion across the band scales as ν^{-2}. As pulses propagate through the interstellar medium, this dispersion results in a frequency dependent delay that smears out the arrival time of the pulse. Tools within the `PRESTO` package adjust for this, shifting the low frequency portion of the signal back in time to line up the pulse across the band. Using the `dmsearch` flag contained within the `PRESTO` command `prepfold`, we processed each of the pulsars and recovered more accurate values of DM. The program adjusts for dispersion and then folds the data at the pulsar's period to line up the pulses in both time and frequency. When `dmsearch` is off,

the program does not tune the DM to maximize S/N; otherwise, the DM which aligns the pulses in frequency is returned as a new DM. In some cases, RFI caused the DM searching algorithm to return erroneous values for DM, and so we were unable to refine the dispersion measure. For these pulsars, we include the previously published DM in Table A.1 and mark them with a double dagger. More often, we were able to improve upon the previously published values of DM. Most of the discrepancies were small, but in some cases, our more precise DM measurement differed from the previous value significantly. For the pulsars with significant changes to their previously catalogued DM, we followed up with `TEMPO`[3] (maintained and distributed by Princeton University and the Australia Telescope National Facility). We split each detection into four subbands and created precise pulse times-of-arrival (TOAs) which can then be utilized to fit for DM. This method provides marginally more precise measurements, and so was only performed on pulsars with significant changes to previous DM measurements ($\geq 3\sigma$). All newly measured DMs are presented in Table A.1, and Table A.2 highlights the pulsars which were followed up with `TEMPO` timing.

2.4 SURVEY SENSITIVITY

2.4.1 Efficiency of GBNCC Survey

In total, there were 5633 unique beams analyzed, yielding 1328 unique detections of the 670 pulsars. Given that there were 102948 beams that had been observed at the beginning of this project, this corresponds to an average number of detections per beam of ~ 0.013 (0.063 detections per square degree), and ~ 0.38 detections per hour of observing. The ability to detect pulsars at 350 MHz is limited most stringently by sky temperature and scattering in the interstellar medium (which correlates with dispersion). The expected

[3] http://tempo.sourceforge.net

S/N for detections is inversely proportional to system temperature, which is dominated by sky temperature near the Galactic plane. At 350 MHz, this effect is quite significant, with temperatures approaching 1000 K in this region. Scattering is especially detrimental in the detection of pulsars with short periods, as even a few milliseconds of smearing can eliminate the pulse entirely. Given a particular spin period and the estimated DM smearing, we can estimate the minimum flux density that will be detected by the survey. This relationship comes from solving Equation 2.2 for flux density and assuming both an average sky temperature and duty cycle for the pulsars in the survey. Plotted in Figure 2.3 are curves corresponding to a number of trial values of DM, showing the sensitivity floor at those values. Because DM and sky temperature are correlated, we determined the average sky temperature for each curve that is plotted, resulting in an increase in minimum detectable signals for higher DM pulsars. Also plotted are flux density measurements for detections made by this survey and expected flux density measurements for the pulsars which were not successfully detected. The colors in the plot correspond to the dispersion measure of each pulsar, showing how pulsars that may be intrinsically bright enough to be detected can still be missed because of dispersive smearing and/or scattering. The minimum flux density expected to be measured in the survey (regardless of spin period) can be determined to be the asymptotic value of the DM curve corresponding to the faintest detection. This value is directly proportional to the minimum S/N which results in a detection, hereafter $\mathrm{S/N_{cut}}$, which was found to be $\sim$3.8. For all detections, we plot both the expected S/N at 350 MHz as well as the measured S/N of the detection. These are plotted in Figure 2.4 along with a line marking unity. There is a large spread about this line, due mostly to stochastic noise sources in the data (telescope noise, temperature fluctuations, scintillation, and variable pulsar emission). When examining these results, several of the more significant outliers were analyzed in closer detail.

One of the three significant outliers in the lower right portion of the plot was found to be a new nulling candidate, and the other two were initially labeled as possible nullers that could not be verified without higher resolution observations.

Low frequency observations can result in significant deterioration of the pulse due to scattering and scintillation effects, as residual dispersive time delay within a frequency channel with finite width increases as ν^{-3} and scattering roughly as ν^{-4} (Lorimer & Kramer, 2004). Both of these phenomena result in a broadened pulse and subsequently a reduction in S/N. To shed light on the causes for some of the missed pulsars, we calculate the expected S/N using information from both the catalog and information about the beams in which we expect to detect them. We predict flux density at 350 MHz calculated as described in §2, determine the masked fraction of the closest beam to the pulsar's position (when measured), and determine T_{sys} for the corresponding sky position. To determine W, we fit a line to our measurements of W_{10} as a function of spin period and draw from this function. This allows for a measurement of the spin period-pulse width relation at 350 MHz, supplementing previous measurements at other frequencies. This best fit line was measured to be $W_{10} = 18.5^{\circ}(4)P^{0.270(10)}$, which is consistent with the relation determined in Johnston & Karastergiou (2019) modulo a frequency-dependent scaling factor (for a more in-depth analysis, see Chen & Wang, 2014). This fit is shown in Figure 2.5.

After drawing widths from either the catalog or the above function (based on availability of previous measurements of W_{10} near 350 MHz), we determined the expected S/N for all non-detections. These are plotted along with the measured S/N for all of the detections in Figure 2.6. The detections have been divided between those found from the catalog and those discovered by the GBNCC survey, and non-detections are divided based on Galactic latitude. These divisions allow for direct comparison between the survey's ability to detect pulsars blindly as well as the limits placed on the survey by high

temperatures and scattering near the Galactic plane. Included in the plot are three different S/N cutoffs placed during different stages of the survey. The least stringent cutoff of S/N = 12 comes from Stovall et al. (2014), where it was used as an estimated cutoff for detection to predict the survey's sensitivity. At this S/N, $\simeq$75% of non-detections are not expected to be detected. Pulsars close to the plane generally have lower S/N as the temperature is so high, while pulsars outside of the plane generally have smaller DM and temperature but more scintillation. The two detection curves show that the GBNCC is sensitive to intrinsically fainter pulsars, as the histogram is skewed toward lower measured S/N than those from the catalog. Note that there was one pulsar discovered by the GBNCC search pipeline with S/N = 5.98, which is the bin to the left of the search S/N cutoff.

In Figure 2.7, we plot all pulsars' periods against their dispersion measure. Each point's color and shape describe whether or not the pulsar was detected, and if not, whether we expect to have detected it. Missed detections that were unexpected are plotted with point sizes reflecting the expected flux density (calculated as described in §2.2) normalized by the value of the effective sensitivity curve for that pulsar, so larger points indicate pulsars with expected flux density much higher than the minimum detectable flux density at the pulsar's position.

In total, there are 116 undetected pulsars plotted in Figure 2.7 that have been classified as "unexpected" by the logic above. Many of these pulsars are quite close to the sensitivity line, and so small errors in other flux density measurements and spectral indices may change them to "expected." Because the effective sensitivity curve includes temperature and bandwidth (RFI, by proxy) information, reasons for missed detections are limited to effects that are harder to characterize. The most likely contributors include scintillation, abnormal pulsar behavior (i.e. nulling), and imprecise previous measure-

ments of pulsar parameters resulting in inflated expected flux densities. Scintillation depends on DM (Cordes & Lazio, 1991), with increased timescales for smaller DM. Many of the non-detected pulsars that are outside of the Galactic plane are in this low-DM high-scintillation regime, and are likely to have been obscured (the expected number of scintles in the observation are on the order of $\sim$10). Many of the other missed detections, especially those from surveys with comparable limiting fluxes, were inspected individually. Many of these were obscured by significant RFI across the band. For example, PSR J0108−1431 (spin period of $\simeq 0.81$ s and DM of 2.38 pc cm^{-3}, to the right of the bottom center of Figure 2.7) should be easily detected but was obscured by RFI. When examining a number of the other sources, it was found that many of the published spectral indices came from a 1400 MHz study conducted by Han et al. (2017), and were unusually steep. This steepness results in high expected values of flux at 350 MHz, which are not reflected in our results.

2.4.2 RFI Analysis

To visualize how RFI affects the efficiency of the survey, we determined the limiting flux density for each beam based on a S/N cutoff of 3.8, the temperature at the sky position of the beam, and the bandwidth available after RFI excision. Figure 2.8 displays a histogram of the beams by their limiting flux, and Figure 2.9 shows these same data projected onto their sky positions. The sky map depicts a few important characteristics of the survey: the most obvious is the decreased sensitivity near the Galactic plane, but also visible are many individual pointings within the completed regions where significant RFI masking has reduced sensitivity. To mitigate this, these beams will be scheduled for reobserving. There is a small discrepancy between the number of observed beams displayed in Figures 2.1 and 2.9 due to a backlog of data which has yet to processed, and so mask fractions have

not been determined for these beams.

2.4.3 Nulling/Mode-Changing Candidates

The large set of data analyzed in this study as well as the "by-eye" verification of all detections allowed for easy identification of potential nulling/mode-changing candidates in the results. This way, we are sensitive to nulling timescales between that of the pulsar spin period and the observation time (120 seconds). These cases were first identified by the appearance of missing pulses in the time-phase plots from processing using the `PRESTO` package. When a pulsar was noted as a candidate, we followed up using the `dspsr`[4] package. We folded the time series data in 10 second integrations, zapped remaining RFI by hand, and integrated across frequency using the `pav` and `pam` commands within `PSRCHIVE`[5]. When it was possible to discern on- and off-pulse regions by eye (i.e. significant changes in intensity for some rotations), the candidates were considered likely to be nulling. Some pulsars exhibited behavior similar to mode-changing, where multiple components of the averaged profile were found to be on during different portions of the observation. These pulsars were not treated differently than other nulling candidates – we folded for single pulses to determine the likelihood that different components were visible. All of these sources will be followed up in later works regarding these data. In total, 223 pulsars were found to exhibit intensity variations similar to nulling or mode-changing during their observations, 62 of which have not previously been found to to do so. These candidates' names are marked in Table A.1 with an asterisk.

[4] http://dspsr.sourceforge.net/index.shtml
[5] http://psrchive.sourceforge.net/index.shtml

2.4.4 The Galactic Pulsar Population

Given its overall sky coverage and the large number of pulsar detections reported here (670), the GBNCC survey will play an important role in future understanding of the Galactic pulsar population. To date, the GBNCC survey has detected 571 non-recycled (long-period) pulsars in the Galactic field and 70 Galactic MSPs, which have undergone recycling and have spin periods, $P < 30$ ms. Remaining detections are either associated with globular clusters (3) or are recycled pulsars with spin periods, $P > 30$ ms (26), and have been intentionally ignored for the following analysis, since our current models do not adequately describe the features of this sub-population.

To estimate expected numbers of non-recycled/millisecond pulsar detections in the GBNCC survey, Galactic populations were simulated using PSRPOPPY2[6], a more recent and currently-maintained version of PSRPOPPY (Bates et al., 2014, and citations within). Pulsar populations were generated using PSRPOPPY2's `populate` function, which simulates pulsars by drawing parameters from predefined distributions until some condition is met. Due to its large sample size, population estimates from the Parkes Multibeam Pulsar Survey (PMPS) provide the best-known sample parameters. For this reason, these results were used to set a limit on the number of pulsars simulated by `populate`. For the non-recycled pulsar population, pulsars were generated until a synthetic PMPS "detected" 1038 sources; for MSPs, the desired population size was set to 30,000 sources. Specific parameters defining pulsars' Galactic radial distribution, as well as scale height, spin period, luminosity, and duty cycle can be found in Swiggum et al. (2014). However, an updated model for the MSP P-distribution (Lorimer et al., 2015) was implemented in simulations here.

Synthetic surveys were conducted with 100 realizations each of the Galactic non-

[6]https://github.com/devanshkv/PsrPopPy2

recycled/millisecond pulsar populations using `survey` and a GBNCC model file, including survey parameters identical to those presented in §2.2 and lists of completed/remaining GBNCC pointing positions. In the first round of simulations, we fixed the S/N limit for detections to $\mathrm{S/N_{cut}} = 3.8$ (as determined in §2.4.1). This simulation predicted 1442/126 simulated detections for non-recycled/millisecond pulsar populations, respectively (on average; compared to 571/70 actual detections). We then fixed the number of simulated non-recycled/millisecond pulsar detections to their actual values (571/70) and found nominal S/N thresholds for each sub-population, $\mathrm{S/N_{cut}} = 15.3/9.1$. The discrepancies between simulated and actual yields suggest uncertainties in population parameters informed primarily by the PMPS survey, which targeted the Galactic plane and was conducted at 1.4 GHz. Population parameters determined by these previous surveys produce over-estimates for GBNCC pulsar yields. As an all-sky, low-frequency search, the GBNCC survey (when complete) will be a valuable counterpoint to further refine non-recycled/millisecond pulsar population parameters. As we will show below, positional and rotational parameters of the simulated populations do not match the detected population when these thresholds are set.

To test the validity of underlying non-recycled/millisecond pulsar populations, we compared cumulative distribution functions (CDFs) of simulated (`sim`) pulsar parameters (P, DM, S_{350}, and b) with those of the actual (`act`) detections using a `scipy` implementation of the 2-sample Kolmogorov–Smirnov (K-S) test. For each parameter, the K-S test statistic and p-value were computed over a range of $\mathrm{S/N_{cut}}$. When $p < 1\%$, the null hypothesis (that `act`/`sim` parameters are drawn from the same underlying distribution) is rejected. Figures 2.10 and 2.11 illustrate these comparisons for non-recycled and millisecond pulsar population parameter distributions, and Table 2.3 summarizes K-S test results when the nominal $\mathrm{S/N_{cut}}$ values for non-recycled/millisecond pulsar sub-

Table 2.3. K-S test statistics and p-values resulting from comparisons between actual/simulated parameter distributions for non-recycled/millisecond pulsars. In cases where the p-value is $< 1\%$, the null hypothesis (that the two distributions are the same) is rejected.

Parameter	Normal[a]		MSP[b]	
	K-S	$p(\%)$	K-S	$p(\%)$
Spin Period (P)	0.20	$\ll 1$	0.14	10
Dispersion Measure (DM)	0.21	$\ll 1$	0.26	< 1
Flux Density (S_{350})	0.13	$\ll 1$	0.21	< 1
Galactic Latitude (b)	0.04	41	0.17	3

[a]For simulated non-recycled pulsars, $\mathrm{S/N_{cut}} = 15.3$.

[b]For simulated MSP population, $\mathrm{S/N_{cut}} = 9.1$.

populations (15.3/9.1) are implemented, though we measured these p-values for a range of imposed $\mathrm{S/N_{cut}}$ values.

Comparing `act/sim` parameters for the non-recycled pulsar population, we find broad agreement between b distributions, regardless of $\mathrm{S/N_{cut}}$. Results for other non-recycled pulsar parameters in Table 2.3 show significant inconsistencies between `act/sim` samples. DM distributions are clearly different for $\mathrm{S/N_{cut}} > 4$, likely due to an over-abundance of low-DM simulated detections. For $\mathrm{S/N_{cut}} = 15.3$, we find twice as many `sim` detections with $\mathrm{DM} < 35\,\mathrm{pc\,cm^{-3}}$. Presumably due to the prevalence of nearby `sim` sources, this sample also has a larger fraction of high-flux density sources, so S_{350} distributions are statistically different for $\mathrm{S/N_{cut}} = 15.3$. However, there is a small window ($10.25 < \mathrm{S/N_{cut}} < 12.25$) where `act/sim` S_{350} distributions become statistically similar, with $p > 1\%$. The null hypothesis is rejected for P due to `act/sim` log-normal distributions having different mean values: $\langle \log P_{\mathrm{act}} \rangle = 2.88$ versus $\langle \log P_{\mathrm{sim}} \rangle = 2.72$ (see Figure

2.10). This discrepancy persists, regardless of chosen $\mathrm{S/N_{cut}}$.

Because the simulated versions of the non-recycled pulsar population were primarily informed by PMPS (e.g. Lorimer et al., 2006), which was conducted at 1.4 GHz and exclusively covered regions of sky near the Galactic plane ($|b| < 5\,^{\circ}$), we expect there to be bias toward highly dispersed pulsars near the plane. Due to more uniform sky coverage and – near the Galactic plane – higher sky temperatures and more significant scattering at 350 MHz, the majority of GBNCC detections (67%) are away from the plane ($|b| > 5\,^{\circ}$). Young pulsars are typically born in the plane and tend to be found nearby, therefore GBNCC's reduced sensitivity to low-latitude sources means that relatively few detections are young pulsars. The P-$\dot{P}$ diagram in Figure 2.12 nicely illustrates this shortage of pulsars detected with characteristic ages, $\tau \leq 1$ Myr. By imposing an age cutoff on non-recycled pulsars in the ATNF catalog, $\tau > 1$ Myr, the resulting simulated spin period distribution is statistically similar to that of GBNCC detections (K-S $p > 1\%$). This selection effect accounts for the apparent differences between `act`/`sim` P-distributions, but can not explain discrepancies in S_{350} and DM distributions for non-recycled pulsars.

K-S tests comparing `act`/`sim` parameter distributions for the MSP population show better agreement (see Table 2.3 and Figure 2.11). For MSPs, selection effects based on Galactic latitude and spin period do not come into play since MSPs are more isotropically distributed and model parameters for this sub-population are based on results from multiple Parkes Telescope surveys (see Lorimer et al. (2015), and references therein). For these reasons, the simulated population's spin periods are statistically similar to the sample detected by GBNCC. This conclusion does not change, regardless of the chosen $\mathrm{S/N_{cut}}$ value. For b, the null hypothesis is still not rejected by our criteria ($p < 1\%$). Based on the b histograms themselves, there appears to be an absence of detections in the `act` sample in/near the Galactic plane, which is not the case for `sim` sources. The null hypothesis is

rejected for S_{350} due to the over-abundance of high-flux-density sources in the `sim` sample compared to those present in the `act` sample. Median flux densities for `act`/`sim` detections are 4.9/6.8 mJy respectively. Comparing `act`/`sim` DM distributions, the `sim` sample consists of a higher fraction of high-DM MSPs and 12% of simulated detections have DMs in excess of the `act` maximum value, $104.5\,\mathrm{pc\,cm^{-3}}$. This is likely related to the bias toward high-flux-density detections noted in S_{350} for `sim` MSPs mentioned above.

Based on discrepancies between predicted yields from simulations and actual numbers of detections by the GBNCC survey, it appears that model parameters need to be further refined in order to generate more realistic Galactic pulsar populations in the future. For now, we proceed with nominal $\mathrm{S/N_{cut}}$ values in order to estimate the GBNCC survey's future yields. In the remaining ≈21,000 pointings, we expect an additional 160/16 non-recycled/millisecond pulsar detections, or $\approx 60/5$ discoveries, accounting for detectable known pulsars in regions of sky remaining (Manchester et al., 2005a).

2.5 CONCLUSIONS

We have provided all detections of currently known pulsars that exist within the area of the 350 MHz GBNCC pulsar survey and performed some preliminary analysis of the resulting data set. Specifically, we have provided new flux density and pulse width measurements as well as pulse profiles for the 670 detections. When possible, we used our flux density measurements with previous measurements at different frequencies to refine spectral index. We also made a measurement of the spin period-pulse width relation, observing a powerlaw correlation of the form $W_{10} \propto P^{-0.27}$. The low frequency of the survey provides increased sensitivity to dispersion, allowing for more precise measurements of DM for many pulsars that have only been measured in high frequency surveys. Using all of this information, we have made quantitative measurements of the survey's efficacy

and the RFI environment at 350 MHz, with a minimum detectable S/N of $\sim$3.8 and a mean limiting flux density of 0.74 mJy. These measurements have allowed us to make realistic predictions about the survey's yield when complete based on the detectability of known pulsars in the dataset, and we expect to detect on the order of 160 non-recycled pulsars and 15 MSPs. The simulations from which these expectations come uncovered discrepancies in DM, spin period, and spatial distribution in the Galaxy for the simulated populations which will be addressed in a future study. Combing through the data following processing has brought many interesting characteristics of pulsars in the survey to light, including 223 pulsars exhibiting evidence of variable intensities suggestive of nulling/mode-changing and 4 showing evidence for broken power-law spectral energy distributions. These kinds of qualitative observations pave the way for follow-up quantitative analyses of these data and the remaining beams that will be observed in the next few years.

ACKNOWLEDGEMENTS

We thank our anonymous referee for their suggestions and guidance. This work was supported by the NANOGrav Physics Frontiers Center, which is supported by the National Science Foundation award 1430284. The Green Bank Observatory is a facility of the National Science Foundation (NSF) operated under cooperative agreement by Associated Universities, Inc. R.S. acknowledges support through the Australian Research Council grant FL150100148. WF acknowledges the WVU STEM Mountains of Excellence Graduate Fellowship. MM and MS acknowledge the National Science Foundation OIA award number 1458952. JvL acknowledges funding from the European Research Council under the European Union's Seventh Framework Programme (FP/2007-2013) / ERC Grant Agreement n. 617199 ('ALERT'), and from Vici research programme 'ARGO' with

project number 639.043.815, financed by the Netherlands Organisation for Scientific Research (NWO). VMK acknowledges the NSERC Discovery Grant, the Herzberg Award, FRQNT and CRAQ, Canada Research Chairs, CIFAR and the Webster Foundation Fellowship, and the Trottier Chair in Astrophysics and Cosmology. Computations were made on the supercomputer Guillimin at McGill University[7], managed by Calcul Quebec and Compute Canada. The operation of this supercomputer is funded by the Canada Foundation for Innovation (CFI), NanoQuebec, RMGA and the Fonds de recherche du Quebec - Nature et technologies (FRQ-NT). The CyberSKA project was funded by a CANARIE NEP-2 grant. PC acknowledges the FRQNT Doctoral Research Award. SMR is a CIFAR Senior Fellow. Pulsar research at UBC is supported by an NSERC Discovery Grant and by the Canada Foundation for Innovation.

[7] www.hpc.mcgill.ca

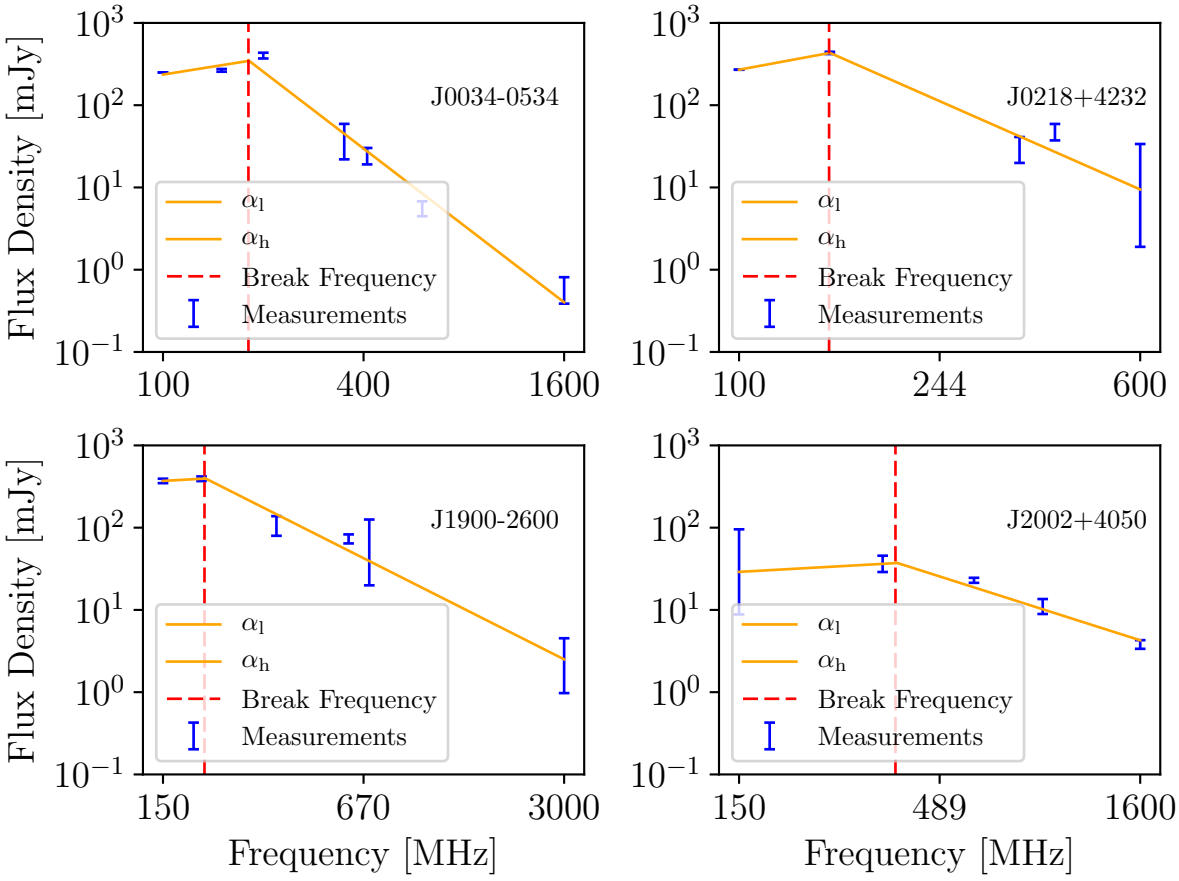

Figure 2.2 Pulsars with broken power-law spectral indices. We plot all available measurements of flux density in the ATNF catalog as well as the 350 MHz measurements made in this study against observing frequency. We fit two disjoint lines to the low- and high-frequency measurements (orange solid lines). The red dashed line indicates the frequency of the turnover in the spectrum, determined by finding the point at which the two lines match up. Information for these measurements is presented in Table 2.2.

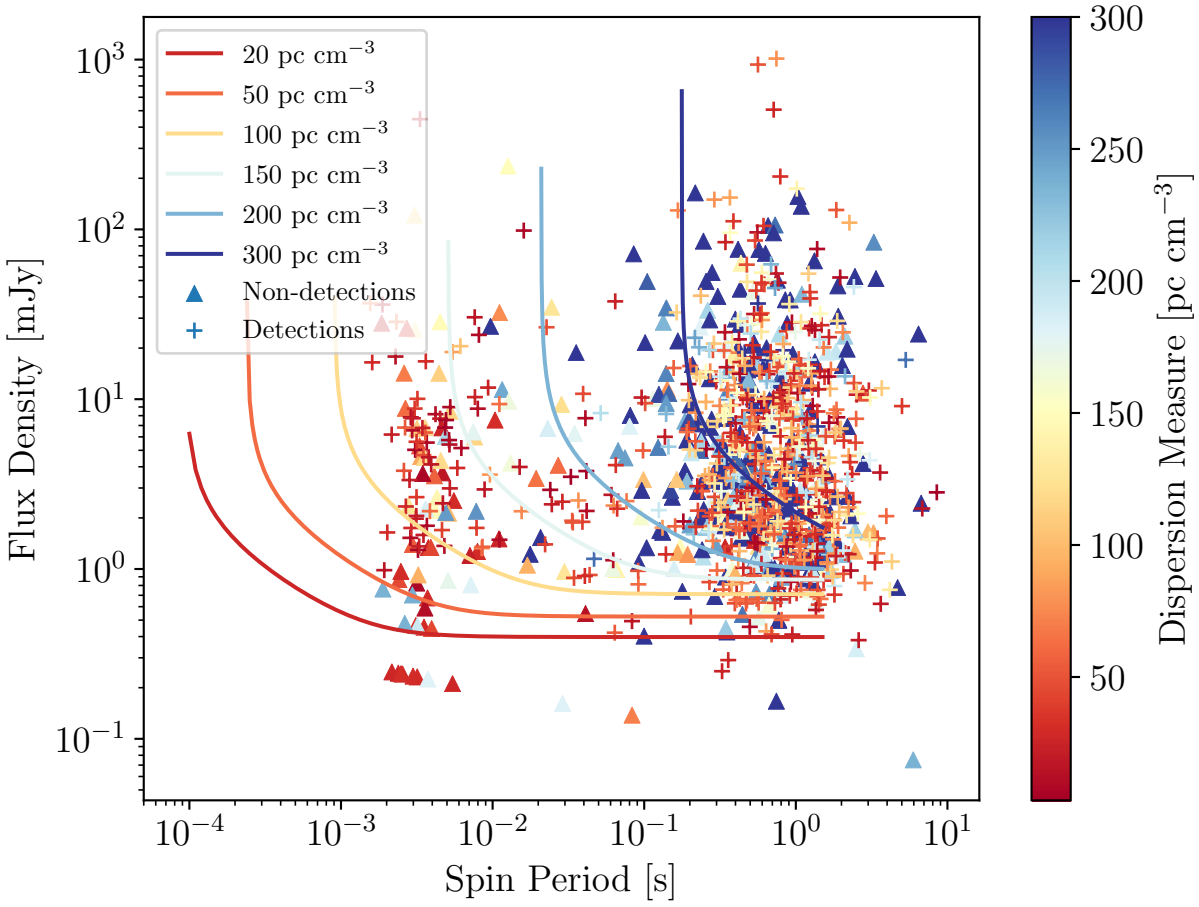

Figure 2.3 Flux density sensitivity in the GBNCC as a function of pulse period. Assuming a duty cycle of 6% and an average unmasked bandwidth of 67 MHz (which incorporates a 20 MHz rolloff in the bandpass), we plot the predicted lower limit on the flux density of detectable pulsars for dispersion measures of 20, 50, 100, 150, 200, and 300 pc cm^{-3}. To determine the sky temperature for the curves, we found the average sky temperature as a function of DM using the sky temperatures at the positions of all detected pulsars. We then drew from this function the temperatures at each DM for which a curve is plotted. For the above DMs, the function returns 95, 126, 171, 208, 237, and 273 K. We glean the minimum detectable S/N for the survey by matching the curves to the faintest detection. This was found to be ∼3.8. Higher DM pulsars are more susceptible to smearing, and so the likelihood of detection is decreased for high DM, short period pulsars. We also plot both the detections (plus symbols) and non-detections (triangles), which are colored by their DM.

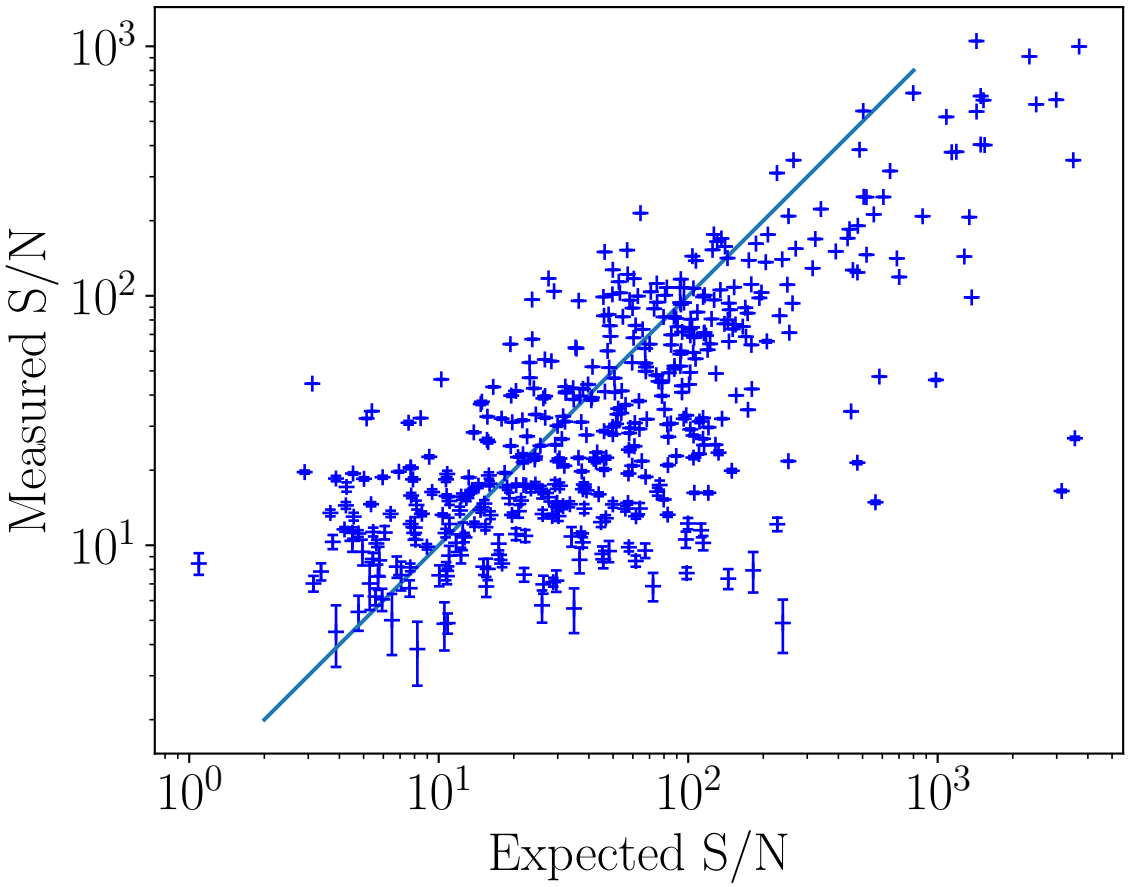

Figure 2.4 Measured S/N vs. expected S/N for detections in the GBNCC survey. Extrinsic contributions to expected S/N include system temperature, telescope gain, scintillation, and offset from the beam center (newer pulsars without full timing solutions may have significant uncertainties in position). Errors in these quantities, previous flux measurements, and spectral indices increase the spread about unity, as does variable pulsar emission, i.e. nulling.

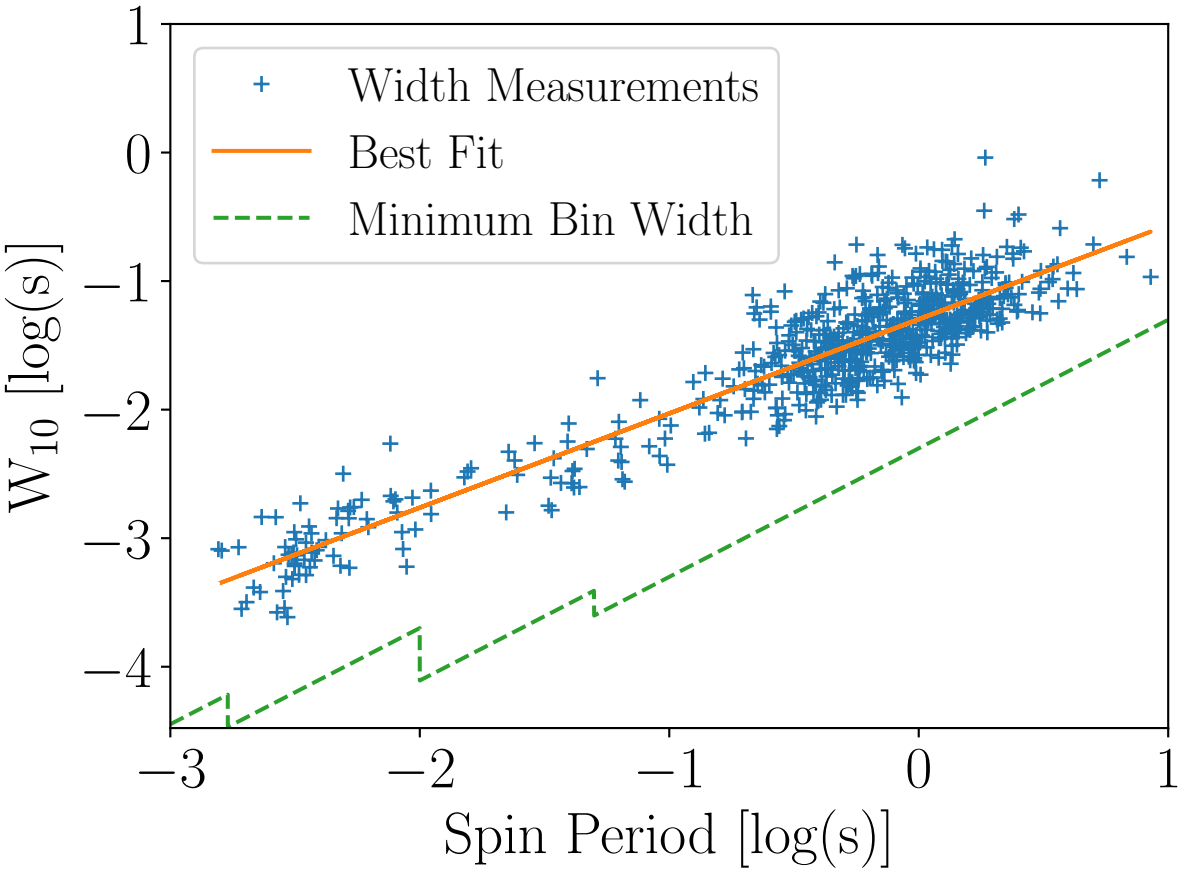

Figure 2.5 Pulse width at 10% of the pulse maximum as a function of spin period. The solid line shows the line of best fit through the data, described by $W_{10} = 18.5^{\circ}(4)P^{0.270(10)}$. The dashed line shows the minimum bin width as a function of period, as described in §2.2.

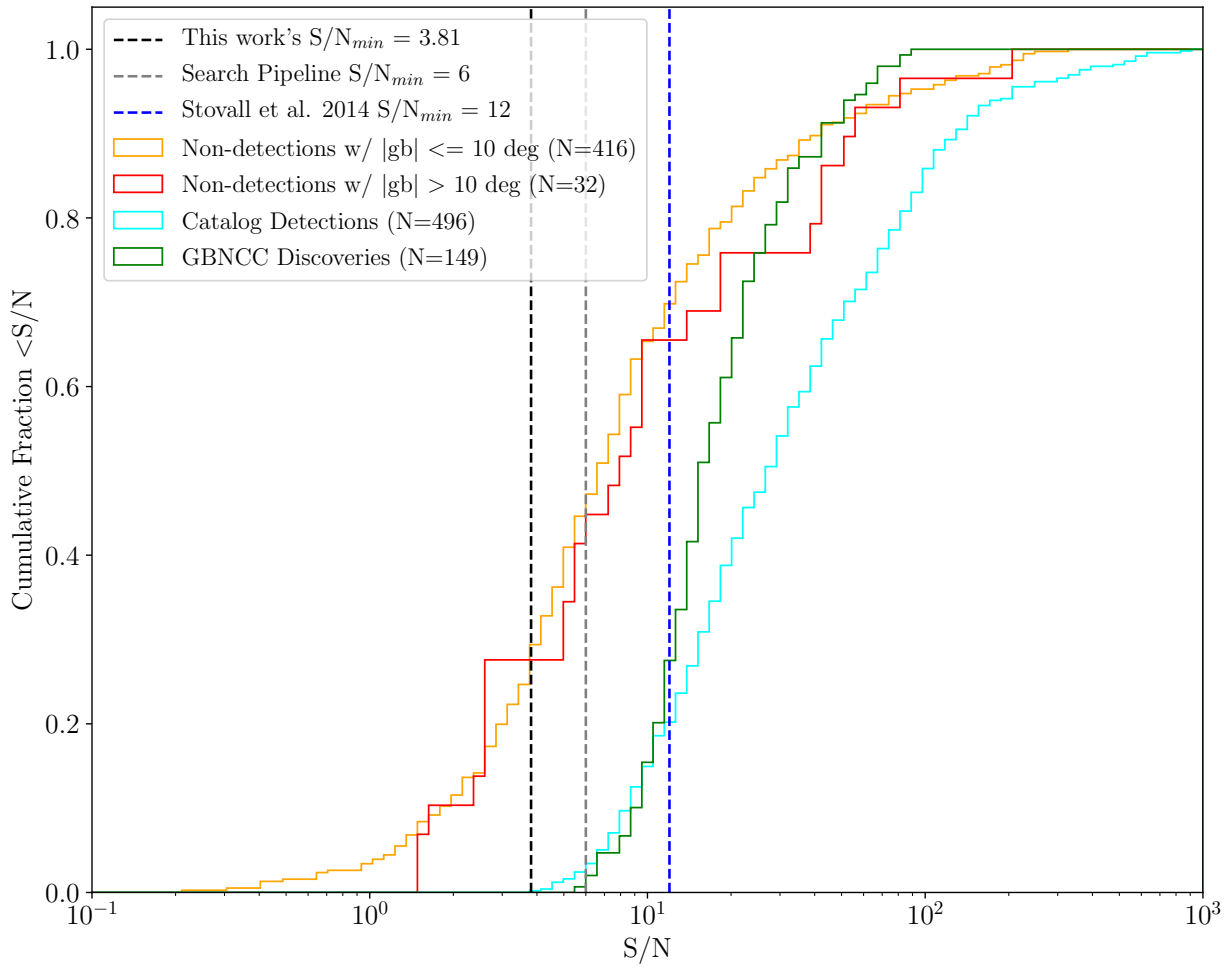

Figure 2.6 Histograms of measured S/N for detections and expected S/N for non-detections. Detections are differentiated by GBNCC discovery/catalog pulsars (green/-cyan lines), and non-detections by distance from the Galactic plane (the red line indicates pulsars that are within 10° from the plane, and the orange line indicates pulsars outside of this region). The dashed lines indicate three different S/N cutoffs: the first line, in black, show the minimum S/N detected in the survey; the second, in grey, indicates the significance down to which candidates are folded in the GBNCC search pipeline; and the third, in blue, shows the predicted S/N limit used in Stovall et al. (2014) to predict sensitivity of the survey.

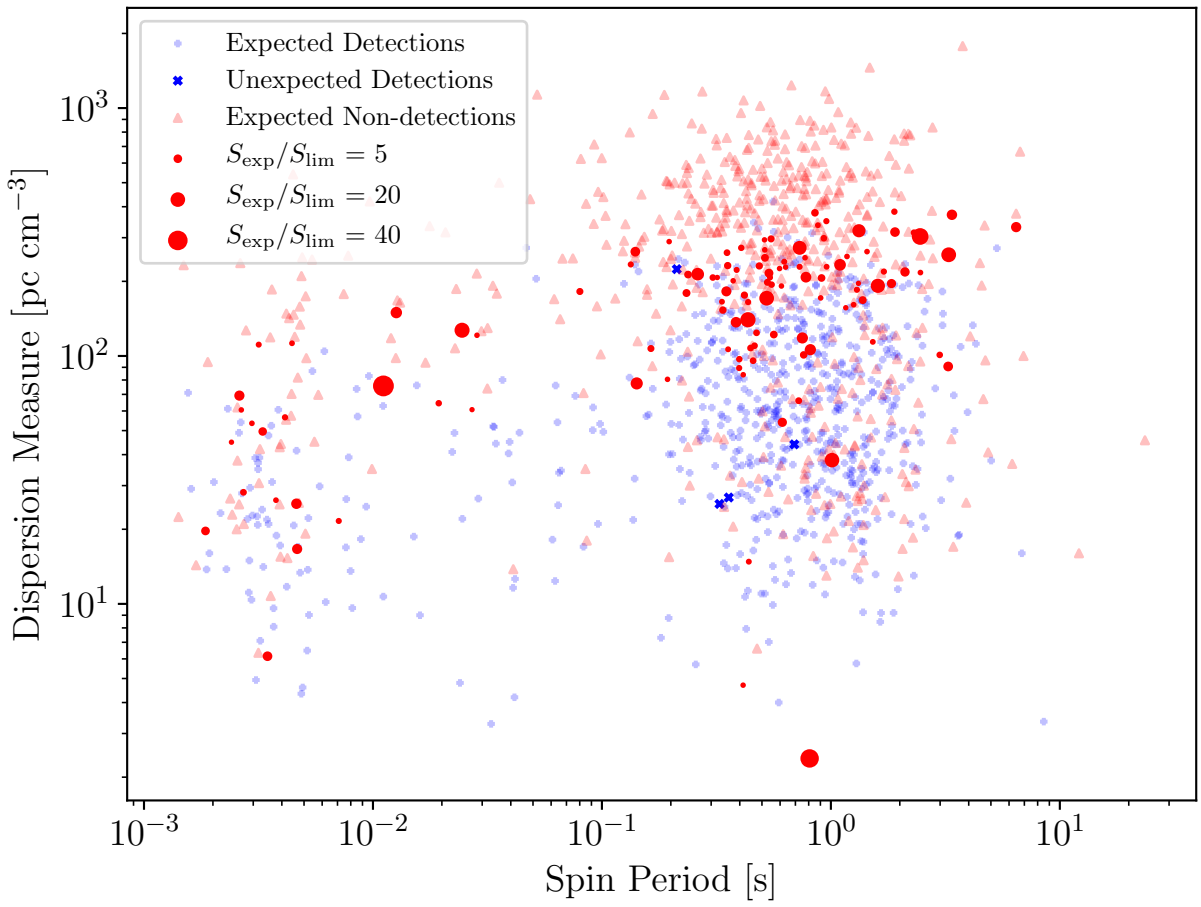

Figure 2.7 Period vs. DM for all included pulsars. Blue symbols indicate detections made by the survey, and red symbols indicate non-detections. Red triangles indicate missed pulsars that were not expected to be detected, in that they lie below the expected sensitivity of the survey. Red circles indicate missed pulsars that lie above their expected sensitivity, and so were unexpected non-detections (see §2.4.1 for details). Blue circles indicate detections that were expected, and blue x symbols indicate detection of pulsars with expected flux densities that were below our sensitivity limit. The area of these points is given by the ratio of expected flux density to the limiting flux density at the pulsar's position.

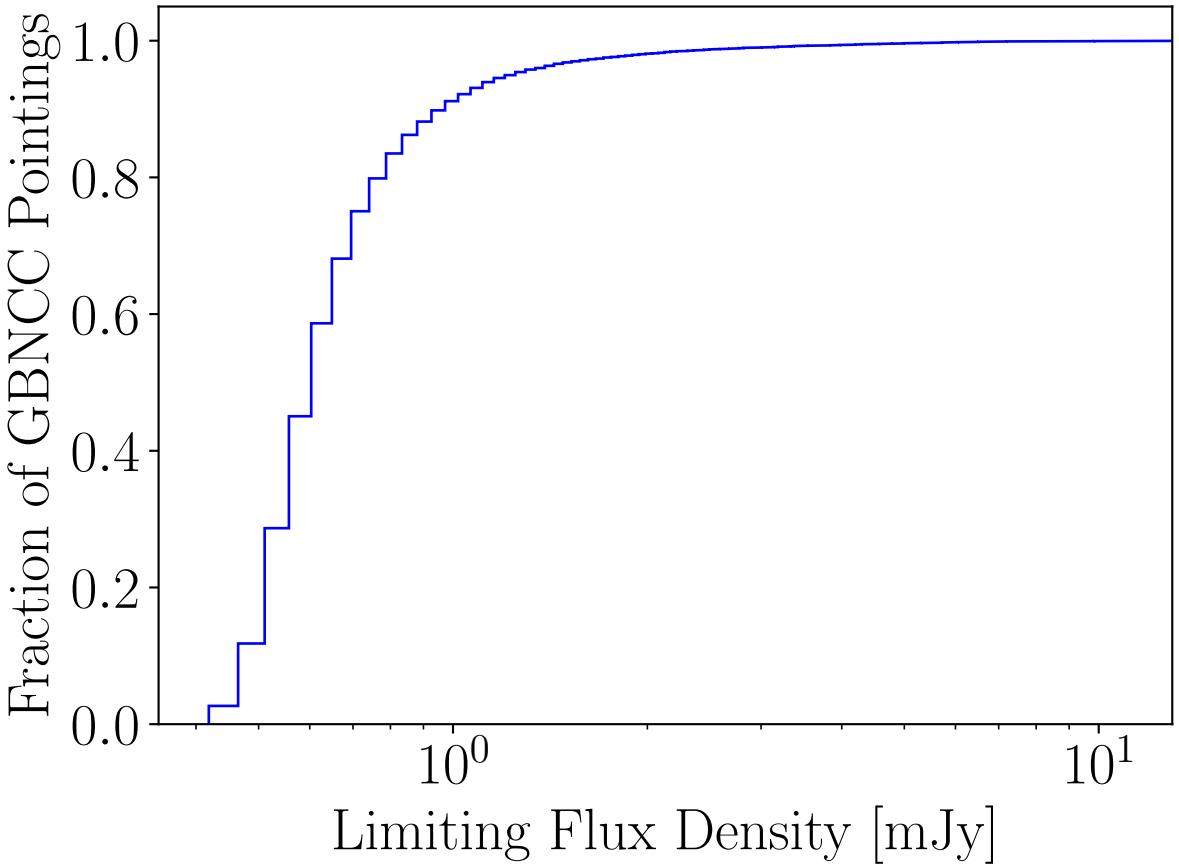

Figure 2.8 Cumulative histogram of limiting flux density for GBNCC. The mean and median limiting flux densities in the histogram 0.74 mJy and 0.62 mJy, and the values range from 0.42 mJy to 47. mJy. All flux density values are given in mJy.

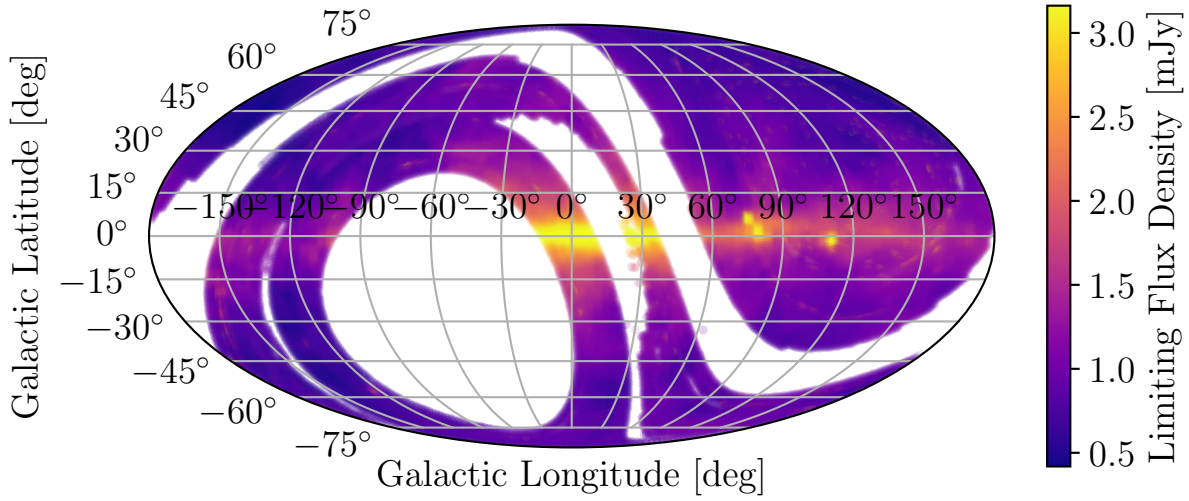

Figure 2.9 Sky map of GBNCC beams, colored by limiting flux density. The map is plotted in Galactic coordinates on a Mollweide projection, and the flux density is given in mJy.

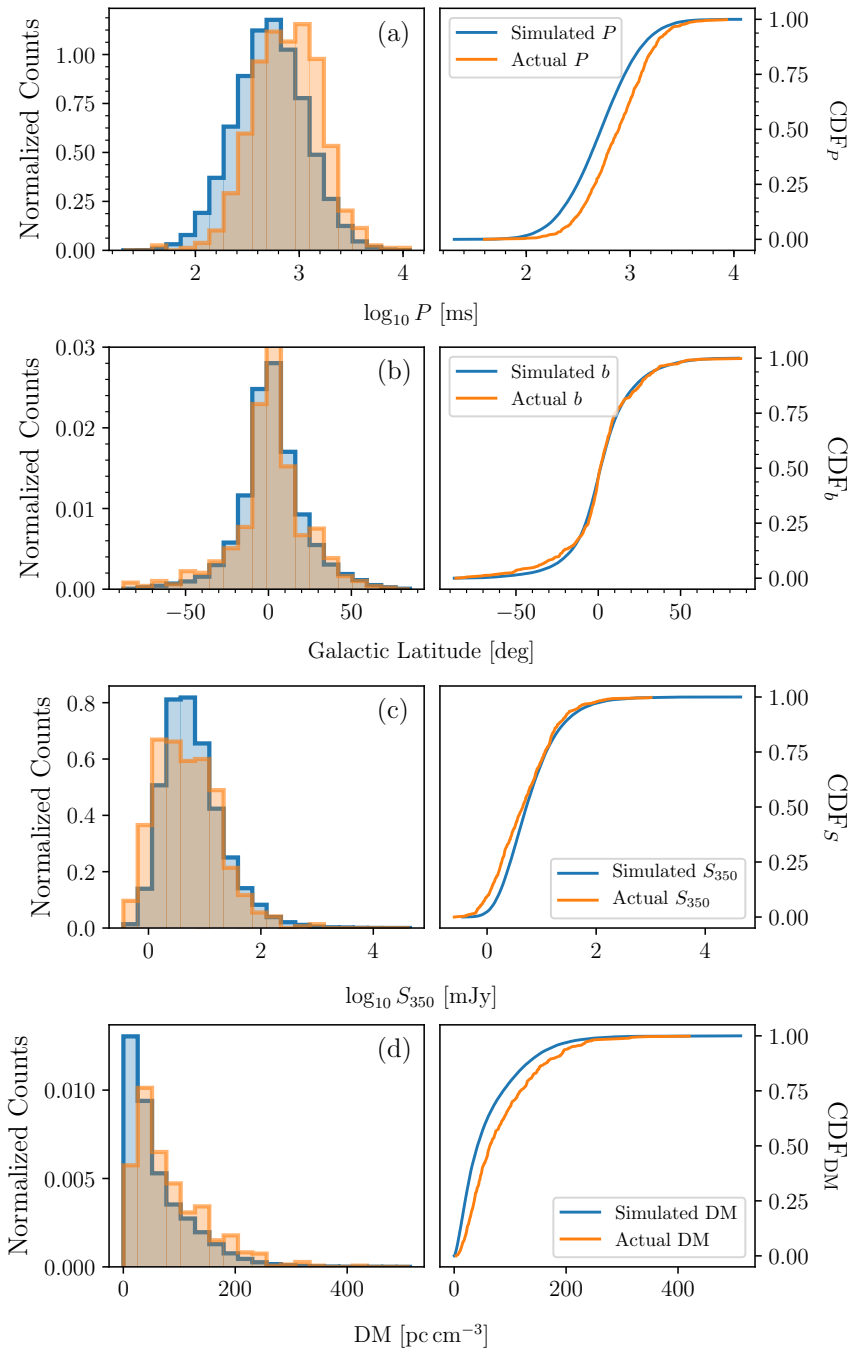

Figure 2.10 Normalized histograms showing comparisons between (a) spin period, P, (b) Galactic latitude, b, (c) flux density, S_{350}, and (d) dispersion measure, DM, distributions for simulated non-recycled pulsars (blue) and actual detections (orange). The rightmost panel in each row compares actual/simulated CDFs for each parameter. K-S tests comparing these CDFs (see Table 2.3 for details) show disagreement between `act/sim` P, S_{350}, and DM distributions, but $p = 41\%$ for b distributions.

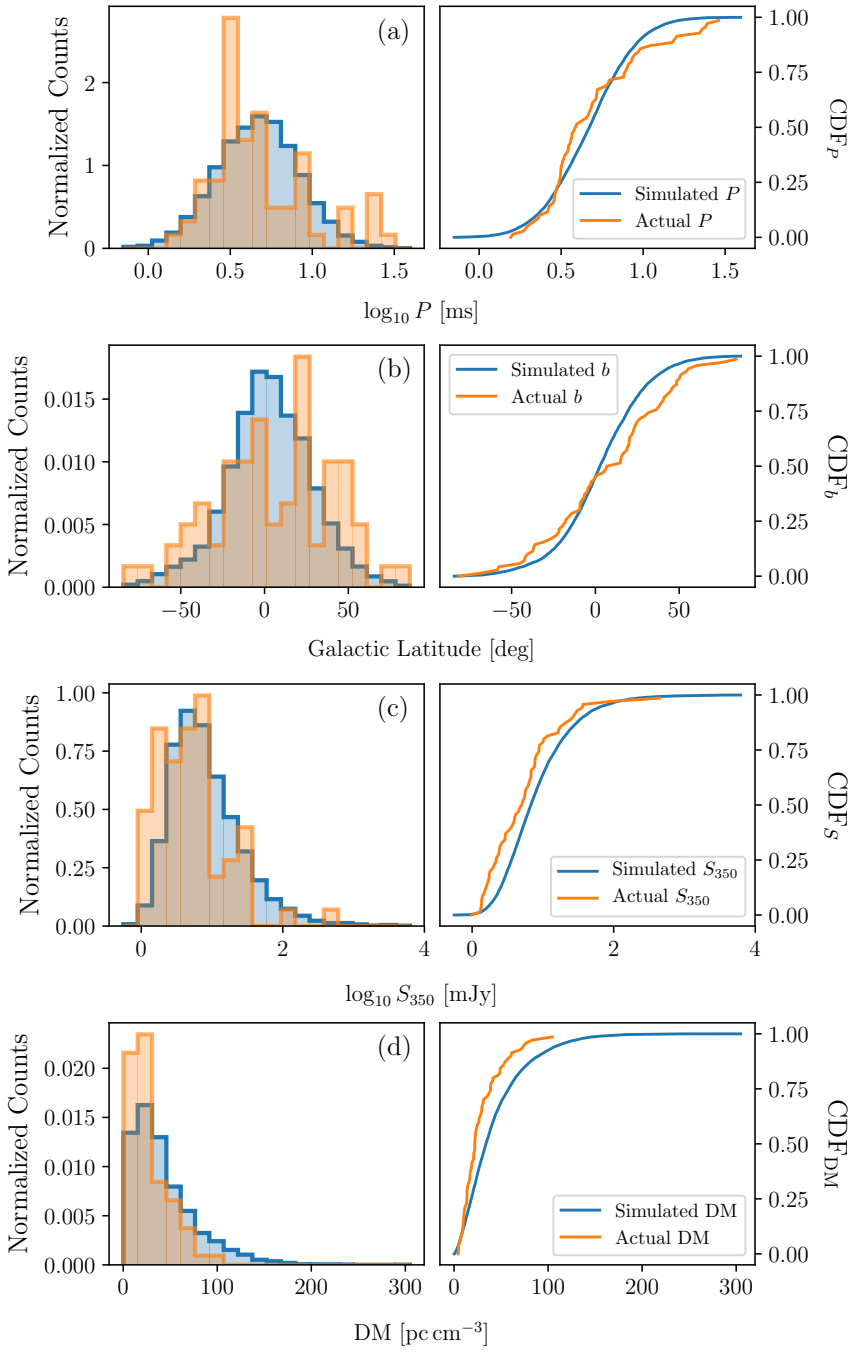

Figure 2.11 Normalized histograms showing comparisons between (a) spin period, P, (b) Galactic latitude, b, (c) flux density, S_{350}, and (d) dispersion measure, DM, distributions for simulated millisecond pulsars (blue) and actual detections (orange). The rightmost panel in each row compares actual/simulated CDFs for each parameter. K-S tests comparing these CDFs (see Table 2.3 for details) show disagreement between `act/sim` S_{350} and DM distributions, but distributions for b and P have $p = 3\%$ and 10%, respectively.

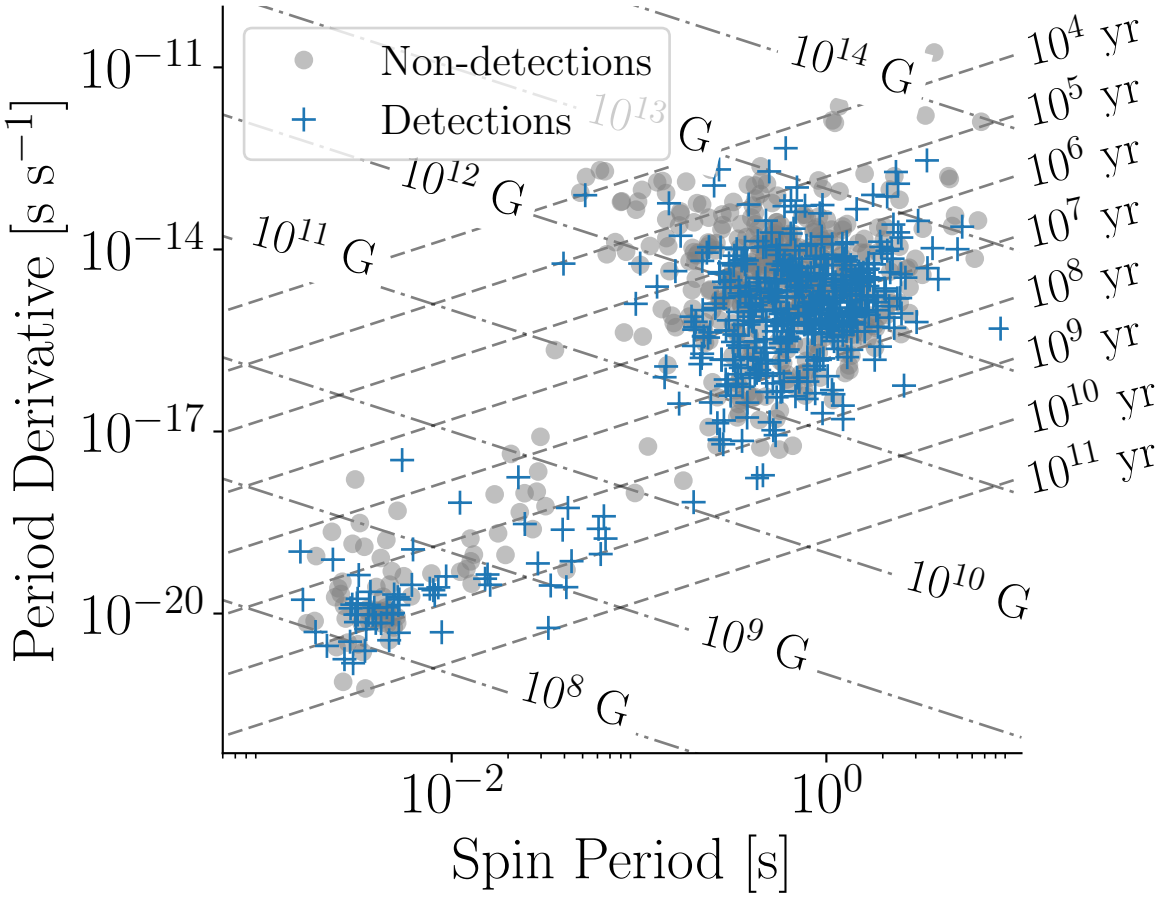

Figure 2.12 Period vs. period derivative for pulsars in GBNCC survey area. Shown in grey are pulsars that were not detected, and blue plus symbols show detections.

CHAPTER 3

The Green Bank 820 MHz Pulsar Survey I: Survey Overview and Initial Results

3.1 INTRODUCTION

As our understanding of the physical laws that provide the scaffolding for the universe improves, laboratories for further study continue to evolve toward the exotic and uncommon. Pulsars are excellent subjects for many such extreme experiments, as their rotational stability (Verbiest et al., 2009) make them unmatched for tracking time across Galactic distances. With masses that are only subordinate to those of invisible black holes, they exist in a fringe region of gravity. This makes them suitable subjects for a host of gravitation experiments, ranging from individual mass measurements and neutron star equation of state (EOS) constraints (Özel & Freire, 2016; Cromartie et al., 2020; Agazie et al., 2021) to measurements of gravitational waves from super massive black hole binaries (both as individual sources, i.e. Babak et al. (2016); Aggarwal et al. (2019); Arzoumanian et al. (2023), and as a stochastic background of all sources, i.e. Shannon et al. (2013); Lentati et al. (2015); Arzoumanian et al. (2020)) and detailed descriptions of the distribution of matter in the interstellar medium (Turner et al., 2021; Wahl et al., 2022).

This potential for extreme science is only limited by the number of sources available. To date, there are > 3300 pulsars listed in version 1.7 of the ATNF catalog[1] (Manchester et al., 2005b). These sources range more than 3 orders of magnitude in period and dispersion measure (DM), and include nearly 400 binary systems. And yet, population models predict tens of thousands more pulsars in the Galaxy than those that are visible to us, if

[1] https://www.atnf.csiro.au/research/pulsar/psrcat/expert.html

only we know where (and how) to look (Swiggum et al., 2014; Kaplan et al., 2019; Sengar et al., 2023). Every new pulsar provides an opportunity for improving our understanding of the population. Pulsar searching is crucial to expand this population, and to continue the search for new scientific avenues.

3.2 SURVEY MOTIVATION AND OVERVIEW

The rate of pulsar discovery has changed rapidly over the past several years. Surveys that cover vast regions of the sky (Manchester et al., 2001; Stovall et al., 2014; Sanidas et al., 2019; Cameron et al., 2020) are complemented by smaller, deeper searches in regions of particular interest (Ridley et al., 2013; Titus et al., 2019; Hisano et al., 2022). Both strategies have been successful, and both are necessary to understand the underlying pulsar population. These searches are made more efficient with ever-improving sensitivity limits set by new instruments (Braun et al., 2019; Jiang et al., 2019; Gautam et al., 2022) and candidate sifting techniques (Karako-Argaman et al., 2020; Yu et al., 2020; Sengar et al., 2023). Cataloging the Galactic pulsar population has only just begun.

The Cygnus region observed in this work is known to harbor many sites of stellar formation, including extensive OB associations (Comerón & Pasquali, 2012; Berlanas et al., 2019; Quintana & Wright, 2021; Orellana et al., 2021; Quintana & Wright, 2022), Wolf-Rayet stars (WRs, Koch-Miramond et al., 2002; Rauw et al., 2015) and HII regions (Beerer et al., 2010; Emig et al., 2022). As such, it has been invaluable for studying the entire life cycle of stars – many of which have formed within the past few million years (van der Walt, S. J. et al., 2021; Beuther et al., 2022). Many of these studies have focused on the relatively nearby ($\simeq 1.4\,\mathrm{kpc}$, Rygl et al., 2012; Orellana et al., 2021) star forming region along this line of sight, known as Cygnus-X (Piddington & Minnett, 1952). Beyond it lie two more Galactic arms, one of which is home to the extensively studied Cygnus

X-3, a microquasar in a binary with a WR star that exhibits both X-ray and radio emission (Trushkin et al., 2017; Broderick et al., 2021; Suryanarayanan et al., 2022; McCollough et al., 2022). Needless to say, studying the Cygnus region has revealed a very complex history of stellar evolution. This makes it a prime target for pulsar surveys, as pulsars are formed following the supernovae of massive stars.

Despite this, searches for pulsars in this region have been somewhat light, and have not covered a particularly wide range of radio frequencies. At the time that this study began, only 15 radio pulsars had been previously identified in the GBT820 region. Given that these sources were identified primarily in low radio frequency surveys (Stokes et al., 1985; Dewey et al., 1985a; Hessels et al., 2008), it was hypothesized that the dense regions of material here may hamper low radio frequency detection of pulsars. Surveys at high radio frequencies that have covered this region include the Parkes Multibeam Pulsar Survey (PMPS, Manchester et al., 2001), the Pulsar Arecibo L-band Feed Array survey (PALFA, Cordes et al., 2006), the High Time Resolution Universe survey (HTRU, Keith et al., 2010b); no new pulsars were detected from these surveys in Cygnus. Observing frequencies above 1 GHz are not subject to the same deleterious scattering/dispersion effects, so an explanation for the dearth of pulsars is likely related to the intrinsic faintness of pulsars.

The GBT820 survey was designed to strike a balance between these two regimes, opting for a mid-range observing frequency of 820 MHz. The average DM of the known pulsars in Cygnus is $\simeq 195\,\mathrm{pc/cm^3}$; maximum DMs from YMW+16 (Yao et al., 2017) and NE2001 (Cordes & Lazio, 2002) reach as much as $500\,\mathrm{pc/cm^3}$, and several recent discoveries significantly exceed this (e.g., PSR J2030+3944g, J2021+4024g, Han et al., 2021). Compared to 400 MHz, pulse smearing in a given frequency channel due to smearing is reduced by a factor of $\simeq 0.04$ (per Equation 5.2 in Lorimer & Kramer (2004)). And assuming

a mean spectral index for pulsar emission of -1.76 (Posselt et al., 2023), pulsars observed at 820 MHz will be about 2.6 times brighter (on average) than they would appear in a comparable scan at 1400 MHz. And so, GBT820 was conceived to find young pulsars buried in the Cygnus region.

3.3 OBSERVATIONS AND DATA REDUCTION

Observations were conducted during the semesters of 2016A and 2017A (Project code GBT16A-349, PI R. Lynch). The region of interest was divided into 4752 grid points covering the region of $75° \leq l \leq 94°$, $-3° \leq b \leq 6.1°$ (172.9 square degrees), though only 3457 of these were actually observed. Scans were taken using the guppi backend (DuPlain et al., 2008) and the GBT's 820 MHz prime focus receiver, covering 200 MHz of bandwidth and lasting 4.5 minutes at 82 us time resolution. The bandwidth was divided into 4096 channels for fine DM resolution and RFI mitigation. We list survey parameters in Table 3.1, and the survey region is shown in Figure 3.1.

Following observations, data were processed on the Béluga supercomputer operated by the Digital Research Alliance of Canada[2]. Processing followed a pipeline similar to the one described in Stovall et al. (2014): raw data were cleaned using an automated radio frequency interference (RFI) zapping scheme and `rfifind` in the `PRESTO` package (Ransom, 2001), dedispersed at a number of trial DMs, and subsequently Fourier transformed. Due to significant RFI near 745 MHz and 885 MHz, we removed a total of 40 MHz from all data before processing, leaving 160 MHz of the survey bandwidth. Peaks in the resulting Fourier spectra were folded and diagnostic plots were produced to be assessed by eye.

Aside from searching in frequency space, searches for significant single pulses were conducted on the data. We utilized tools in `PRESTO` to identify and validate these candi-

[2] https://docs.alliancecan.ca/wiki/Beluga/en

Table 3.1. Overview of survey parameters. Aside from the observation setup and sky coverage, we include the number of pulsars detected/discovered in the survey and minimum detected flux density.

Parameter	Value/Range
Galactic Latitude b (deg)	$[-3, 6.1]$
Galactic Longitude l (deg)	[75, 84]
Sky Area (deg^2)	172.9
$N_{\rm obs}/N_{\rm surv}$	3457/4752
Center Frequency ν (MHz)	820
Bandwidth $\Delta\nu$ (MHz)	200
Dwell Time $T_{\rm obs}$ (s)	270
Pulsars Discovered/Detected	4/20
Minimum Flux Density $S_{\rm min}$ (mJy)	0.08

dates, and broadband pulses peaking at non-zero DMs were categorized as possible Rotating Radio Transient (RRAT, McLaughlin et al., 2006) or Fast Radio Burst (FRB, Petroff et al., 2022) candidates.

3.4 CANDIDATE INSPECTION/FOLLOW-UP

Candidates from the survey pipeline were checked by eye following the automatic folding. When a candidate was identified, an initial position (from the beam in which it was detected) and an initial rotational model was used to search for the sources using the Canadian Hydrogen Intensity Mapping Experiment (CHIME) telescope (CHIME/Pulsar Collaboration et al., 2021). To compare the sensitivity of the two instrumental setups, we can compare the minimum predicted flux density detectable in a given observation with both telescopes. We use published mean system equivalent flux densities for both CHIME

(55 Jy, Merryfield et al., 2023) and the GBT (15 Jy, from the GBT proposer's handbook[3]. Because CHIME is a static transit telescope, the gain and observation duration is dependent on declination. This makes predictions somewhat more complex; for simplicity, we assume an average duration of about 15 minutes and an average bandwidth of 160 MHz to account for RFI. With these factors in mind, we expect that the ratio of minimum flux densities measurable in a GBT820 survey scan to a CHIME confirmation scan to be approximately 0.7 (though this will depend on the exact sky temperature and how scattered the pulsar is). Despite this loss in sensitivity for a single observation, the availability of daily cadence with CHIME allows for multiple observations to be summed in short order. Still, non-detections at CHIME are less conclusive than those made with the GBT with better sensitivity, and were followed up with GBT observations as is described in Section 3.5.

3.4.1 Periodic Candidates

Candidate signals that reached a significance threshold $(6\,\sigma)$ in the Fourier spectrum of dedispersed data were folded using `prepfold` from the `PRESTO` package. This process produces descriptive plots that include temporal, spectral, and diagnostic information about the observation and candidate. Signals from data dedispersed with DM $> 0\,\mathrm{pc\,cm^{-3}}$ that persist in frequency and time at a given rotation phase indicate astrophysical, repeating sources, and therefore warrant follow-up. When pulsars are accelerated (e.g., by binary motion), the observed signal will be modulated by its motion, which can appear as a sinusoidal variation when the binary period is short enough. This is not typically the case for short survey scans like the ones used in GBT820. More common are orbits with $P_{\mathrm{orb}} \gg T_{\mathrm{obs}}$, where this variation is limited to a small orbital phase range and is better

[3] https://www.gb.nrao.edu/scienceDocs/GBTpg.pdf

approximated as a linear or parabolic drift in the pulsar's period. To account for this motion (and search for such sources), we also implemented the `accelsearch` routine from PRESTO, which searches over a specified range of pulsar accelerations and removes the modeled signature from the time series data. From the 3457 beams that were searched, 140490 FFT candidate plots were produced. Included in the search pipeline are tools for single pulse analysis, but this was left for a future work.

3.4.2 Known Pulsars

The survey area contains 50 known pulsars, 32 of which are listed in the ATNF catalog. The remaining sources are posted on survey websites that are linked in Tables 3.2 and 3.3 and searched via the `pulsar survey scraper` (Kaplan, 2022). Of these sources, 43 are in the region where observations have been completed, and 20 are detected in these data. For these pulsars, we measure pulse widths and flux density at 820 MHz using the brightest (highest signal to noise, or S/N) detection. We define the S/N as

$$\mathrm{S/N} = \sum_i \frac{p_i - \bar{p}_{\mathrm{off}}}{\sigma_{\mathrm{off}}\sqrt{W_b}}, \tag{3.1}$$

where p_i is the intensity as measured in a given phase bin, $\bar{p}_{\mathrm{off}}$ and σ_{off} are the mean and standard deviation of the off-pulse bins, and W_b is the pulse window in phase bins. Note that this width differs slightly from the widths reported in Table 3.2 (W_{50} and W_{10}), as W_b includes the entire on-pulse window. For the measurements of W_{50} and W_{10}, we first identify W_b by flattening the profile (removal of a polynomial fit to the off-pulse region; this eliminates additional RFI contamination) and choosing a window that includes all phase bins above the mean off-pulse noise. We then find where in this window the profile drops below 50% and 10% of the pulse maximum, respectively.

Using the S/N measured above, we can translate to pulsar flux density using the ra-

diometer equation (Lorimer & Kramer, 2004):

$$S_{820} = \beta \frac{(\mathrm{S/N}) T_{\mathrm{sys}}}{G\sqrt{n_p t_{\mathrm{int}} \gamma \Delta\nu}} \sqrt{\frac{W}{P-W}} \tag{3.2}$$

where S_{820} is the flux density at 820 MHz, $\beta = 1.1$ is a correction factor due to data digitization, $T_{\mathrm{sys}} = T_{\mathrm{sky}} + T_{\mathrm{rec}} + T_{\mathrm{CMB}}$ is the sum of sky, receiver, and CMB temperatures, $G = 2\,\mathrm{K/Jy}$ is the gain of the GBT, $\mathrm{n_p} = 2$ is the number of summed polarizations, $t_{\mathrm{int}} = 4.5\,\mathrm{min}$ is the observation duration, $\Delta\nu = 200\,\mathrm{MHz}$ is the full bandwidth that is adjusted by the masking fraction γ, W is the pulse width, and P is the pulse period. Sky temperatures in the survey region (calculated using PyGDSM[4]) are mostly in the range of $8 - 50\,\mathrm{K}$, though some points exceed 300 K. Manual excision removed 20% of bandwidth for all beams, with an additional 5–10% from `rfifind`; the mean mask fraction for the survey is $\gamma = 0.79$.

In most cases, the pulsars are detected in multiple nearby survey beams; for the brightest pulsars, this is as many as ten survey beams. For all analyses, we use the detection with the highest S/N. These measurements are presented in Table 3.2, and all pulsars in the survey region are shown in both plots of Figure 3.1.

We examined the 23 missed pulsars to explain their non-detections, and in all cases, non-detections are not surprising. Many of these pulsars have large DMs (only three of the missed sources have DMs $< 250\,\mathrm{pc/cm^3}$), and have been discovered in surveys using the Five Hundred meter Aperture Spherical Telescope (FAST, Jiang et al., 2019, and references therein) at frequencies $\geq 1\,\mathrm{GHz}$ (e.g., J2021+4024g, J2022+3845g, and J2052+4421g, Han et al., 2021, and others listed on the FAST-GPPS website), where scattering has less of an impact and fainter pulsars are still above the telescope's sensitivity limit. Also among the missed detections are a small collection of pulsars discovered via high-energy emis-

[4] https://github.com/telegraphic/pygdsm/tree/master, which uses Haslam et al. (1981).

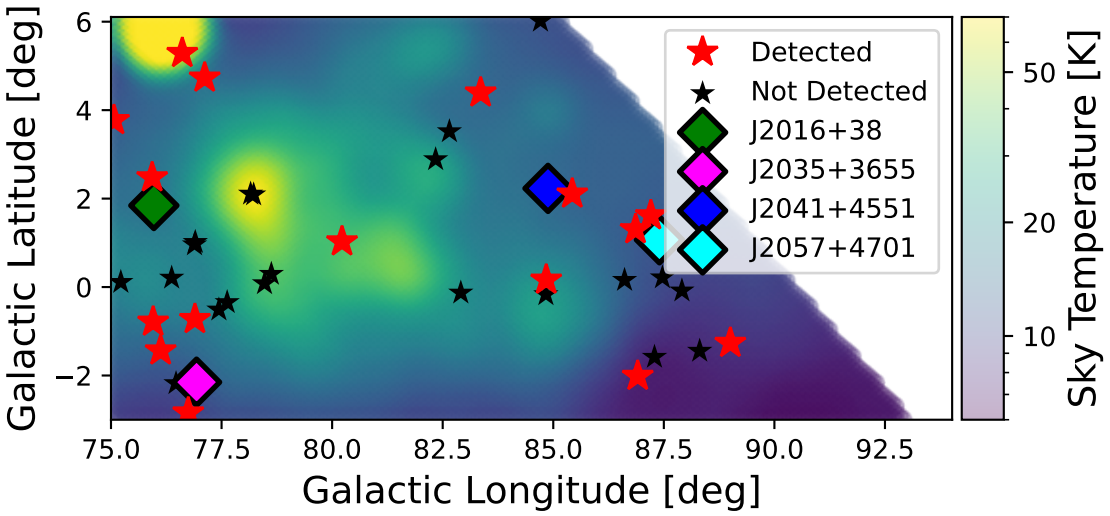

Figure 3.1 GBT820 survey observing coverage. We show a Galactic map of the survey region. Stars indicate pulsars (both from the ATNF catalog and from survey websites, as listed in Tables 3.2 and 3.3), and colors indicate whether the pulsar was detected. We also plot the new discoveries from the survey with diamonds. The background color reflects the system temperature in the survey calculated from PyGDSM and scaled using a powerlaw with spectral index -2.6 (Haslam et al., 1982). The bright source at $l = 76.2°$, $b = +5.8°$ is the radio galaxy Cyg ACygnus A ($S_{820\,\mathrm{MHz}} \approx 3\,\mathrm{kJy}$; Kellermann et al. 1969.) The bright source at $l = 78.2°$, $b = 2.1°$ is the complex region containing the SNR G78.2+2.1SNR G78.2+2.1 (γ Cygni).

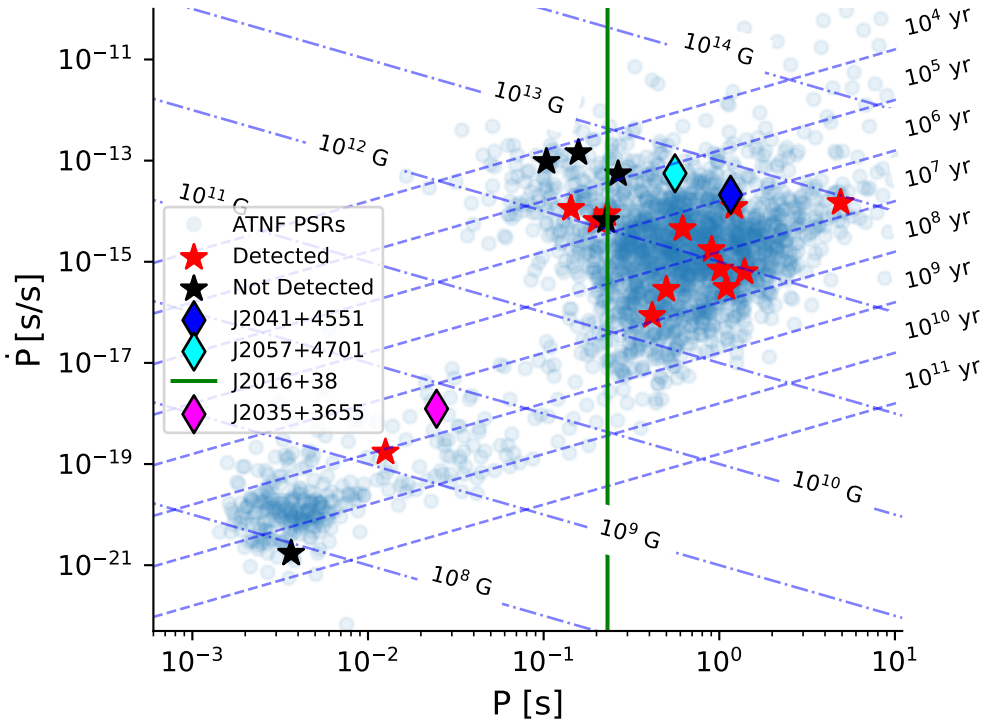

Figure 3.2 $P - \dot{P}$ plot of pulsars. Stars indicate pulsars from the ATNF catalog in our survey region, and colors indicate whether the pulsar was detected. We also include the remaining pulsars in the ATNF catalog as blue circles. Due to the lack of a constraint on $\dot{P}$ for discovery PSR J2016+38, we include a vertical line at its period.

Table 3.2. Flux densities and pulse widths for known pulsars detected in the GBT820 survey. Asterisks in the first column correspond to survey discoveries, and superscripts indicate pulsars discovered in other surveys that have not yet been published.

PSR	S/N	S_{820} (mJy)	W_{50} (ms)	W_{10} (ms)
J2002+4050	235(19)	7(2)	17.5(2)	51.34(5)
J2005+38[1]	7(5)	0.17(13)	102.18(4)	109.61(4)
J2006+4058	36(15)	0.9(4)	18.216(8)	22.373(8)
J2013+3845	191(5)	9(2)	15.28(13)	28.3(2)
J2016+38*	10(3)	0.29(10)	9.842(4)	26.137(4)
J2026+3656g[2]	4(5)	0.08(9)	27.27(3)	79.62(3)
J2027+4557	164(6)	6(2)	19.7(4)	68.3(8)
J2029+3744	105(8)	3.2(8)	19.9(4)	38.8(8)
J2030+3641	19(3)	0.8(3)	9(3)	17(4)
J2032+4127	12(4)	0.6(2)	6.8(4)	12.29(12)
J2035+3655*	12(3)	0.44(13)	0.6840(4)	3.0770(4)
J2037+3621	145(7)	3.7(11)	12.6(11)	35.2(11)
J2041+4551*	30(4)	1.1(2)	45.17(2)	180.12(2)
J2044+4614	80(4)	26.2(9)	26.2(9)	121(13)
J2051+4434g	16(2)	0.6(2)	229.81(2)	378.36(2)
J2053+4650	51(2)	2.6(6)	1.4010(2)	3.4940(2)
J2053+4718	29(3)	1.5(4)	52.25(8)	167.07(8)
J2057+4701*	13(4)	0.28(11)	8.267(9)	22.602(9)

sion, many of which appear to be radio-quiet. Missed detections are included with explanations and references in Table 3.3.

J2024+48 was originally discovered at 350 MHz (GBT350 survey, Hessels et al., 2008) and has a relatively long period (1.2 s) and low DM ($99\,\mathrm{pc\,cm^3}$), initially making its non-detection puzzling. However, subsequent observations have determined an improved position for this pulsar which places it outside of the GBT820 survey area (Jason Hessels, private communication).

Table 3.2 (cont'd)

PSR	S/N	S_{820} (mJy)	W_{50} (ms)	W_{10} (ms)
J2108+4441	371(7)	14(5)	24.1(5)	37.3(4)
J2113+4644	675(7)	36(12)	60.5(15)	203(2)

Note. — Searches through other surveys were done using the `pulsar survey scraper` (Kaplan, 2022). Uncertainties in parentheses are 1σ on the last digit.

[1]Listed on the CHIME-Pulsar (CHIME/Pulsar Collaboration et al., 2021) Discovery page: http://catalog.chime-frb.ca/galactic

[2]Listed on the FAST-GPPS (Han et al., 2021) Discovery page: http://zmtt.bao.ac.cn/GPPS/GPPSnewPSR.html

Table 3.3. Non-detections of known pulsars in GBT820. All of these nondetections have simple explanations, with the majority of missed sources due to the high sensitivity of FAST to high-DM sources in the Galactic plane.

PSR	Explanation	Reference
J2001+4209g	single pulse source	FAST Discovery[1]
J2021+3651	radio-quiet	Abdo et al. (2009)
J2021+4024g	below sensitivity	Han et al. (2021)
J2021+4026	radio-quiet	Ray et al. (2011)
J2022+3842	scattered X-ray pulsar	Arzoumanian et al. (2011)
J2022+3845g	below sensitivity	Han et al. (2021)
J2024+3751g	below sensitivity	FAST Discovery[1]
J2024+48	updated position	Hessels et al. (2008)
J2029+4453g	below sensitivity	FAST Discovery[1]
J2030+3818g	below sensitivity	Han et al. (2021)
J2030+3833g	single pulse source	FAST Discovery[1]
J2030+3929g	below sensitivity	Han et al. (2021)
J2030+3944g	below sensitivity	Han et al. (2021)
J2030+4415	gamma-ray pulsar	Pletsch et al. (2012)
J2034+3632	gamma-ray pulsar	Fermi-LAT[2]
J2042+4550g	below sensitivity	FAST Discovery[1]
J2046+4253g	below sensitivity	FAST Discovery[1]
J2052+4421g	below sensitivity	Han et al. (2021)
J2058+4555g	below sensitivity	FAST Discovery[1]

Table 3.3 (cont'd)

PSR	Explanation	Reference
J2101+4636g	below sensitivity	FAST Discovery[1]
J2104+4644g	below sensitivity	FAST Discovery[1]
J2108+4516	scattered binary system	Good et al. (2021)
J2111+4606	gamma-ray pulsar	Pletsch et al. (2012)

[1]Listed on the FAST GPPS Discovery page: http://zmtt.bao.ac.cn/GPPS/GPPSnewPSR.html

[2]Listed on the Fermi-LAT Discovery page: https://einsteinathome.org/gammaraypulsar/FGRP1_discoveries.html

3.5 DISCOVERIES

At the time of this study, the GBT820 survey had discovered three new pulsars: J2016+38, J2041+4551, and J2035+3655. Another source, J2057+4701, was identified in GBT820 data in February of 2022 and included in a confirmation proposal for spring 2023. However, it has since been published in a recent CHIME paper (Dong et al., 2022). We include it here as a co-discovery. Pulsar parameters for the three new sources are presented in Table 3.4 (including those measured from timing campaigns where appropriate), and will be discussed in more detail below. We also include information about the follow-up conducted for relevant sources in Table 3.5.

During the time of this study, a reprocessing of the GBT820 data using the GPU-based PEASOUP algorithm (detailed in Sengar et al., 2023) was conducted. This pipeline is particularly sensitive to slow pulsars for which multiple harmonics are necessary for detection. In the original PRESTO pipeline, these harmonics are often removed as RFI, and so slow pulsars can be missed. This reprocessing resulted in the identification of two more pulsar candidates, PSRs J2016+4231 and J2019+3810. These sources were subse-

Table 3.4. Measured position/spin parameters and related derived parameters for GBT820 pulsar discoveries.

Parameter Name	J2016+38	J2035+3655	J2041+4551
Measured Quantities			
Right Ascension [deg]	20.2(2)	20.5892119(3)	20.69464(3)
Declination [deg]	38.3(2)	36.931172(4)	45.8496(3)
Dispersion Measure [$\mathrm{pc/cm^3}$]	198.4(10)	136.790(9)	310.0(3)
Spin Frequency [Hz]	4.329043438(98)	40.70837860639(7)	0.8622090188(3)
Spin Frequency Derivative [Hz/s]	–	$-2.0557(9) \times 10^{-15}$	$-1.5704(5) \times 10^{-14}$
Epoch of Period Measurement [MJD]	57524	59328	59360
Derived Quantities			
Spin Period [s]	0.230997913(5)	0.02456496756280(4)	1.1598115749(4)
Spin Period Derivative [s/s]	–	$1.2405(6) \times 10^{-18}$	$2.1125(7) \times 10^{-14}$
Galactic Longitude [deg]	76.0(5)	76.9518573(9)	84.76111(14)
Galactic Latitude [deg]	1.6(4)	$-2.15755730(3)$	2.312631(4)
Surface Magnetic Flux Density [Gauss]	–	5.59×10^{9}	5.01×10^{12}
Spin-down Energy [ergs/s]	–	3.31×10^{33}	5.35×10^{32}
Characteristic Age [Myr]	–	3.13×10^{2}	8.67×10^{-1}
DM Distance [kpc]	6.04	5.41	9.00

Note. — Uncertainties in parentheses are 1σ on the last digit. The range of precision for measured values is due to varied baselines: J2035+3655's binary follow-up included many observations over several years, and so a full timing solution was determined; J2041+4551 was observed at 1400 and 820 MHz with the GBT and also at CHIME (600 MHz); and J2016+38 was confirmed via detection in several survey beams, but was not followed up otherwise. DM distances are calculated using YMW+16; we assume a braking index of 3 to calculate age, and moment of inertia $I = 10^{45}\,\mathrm{g\,cm^2}$ to calculate surface magnetic flux density.

quently confirmed in July 2023. Due to time constraints, they are not included in the rest of this work, but are listed with all of the discoveries on the survey's website, located at https://gbncc.github.io/GBT820_results/gbt820.html.

3.5.1 PSR J2057+4701

Initially noted as a faint FFT candidate, PSR J2057+4701 was added to an internal list of sources needing confirmation in February 2022. It was subsequently included in a list of candidates to be confirmed in early 2023. Its subsequent publication (Dong et al., 2022) prompted a revisit, when we found that the source is notably brighter in a second beam that is $\sim 0.3\,\mathrm{deg}$ away from the first, and had failed in initial processing. We then searched archival GBNCC data and noted a highly scattered pulse there as well, which we discuss

Table 3.5. Follow-up observation information for GBT820 discoveries.

Observatory	MJD	ν, $\Delta\nu$ (MHz)	Duration (min)	$N_{\rm TOAs}$
J2035+3655				
GBT	59328	820, 200	16	10
	59364	820, 200	10	6
	59367	820, 200	10	6
	59368	820, 200	7	6
	59400	1500, 400	20	6
	59611	1500, 400	200	60
	59617	1500, 400	215	60
	59622	1500, 400	224	60
J2041+4551				
GBT	59364	820, 200	20	48
	59400	1500, 400	18	60
CHIME	59270–59385	600, 400	10/day[1]	145

Note. — Due to scheduling complexities, CHIME observations were not strictly daily, but averaged about 5 scans/week.

in Section 3.6.1.

3.5.2 PSR J2016+38

PSR J2016+38 was initially identified in two neighboring survey beams and later found in two other beams. This pulsar is notable for its similarities to PSR J2013+3845 (Hobbs et al., 2004b) in spin period ($\leq 1\%$ difference) and position ($\simeq 50'$ offset). However, the dispersion measure differs by $\simeq 39\,\mathrm{pc/cm^{-3}}$. While discovery parameters for J2016+38 are limited in precision, previous timing of J2013+3845 in Hobbs et al. (2004b) indicate that these parameter differences are very significant ($> 100\,\sigma$ in period and DM).

Using software contained in the `PRESTO` suite, the five detections of this pulsar were manually cleaned of RFI and used to produce arrival times for the pulses (hereafter called times-of-arrival, or TOAs). These TOAs were then timed using `PINT` (Luo et al., 2021). The four detections in survey data span less than a week, but the confirmation scan was conducted over 5 years later. Given this sparse dataset (and the many covariant model components that impact the predicted pulse phase over such a gap), we can only place weak upper limits on the pulsar's model. We report the spin period from timing in Table 3.4, but the position reported there is left uncertain to within a survey beam, and the period derivative is not constrained.

3.5.3 PSR J2041+4551

PSR J2041+4551 was the first discovery in the survey, and is a slower pulsar (spin period of 1.16 s). It was detected in four survey beams, and followup was conducted using CHIME over several days (for an overview of the CHIME system, see CHIME/Pulsar Collaboration et al., 2021). While the pulse was not visible in a single day's observation, summing together six 20-minute observations produced a detection of a highly scattered

pulse. We continued to observe with CHIME for 74 days and split the 400 MHz of bandwidth into two subbands for DM refinement through timing. It was also included in a DDT proposal for the GBT (GBT21A-405, PI: A. McEwen) along with J2035+3655, which included a total of 2.5 h of observations using the 820-MHz receiver. Most of this time was used for J2035+3655, but ∼20 minutes were used to drift over J2041+4551's position in both right ascension and declination (on-the-fly mapping, as in Swiggum & Gentile, 2018) and localized the pulsar to well within a 820-MHz beam at the GBT. The final observations were conducted using the 1400 MHz L-band receiver on the GBT, and consisted of a single 17-min scan. Using the detections in the survey, the CHIME data, and the GBT observations, pulse times-of-arrival (TOAs) were generated using tools within `PRESTO` and timed using `PINT`. The resulting parameters of the fit are included in Table 3.4, and the residuals are shown in Figure 3.3.

3.5.4 PSR J2035+3655

PSR J2035+3655 (J2035) was discovered in two adjacent survey beams with an observed spin period of 24 ms. This period localizes J2035 to a sparse region of the $P - \dot{P}$ plane containing partially-recycled binaries and young, energetic pulsars (see Figure 3.1). These two sub-populations are distinguished by intrinsic $\dot{P}$, which is not generally detectable in survey scans. In the former, the companion undergoes a supernova before the pulsar has accreted enough material to reach a $<$10 ms rotation period. The supernova occurs when the companion is a more massive star; therefore, it is a marker for potential double-neutron star systems (Tauris et al., 2017).

This possibility spurred immediate follow-up observations at CHIME and the DDT proposal described in section 3.5.3. Unfortunately, J2035 was not detected at CHIME, so high cadence observations were not possible. The mapping scans were successful,

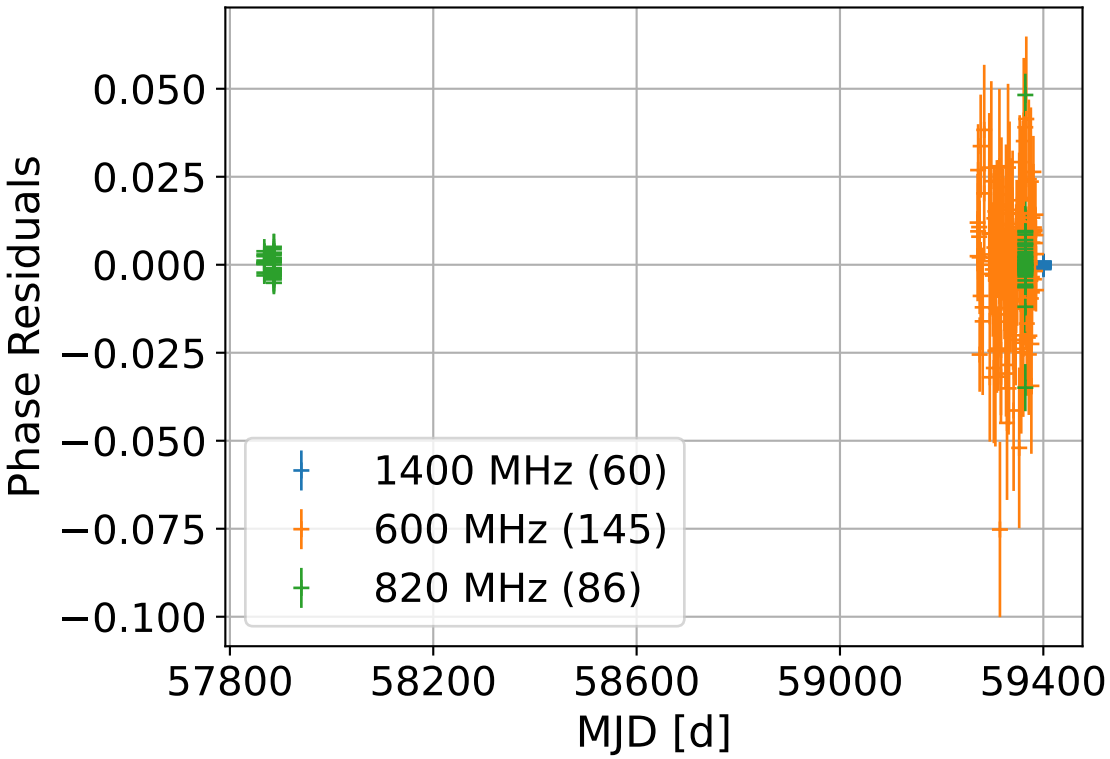

Figure 3.3 Timing Residuals for PSR J2041+4551. Shown as residuals in pulse phase, we include TOAs from three observing setups: green points are the GBT820 survey data, orange are from CHIME (two frequency bands/epoch), and blue are from the 1.4-GHz DDT observations with the GBT.

greatly improving the position and providing evidence of a time-varying spin period. A subsequent proposal (GBT22A-053, PI: A. McEwen) for 12 hours of observations at 1400 MHz with the GBT was accepted, and the time was split over three 4 hr observations spanning a week. This cadence allowed us to observe a significant portion of the binary orbit in a single observation and maintain coherence over the week.

With these data, we measured the parameters of the binary orbit with high significance. These constraints (along with those from the mapping scans) reduced our phase uncertainty enough to connect all of the data, including those in the initial survey beams. The resulting data set contained 227 TOAs spanning >2000 d and grouped in 11 epochs. Using `PINT` and the binary model measured in the high-cadence data, we constrained the rotational model for the pulsar. The rotational parameters are included in Table 3.4, and the binary model is in Table 3.6.

With the phase-connected solution covering superior conjunction in hand, we attempted to measure the Shapiro delay (for original derivation, see Shapiro (1966); for its measurement in the context of pulsar timing, see Kramer et al. (2006)). To do this, we conducted a grid search over the orbital inclination and companion mass and calculated the resulting RMS of the residuals. We limited the search to solutions in which the pulsar mass $M_{\rm P} > 1 M_\odot$ and the companion mass $M_{\rm C} < 2 M_\odot$. This technique resulted in a marginal ($\simeq 2\sigma$) detection of $M_{\rm C}$ and the sine of the orbital inclination $\sin i$. The grid and 1-D projections of the χ^2 for grid points close to the best-fit are shown in Figure 3.4, where we have zoomed in on $\sin i > 0.97$ to highlight the region of most support. We also include timing residuals in Figure 3.5 with the putative Shapiro delay signal shown.

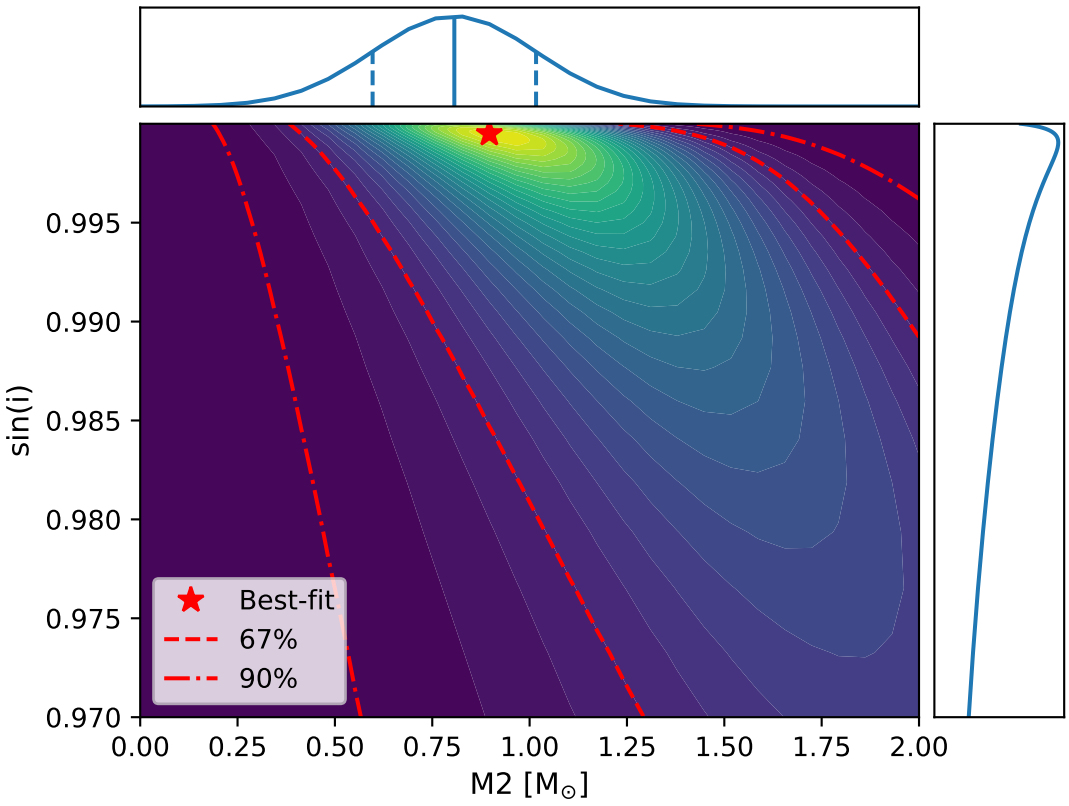

Figure 3.4 Results of $\mathrm{M_C} - \sin \mathrm{i}$ Grid for PSR J2035+3655. We show the map of grid values with contours of constant PDF, and include a marker for the best-fit point and contours for the 67% and 90% confidence levels. This measurement equates to a $\simeq 2\sigma$ detection of the Shapiro delay parameters. Also plotted are the marginal probability density functions of both measured parameters, along with the mean (solid) and 1σ (dashed) lines for M2. The grid used for $\sin i$ extended below 0.97, but only this region is included as it has the most support.

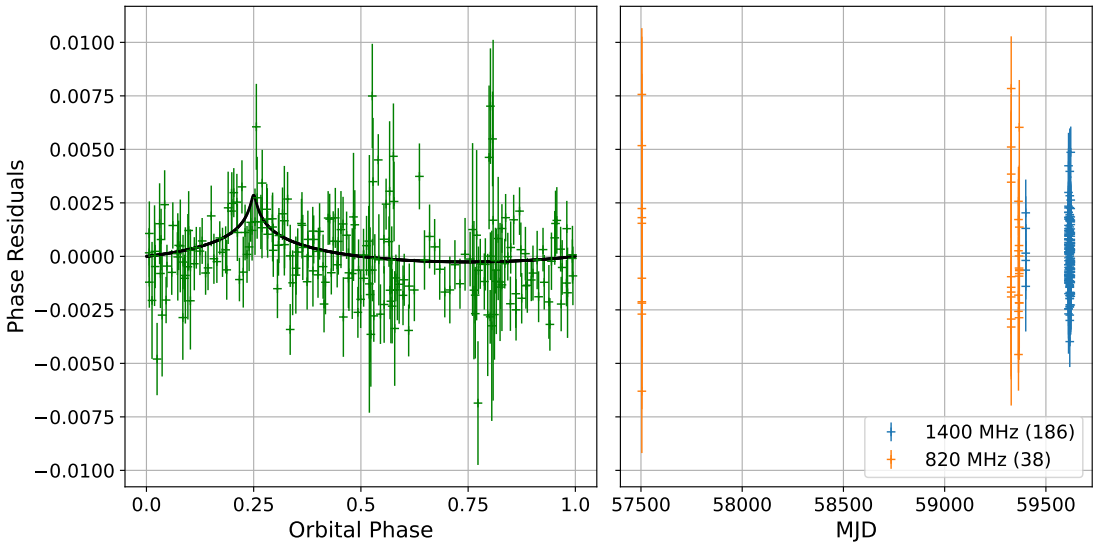

Figure 3.5 Timing Residuals for PSR J2035+3655. In the left panel, we plot the phase residuals against orbital phase, and plot the measured Shapiro Delay signal in black. Note that the model used to produce these residuals does not include the SD parameters. On the right, we plot all residuals colored by observing frequency. Unlike the left panel, these residuals do include the SD model.

Table 3.6. Binary parameters for PSR J2035+3655.

Parameter	Value	Unit
Measured Quantities		
Orbital Period, P_B	0.19272782022(18)	d
Projected Semi-Major Axis, A_1	2.180121(3)	lt-s
Epoch of Ascending Node, $T_{\rm ASC}$	59611.66149639(5)	MJD
Laplace-Lagrange parameter 1, ϵ_1	2(3)	10^{-6}
Laplace-Lagrange parameter 2, ϵ_2	21(3)	10^{-6}
Companion Mass, M_C	0.9(5)	$M_\odot$
Derived Quantities		
Orbital Eccentricity, e	21(4)	10^{-6}
Inclination, i	$88.2^{+0.1}_{-50.6}$	deg
Pulsar Mass, M_p	0.7(7)	$M_\odot$

Note. — Uncertainties in parentheses are 1σ on the last digit.

3.6 ANALYSIS AND DISCUSSION

3.6.1 Pulse Scattering

In a simplified Galactic model, GBT820 peers through three spiral arms – the local/Orion arm, the Perseus arm, and a distant third arm. Since stars primarily form in the Galactic arms, we expect that pulsars may be clustered in DM around the mean values for each arm. In reality, the distribution of material in this direction is still under debate, as many recent *Gaia* studies have provided new measurements of the distribution of dust in Cygnus (Orellana et al., 2021; Vergely et al., 2022). Nevertheless, detections of pulsars sample the ISM along lines of sight through these arms, and examining the effects of scattering on their profiles provides another measure of the content of this material. To measure the scattering timescale for a given profile, we assume that the broadened pulse

can be described as (Krishnakumar et al., 2017)

$$P(t) = P_i(t) * s(t) * D(t) * I(t), \tag{3.3}$$

where P_i is the intrinsic (unscattered) pulse, $s(t)$ describes the impulse response from scattering, $D(t)$ is a step function with width specified by the predicted DM smearing due to finite channelization, and $I(t)$ contains additional temporal smearing due to finite phase binning. In this expression, $*$ denotes convolution. Here, the frequency channel/phase bin widths are small enough that smearing due to $D(t)$ and $I(t)$ can be neglected. The impulse response for exponential scattering is modeled as

$$s(t) = \exp(-t/\tau_{sc})\mathrm{U}(t - t_p), \tag{3.4}$$

where τ_{sc} is the scattering timescale and U(t) is a step function that defines the first bin of the exponential kernel, located at t_p. To enrich our results, we supplement the profiles as measured in the GBT820 survey with additional profiles at different frequencies. For 7 of these sources, listed in Table 3.7, additional profiles come from detections in the GBNCC survey at 350 MHz. Pulsars J2035+3655 and J2041+4551, discoveries from the GBT820 survey, were not detected in GBNCC. However, other follow-up for these sources was conducted at 1400 MHz (with the GBT), and J2041+4551 was observed at 600 MHz (with CHIME). For these sources, we use the 1400 MHz profile as the intrinsic profile. We also use J2041+4551's CHIME profile as the "scattered" profile. For all other pulsars, we use the 820 MHz profile as the intrinsic profile. After subtracting the baselines, we normalize profiles from both datasets by their sums and convolve the higher-frequency profile with $s(t)$. We then subtract the broadened pulse from the lower-frequency profile and calculate the χ^2 of the residuals. With this scheme, we performed a grid search over t_p and τ_{sc} to

Table 3.7. Scattering timescales from multi-frequency profile comparison.

PSR	τ_{sc} (ms)	DM ($\mathrm{pc/cm^3}$)
J2002+4050	22.0(4)	131.5
J2006+4058	70(20)	259.5
J2013+3845	16.3(6)	238.2
J2027+4557	30(2)	229.6
J2029+3744	13.9(9)	190.7
J2035+3655	1.0(2)	136.7
J2037+3621	10.8(6)	93.6
J2041+4551	186(4)	310.0
J2057+4701	27(7)	219.0

Note. — The values in parentheses are uncertainties on the last digit that have been scaled such that the reduced χ^2 values for the fits to the profiles are 1.

minimize the χ^2. These fits, along with their matching low- and high- frequency profiles, are shown in Figure 3.6, with the inferred scattering timescales in Table 3.7.

To put our scattering measurements in context, we plot them with several comparisons in Figure 3.7. Measurements for all nine sources are included with the predictions from NE2001 and YMW+16. Scatter about the Bhat et al. (2004) best-fit line (orange dashed line) is expected, as is evident from other catalog measurements of τ_{sc} (grey crosses in Figure 3.7), though it is apparent that the NE2001 predictions are systematically low. There may be a plateau in our measured τ_{sc} for sources below $300\,\mathrm{pc/cm^3}$, which matches Bhat et al. (2004) and Krishnakumar et al. (2015) more closely towards higher DMs.

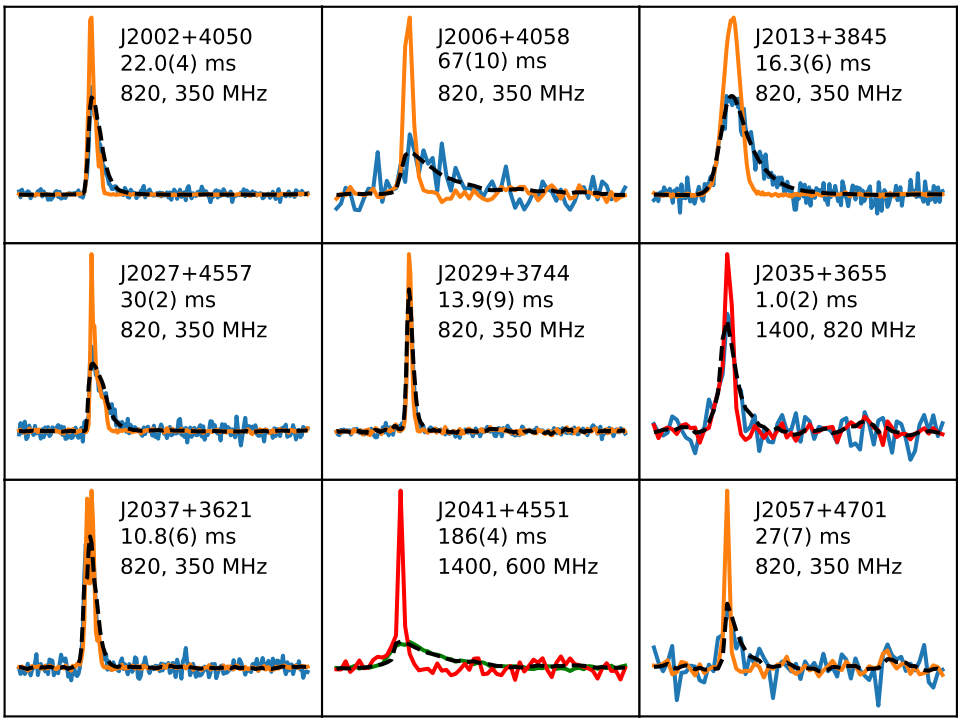

Figure 3.6 Scattered Profiles. Shown in solid lines are the profiles used to measure scattering. Colors correspond to different observing frequencies, where blue is 350 MHz, green is 600 MHz, orange is 820 MHz, and red is 1400 MHz. We include the scattering timescale measurement and the observing frequencies for the reference and scattered profiles in each panel. For all pulsars except the survey discoveries (J2035+3655 and J2041+4551), the GBT820 detection is the reference profile, and the GBNCC detection is the scattered counterpart. For J2035+3655, the 1400 MHz observation serves as the reference profile and the 820 detection is scattered. For J2041+4551, the 1400 MHz observation is the reference, and CHIME data is the scattered profile. With dashed black lines, we show the convolution of the reference pulse with an exponential scattering kernel.

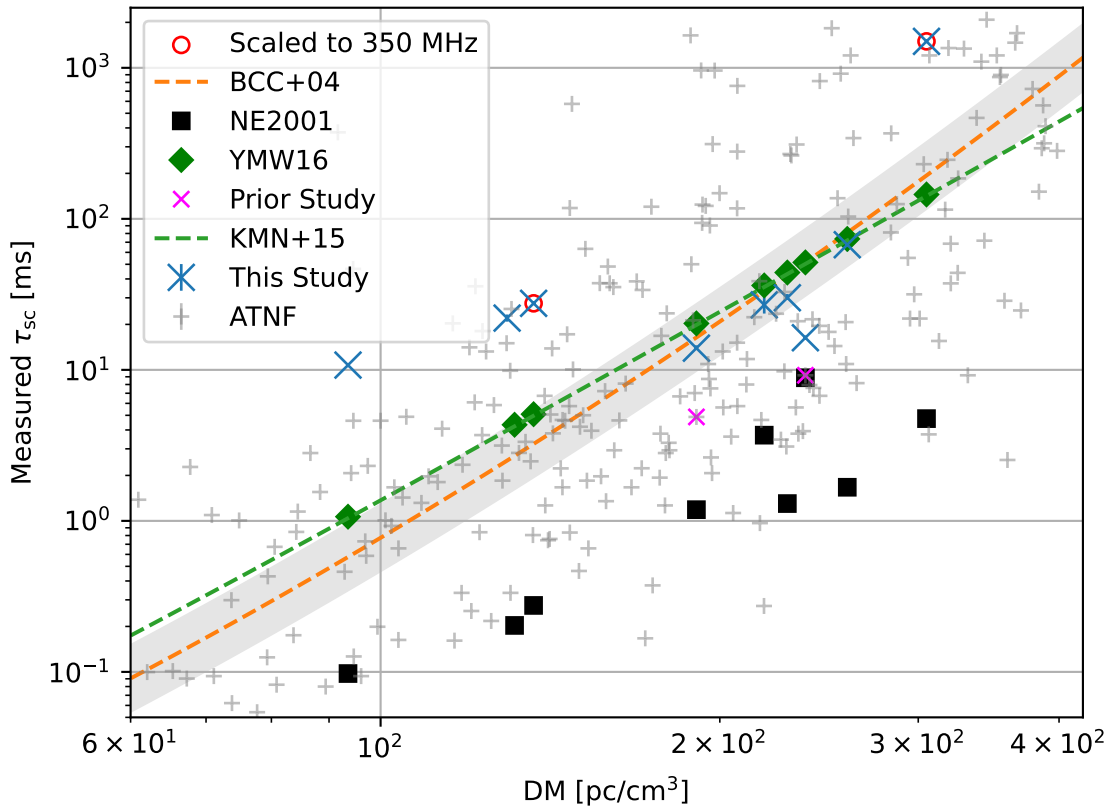

Figure 3.7 Scattering timescales pulsars measured in the GBT820 data, along with archival data. Plotted with blue Xs are the measurements made in this study, listed in Table 3.7; those that are highlighted with red circles indicate pulsars for which we measure τ_{sc} at a frequency other than 350 MHz and scale using a power-law with index $\alpha = 3.86$ from Bhat et al. (2004). We include the relation published in that work in orange with the 3σ uncertainty region on α in grey. A more recent review (Krishnakumar et al., 2015) published a similar relation, which we plot using a green dashed line. For each pulsar, we calculate the scattering timescale as predicted by both NE2001 (Cordes & Lazio, 2002) and YMW+16 (Yao et al., 2017) and plot them using black squares and green diamonds, respectively. We also include all ATNF measurements of τ_{sc} for pulsars in this range of DMs, shown in grey. We have scaled these from 1 GHz to 350 MHz using $\alpha = 3.86$, though there may be additional scatter from different observing setups. Two sources included in this study (J2029+3744 and J2013+3845, with DMs of 190.6 and 238.2 $\mathrm{pc/cm^3}$) have values of τ_{sc} published in ATNF; these are plotted as magenta Xs.

3.6.2 Cygnus Pulsar Population

At the time of the survey proposal (2016), estimates for the survey's yield predicted as many as 65 new pulsars in the Cygnus region, including five new MSPs. Given that about 2/3 of the survey was observed, we might have expected close to 40 new pulsars in this region. Our discovery of only 4 pulsars, one of which could be classified as an MSP, suggests a relative dearth of sources detectable at 820 MHz using the GBT. Subsequent surveys utilizing FAST have uncovered several sources in this region that lie below this survey's predicted sensitivity limit, which we illustrate in Figure 3.10. To quantify the sensitivity of the survey, we plot the predicted flux density at 820 MHz as calculated by Equation 3.2. We utilize the minimum S/N of a detection in the survey (4.1, below the search threshold of 6) to scale these curves, and account for pulse smearing due to scattering by modeling the width of a pulse as

$$W_{\rm sm} = \sqrt{W_{\rm int}^2 + \tau_{\rm sc}^2}. \tag{3.5}$$

We assume the intrinsic pulse width ($W_{\rm int}$) to be 6% of the pulse period (Johnston & Karastergiou, 2019; McEwen et al., 2020) and calculate the predicted scattering $\tau_{\rm sc}$ using the expression in Bhat et al. (2004). This results in the asymptotic behavior seen in the flux density curves toward short periods, as pulses with widths that are greater than or equal to the pulse period will not be detectable. With these parameters, we find the minimum flux density measurable in the survey to be 0.08 mJy.

Given the discrepancy between the predictions and survey yield, we examined the differences between the simulated discoveries and the pulsars known to exist in the region, as well as those discovered by GBT820. To do so, we utilized `PsrPopPy`[5] (Bates et al., 2014) to generate pulsars in this region and attempted to "detect" them using pa-

[5] https://github.com/samb8s/PsrPopPy

rameters for GBT820. This will depend on the pulsar's intrinsic brightness as well as its period/DM combination, as shown in Figure 3.10. To produce simulated populations, `PsrPopPy` draws from user-specified distributions of pulsar spin and position parameters. The simulated position is mapped onto Galactic models of the ISM, and the expected DM is calculated. With these parameters, the code then assesses the detectability of the pulsar in a collection of user-specified pulsar surveys. These surveys are chosen to cover a wide range of observing frequencies and sky positions to avoid biases from individual survey setups. The simulations here utilized the total number of pulsar/MSP detections from the following surveys, where we define an MSP as having a period $\leq 30\,\mathrm{ms}$: GBNCC (670/70, McEwen et al., 2020), AODrift (75/33, Martinez et al., 2019), PALFA (207/46, Parent et al., 2022), LOTAAS (300/11, van der Wateren et al., 2023), PMPS (916/28, Sengar et al., 2023), and PKS70 (298/17, Lyne et al., 1998). We supplied the total number of detections from all of these surveys N_{tot}, and `PsrPopPy` generates pulsars until N_{tot} are detected. At this point, the simulated population of pulsars can be "observed" by a model for the GBT820 survey, and the number/characteristics of simulated sources that are detected can be compared to actual detections.

By determining the median value of pulsar parameters as a function of the number of populations included, we found that all parameters stabilize with ≥ 100 independent populations. For the following analysis, we included 300 such populations. Given the input survey information listed above, we find that predictions for the number of MSPs detected match the actual survey yield (2). However, canonical pulsar detections are underpredicted, with a median of 10 simulated detections compared to 18 detections.

Beyond the number of sources, we examined the distribution of spin period and DM for the simulated detections against those of the real pulsars in the survey region. We find some notable discrepancies, particularly in DM, where there are many simulated pulsars

Table 3.8. Overview of relevant PsrPopPy parameters. Parameters omitted from this list were left to default values as shown in PsrPopPy documentation (https://github.com/samb8s/PsrPopPy).

Parameter Name	Value/Range	Description
	All Simulations	
`surveys`	'GBNCC', 'AODRIFT', 'LOFAR', 'PALFA3', 'PMSURV', 'PKS70'	Surveys used to produce simulated populations (see note)
	Pulsars	
`ngen`	670, 75, 300, 207, 916, 298	Pulsar detections in above surveys
`pDistType`	'lnorm'	lognormal
`pDistPars`	[3,1]	μ, σ of period distribution [log(ms)]
	MSPs	
`ngen`	70, 33, 11, 46, 28, 17	MSP detections in above surveys
`pDistType`	'lorimer12'	Lorimer et al. (2015)
`pDistPars`	[1.5,0.58]	μ, σ of period distribution [log(ms)]

Note. — Detection counts for the surveys come from the following: GBNCC (McEwen et al., 2020), AODrift (Martinez et al., 2019), PALFA (Parent et al., 2022), LOTAAS (van der Wateren et al., 2023), PMPS (Sengar et al., 2023), and PKS70 (Lyne et al., 1998).

with DMs $\leq 100\,\mathrm{pc/cm^3}$. In Figures 3.8 and 3.9, we include histograms of both period and DM of the simulated population with the actual pulsars in this survey region (both detected and non-detected sources are shown). For each sub-population, we calculate the median value of both parameters and plot them with their 1σ region shaded.

The median spin period for the simulated canonical pulsars (spin period $\geq 30\,\mathrm{ms}$, Figure 3.8) is slightly higher than the median of either the detected or non-detected populations, though the more clearly discrepant parameter is pulsar DM. Simulations produced nearly half of all detections with DMs below that of the nearest known pulsar in the survey (J2108+4516, $\mathrm{DM} = 84.0\,\mathrm{pc/cm^3}$). As the GBT820 survey should be quite sensitive to such DMs from a scattering perspective (for $\mathrm{DM} \leq 100\,\mathrm{pc/cm^3}$, predicted $\tau_{sc} \leq 21\,\mathrm{us}$, likely much less than 10 percent of the width of a pulse), and scintillation would only result in significant modulation to sources $\lesssim 10\,\mathrm{pc/cm^3}$, this may imply an overestimate of low-DM sources in population models. Such an overestimate could be explained by an overdense region of the Galaxy (like the Cygnus region) in which a given line of sight will accumulate dispersive delays quickly over a relatively short distance. This would imply:

- the maximum DM in the survey region is larger than what is predicted;
- DMs of pulsars in the Cygnus region with independent distance measurements will be higher on average than what is predicted using standard distance-to-DM models (YMW+16 and NE2001); and
- there are fewer-than-average detectable radio MSPs.

The first may be supported by the growing collection of sources detected by the FAST-GPPS survey (Han et al., 2021) with excessive DMs. The maximum DM predicted in the survey region is $508/504\,\mathrm{pc/cm^3}$ for NE2001/YMW+16; this threshold is surpassed by 6 of the sources listed (including J2051+4434g, detected in GBT820). The second point can

be tested using catalog measurements of distance. Three of the pulsars in the survey with published DMs have independent distance measurements: J2022+3842 (10 kpc, SNR association; Arzoumanian et al., 2011), J2021+3651 (1.8 kpc, red star association; Kirichenko et al., 2015), and J2032+4127 (1.33 kpc, spectroscopic observations of eclipsing binaries; Kiminki et al., 2015). All of these distance measurements are well below what is predicted by their DMs (13.2, 10.5, and 4.6 kpc, per YMW+16). In fact, such an overdensity in DM is mentioned by Arzoumanian et al. (2011) to explain this discrepancy for J2022+3842, and Table 5 of Cordes & Lazio (2002) includes measurements of so-called "clump parameters" used to account for excess scattering along many Cygnus lines of sight. Also notable in that sample is the difference in distances for J2021+3651 and J2032+4127 (0.5 kpc) compared to the difference in their DMs ($253\,pc/cm^3$). *Gaia* observations have been used to find clusters of dusty OB regions at distances $\simeq$ 1.4 kpc (Orellana et al., 2021; Quintana & Wright, 2022), which may support a complex line-of-sight dependence for DM.

For MSPs, simulated populations reflect the opposite situation: the median detected period of these sources are discrepant (though less so), while DM is in more agreement. However, with so few MSPs in this direction (J2035+3655 and J2053+4650 are the only known radio-bright MSPs), making meaningful statements about their characteristics is difficult. This relative dearth of MSPs supports the argument above: if DMs are larger than average along the line of sight, scattering will mask even the brightest MSPs. So while there may be many more MSPs in the region, radio detection will be difficult, regardless of telescope sensitivity. However, higher frequency observations may be more fruitful, as they sidestep the issue of dispersive smearing. This is reflected in the number of gamma-ray and X-ray sources that are known in Cygnus.

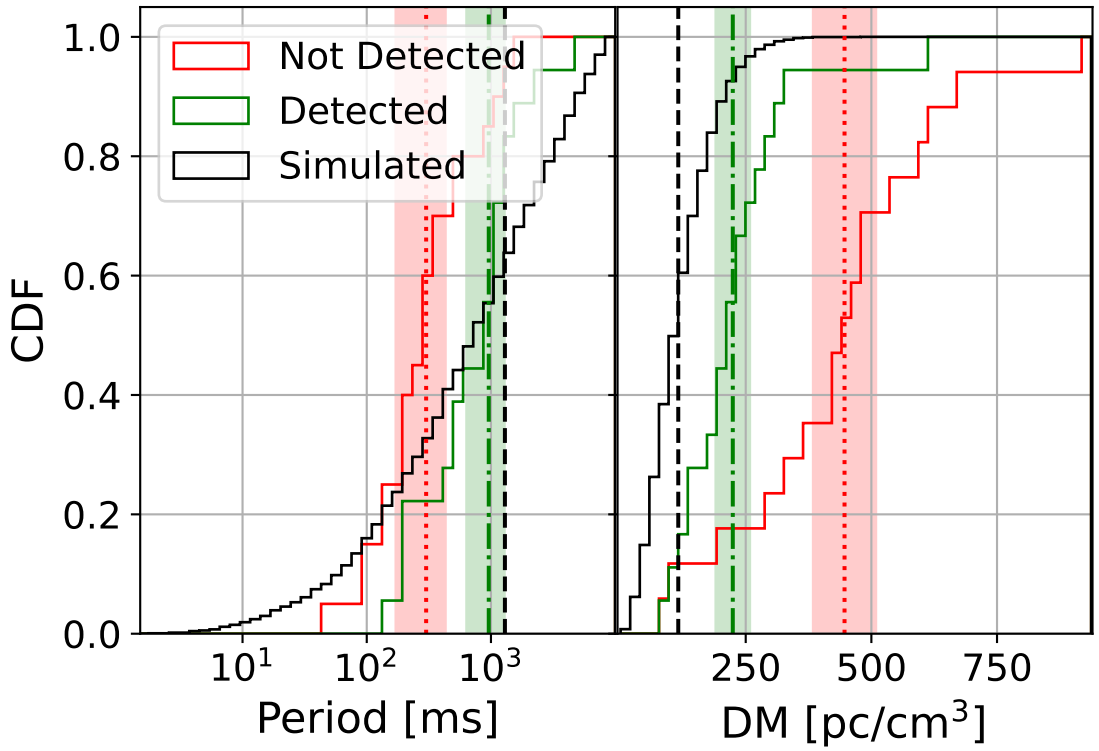

Figure 3.8 Comparison of Known Canonical Pulsars to Simulations. We plot the cumulative distributions of spin period (left) and DM (right) for three sub-populations: the simulated sources (black), the known pulsars that were detected in GBT820 (green), and those that were not detected (red). For each, we plot a vertical line (dashed, dot-dashed, or dotted for each respective sub-population) at the median value and shade the 1σ region. We excluded some simulated detections with periods too large ($P \geq T_{\rm obs}/2$) to be detected in GBT820. All sources have spin periods greater than 30 ms. The period distributions are fairly well matched, but simulated pulsars have significantly smaller DMs on average.

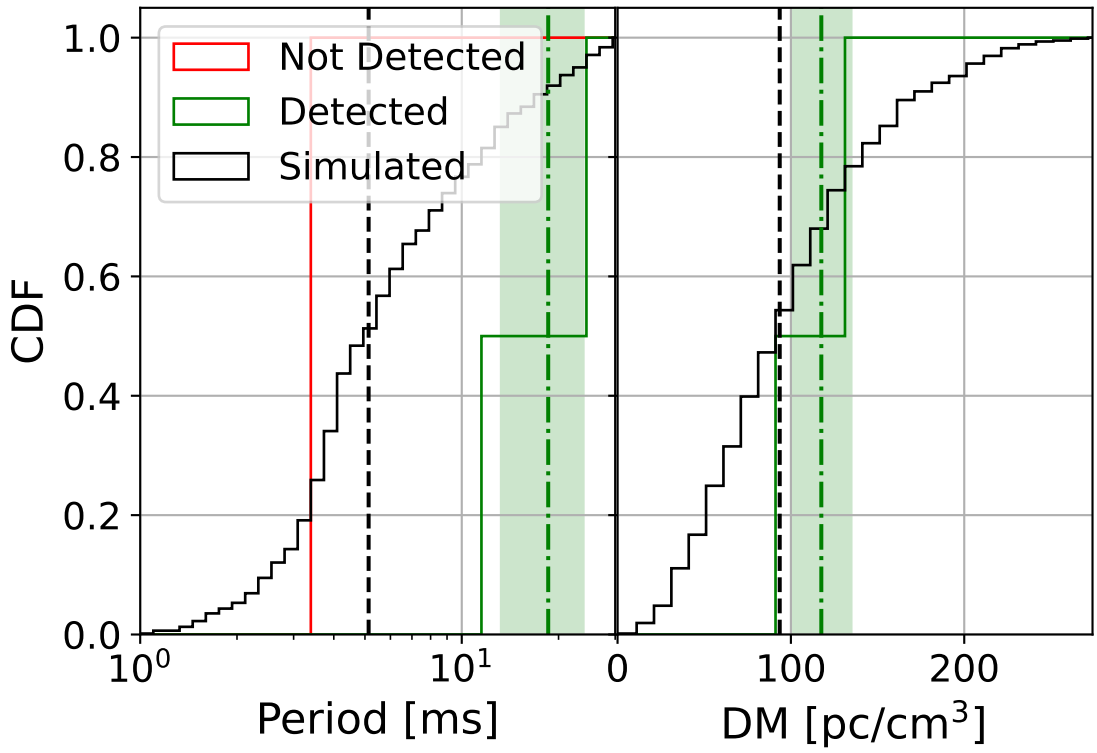

Figure 3.9 Comparison of Known Millisecond Pulsars to Simulations. The coloring and formatting here is the same as in Figure 3.8, but here we only include sources with spin periods below 20 ms. The discrepancy between median values is more significant for period than DM here, though the small number of MSPs in the region (detected or otherwise) limits our certainty. The only known MSP not detected (J2034+3632) is a gamma ray source, and so the DM is not known; it is therefore omitted from the right plot.

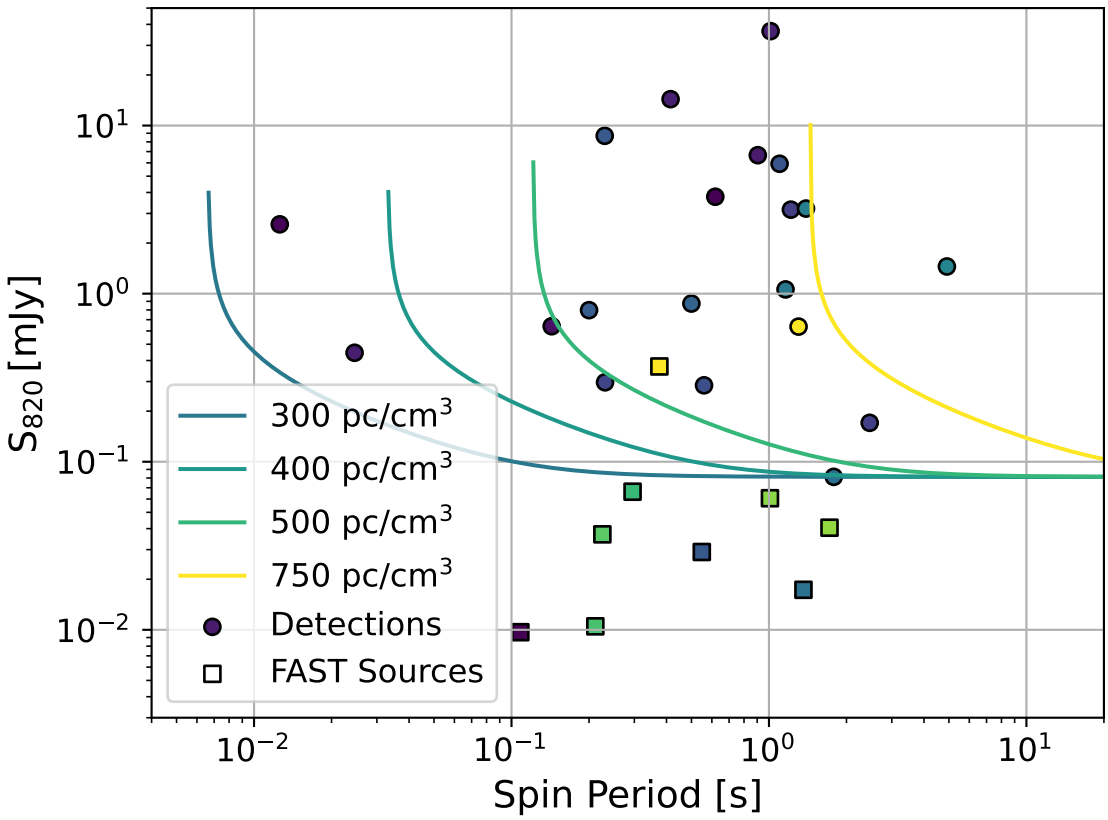

Figure 3.10 GBT820 Sensitivity Curve. We plot all of the pulsars that are detected in GBT820 using filled circles and the FAST discoveries that were not detected in the survey with filled squares. All sources are colored by their DM. Curves show lines of constant DM; asymptotes at short periods are the result of modeled pulse smearing, which spans beyond a single rotation for fast, distant sources.

3.7 CONCLUSIONS

The GBT820 survey of the Cygnus region has yielded three previously undiscovered pulsars, including two canonical pulsars (J2041+4551 and J2016+38) and an MSP in a close, near-circular binary, likely with a white dwarf companion (J2035+3655). We have measured spin and position parameters for all of these sources, though with widely varying precision due to different follow-up strategies. We also utilized published parameters/profiles for the known sources in the region to measure flux density for each and estimate the survey's sensitivity. Finally, we measured scattering parameters for nine pulsars.

While these discoveries fall quite short of the initial predictions for this region, we find that the future may not be so dim. If it is true that this region has an overdensity of free electrons that reduces the efficiency of radio searches, then non-detections may only indicate that the region should be observed using higher frequency, and may still be full of exotic sources. FAST surveys in this region have continued to fill out the true DM range of its pulsars; it is likely that most/all radio pulsars in Cygnus will be found in these surveys. Searches using X-ray and gamma-ray observatories will not only see clearly though radio-opaque regions, they will find the young, energetic magnetars and gamma ray repeaters born in these regions.

ACKNOWLEDGEMENTS

This work was supported by the NANOGrav Physics Frontiers Center, which is supported by the National Science Foundation award 1430284. The Green Bank Observatory is a facility of the National Science Foundation (NSF) operated under cooperative agreement by Associated Universities, Inc. CHIME is funded by grants from the Canada Foundation for Innovation (CFI) 2012 Leading Edge Fund (Project 31170), the CFI 2015 Inno-

vation Fund (Project 33213), and by contributions from the provinces of British Columbia, Quebec, and Ontario.

CHAPTER 4

The Green Bank North Celestial Cap Survey IX: Timing Follow-up for 128 Pulsars

4.1 INTRODUCTION

Since the discovery of pulsars in the late 1960s (Hewish et al., 1968), they have been the subjects of intense study. As these stars rotate, their magnetic fields beam radio waves from their poles like a lighthouse. On Earth, this rotation is detectable as a series of pulses. Precise measurements of these pulses at Earth track the passage of time in the pulsar's frame, and the timing models compare this clock to those on Earth. Deviations from predicted arrival times of pulses encode information about the pulsar and material along the line of sight to it in a process called "pulsar timing." (e.g., Lorimer & Kramer, 2004).

Through pulsar timing, researchers have uncovered the excellent scientific potential of pulsars in a wide range of areas (Backer, 1975; Hewish, 1975; Detweiler, 1979; Taylor & Weisberg, 1982; Backer, 1984; Taylor et al., 1992). For instance, pulsar astronomy has provided some of the most stringent constraints on the behavior of ultra-dense matter (Özel & Freire, 2016; Bogdanov et al., 2019; Hu et al., 2020; Pang et al., 2021; Lattimer, 2021). Their immense moments of inertia make them some of the most stable clocks in the universe (Manchester, 2017; Yin et al., 2017). And the most stable millisecond pulsars can be used as an ensemble to search for low-frequency gravitational waves (Detweiler, 1979; Reardon et al., 2016; Desvignes et al., 2016; Arzoumanian et al., 2020; Antoniadis et al., 2022).

Many of these topics benefit from ongoing searches for pulsars which continue to in-

crease the known population. These searches implement ever-improving technology and searching algorithms that have discovered over 3000 pulsars to date (e.g., Manchester et al., 1978; Stairs et al., 1999a; Deneva et al., 2013; Stovall et al., 2014; Manchester et al., 2016; Sanidas et al., 2019; Cruces et al., 2021; Sengar et al., 2023, etc.). Many of these pulsars have been timed to amazing precision, and have been used to characterize the pulsar population.

This timing process is hampered by many components of pulsar evolution. Young pulsars are born following the supernova of massive progenitors; these highly magnetized neutron stars rotate the least stably and slow the most quickly (Antonelli et al., 2023). This slowing is due at least in part to magnetic dipole radiation, but typically does not follow so simple a model. Many pulsars, especially young pulsars, exhibit some form of timing noise (Parthasarathy et al., 2019; Lower et al., 2020; Singha et al., 2022). This can manifest as a long-term, random drift in the observed spin of a pulsar that deviates from “pure" spin-down due to magnetic dipole radiation. In a simple dipole model, the pulsar’s spin-down $\dot{\nu}$ follows a powerlaw in spin ν with a well defined index ($n = 3$). This hypothesis can be tested using measurements of ν, $\dot{\nu}$, and a second spin derivative $\ddot{\nu}$, all of which are attainable from pulsar timing. These measurements have shown that the $n = 3$ model is very rarely true, suggesting a more complex relationship between these parameters (Lower et al., 2020). More generally, the adolescent pulsar’s spin will follow a random walk in ν and $\dot{\nu}$. From the timing side, this noise is often removed by fitting and subtracting polynomials from the residuals – a process known as “polynomial whitening" (Hobbs et al., 2004b).

Along with this drift, some pulsars show abrupt changes in spin period called “glitches" (Espinoza et al., 2011; Fuentes et al., 2017; Basu et al., 2022; Zhou et al., 2022a,b). Theories to explain these events largely utilize either:

- a starquake model where the crust of the neutron star abruptly changes shape and the change in its moment of inertia drives the observed momentum-conserving change in rotation (Alpar et al., 1994; Lai et al., 2018; Lu et al., 2023), or
- differential rotation of the solid crust and a superfluid interior that is coupled by the pinning of vortices in this superfluid (Alpar, 1977; Link et al., 1992; Haskell et al., 2020; Melatos & Millhouse, 2023; Layek et al., 2023).

While the process that causes pulsars to glitch is still not definitively identified, their impacts on timing have been addressed in many studies (e.g., Lower et al., 2021; Dunn et al., 2022; Zubieta et al., 2023). In a simple case, the glitch appears in timing residuals as an instantaneous change in the slope. This change is also accompanied by a change in the spin-down rate of the pulsar, which introduces an additional accumulation of phase offset in the residuals. Many observed glitches are then followed by an exponential recovery of the affected parameters back to their pre-glitch values. All of these components manifest as changes in pulsar spin parameters, and complicate measurements of spin/spin-down.

On the other hand, the rotation of old pulsars are typically much more stable, particularly those that have been captured in a binary system. In many cases, these pulsars will harvest rotational momentum from the orbit via the Roche-lobe overflow of the companion. This process decreases the rotation period of the pulsar, potentially down to the millisecond level. It also greatly dampens their magnetic fields, reducing the long-term spin-down rate from dipole radiation (Bisnovatyi-Kogan & Komberg, 1974; Shibazaki et al., 1989). These pulsars, called millisecond pulsars (or MSPs), have been utilized for the majority of high-precision pulsar science (Alam et al., 2021; Falxa et al., 2023; Miles et al., 2023; Arzoumanian et al., 2023). Aside from their stability, the timing procedure is sensitive to Doppler shifts due to binary motion. These shifts can be used to determine three of the Keplerian parameters of the orbit, including the orbital period, the pulsar's semi-

major axis, and the initial phase of the binary (relative to the time of measurement). These can be used to place limits on the masses in the system via the Keplerian mass function. Some binary orbits are compact enough that the pulsar reaches relativistic speeds during the orbit; these systems induce additional complexities in the timing procedure that can be used to directly measure the mass of the pulsar and its companion (Demorest et al., 2010; Özel & Freire, 2016; Cromartie et al., 2020). Given that this measurement is nearly impossible to make otherwise, binary pulsars are unique and powerful laboratories for gravitation and ultra-dense matter.

Here, we discuss the continued efforts of a pulsar survey that has reached its observational end: the Green Bank North Celestial Cap pulsar survey (GBNCC). We discuss the survey's conclusion and current objectives in Section 4.1.1. In Section 4.2, we describe the sample of pulsars we have examined in this study and how we produce data products. Section 4.4 covers the results from our study and highlights some particularly interesting measurements. Finally, Section 4.5 summarizes our results. We also include an Appendix with additional figures. The work below includes comparisons with the ATNF Pulsar Catalogue (ver. 1.70 Manchester et al., 2005a)[1].

4.1.1 GBNCC Survey Overview and Completion

Over the last decade, the GBNCC survey has covered the sky north of $\delta = -40^\circ$ with 124,852 pointings of 2.5 min duration with the 100-m Green Bank Telescope (GBT) at 350 MHz. Full specifications of survey observations and processing are detailed in previous GBNCC publications (Stovall et al., 2014; Lynch et al., 2018b). This choice of central frequency provides additional sensitivity to steep spectrum sources, in particular older pulsars outside of the Galactic plane (McEwen et al., 2020). The survey is one of the

[1] http://www.atnf.csiro.au/research/pulsar/psrcat.

largest single surveys in terms of sky coverage, covering $46,800\,\mathrm{deg}^2$.

To date, the GBNCC survey has discovered 195 sources, including 33 millisecond pulsars (MSPs), 24 binaries, 24 rotating radio transients (RRATs, McLaughlin et al., 2006), and a fast radio burst (FRB, Lorimer, 2018), which have been published in a series of survey papers (Stovall et al., 2014; Kawash et al., 2018; Lynch et al., 2018b; Aloisi et al., 2019; Parent et al., 2020; Agazie et al., 2021; Fiore et al., 2023; Swiggum et al., 2023). These discoveries have included some of pulsar astronomy's most exotic sources and important measurements, including the record-breaking mass of PSR J0740+6620 (Cromartie et al., 2020), eclipsing black widow pulsars that are ablating their companions (Swiggum et al., 2023), many nulling pulsars (Anumarlapudi et al., 2023), and double neutron star binaries (Aloisi et al., 2019; Lynch et al., 2018b). These studies and others have amassed a huge amount of data on GBNCC discoveries, much of which is currently available from the public-facing GBNCC GitHub repository[2].

During the summer of 2022, the final GBNCC survey positions were observed (aside from ≤ 500 points which will be reobserved for reasons related to radio frequency interference and observation complications). Efforts to identify new pulsars are continuing, both with our existing pipeline and with new pipelines that improve sensitivity to certain regions of parameter space (Sengar et al., 2023). For this study, we instead focus on the continued timing of prior discoveries by connecting archival data with new observations. Note that there are also twelve sources included in this paper that were discovered in the GBT350 survey of the Northern Galactic Plane (Hessels et al., 2008). They were followed up at 820 MHz using the GBT during an earlier timing campaign (project code AGBT13B_290, PI R. Rosen), and are included among the CHIME/Pulsar sources.

[2] https://github.com/GBNCC/data

4.2 SAMPLE ASSEMBLY

4.2.1 Observations

Following identification, candidates were observed in test scans using either the GBT (earlier discoveries) or CHIME/Pulsar (starting in early 2020). In the former case, 2–3 ten minute scans were taken over the course of a few weeks during other survey observations to confirm discoveries. New pulsars were then included in follow-up proposals with the GBT to establish phase-connected timing solutions. The observing specifications of these proposals vary slightly to account for complex timing models, but typically included $\simeq 10$ follow-up observations ($10-20$ minutes on-source per scan) with the GBT using either the 350 MHz, 820 MHz, or 1400 MHz receiver. Depending on the success of the timing campaign and potential scientific benefits, some pulsars were included in subsequent proposals using other instruments like LOFAR (van Haarlem et al., 2013) and Arecibo.

Following an agreement between the CHIME/Pulsar and GBNCC collaborations in late 2019, candidates (and pulsars) identified in GBNCC data could be followed-up using the CHIME/Pulsar instrument with minimal latency ($\simeq 1\,\mathrm{day}$). During the spring semester of 2020, many previously discovered (and in some cases, previously published) GBNCC pulsars were observed using the 600 MHz receiver on CHIME with cadences of 1–7 days. Scan length depends on the declination of the source, as pulsars close to the southern horizon are visible for a shorter time compared to those directly overhead. Despite the slight decrease in sensitivity between the GBT vs. CHIME, the high cadence of these observations provides unprecedented sensitivity to the pulsar behavior, and models can be updated on a regular basis. The reduction in beam size further constrains the error in position for the sources, particularly when gridding observations were taken. Normal 350 MHz survey observations continued during the intervening years, and new

candidates were confirmed/rejected using both GBT test scans and CHIME/Pulsar daily observations. As the CHIME/Pulsar schedule filled, the priority (and cadence) of some sources was reduced to accommodate for those with incomplete/exotic models. A few (8) pulsars discovered with declinations below CHIME's horizon ($-10°$) were also included in our timing analysis. These sources were observed solely with the GBT in dedicated timing campaigns.

4.2.2 GBNCC/CHIME Pipeline

As part of the observing activities automatically undertaken by CHIME/Pulsar, a simplified data reduction and pulse time-of-arrival (TOA) extraction procedure is applied to each observation in order to assess data quality and generate initial timing data products. The procedure is uses a Python-based workflow that interacts with the data via the standard `PSRCHIVE` (van Straten et al., 2012) Python interface. The automated workflow, running on the Cedar supercomputing cluster[3], will identify any new observation data products that were transferred from the observatory to the storage system. Subsequently, standardized radio frequency interference (RFI) mitigation is performed on the data using `clfd` (Morello et al., 2019), including the excision of known corrupted frequency channels for that observation obtained via CHIME/Pulsar utilities. Two reduced copies of the cleaned archive are then retained; one with 32 subbands and 1-minute subintegrations, and another one with 1024 frequency channels and fully averaged in time.

Using daily CHIME/Pulsar observations greatly increased the data volume for many GBNCC sources. To best utilize these data, a pipeline was established between the data-taking and data-processing via GitHub. As new data are taken, single-epoch and frequency-averaged TOAs are generated using preliminary timing models and a detection pulse

[3]Operated by the Digital Research Alliance of Canada, https://docs.alliancecan.ca/wiki/Cedar.

template. These TOAs are then uploaded in batches to a shared private GitHub repository, where they can be accessed by GBNCC. With the new data, timing models are updated using fitting tools in `PINT` (Luo et al., 2021). When a solution has been updated, it can then be passed back to CHIME/Pulsar for future observations as necessary. In some cases, new timing models change the pulse profile enough to justify updating the TOA template, and therefore requires re-extraction of TOAs from all previous observations. Phase-connected solutions offer positional precision well within the observing beam size ($\sim$0.5° at 400 MHz, $\sim$0.25° at 800 MHz), particularly after a year of observing. Improved positions from timing result in brighter detections and more precise TOAs.

4.3 DATA ANALYSIS

4.3.1 TOA Excision

The dataset contains 78,585 TOAs from four telescopes (GBT, Arecibo, LOFAR, and CHIME). As the timing models develop, measured TOA uncertainties will reduce as the profile is improved. In some cases, position improvements from phase connection dramatically improve the S/N of detections. In others, individual CHIME observations resulted in low S/N detections, even with a timing-derived position. In these cases, multiple observations were summed together before producing TOAs, resulting in fewer (but more precise) TOAs. The wealth of data coming from CHIME allows us to be more selective with TOAs, and we implement TOA zapping as a part of the timing pipeline. Many of the zapped TOAs are due to faint detections and excess RFI. There are also a few epochs of known TOA issues which have been removed more broadly from our dataset. As discussed in Andersen et al. (2022), improper packaging of CHIME/Pulsar data prior to MJD 58550 resulted in corrupted data. These TOAs were zapped from all of the sources.

4.3.2 Timing Procedure

Timing baselines for pulsars included in this dataset are highly source-dependent. A large number of sources (95) include archival data (pre-2019) from GBT and other telescopes, and nearly all (120) sources have data taken with CHIME (post-2019). There are 7 pulsars not visible with CHIME, and so solutions were determined from GBT observations only. For this project, data are only included up to 2023 May, and a minimum baseline of 1 year was imposed.

After excising uninformative data, predicted pulse times of arrival were compared with the timestamps of observed pulses. Correlated deviations indicate errors in the timing model that are fit using a least-squares algorithm. Determining the appropriate parameters to include in this fit is difficult, as covariance is high for any parameters that influence the residuals on timescales larger than the baseline. The combination of sinusoidal (position, velocity, orbital motion) and quadratic (rotation rate and deceleration) limits the prediction power of timing models when the baseline is short. In many cases, the gap between GBT timing campaigns and CHIME/Pulsar daily scans is $> 2000\,\mathrm{days}$. Fitting models over this gap is very constraining, but requires a long enough baseline on one side of the gap to reduce phase uncertainty at the other side to within a single rotation.

When starting a timing solution from scratch, a preliminary solution with discovery parameters is used to fit TOAs over a short time period (typically a single observation). This fit only constrains the rotation rate of the pulsar as it is the only parameter with significant influence on short timescales. The improved frequency is then used to model TOAs at the MJD of the nearest observation, and a fit to both days provides a more precise measurement. The regular cadence of CHIME/Pulsar observations can introduce a subtle aliasing error into the model, as the pulsar rotation can become degenerate with the ob-

servation spacing. To mitigate this, single CHIME observations can be split into multiple TOAs to find an appropriate starting model to fit to subsequent days. This procedure is repeated until the model no longer appropriately fits the data and additional parameters must be included. When multi-band data exist for a pulsar, additional constraints are set on its dispersion measure (DM). Errors in DM lead to a smeared pulse and reduced S/N, so implementing new DM measurements further improves TOA precision.

Included among the pulsars in this project are 19 binary pulsars. These sources require special attention in the timing process, especially when the orbital period is $\geq 1\,\mathrm{year}$. For short orbital periods, a large portion of the orbit can be covered in a single observing session, and can be constrained almost immediately afterwards. When the orbital period is long, covariance with Earth's motion and the pulsar's intrinsic spin-down become significant. For these cases, fitting timing residuals with quadratic functions of order ≥ 2 captures the apparent spin derivatives due to the orbital motion, and can be used to approximate the orbital parameters. Ultimately, these derivatives are replaced by orbital parameters when possible.

4.4 RESULTS

We have assembled timing data for 128 sources; timing residuals for all sources are given in Appendix B, and a period-period derivative plot is shown in Figure 4.1. Many of the sources included have had detailed timing analyses published in previous/upcoming GBNCC publications. For these sources, we focus on maintaining phase coherence over long baselines and measurements of new parameters. For others, we provide new timing-derived solutions for spin and position parameters.

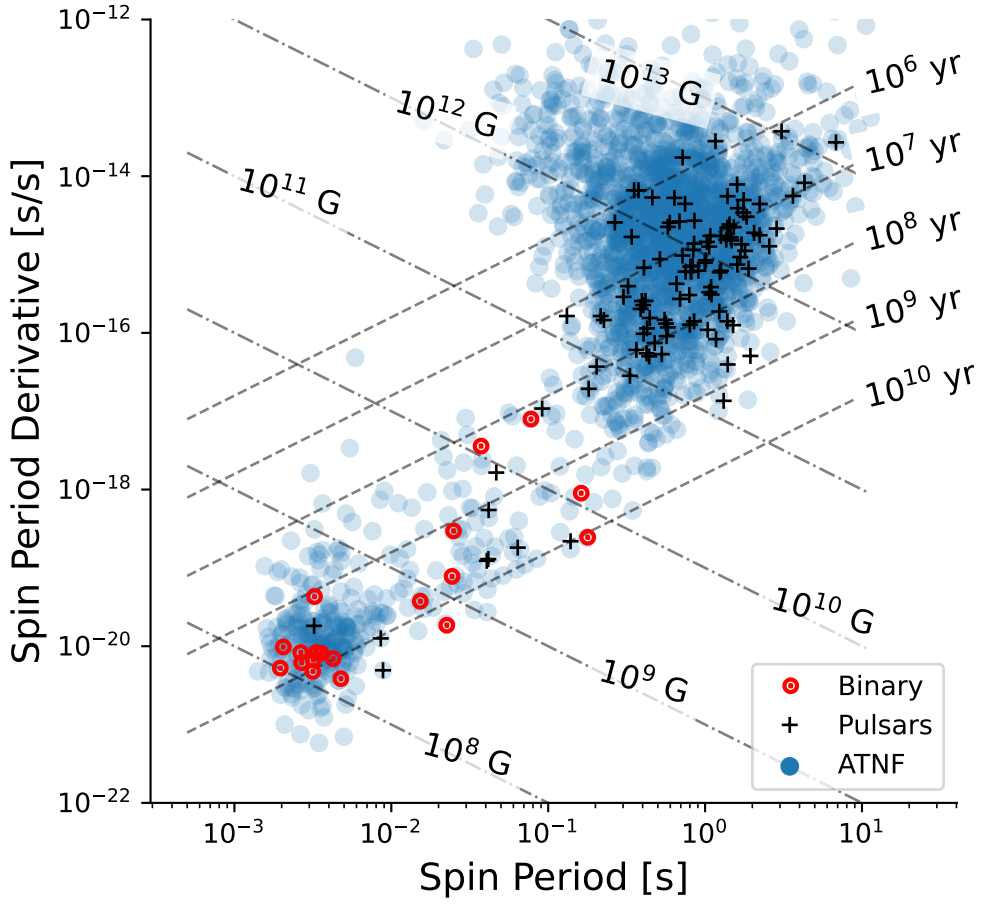

Figure 4.1 Spin period vs. period derivative for all sources timed in this work. Black and red markers indicate sources we have timed, with the latter indicating binary sources. We also plot all pulsars from the ATNF Pulsar Catalogue (Manchester et al., 2005a).Dashed and dash-dotted lines indicate constant characteristic ages and magnetic fields, respectively.

4.4.1 New Pulsars

The majority of pulsars timed in this study have been published in preceding GBNCC survey papers (Stovall et al., 2014; Lynch et al., 2018a; Kawash et al., 2018; Aloisi et al., 2019; Agazie et al., 2021), but there are 30 sources that have been discovered within the past 2–3 years for which no timing solution has been previously available. These sources, listed in Tables 4.1 and 4.2, include a wide range of periods and DMs. Because they were discovered following the CHIME/GBNCC MoU, many of these sources only have TOAs from CHIME observations. Along with the GBNCC discoveries, we provide timing solutions for the sources that were discovered in the GBT350 NGP survey (Hessels et al., 2008). These 12 sources are included in Table 4.3.

Table 4.1. Spin parameters for previously unpublished discoveries from the GBNCC survey.

PSR	ν [Hz]	$\dot{\nu}$ [10^{-14} Hz/s]	$\dot{E}$ [10^{30} erg/s]	τ_c [Myr]	$B_{\rm S}$ [10^8 G]
J0032+6946	27.1711189496937(3)	−0.2650134(3)	2842.7	162.4	116.3
J0110−2223	0.79241833567(2)	−0.039(2)	12.2	32.3	8947.4
J0120+1837	0.761391192926(2)	−0.00079(2)	0.2	1533.7	1350.8
J0141+6303	21.422324384511(12)	−0.075548(12)	638.9	449.3	88.7
J0406+3039	383.339448073778(9)	−0.122083(8)	18475.6	4975.0	1.5
J0415+6111	2.27174930502(2)	−0.02587(2)	23.2	139.1	1503.3
J0530−3847	1.10314158660(2)	−0.0756(2)	32.9	23.1	7594.2
J0749+5720	0.8511150531782(2)	−0.006017(2)	2.0	224.1	3161.2
J0758−3002	0.915860185362(9)	−0.0322(2)	11.7	45.0	6554.5
J1327+3423	24.0890080713045(2)	−0.0075032(2)	71.4	5086.8	23.4
J1354+2453	1.174999892192(7)	−0.019339(9)	9.0	96.3	3493.9
J1602−1009	320.947209606060 5(97)	−0.04918(4)	6231.0	10340.4	1.2
J1604−0057	0.596705240257(8)	−0.0330(2)	7.8	28.6	12620.2
J1639−1126	0.698961222411(11)	−0.11834(11)	32.7	9.4	18838.1
J1647+6609	0.625078358705(3)	−0.306617(3)	75.7	3.2	35854.7
J1741−2152	0.38977960839(8)	−0.0194(8)	3.0	31.9	18304.1
J1819+0322	1.25130512248(2)	−0.0199(3)	9.8	99.5	3227.2
J1930+6205	0.686758970941(3)	−0.078006(3)	21.1	13.9	15703.9
J1948−2730	3.01539684110(3)	−0.026(2)	30.7	185.3	981.2
J1954+4347	0.720958989860(3)	−0.114606(2)	32.6	10.0	17696.5
J2018−0414	24.62313693500(3)	−0.00746(7)	72.5	5229.2	22.6
J2023+0937	0.62315481163(2)	−0.0289(2)	7.1	34.2	11060.3
J2040−2156	1.77753964687(2)	−0.0415(13)	29.1	67.8	2751.0

Table 4.1 (cont'd)

PSR	ν [Hz]	$\dot{\nu}$ [10^{-14} Hz/s]	$\dot{E}$ [10^{30} erg/s]	τ_c [Myr]	$B_{\rm S}$ [10^8 G]
J2104+2830	2.464698618670(6)	−0.059259(5)	57.7	65.9	2013.2
J2145+2158	0.704725369840(4)	−0.110352(4)	30.7	10.1	17968.4
J2158−2734	2.0955667619757(99)	−0.03260(12)	27.0	101.8	1904.7
J2210+5712	0.487055824584(3)	−0.044886(3)	8.6	17.2	19945.2
J2252+2455	0.5562019181950(7)	−0.034476(7)	7.6	25.6	14323.9
J2316+5619	0.941974122159(14)	−0.1119377(99)	41.6	13.3	11710.6
J2326+6243	3.75729134993(8)	−3.62843(2)	5382.1	1.6	8369.5

Note. — Values in parentheses are the 1σ uncertainty in the last digit as reported by `PINT`.

Table 4.2. Position parameters for previously unpublished discoveries from the GBNCC survey.

PSR	Longitude [deg]	Latitude [deg]	α [deg]	δ [deg]	$d_{\rm NE}$ [kpc]	$d_{\rm YMW}$ [kpc]
J0032+6946	50.71621375(8)	57.28423181(5)	8.2	69.8	2.8	2.3
J0110−2223	6.75994(12)	−27.42791(12)	17.6	−22.4	1.0	25.0
J0120+1837	25.529881(7)	9.43371(4)	20.1	18.6	0.6	1.0
J0141+6303	52.5025597(6)	47.7773462(5)	25.4	63.1	44.3	8.8
J0406+3039	65.51429844(8)	9.6019364(5)	61.6	30.7	1.7	1.6
J0415+6111	74.168570(14)	39.18162(2)	64.0	61.2	2.3	1.8
J0530−3847	77.59187(7)	−61.90318(4)	82.5	−38.8	47.5	25.0
J0749+5720	107.7939243(12)	35.590651(2)	117.4	57.3	1.0	1.6
J0758−3002	131.02797(4)	−49.34832(2)	119.6	−30.0	0.6	0.4
J1327+3423	184.19721728(3)	39.79648991(3)	201.8	34.4	0.5	0.3
J1354+2453	196.126270(12)	33.966657(15)	208.6	24.9	25.8	25.0
J1602−1009	240.53824969(4)	10.3230616(3)	240.6	−10.2	1.6	2.4
J1604−0057	239.19070(3)	19.43743(11)	241.1	−1.0	1.6	3.1
J1639−1126	250.04038(3)	10.6267(2)	250.0	−11.4	50.0	6.3
J1647+6609	174.98236(6)	82.746773(9)	251.9	66.1	1.3	2.1
J1741−2152	265.8115(3)	1.50(2)	265.5	−21.9	3.2	4.6
J1819+0322	275.38135(5)	26.72327(9)	274.8	3.4	3.2	5.8
J1930+6205	346.08233(5)	79.285930(11)	292.7	62.1	5.7	10.7
J1948−2730	294.11015(3)	−6.3255(5)	297.2	−27.5	2.1	6.8
J1954+4347	318.69175(2)	62.638821(8)	298.7	44.0	7.1	10.1
J2018−0414	305.834950(2)	15.008889(8)	304.5	−4.2	1.5	1.8
J2023+0937	310.87125(6)	28.13128(13)	305.8	9.6	3.2	5.2
J2040−2156	306.740996(13)	−3.4638(5)	310.1	−21.9	1.0	1.7

Table 4.2 (cont'd)

PSR	Longitude [deg]	Latitude [deg]	α [deg]	δ [deg]	$d_{\rm NE}$ [kpc]	$d_{\rm YMW}$ [kpc]
J2104+2830	329.759412(2)	42.872175(2)	316.1	28.5	3.7	5.7
J2145+2158	337.233375(11)	33.23655(2)	326.3	22.0	2.8	5.5
J2158−2734	321.99966(2)	−14.21393(4)	329.5	−27.6	0.9	2.7
J2210+5712	12.362112(15)	60.538546(8)	332.5	57.2	6.2	3.9
J2252+2455	355.093609(5)	29.454280(9)	343.1	24.9	2.1	4.1
J2316+5619	23.352536(8)	53.631911(8)	349.1	56.3	2.8	2.4

Note. — Latitude and longitude are presented in the ecliptic frame. We include distance estimates from NE2001 (Cordes & Lazio, 2002) and YMW+17 (Yao et al., 2017). Values in parentheses are the 1σ uncertainty in the last digit as reported by `PINT`.

4.4.2 Glitches and Timing Noise

In this dataset, sources with spin derivatives of order > 2 and/or apparent discontinuities in timing residuals were examined as possible glitching pulsars. To model such a glitch, up to four parameters are used: the epoch of the glitch (given in MJD), the magnitude of the change in spin frequency ($\Delta\nu$ given in Hz), and the magnitude of the change in first and second frequency derivatives ($\Delta\dot{\nu}$ in Hz/s and $\Delta\ddot{\nu}$ in $\mathrm{Hz/s^2}$). In some cases (especially those where the glitch occurs in a low observing cadence epoch), only one of these parameters can be reliably measured. With a high observing cadence (and a high-significance glitch with magnitude typically of order $\geq 10^{-10}\nu$), glitches are relatively simple to resolve: a precise enough pre-glitch model can make the sudden period change quite stark. Sources that experienced glitches during the CHIME/Pulsar data are in this regime, as near-daily cadences greatly reduce our uncertainty on the glitch epoch. However, many of the sources included in this project have two or more temporally disparate observing epochs, and observations on either side of gaps are generally taken using different instruments. Distinct observing systems can introduce additional pulse phase uncertainty due

Table 4.3. Timing solutions for discoveries from the GBT350 survey of the North Galactic Plane (Hessels et al., 2008).

PSR	ν [Hz]	$\dot{\nu}$ [10^{-14} Hz/s]	DM [pc/cm^3]	Longitude [deg]	Latitude [deg]
J0054+6650	0.719311913668(6)	−0.287226(5)	14.6(1)	49.753944(8)	53.746402(5)
J0420+4451	0.805719788443(4)	−0.038462(4)	71.67(9)	71.064362(4)	23.035516(9)
J2029+5459	1.727386681(3)	−0.673(2)	59.75(4)	345.06570(9)	68.90190(4)
J2038+3447	6.243567095307(1)	−0.003510(1)	57.933(1)	325.953557(2)	50.833982(1)
J2202+5040	1.34159887359(6)	−0.79925(1)	76.1(3)	2.30884(1)	56.452520(6)
J2214+5357	1.331212824278(3)	−0.107256(3)	160.655(2)	8.906721(4)	57.723430(3)
J2242+6346	2.16939642526(3)	−2.515(2)	91.8(2)	28.09977(2)	61.80138(3)
J2316+5619	0.94197412216(1)	−0.11194(1)	72.7(3)	23.352536(8)	53.631911(8)
J2319+6411	4.629236907931(8)	−0.3514(2)	246.10(6)	33.899703(8)	58.908186(5)
J2351+6500	0.8584551911(2)	−2.06348(3)	154.294(7)	39.38388(1)	56.896464(6)

Note. — Values in parentheses are the 1σ uncertainty in the last digit as reported by `PINT`.

to both instrumental and profile evolution effects; to mitigate this, we typically include a free “jump" parameter between different systems/frequencies. This greatly improves fits between multiple telescopes, but it does reduce sensitivity to glitches in the gaps, as the jump is highly covariant with the glitch epoch. We also acknowledge that the GBNCC survey has been shown to be more sensitive to older pulsars (McEwen et al., 2020), which are less likely to glitch than their younger counterparts (Espinoza et al., 2011; Millhouse et al., 2022). Nevertheless, we find some pulsars in our dataset seem to contain evidence for glitches and report on their characteristics here. We compare the measured glitch parameters to all published glitches in the ATNF glitch database[4] in Figure 4.2 and find that all measured glitch magnitudes appear well in line with previous measurements, both in $\Delta\nu$ and $\Delta\dot{\nu}$. Fit parameters for all included glitches are given in Table 4.4, and residuals before and after adding glitches are shown in Figures 4.3 – 4.6.

[4] https://www.atnf.csiro.au/people/pulsar/psrcat/glitchTbl.html

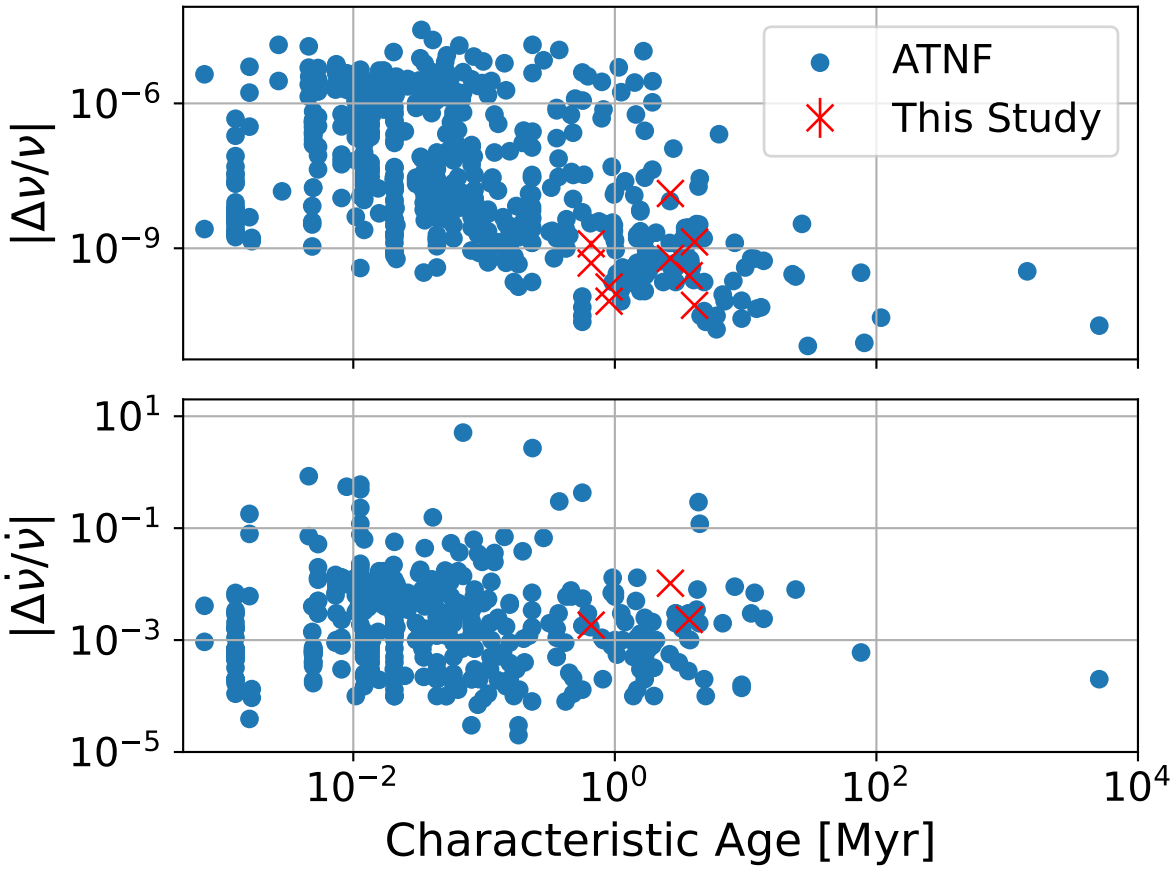

Figure 4.2 Glitch magnitude versus characteristic age. Fractional changes in both spin frequency (top panel) and frequency derivative (bottom panel) are shown in red, while published glitches from the ATNF glitch catalog are shown in blue.

Table 4.4. Glitches in GBNCC pulsars.

PSR	Epoch [MJD]	Δf [10^{-10} Hz]	$\Delta \dot{f}$ [10^{-17} Hz/s]	$\Delta \ddot{f}$ [10^{-25} Hz/s^2]
J0212+5222	56571(5)	4.2(4)	–	–
	59203(4)	2.13(7)	−0.01(5)	−2.15(11)
J1923+4243	59528(2)	4.6(2)	−1.68(12)	5.4(6)
J2029+5459	59531(8)	1.06(3)	–	–
	58000*	23.4(15)	–	–
J2202+5040	59657(4)	−8.4(4)	−8.3(3)	–
	58000*	−182.9(6)	–	–
J2351+6500	59332(4)	4.2(2)	−3.82(4)	–

*The second listed glitch for PSRs J2029+5459 and J2202+5040 occurred in a large data gap between GBT and CHIME/Pulsar observations; because of this, the glitch epochs are not uniquely determined. Instead, we include the epoch used in the models, which were arbitrarily chosen.

Note. — Values in parentheses are the 1σ uncertainty in the last digit as reported by `PINT`.

4.4.2.1 J0212+5222

The timing residuals for PSR J0212+5222 developed similarly to those of PSR J1923+4243: solutions after $\simeq 59200$ required an increasing number of spin derivatives and still showed some signature in the TOAs. We replaced the derivatives (third order and above, maintaining the first and second) with a glitch model as described for J1923+4243, and the model did improve. However, the residuals did not become decisively flat as they had for the prior source. In particular, with the improved fit, another glitch-like event became evident in the archival GBT observations. We added a second glitch component and refit only archival data; we measured a second glitch with reasonable magnitude close to MJD 56551 (F-test comparison before/after this glitch in archival data returned 10^{-20}). We do not measure any significant recovery terms for this glitch. Including the magnitude and epoch parameters in the model when we fit all TOAs flattened the residuals. The residu-

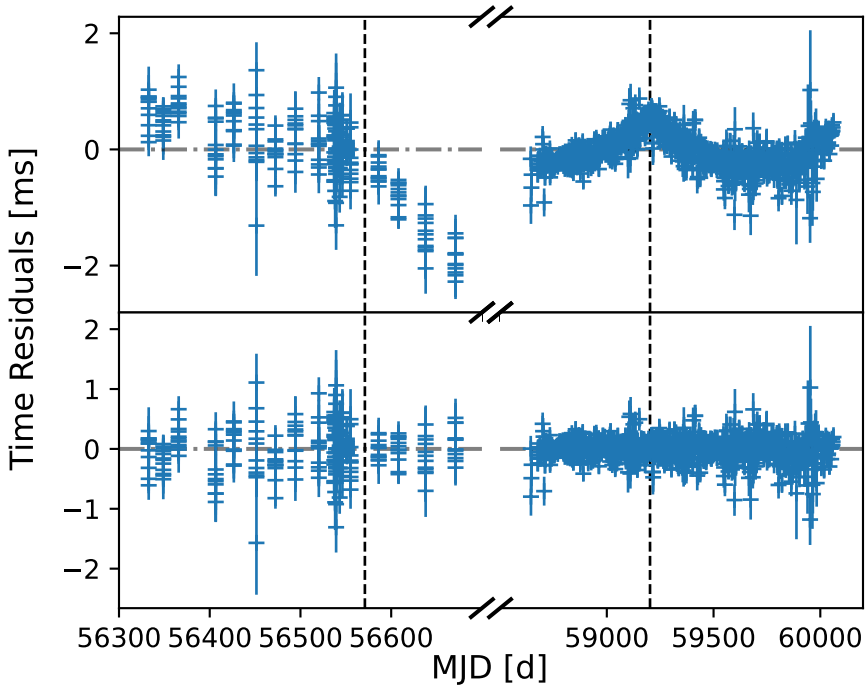

Figure 4.3 Glitches in PSR J0212+5222 timing residuals. Dashed vertical lines highlight the epochs of the two measured glitches; we use a broken horizontal axis for clarity.

als before and after adding the glitches are included in Figure 4.3, and the parameters for the glitches are provided in Table 4.4.

4.4.2.2 J1923+4243

PSR J1923+4243 was included in two timing campaigns in 2013 (Lynch et al., 2018b) prior to observations at CHIME. This campaign resulted in a well constrained timing model, making phase connection to the CHIME/Pulsar observations that began in 2020 trivial. However, following MJD $\simeq 59500$, the solution began to drift, and the RMS of the residuals began to grow. Initial attempts included adding higher order frequency derivatives; while this did improve the fit, the parameters were not stable, and changed as more data was added. We substituted the frequency derivative terms for glitch parameters (glitch

epoch and glitch magnitude), and the fit dramatically improved (reduced $\chi^2 = 64$ with 333 degrees of freedom initially and 2.3 for 331 DOF). We used an F-test to compare the fits; comparing the model after adding glitch epoch and magnitude included to the model without a glitch, the F-statistic is $\approx 10^{-241}$.

While this fit is much better than pre-glitch with spin frequency derivatives, some additional structure remained in the residuals. In an attempt to reduce this, we also tried a model that included terms for the second frequency derivative and glitch recovery (first and second frequency derivatives). Given that glitches typically correlate with significant timing noise (Lower et al., 2021), this choice is reasonable. The resulting fit no longer contained any apparent structure, the reduced χ^2 dropped to 1.2 (DOF now 329), and an F-test comparing it to the pre-glitch fit returned $\approx 10^{-281}$. Comparing instead to the simpler glitch model (containing only the epoch and magnitude of the glitch), the F-statistic is $\approx 10^{-44}$ in preference for the more complex model. We plot the timing residuals before and after including the glitch model in Figure 4.4, and the parameters for the glitch is given in Table 4.4.

4.4.2.3 J2029+5459

As with the other glitching sources, fits to PSR J2029+5459's timing residuals using standard timing parameters were insufficient in removing structure from the TOAs. Unlike many other sources, the phase JUMP between archival GBT data and CHIME/Pulsar observations was not enough to solve the source and so owe focused on the higher-cadence CHIME/Pulsar observations. A glitch was inserted near MJD 59536, and the CHIME/Pulsar TOAs flattened. However, connection to the archival data was still not possible, and it appeared as though there was a discontinuity in spin frequency between the two observing epochs that was too large to be due to quadratic spin-down. A sec-

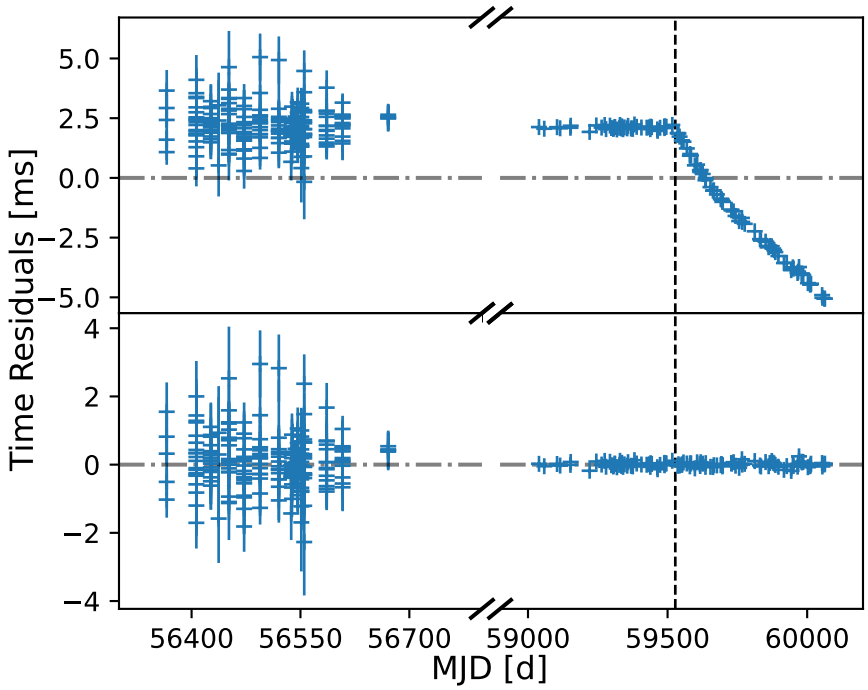

Figure 4.4 Glitch in PSR J1923+4243 timing residuals. The dashed vertical line indicates the epoch of the glitch. For clarity, the horizontal axis is broken to omit the data gap between MJD 56700 and 59000.

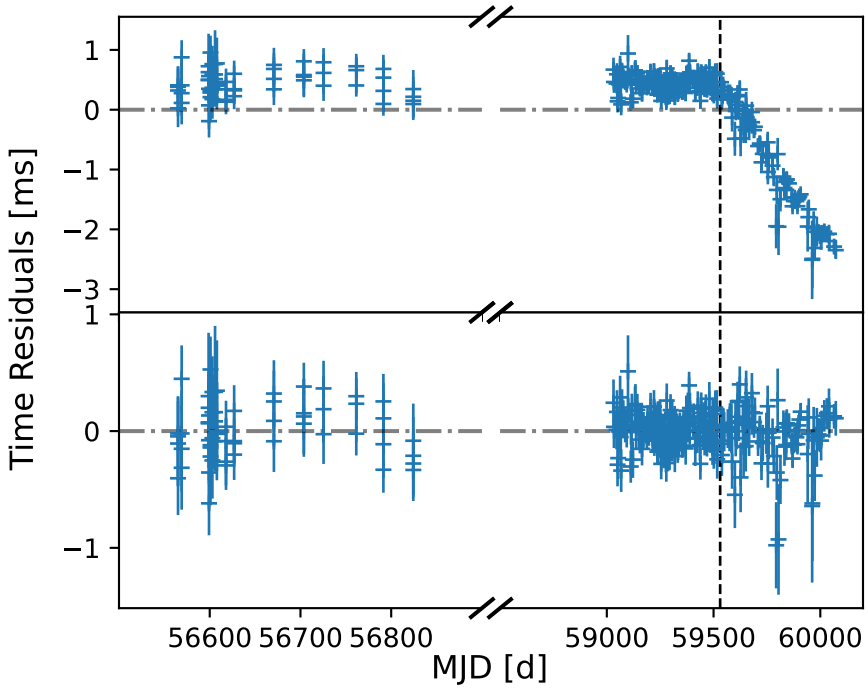

Figure 4.5 Glitch in PSR J2029+5459 timing residuals. The epoch of the glitch is marked with a vertical dashed line, and the horizontal axis is broken for clarity. For this source, we also fit a glitch in the gap between the GBT data and CHIME data. We are not able to constrain the epoch of this glitch, so it is omitted from the plot.

ond glitch was inserted in the gap (MJD 58000) and phase connection was made possible. Due to the lack of data, the epoch of this glitch is entirely covariant with the GBT-CHIME jump, and so we are unable to precisely measure it. The F-test comparing the pre- and post-glitch fits returned $\leq 10^{-230}$. Residuals for the data are shown in Figure 4.5 and the measured parameters are included in Table 4.4.

4.4.2.4 J2202+5040

Identifying the glitch progressed similarly to other sources; a model without a glitch included required several high-order polynomials to flatten TOAs, and was exchanged for

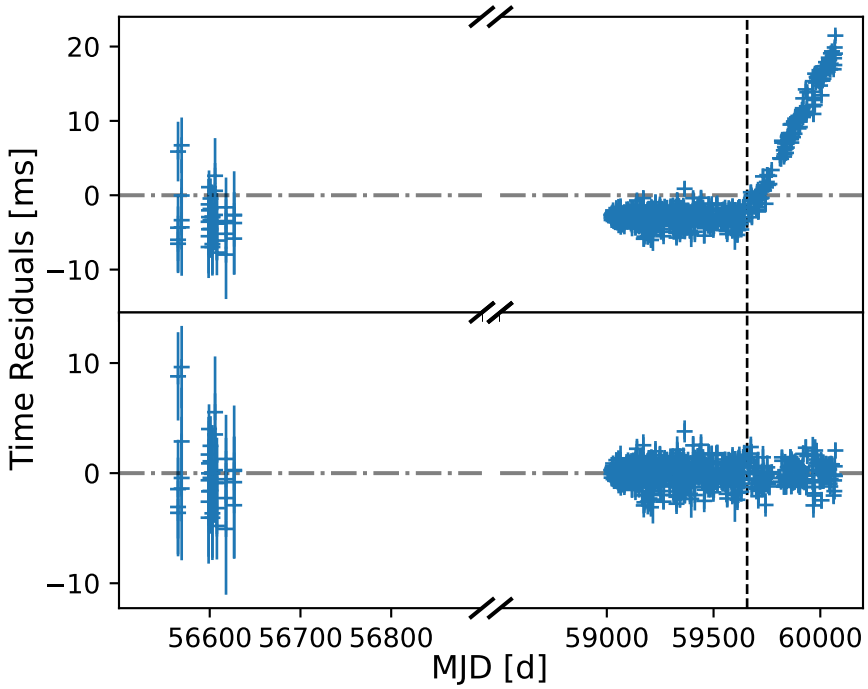

Figure 4.6 Glitch in PSR J2202+5040 timing residuals. The epoch of the glitch is marked with a vertical dashed line, and the horizontal axis is broken for clarity. For this source, we also fit a glitch in the gap between the GBT data and CHIME data. We are not able to constrain the epoch of this glitch, so it is omitted from the plot.

a model with a glitch near MJD 59650. Similar to J2029+5459, this sufficiently flattened residuals in the CHIME data, but connection to archival GBT data required an additional glitch in the data gap. A marked difference in this source's solution is the sign of the glitches, which are both negative in Hz/s (indicating a spin-down glitch). Residuals are shown in Figure 4.5 and glitch parameters are included in Table 4.4.

4.4.2.5 J2351+6500

Timing residuals for this source hinted at the presence of a glitch shortly after MJD 59500, when the otherwise simple model no longer flattened the residuals. Fits with a glitch im-

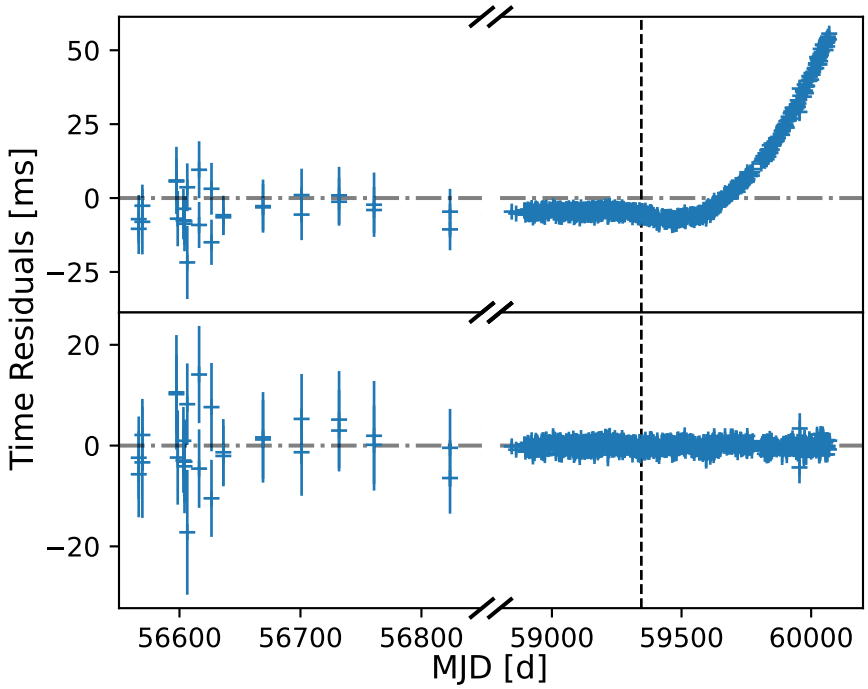

Figure 4.7 Glitch in PSR J2351+6500 timing residuals. The epoch of the glitch is marked with a vertical dashed line, and the horizontal axis is broken for clarity.

mediately resolved the problem. The measured glitch parameters (included in Table 4.4) are similar to those measured in PSRs J0212+5222 and J1923+4243, where the change in ν is positive (i.e. spin-up glitch) and the change in $\dot{\nu}$ is negative. This is apparent in the timing residuals (Figure 4.7, where the epoch of the glitch precedes a downward trend that recovers quadratically.

4.4.2.6 Timing Noise and Unconfirmed Glitch Candidates

The vast majority of pulsars in this dataset have been solved, meaning that their timing models correctly predict the arrival times of pulses extending into the future. There is a small subset of pulsars for which this is not true; in many of these cases, timing residuals contain additional structure that is not well fit by standard rotational/position-

al/binary parameters. In fact, data for PSR J1954+3852 can be fit with as many as four significant spin derivatives. Binary motion can manifest as apparent spin derivatives in timing data when the orbital period is much larger than the data span (for one such example, see Bassa et al., 2016), but no such model improves the fit. We assume that the residual structure is due to timing noise; the daily cadence at CHIME gives us unprecedented sensitivity to variations in period on short timescales. This can be quantified in a simple case where we assume the uncertainty in the measurement of polynomial scales as $\sigma_{\mathrm{TOA}}/\sqrt{\mathrm{N}}$. The TOA uncertainty will depend on the telescope used and the pulsar's intrinsic brightness; given that the CHIME system's sensitivity is approximately 70% that of the 820 MHz system used for the GBT and that pulsar flux density scales with observing frequency (average spectral index of -1.4, Bates et al., 2014), we can directly compare the (analytic) uncertainties on timing noise measurement. We have assumed the pulse width does not change significantly between the observing frequencies, which is not always true. However, between 600 and 820 MHz, this change is likely negligible. GBT timing campaigns for canonical pulsars typically include roughly 1 observation/month with duration $\geq 30\,\mathrm{min}$. Comparing this to weekly 10 minute CHIME scans, the GBT measurement uncertainty is approximately twice that of CHIME; to match CHIME uncertainty, $\geq 100\,\mathrm{min}$ scans would be needed at GBT. Usage of a lower frequency at GBT can help this, but only for sources with steep spectral indices - and CHIME cadences/durations are generally greater than those used above.

One metric used to quantify timing noise is the stability parameter, defined as (Arzoumanian et al., 1994):

$$\Delta_8 = \log\left(\frac{1}{6\nu}|\ddot{\nu}|T_8^3\right) \tag{4.1}$$

where ν is the pulsar spin frequency, $\ddot{\nu}$ is its second derivative, and $T_8 = 10^8\,\mathrm{s}$ is the

baseline over which the former parameters are measured. This study has produced measurements of $\ddot{\nu}$ for 15 sources; for these and all other sources, we check for baselines in CHIME-only data that span at least $0.8\,T_8$ and fit for $\ddot{\nu}$ over this period. These measurements are shown in Figure 4.8 with our best-fit line (with 3σ uncertainty) and the line published in Arzoumanian et al. (1994) for comparison. We note that our measurements deviate from those of Arzoumanian et al. (1994) slightly, particularly for sources with larger spin-down (i.e. younger pulsars). Models that did not previously include $\ddot{\nu}$ (plotted in green in Figure 4.8) agree more closely with those results. In general, though, the spread is fairly large.

4.4.3 Proper Motions

Measurements of pulsar proper motion can be difficult to reliably disentangle from position, as errors in the two components will manifest as annual sinusoids. Breaking this degeneracy is possible with high cadence and long observation baselines, which we have achieved for many sources included in this study. Table 4.5 provides all of the sources for which we have measured proper motion. Many of these sources have been measured in previous studies; we utilize this archival data to greatly supplement our measurements. Sources for which no previous measurements exist are marked with an asterisk.

For each measurement of proper motion, we also estimate the pulsar's transverse velocity using the DM distance of the pulsar, which we calculate using both NE2001 (Cordes & Lazio, 2002) and YMW+16 (Yao et al., 2017). With a distance and a velocity measurement, we can further refine the pulsar's rate of spin-down by accounting for two effects: Galactic acceleration and transverse motion (Shklovskii, 1970). These terms can be calculated and removed from the measured period derivative of a pulsar to calculate a more accurate magnetic field and spin-down luminosity. For a full description of the procedure

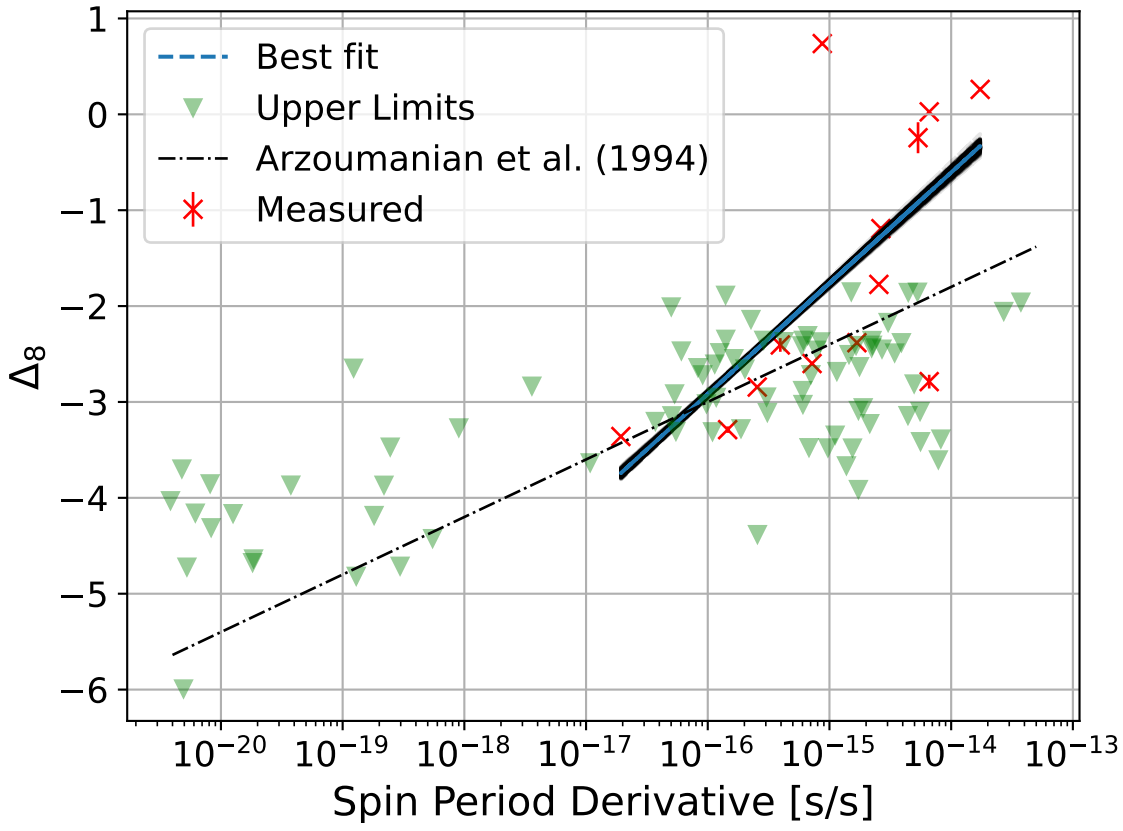

Figure 4.8 Timing stability parameter Δ_8 for GBNCC sources. For each source, we limited the baseline to $\approx 10^8\ s$ in CHIME-only data. Red points indicate sources where $\ddot{\nu}$ had been incorporated in the timing model previously; green triangles indicate sources where we added $\ddot{\nu}$ to the model to determine a limit. The black dash-dotted line is the fit line from Arzoumanian et al. (1994), and the blue dashed line is a best-fit to the red points. We also include the 3σ region for the best-fit line, which shows apparent discrepancy with the prior fit; we attribute this to the number of points observed and implicit scatter in the Δ_8 parameter.

used to estimate these terms, see Lynch et al. (2018b).

Of the 19 sources for which we measure proper motion, 13 are new measurements. The remaining 6 sources (J0645+5158, J1125+7819, J1641+8049, J1710+4923, J1816+4510, and J1955+6708) have published proper motions in the ATNF catalog (ver. 1.70, Manchester et al., 2016). Except for PSR J1125+7819, our measurements differ from these published values by as much as 79σ, or nearly 40 mas/yr. We include in Figure 4.9 a comparison between these previous measurements and those coming from this study. PSRs J0645+5158, J1125+7819, and J1816+4510 are fairly consistent, and the other three are very disparate. PSR J1641+8049 is a spider pulsar (for an overview, see Fruchter et al., 1988), which is actively ablating its companion. These systems often exhibit variable orbital parameters due to their dynamic environment (e.g., see Polzin et al., 2019). As noted in Mata Sánchez et al. (2023), proper motion measurements for this source from Lynch et al. (2018b) are likely overestimated, and are at odds with measurements from optical data. This is likely what is reflected in our new measurement, as the timing baseline in this work is approximately twice that used in Lynch et al. (2018b). The timing baseline for PSRs J1955+6708 and J1710+4923 have doubled as well, which may have resulted in the significant change.

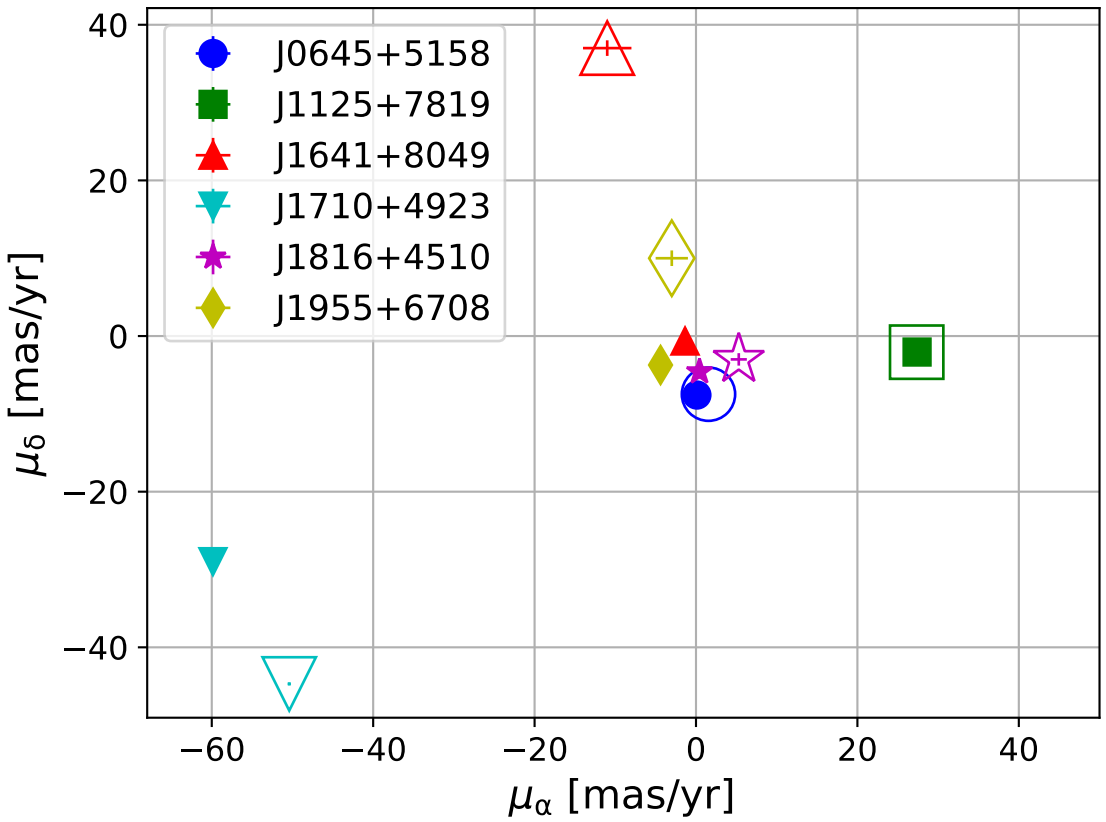

Figure 4.9 Comparison of proper motion measurements to previously published values. For each of the 6 sources with measurements of proper motion, we plot a hollow marker for the previous value and a filled marker for our measurement. All points have error-bars, but they are small in most cases. The dramatic change in proper motion for PSR J1641+8049 is supported by optical results published by Mata Sánchez et al. (2023).

Table 4.5. Proper motion measurements and spin corrections for GBNCC sources.

PSR	$\mu_{\rm long}$ [mas/yr]	$\mu_{\rm lat}$ [mas/yr]	d kpc	$v_{\rm tot}$ km/s	$\dot{P}_{\rm Gal}$ 10^{-21} s/s	$\dot{P}_{\rm S}$ 10^{-21} s/s	$\dot{P}_{\rm int}$ 10^{-21} s/s	B 10^8 G	$\tau_{\rm c}$ Gyr	$\dot{E}$ 10^{33} erg/s
J0214+5222*	11.6(3)	4.5(5)	1.0	60.8	−0.04	9.52	286.92	26.9	1.4	0.8
			1.2	68.4	−0.02	10.71	285.71	26.8	1.4	0.8
J0406+3039*	2.37(8)	−4.6(5)	1.7	42.9	0.18	0.30	7.82	1.4	5.3	17.4
			1.6	40.1	0.17	0.28	7.86	1.4	5.3	17.5
J0509+3801*	3.1(3)	−7(2)	1.9	66.6	10.17	19.07	7905.96	248.9	0.2	0.7
			1.6	54.0	8.53	15.47	7911.19	249.0	0.2	0.7
J0645+5158	0.80(2)	−7.54(4)	0.7	25.2	0.10	0.87	3.96	1.9	35.4	0.2
			0.7	24.1	0.09	0.83	4.01	1.9	35.0	0.2
J0742+4110*	−8.47(12)	−12.7(6)	0.7	51.8	−0.01	1.27	5.43	1.3	9.2	6.9
			0.5	37.8	−0.02	0.93	5.78	1.4	8.6	7.4
J1125+7819	16.151(13)	22.22(2)	0.6	82.4	−0.36	4.87	2.43	1.0	27.4	1.3
			0.8	108.6	−0.41	6.42	0.94	0.6	70.8	0.5
J1221−0633*	−0.56(12)	−6(2)	0.7	21.0	−0.29	0.12	5.42	1.0	5.7	29.6
			1.3	35.2	−0.38	0.21	5.42	1.0	5.7	29.6
J1327+3423*	−8.49(3)	1.44(4)	0.5	19.4	−5.84	3.56	131.58	23.7	5.0	0.1
			0.3	14.0	−4.92	2.57	131.65	23.7	5.0	0.1
J1434+7257*	7.31(14)	−7.1(2)	0.7	34.4	−4.96	7.49	545.83	48.3	1.2	0.3
			1.0	47.0	−5.87	10.22	544.00	48.2	1.2	0.3
J1628+4406*	−0.5(2)	−20.3(2)	0.6	58.8	−21.00	111.00	19238.61	597.4	0.1	0.1
			0.5	52.0	−19.46	98.30	19249.77	597.6	0.1	0.1
J1641+8049	1.50(2)	−0.14(2)	1.7	11.8	−0.31	0.02	10.07	1.4	3.2	48.2
			3.0	21.6	−0.42	0.03	10.17	1.5	3.1	48.6
J1710+4923†	−49.65(4)	−44.25(4)	0.7	207.8	−0.36	22.81	–	–	–	–
			0.5	159.6	−0.30	17.51	0.99	0.6	51.7	1.2
J1806+2819*	−1.7(6)	−11.6(9)	1.3	74.1	−1.59	6.69	32.45	7.1	7.4	0.4
			1.3	73.6	−1.58	6.64	32.49	7.1	7.4	0.4
J1816+4510	0.07(2)	−4.60(2)	2.4	52.8	−0.84	0.40	43.52	3.8	1.2	52.8
			4.4	95.1	−1.42	0.72	43.78	3.8	1.2	53.1
J1938+6604*	2.95(10)	0.67(8)	2.3	33.5	−4.76	1.16	22.14	7.1	15.9	0.1
			3.4	48.5	−5.99	1.68	22.86	7.2	15.4	0.1

Table 4.5 (cont'd)

PSR	$\mu_{\rm long}$ [mas/yr]	$\mu_{\rm lat}$ [mas/yr]	d kpc	$v_{\rm tot}$ km/s	$\dot{P}_{\rm Gal}$ 10^{-21} s/s	$\dot{P}_{\rm S}$ 10^{-21} s/s	$\dot{P}_{\rm int}$ 10^{-21} s/s	B 10^8 G	$\tau_{\rm c}$ Gyr	$\dot{E}$ 10^{33} erg/s
J1955+6708	−4.46(14)	3.64(13)	3.4	92.3	−2.19	2.33	12.44	3.3	10.9	0.8
			5.3	144.8	−2.69	3.66	11.61	3.2	11.7	0.7
J2022+2534*	−5.42(7)	−4.49(10)	3.3	110.6	−0.83	1.06	5.93	1.3	7.1	12.6
			4.0	134.0	−1.03	1.28	5.91	1.3	7.1	12.6
J2123+5434*	−13.7(7)	4.9(7)	2.1	144.3	−23.05	149.80	91.90	36.2	23.9	0.0
			1.8	125.2	−20.49	130.01	109.12	39.4	20.2	0.0
J2150−0326*	1.60(13)	−11.12(96)	1.1	56.2	−0.46	1.14	7.48	1.6	7.4	6.8
			2.0	105.2	−0.68	2.13	6.71	1.6	8.3	6.1

*New measurements of proper motion.

†Proper motion measurements for PSR J1710+4923 imply a negative intrinsic spin-down. This is most likely due to an error in the distance estimate and leads to an erroneous magnetic field and characteristic age. For this reason, we omit terms for this source from the final three columns. Note that this was also mentioned in Lynch et al. (2018b).

Note. — Pulsar proper motions are given in the ecliptic frame. For each source, we calculate quoted parameters using distance predictions from both NE2001 (Cordes & Lazio, 2002) and YMW+16 (Yao et al., 2017) and estimate the Galactic potential using results from Guo et al. (2021). Values in parentheses are the 1σ uncertainty in the last digit as reported by `PINT`. Uncertainties on distances are generally $\simeq 30\%$.

4.4.4 Binary Pulsars

The GBNCC survey has been an incredible tool for discovering exotic systems, not the least of which are the binary pulsars it has found. In total, the survey has discovered 24 such systems; here, we have included long-term timing solutions for 18 of them, plus a binary pulsar from the GBT350 survey (Hessels et al., 2008). These sources span a wide range of orbital periods ($0.1 \leq P_{\rm B} \leq 528\,{\rm d}$) and eccentricities ($10^{-6} \leq e \leq 0.6$), encompassing many evolutionary pathways and timing strategies. We plot each binary system's orbital period and minimum companion mass in Figure 4.10. Tables 4.6 and 4.7 include the measured/derived binary parameters for all sources included in this dataset. The first includes sources which use the ELL1 binary model (Lange et al., 2001), a parameterization that is appropriate for sources in nearly circular orbits. The second includes sources that use either the more generalized binary model (BT, Blandford & Teukolsky, 1976) or the relativistic parameterization (DD, Damour & Deruelle, 1985, 1986) for sources with signif-

icant pulsar acceleration. Many of these binary systems have been published elsewhere, though few datasets have the long baselines/high cadences reported here. We include parameters for 9 new binary solutions, and focus on one source of particular interest in section 4.4.4.1: PSR J2038+3447.

Interestingly, despite the dramatic increase in timing baselines for these sources, no post-Keplerian terms have been added to our binary models. For all binaries, we calculated estimates of these parameters using the equations 8.48-8.52 in Lorimer & Kramer (2004) and determined how these the inclusion of these estimates would impact our timing solutions. Aside from the few sources with PK measurements from previous works (see below), none of these parameters are predicted to be measured significantly. We also added them to the fit parameters as a test, and no measurements were significant above 2σ. PSRs J0509+3801 (Lynch et al., 2018b) and J1759+5036 (Agazie et al., 2021) are both in relativistic orbits with prior measurements of the advance of periastron $\dot{\omega}_{\rm orbit}$ – the former also has previous measurements of orbital decay $\dot{P}_{\rm B}$ and the Einstein delay parameter γ. We improve previous constraints on these parameters, and these improvements are included in Table 4.8. All measurements are consistent with those made in previous works.

4.4.4.1 J2038+3447

PSR J2038+3447 (J2038) was originally discovered in the NGP survey (Hessels et al., 2008) and subsequently observed in 820 MHz observations that spanned $\simeq 226$ days. The first of these observations included gridding to localize the pulsar to within an 820 MHz beam. Subsequent observations were centered on the improved position at a varying cadence (generally in groups with a few weeks between groups). Timing analysis of these data uncovered a significant period drift between observations much larger than expected from spin-down, suggesting binary motion. However, the data span was insufficient to

Table 4.6. Binary pulsars that utilize ELL1 models.

PSR	Measured					Derived	
	$P_{\rm B}$ [days]	$a \sin i/c$ [s]	$T_{\rm asc}$ [MJD]	ϵ_1 $[10^{-6}]$	ϵ_2 $[10^{-6}]$	$f_{\rm M}$ $[10^{-4} M_\odot]$	$M_{\rm c,min}$ $[M_\odot]$
J0406+3039**	6.955717217(2)	2.3192820(2)	57451.8533146(4)	3.7(2)	−11.7(2)	2.7686	0.08
J0742+4110*	1.3853611813(6)	0.5564571(11)	56045.1468648(13)	1(4)	−0(4)	0.96394	0.06
J1125+7819	15.3554459628(3)	12.19242105(9)	56157.47634435(5)	−12.856(15)	0.83(2)	82.533	0.29
J1221−0633*	0.3863495385(4)	0.0552868(5)	57906.1230476(11)	230(20)	40(20)	0.012156	0.01
J1239+3239*	4.0854016578(12)	2.3711240(10)	59282.5326304(3)	7.0(9)	2.0(9)	8.5758	0.13
J1602−1009**	0.12445961397(13)	0.0346079(3)	58988.1081132(2)	200(20)	−40(20)	0.028731	0.02
J1720−0534	0.1316985759(2)	0.0596156(9)	59144.1417331(3)	20(30)	−20(20)	0.13116	0.03
J1816+4510	0.36089348174(2)	0.5954001(2)	55771.1046588(2)	4.4(6)	−1.6(6)	17.4	0.16
J1816+4510	0.360893481832(4)	0.5953998(2)	55771.10465783(3)	4.1(5)	−0.7(5)	17.4	0.16
J1938+6604	2.46716272965(6)	8.9507426(6)	56366.09670039(6)	5.85(13)	−27.35(13)	1264.9	0.87
J2022+2534*	1.2837028285(2)	0.6092408(3)	57535.5638692(3)	1.05(98)	1.4(9)	1.4734	0.07
J2150−0326*	4.0445506010(5)	3.3207135(6)	57510.6590599(2)	3.7(3)	9.5(3)	24.035	0.18

*Published rotational models, but no previously measured binary parameters.

**Not published prior to this work.

Note. — All timing models presented here use the ELL1 binary model, which is appropriate for low-eccentricity orbits. Values in parentheses are the 1σ uncertainty in the last digit as reported by `PINT`.

Table 4.7. Binary pulsars that utilize DD/BT models.

PSR	Measured					Derived	
	$P_{\rm B}$ [days]	$a \sin i/c$ [s]	T_0 [MJD]	ω [°]	e	$f_{\rm M}$ $[10^{-2} M_\odot]$	$M_{\rm c,min}$ $[M_\odot]$
J0032+6946	527.62131333(13)	178.6747603(4)	57142.9728(6)	147.5262(4)	0.000531747(4)	2.2000	0.42
J0214+5222	512.0397765(5)	174.565753(2)	56126.6029(4)	210.5889(3)	0.00532803(3)	2.1785	0.42
J0509+3801	0.37958378732(9)	2.05046(3)	58054.1829999(4)	144.2024(7)	0.586409(3)	6.4242	0.65
J1045−0436*	10.27364598(2)	22.252634(7)	57481.373(13)	321.9(4)	$7.46(8) \times 10^{-5}$	11.209	0.82
J1759+5036	2.042983903(14)	6.82456(2)	57604.492222(11)	92.132(2)	0.308269(4)	8.1767	0.72
J1806+2819	43.86695922(5)	21.608786(3)	57028.28(2)	257.5(2)	$8.68(2) \times 10^{-5}$	0.56299	0.25
J2038+3447*	461.362059(3)	144.727612(9)	58991.3045(99)	70.212(8)	0.00081673(10)	1.5292	0.36

*Published rotational models, but no previously measured binary parameters.

Note. — All timing models presented here use DD/BT binary models. Values in parentheses are the 1σ uncertainty in the last digit as reported by `PINT`.

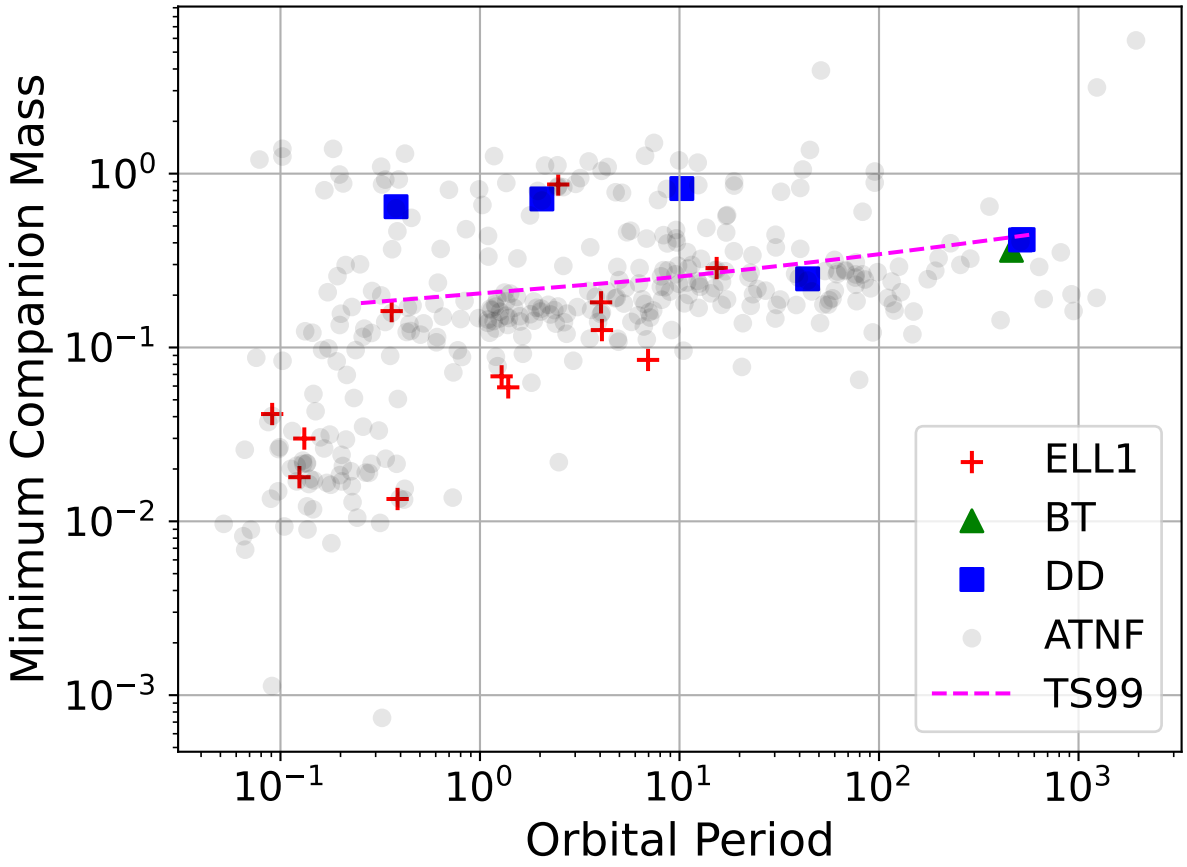

Figure 4.10 Orbital period vs. companion mass. Bold points indicate pulsars in our sample, and fainter points come from the ATNF catalog. Marker type indicates what binary model is used. The dashed magenta line shows the relationship between white dwarf mass and orbital period given in Tauris & Savonije (1999).

Table 4.8. Updates to post-Keplerian parameters.

PSR	Parameter	Measurement
J0509+3801	Advance of periastron $\dot{\omega}_{\rm orbit}$ [mas/yr]	3.03476(11)
	Einstein delay γ [s]	0.00444(3)
	Orbital decay $\dot{P}_{\rm B}$ [10^{-12}]	$-1.37(7)$
J1759+5036	Advance of periastron $\dot{\omega}_{\rm orbit}$ [mas/yr]	0.1289(4)

Note. — Values in parentheses are the 1σ uncertainty in the last digit as reported by `PINT`.

fully disentangle its rotational, positional, and binary parameters. Further 820 MHz and 350 MHz observations with the GBT were conducted in late 2019/early 2020, but phase connection was still not reached.

J2038 was among the first sources to be added to the CHIME/Pulsar regular observations following the CHIME/GBNCC MoU, and has since been observed with near daily cadence. Given the many observations and lack of binary constraint, we assumed the binary period was $\gg 1$ year. To handle this, we opted to include measurements of frequency derivatives in our model to capture the orbital motion (for a similar case, see Kaplan et al. 2016 and Bassa et al. 2016). These apparent period changes are actually due to binary-induced Doppler shifts in the pulsar signal, and can therefore be mapped back onto the orbital phase/orbital period plane. After $\simeq 100$ days of CHIME/Pulsar observations, this technique allowed us to predict a binary model that was phase connected with the archival GBT data. Further observations broke covariance between position and spin-down and fully solved the system.

Determination of these parameters showed that J2038 is a relatively slow rotator ($P \simeq 160$ ms) in a large, nearly circular orbit ($P_{\rm B} \simeq 462$ d, $A_1 \simeq 142\,{\rm lt-s}$, $e < 10^{-3}$). These mea-

surements place it in a somewhat sparse region of the orbital period/spin period plane, as we show in Figure 4.11. Nearby binaries are either in highly eccentric orbits with main sequence companions or circular orbits with degenerate (mostly CO or He WD) companions. Given J2038's low eccentricity and its minimum/median mass of $0.36/0.43\,\mathrm{M}_\odot$ (calculated from the binary mass function), the companion is most likely to be a He-core WD.

With the full timing solution now constrained, we examined the possibility for J2038 to be utilized for tests of the strong equivalence principle (SEP) as outlined in Stairs (2003). The so-called Nordtvedt Effect (Nordtvedt, 1968) describes a deviation from GR predictions due to a difference in the inertial and gravitational mass of the objects in the orbit. As the two stars orbit one another in the gravitational potential of the Galaxy, this difference gives rise to an additional acceleration that will gradually align the eccentricity vector of the orbit with the Galactic gravitational force vector. For small eccentricities, the magnitude of the forced eccentricity vector $\mathbf{e}_\mathrm{F}$ will depend on the binary parameters as (Stairs, 2003)

$$|\mathbf{e}_\mathrm{F}| = \frac{1}{2}\frac{(\Delta_\mathrm{P} - \Delta_\mathrm{C})\,\mathbf{g}_\perp c^2}{GM(2\pi/P_\mathrm{B})}, \tag{4.2}$$

where $\mathbf{g}_\perp$ is the projection of the Galactic gravitational field in the plane of the orbit, G is Newton's constant, M is the total mass of the system, and P_B is the orbital period. The Δ_P and Δ_C parameters describe the fractional difference between the pulsar's/companion's gravitational and inertial masses, i.e. for object i,

$$\left(\frac{M_\mathrm{grav}}{M_\mathrm{inertial}}\right)_i = 1 + \Delta_\mathrm{i}. \tag{4.3}$$

Using this description, candidates for SEP tests are subject to three notable criteria:

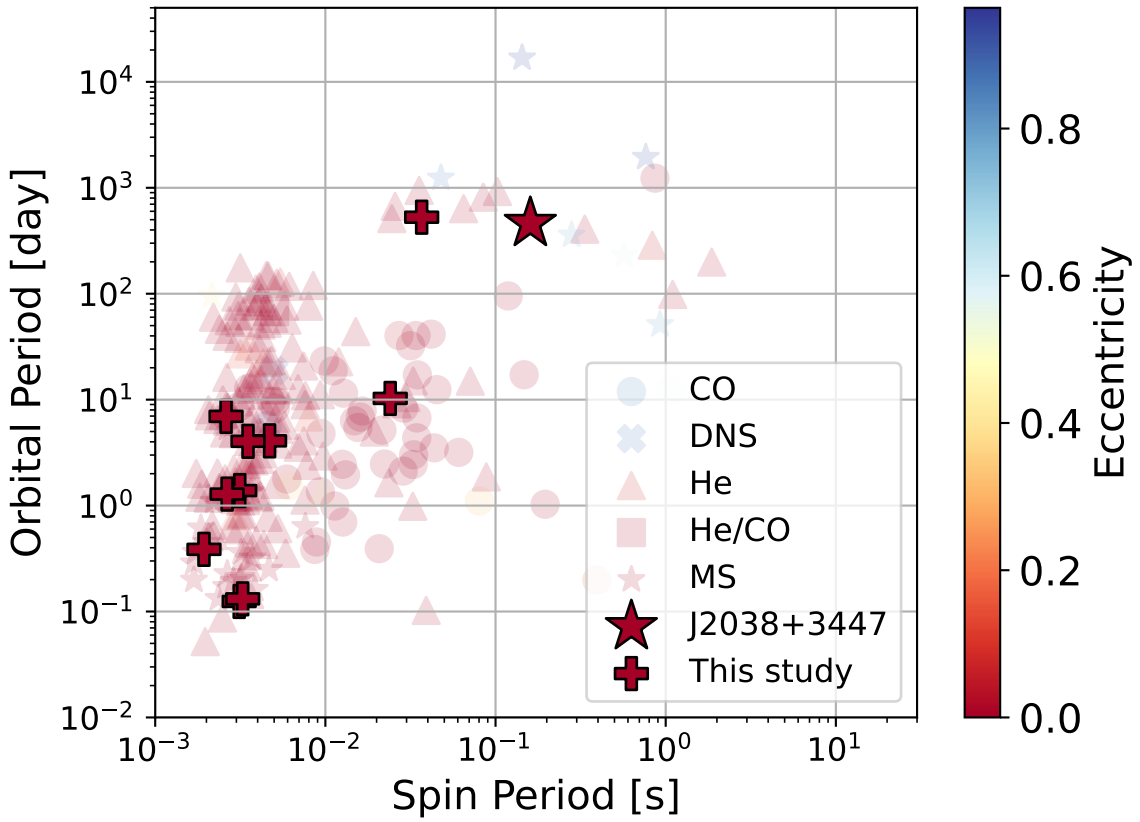

Figure 4.11 Comparison of PSR J2038+3447's spin and orbital periods to other known binaries. We include points for carbon-oxygen companions (CO, circles), double neutron star companions (DNS, filled Xs), helium/helium-CO companions (He and He/CO, triangles and squares), and main sequence companions (MS, stars). The filled and outlined star indicates J2038. Filled plus sign markers highlight the other binaries published in this paper. For all points, colors indicate the orbital eccentricity.

- $P_{\rm B}^2/e > 10^7 {\rm day}^2$. This sets the "forced" eccentricity term (the component of the eccentricity vector due to the gravitational potential of the Galaxy) to be significant enough to measure (Wex, 1997).

- $\dot{\omega}_{\rm orbit} > \dot{\omega}_{\rm Galaxy}$. This implies that the projection of the Galactic gravitational acceleration is constant.

- $\tau_c \gg 2\pi/\dot{\omega}_{\rm orbit}$. In this limit, it can be assumed that the system has completed many orbits, and the time-dependent eccentricity vector is randomly oriented. For pulsars, $\tau_c = P/2\dot{P}$.

For J2038+3447, the first criteria is satisfied ($P_{\rm B}^2/e > 10^8 {\rm day}^2$). For the second and third terms, we must make a prediction for $\dot{\omega}_{\rm orbit}$ using (from A2.7 in Lorimer & Kramer, 2004)

$$\dot{\omega}_{\rm orbit} \approx 39.73^\circ \, {\rm yr}^{-1} \left(\frac{P_{\rm B}}{\rm hr}\right)^{-5/3} \left(\frac{1}{1-e^2}\right) \left(\frac{M}{{\rm M}_\odot}\right)^{2/3}. \tag{4.4}$$

Using the minimum predicted companion mass of $0.36\,{\rm M}_{\rm sun}$ and a fiducial pulsar mass of $1.4\,{\rm M}_{\rm sun}$, we estimate a minimum $\dot{\omega}_{\rm orbit} = 1.05 \times 10^{-5\circ}/{\rm yr}$. Using the DM distance of 3.8 kpc (as predicted by YMW+16, Yao et al. 2017) and J2038's position, we can estimate the rate of Galactic rotation to be $\leq 10^{-8}\,{\rm deg/yr}$ – satisfying the second criterion. Finally, J2038's period derivative is fairly low relative to its period, pushing its τ_c above 2.8 Gyr. This is well above our prediction for $2\pi/\dot{\omega}_{\rm orbit} \leq 35{\rm Myr}$, which satisfies the third criterion. So, pending the measurement of $\dot{\omega}_{\rm orbit}$, J2038 seems to be a good candidate for SEP tests.

At the moment, $\dot{\omega}_{\rm orbit}$ is not measurable in the timing residuals of J2038. This is due largely to the covariance of the remaining binary model parameters with $\dot{\omega}_{\rm orbit}$, in particular $P_{\rm B}$. Many orbits are needed to disentangle the two; since the binary period is so large, this translates to a long baseline. To set an upper bound on $\dot{\omega}$, we injected values of $\dot{\omega}$ in the range of $10^{-4} - 10^{-1}{\rm deg/yr}$ into the measured TOAs for J2038. We then fit

these TOAs for the position, spin, and binary parameters (including $\dot{\omega}$) and examined the significance of the recovered parameters. With this simulation, we determine a 3σ upper limit of $1.5 \times 10^{-2}\,\mathrm{deg/yr}$.

Given our current timing uncertainty (residual RMS is $122\,\mu\mathrm{s}$), and our prediction for a minimum $\dot{\omega}_{\mathrm{orbit}}$, we can estimate the time to detection. To do so, we simulate CHIME/Pulsar TOAs with daily cadence and uncertainty equal to the mean measured CHIME/Pulsar TOA uncertainty ($169\,\mu\mathrm{s}$). We use a model identical to our current timing model for J2038 except we include our prediction for $\dot{\omega}_{\mathrm{orbit}}$. We can then iteratively add data and fit for $\dot{\omega}_{\mathrm{orbit}}$ (as well as standard rotation/position parameters) until a sufficient uncertainty threshold is reached. Using this procedure, we anticipate that a measurement of the minimum $\dot{\omega}_{\mathrm{orbit}}$ will only become significant to 3σ after $\approx 20\,\mathrm{yr}$. We do note, however, that average TOA uncertainties for the different observing bands suggest that J2035 may have a relatively flat spectrum, and so future observations at 350 MHz or similar may accelerate the detection timeline.

4.5 CONCLUSION

In this work, we have analyzed timing data for 128 sources discovered in GBNCC and the GBT NGP surveys. When available, we incorporate both archival data from GBT, Arecibo, and LOFAR with recent high-cadence CHIME/Pulsar data. Following a memorandum of understanding between the CHIME and GBNCC collaborations, we have connected TOA-generation and pulsar timing tools to produce a user-friendly, self-auditing pipeline for managing large and disjoint baselines. Using these data, we fit for typical spin and position parameters for all sources, including 42 newly published timing solutions. Timing residuals for all sources are provided in Appendix B. For 19 sources (13 of which are new), we measure proper motion and infer kinematic corrections to the observed spin-

down. The dataset has also provided measurements of binary parameters for 19 sources and has uncovered 7 glitches in 4 pulsars. We briefly analyzed timing noise in the population, though we leave a more sophisticated analysis for a future work. We provide timing models, TOAs, and configuration files for reproduction of results presented here on the GBNCC GitHub page[5].

As a result of its timing analysis, PSR J2038+3447 was found to be in a large, circular orbit with a $\approx 0.4\,\mathrm{M}_\odot$ companion. We examined the suitability of this system to test the strong equivalence principle. While it seems to be an optimal binary system for such a study, we were unable to measure $\dot{\omega}_{\mathrm{orbit}}$, and simulations of CHIME observations predict that a 3σ measurement will require several decades of continued timing.

4.6 ACKNOWLEDGEMENTS

The Green Bank Observatory is a facility of the National Science Foundation (NSF) operated under cooperative agreement by Associated Universities, Inc. The National Radio Astronomy Observatory is a facility of the NSF operated under cooperative agreement by Associated Universities, Inc. The Arecibo Observatory is a facility of the NSF operated under cooperative agreement (AST-1744119) by the University of Central Florida (UCF) in alliance with Universidad Ana G. Méndez (UAGM) and Yang Enterprises (YEI), Inc.

We acknowledge that CHIME is located on the traditional, ancestral, and unceded territory of the Syilx/Okanagan people. We are grateful to the staff of the Dominion Radio Astrophysical Observatory, which is operated by the National Research Council of Canada. CHIME is funded by a grant from the Canada Foundation for Innovation (CFI) 2012 Leading Edge Fund (Project 31170) and by contributions from the provinces of British Columbia, Québec and Ontario. The CHIME/FRB Project, which enabled de-

[5] https://github.com/GBNCC/data

velopment in common with the CHIME/Pulsar instrument, is funded by a grant from the CFI 2015 Innovation Fund (Project 33213) and by contributions from the provinces of British Columbia and Québec, and by the Dunlap Institute for Astronomy and Astrophysics at the University of Toronto. Additional support was provided by the Canadian Institute for Advanced Research (CIFAR), McGill University and the McGill Space Institute thanks to the Trottier Family Foundation, and the University of British Columbia. The CHIME/Pulsar instrument hardware was funded by NSERC RTI-1 grant EQPEQ 458893-2014.

J.K.S., D.L.K., M.A.M., M.E.D., T.D., S.M.R., and X.S. are supported by the NANOGrav NSF Physics Frontiers Center award numbers 1430284 and 2020265. E.P. is supported by an H2020 ERC Consolidator Grant 'MAGNESIA' under grant agreement No. 817661 and National Spanish grant PGC2018-095512-BI00. Z.P. is a Dunlap Fellow. J.vL. acknowledges funding from the European Research Council under the European Union's Seventh Framework Programme (FP/2007-2013) / ERC Grant Agreement n. 617199 ("ALERT"), and from Vici research programme "ARGO" with project number 639.043.815, financed by the Netherlands Organisation for Scientific Research (NWO). M.A.M. and E.F.L. are supported by NSF OIA-1458952 and NSF Award Number 2009425. S.M.R. is a CIFAR Fellow. Pulsar research at UBC is supported by an NSERC Discovery Grant and by the Canadian Institute for Advanced Research. M.S. acknowledges funding from the European Research Council (ERC) under the European Union's Horizon 2020 research and innovation programme (grant agreement No. 694745). M.E.D. acknowledges support from the Naval Research Laboratory by NASA under contract S-15633Y. T.D. is supported by an NSF Astronomy and Astrophysics Grant (AAG) award number 2009468.

This work has made use of data from the European Space Agency (ESA) mission *Gaia* (https://www.cosmos.esa.int/gaia), processed by the *Gaia* Data Processing and Analysis

Consortium (DPAC, https://www.cosmos.esa.int/web/gaia/dpac/consortium). Funding for the DPAC has been provided by national institutions, in particular the institutions participating in the *Gaia* Multilateral Agreement. This research was enabled in part by support provided by the BC Digital Research Infrastructure Group and the Digital Research Alliance of Canada (https://alliancecan.ca).

CHAPTER 5

Conclusion

In this dissertation, I have analyzed data from two major pulsar surveys, both using the Green Bank Telescope. The former, GBNCC, is a massive, all-sky, low-frequency survey that has discovered many interesting (and scientifically valuable) pulsars (Stovall et al., 2014; Lynch et al., 2018b; Agazie et al., 2021; Swiggum et al., 2023; Fiore et al., 2023). This sample shed some light on the older pulsar population, to which it is most sensitive. Following an assessment of the survey's sensitivity (Chapter 2), we revisited common pulsar population models, which have been developed using primarily high-frequency surveys. By comparing simulated pulsar populations to the actual survey results, it became evident that there is a bias in the models toward the results of these former surveys – in particular, they do not properly account for excess dispersion measure (DM) toward the Galactic center where the background sky temperature bury pulsar signals. This low frequency has advantages, which we utilized to make precise measurements of DM and spectral index for nearly 670 pulsars. This census of pulsars detected in the survey included new measurements of flux density at 350 MHz along with pulse profiles for all sources.

The second survey analyzed here, GBT820 (Chapter 3), provides a complementary survey scheme where an area of prior interest was probed much more deeply. The Cygnus region is home to many of the most complex and dynamic regions of the nearby Galaxy, evidenced not only by the pulsars in the region but also by their extraordinarily high DMs. We analyzed the distribution of these DMs compared to those predicted using typical Galactic models and provide evidence that these models woefully underestimate the material in this direction. We quantify this using profiles measured in data from this

survey and elsewhere to measure scattering timescales for 9 pulsars. In this first analysis of the search data, only 3 new pulsars were discovered; however, our DM discussion implies that this may not be due to a lack of pulsars here, but instead an excess of dispersive material. If this is the case, then deeper searches (like those currently underway using FAST, e.g. Han et al. 2021) may still be fruitful in this region. And regardless of the few discoveries, PSR J2035+3655 sits in an uncommon region of the P-$\dot{\mathrm{P}}$ plane, which prompted a series of exciting timing proposals to nail down its binary parameters. These observations culminated in a weak constraint on the pulsar's mass via measurement of the Shapiro delay. This measurement is significant to the $\approx 2\sigma$ level; future observations with high cadence may sharpen these constraints. Using our detections in GBT820, we provide an estimate of the survey's sensitivity.

In Chapter 4, I returned to the GBNCC survey on the candidate follow-up side. Specifically, we built a pipeline to handle the large datasets that are available for many of the survey discoveries. In some cases, these data span over a decade, and generally include observations from multiple telescopes. These enormous baselines coupled with high-cadence observations with CHIME provide excellent sensitivity to timing effects on both short and long timescales. As such, we used them to make improved measurements of timing noise parameters, proper motion, binary parameters, and more. A subset of these pulsars had not been published prior to this work; for these sources, we produced full timing models using several years of CHIME observations. We also detected glitches in several sources, and placed these sources in context with other glitching pulsars. While much of the work in this chapter focused on corralling the data and updating many complex models, we examined one binary pulsar intently: PSR J2038+3447. This pulsar is orbiting a white dwarf companion in a large (462 day) orbit. The details of this orbit make it a good candidate for tests of the strong equivalency principle, an implicit requirement

for the validity of GR. Following many years of timing observations, we discussed the prospects for measuring the advance of periastron in this orbit (necessary for GR tests). While the daily CHIME observations may not quite provide the sensitivity required to make such a measurement, the prospects for its determination via other methods are good.

This work has incorporated an immense quantity of data taken with several telescopes, primarily the 100 m Green Bank Telescope. In total, I observed 232.25 hours on the GBT, 20.75 of which were for projects on which I was the PI. Some of these observations were utilized to confirm candidate signals, and from those data I successfully confirmed four new pulsars. An additional candidate that I identified was subsequently confirmed in an adjacent survey beam. Counting the number of pulsars that I solved is a bit more difficult, as many pulsar solutions were built with help from others and in a piecemeal way over long periods of timing; a conservative estimate for the number of pulsars I solved from scratch is 20, including two binaries (one in very tight 4.5 hour orbit, the other a very wide 461 day orbit). I have generated upwards of 70,000 TOAs (data cleaning and folding), and in the two major surveys described in this dissertation, I led/co-led processing of approximately 85 TB of search data.

Moving forward, the landscape of pulsar searching is evolving with new instrumentation and methodologies to search for candidates. Many archival survey datasets are still turning up new pulsars, and motivation for reanalysis continues to grow. The young pulsar population that lives in the dense, radio-loud Galactic plane is still largely hiding from us; this will likely change significantly in the next few years with wide-band receivers, high-frequency telescopes, and ever-improving computing resources. These searches are only as good as their follow-up, however; telescopes like the CHIME (CHIME/Pulsar Collaboration et al., 2021) and UTMOST (Jankowski et al., 2019) telescopes (and eventu-

ally, DSA-2000; Hallinan et al., 2019) have signaled a paradigm change from episodic, a few TOAs/year timing campaigns to cheap and efficient daily observations. Not only does such a change provide an excellent boon for high precision timing, it also greatly lowers the bar for observing the so-called "normal" pulsar population. These sources have historically only been observed for as long as it takes to nail down the period, its derivative, and position. Going forward, large-scale timing campaigns will probe deeply into the timing noise that young pulsars exhibit, and will provide new insights on neutron star composition through detection of glitches.

BIBLIOGRAPHY

Abdo A. A., et al., 2009, The Astrophysical Journal, 700, 1059

Agazie G. Y., et al., 2021, Astrophysical Journal, 922, 35

Agazie G., et al., 2023, Astrophysical Journal Letters, 951, L9

Aggarwal K., et al., 2019, Astrophysical Journal, 880, 116

Alam M. F., et al., 2021, Astrophysical Journal Supplement, 252, 4

Aloisi R. J., et al., 2019, Astrophysical Journal, in press

Alpar M. A., 1977, Astrophysical Journal, 213, 527

Alpar M. A., Chau H. F., Cheng K. S., Pines D., 1994, Astrophysical Journal Letters, 427, L29

Andersen B. C., et al., 2022, arXiv e-prints, p. arXiv:2209.06895

Antonelli M., Basu A., Haskell B., 2023, Monthly Notices of the Royal Astronomical Society, 520, 2813

Antoniadis J., et al., 2022, Monthly Notices of the Royal Astronomical Society, 510, 4873

Antoniadis J., et al., 2023, arXiv e-prints, p. arXiv:2306.16226

Anumarlapudi A., Swiggum J. K., Kaplan D. L., Fichtenbauer T. D. J., 2023, Astrophysical Journal, 948, 32

Arzoumanian Z., Nice D. J., Taylor J. H., Thorsett S. E., 1994, Astrophysical Journal, 422, 671

Arzoumanian Z., Gotthelf E. V., Ransom S. M., Safi-Harb S., Kothes R., Landecker T. L., 2011, Astrophysical Journal, 739, 39

Arzoumanian Z., et al., 2020, Astrophysical Journal Letters, 905, L34

Arzoumanian Z., et al., 2023, arXiv e-prints, p. arXiv:2301.03608

Ashworth M., Lyne A. G., 1981, Monthly Notices of the Royal Astronomical Society, 195, 517

Askew J., Reardon D. J., Shannon R. M., 2023, Monthly Notices of the Royal Astronomical Society, 519, 5086

Babak S., et al., 2016, Monthly Notices of the Royal Astronomical Society, 455, 1665

Backer D. C., 1975, Astronomy and Astrophysics, 43, 395

Backer D. C., 1984, Journal of Astrophysics and Astronomy, 5, 187

Bailes M., et al., 1997, Astrophysical Journal, 481, 386

Barr E. D., et al., 2013, Monthly Notices of the Royal Astronomical Society, 435, 2234

Bassa C. G., et al., 2016, Monthly Notices of the Royal Astronomical Society, 460, 2207

Basu A., et al., 2022, Monthly Notices of the Royal Astronomical Society, 510, 4049

Bates S. D., Lorimer D. R., Rane A., Swiggum J., 2014, Monthly Notices of the Royal Astronomical Society, 439, 2893

Beerer I. M., et al., 2010, Astrophysical Journal, 720, 679

Bell M. E., et al., 2016, Monthly Notices of the Royal Astronomical Society, 461, 908

Berlanas S. R., Wright N. J., Herrero A., Drew J. E., Lennon D. J., 2019, Monthly Notices of the Royal Astronomical Society, 484, 1838

Beuther H., et al., 2022, Astronomy and Astrophysics, 665, A63

Bhat N. D. R., Cordes J. M., Camilo F., Nice D. J., Lorimer D. R., 2004, Astrophysical Journal, 605, 759

Bhattacharyya B., et al., 2013, Astrophysical Journal Letters, 773, L12

Biggs J. D., Bailes M., Lyne A. G., Goss W. M., Fruchter A. S., 1994, Monthly Notices of the Royal Astronomical Society, 267, 125

Bilous A. V., et al., 2016, Astronomy and Astrophysics, 591, A134

Bisnovatyi-Kogan G. S., Komberg B. V., 1974, Soviet Astronomy, 18, 217

Blandford R., Teukolsky S. A., 1976, Astrophysical Journal, 205, 580

Bogdanov S., et al., 2019, Astrophysical Journal Letters, 887, L25

Boyles J., et al., 2013, Astrophysical Journal, 763, 80

Braun R., Bonaldi A., Bourke T., Keane E., Wagg J., 2019, arXiv e-prints, p. arXiv:1912.12699

Brinkman C., Freire P. C. C., Rankin J., Stovall K., 2018, Monthly Notices of the Royal Astronomical Society, 474, 2012

Broderick J. W., et al., 2021, Monthly Notices of the Royal Astronomical Society, 504, 1482

Burgay M., et al., 2006, Monthly Notices of the Royal Astronomical Society, 368, 283

Burgay M., et al., 2013, Monthly Notices of the Royal Astronomical Society, 429, 579

CHIME/Pulsar Collaboration et al., 2021, Astrophysical Journal Supplement, 255, 5

Cameron A. D., et al., 2020, Monthly Notices of the Royal Astronomical Society, 493, 1063

Camilo F., 1995, PhD thesis, PRINCETON UNIVERSITY.

Camilo F., Nice D. J., 1995, Astrophysical Journal, 445, 756

Camilo F., Nice D. J., Taylor J. H., 1996a, Astrophysical Journal, 461, 812

Camilo F., Nice D. J., Shrauner J. A., Taylor J. H., 1996b, Astrophysical Journal, 469, 819

Champion D. J., et al., 2005, Monthly Notices of the Royal Astronomical Society, 363, 929

Chandler A. M., 2003, PhD thesis, CALIFORNIA INSTITUTE OF TECHNOLOGY

Chatterjee S., Goss W. M., Brisken W. F., 2005, Astrophysical Journal Letters, 634, L101

Chen J. L., Wang H. G., 2014, Astrophysical Journal Supplement, 215, 11

Coenen T., et al., 2014, Astronomy and Astrophysics, 570, A60

Cognard I., et al., 2011, Astrophysical Journal, 732, 47

Coleman M. S. B., Burrows A., 2022, Monthly Notices of the Royal Astronomical Society, 517, 3938

Comerón F., Pasquali A., 2012, Astronomy and Astrophysics, 543, A101

Cordes J. M., Lazio T. J., 1991, Astrophysical Journal, 376, 123

Cordes J. M., Lazio T. J. W., 2002, arXiv e-prints, pp astro–ph/0207156

Cordes J. M., Rickett B. J., 1998, Astrophysical Journal, 507, 846

Cordes J. M., et al., 2006, Astrophysical Journal, 637, 446

Costa M. E., McCulloch P. M., Hamilton P. A., 1991, Monthly Notices of the Royal Astronomical Society, 252, 13

Cromartie H. T., et al., 2020, Nature Astronomy, 4, 72

Cruces M., et al., 2021, Monthly Notices of the Royal Astronomical Society, 508, 300

Damour T., Deruelle N., 1985, Annales de L'Institut Henri Poincare Section (A) Physique Theorique, 43, 107

Damour T., Deruelle N., 1986, Annales de L'Institut Henri Poincare Section (A) Physique Theorique, 44, 263

Dembska M., Kijak J., Jessner A., Lewandowski W., Bhattacharyya B., Gupta Y., 2014, Monthly Notices of the Royal Astronomical Society, 445, 3105

Demorest P. B., Pennucci T., Ransom S. M., Roberts M. S. E., Hessels J. W. T., 2010, Nature, 467, 1081

Deneva J. S., Stovall K., McLaughlin M. A., Bates S. D., Freire P. C. C., Martinez J. G., Jenet F., Bagchi M., 2013, Astrophysical Journal, 775, 51

Desvignes G., et al., 2016, Monthly Notices of the Royal Astronomical Society, 458, 3341

Detweiler S., 1979, Astrophysical Journal, 234, 1100

Dewey R. J., Taylor J. H., Weisberg J. M., Stokes G. H., 1985a, Astrophysical Journal Letters, 294, L25

Dewey R. J., Taylor J. H., Weisberg J. M., Stokes G. H., 1985b, Astrophysical Journal Letters, 294, L25

Dicke R. H., 1946, Review of Scientific Instruments, 17, 268

Dong F. A., et al., 2022, arXiv e-prints, p. arXiv:2210.09172

DuPlain R., Ransom S., Demorest P., Brandt P., Ford J., Shelton A. L., 2008, in Bridger A., Radziwill N. M., eds, Society of Photo-Optical Instrumentation Engineers (SPIE) Conference Series Vol. 7019, Advanced Software and Control for Astronomy II. p. 70191D, doi:10.1117/12.790003

Dunn L., et al., 2022, Monthly Notices of the Royal Astronomical Society, 512, 1469

Emig K. L., et al., 2022, Astronomy and Astrophysics, 664, A88

Espinoza C. M., Lyne A. G., Stappers B. W., Kramer M., 2011, Monthly Notices of the Royal Astronomical Society, 414, 1679

Falxa M., et al., 2023, Monthly Notices of the Royal Astronomical Society, 521, 5077

Fiore W., et al., 2023, arXiv e-prints, p. arXiv:2305.13624

Fomalont E. B., Goss W. M., Lyne A. G., Manchester R. N., Justtanont K., 1992, Monthly Notices of the Royal Astronomical Society, 258, 497

Fonseca E., Stairs I. H., Thorsett S. E., 2014, Astrophysical Journal, 787, 82

Foster R. S., Fairhead L., Backer D. C., 1991, Astrophysical Journal, 378, 687

Fragione G., Loeb A., 2023, arXiv e-prints, p. arXiv:2305.08920

Frail D. A., Jagannathan P., Mooley K. P., Intema H. T., 2016, Astrophysical Journal, 829, 119

Fruchter A. S., Stinebring D. R., Taylor J. H., 1988, Nature, 333, 237

Fruchter A. S., et al., 1990, Astrophysical Journal, 351, 642

Fuentes J. R., Espinoza C. M., Reisenegger A., Shaw B., Stappers B. W., Lyne A. G., 2017, Astronomy and Astrophysics, 608, A131

Gautam T., et al., 2022, Astronomy and Astrophysics, 664, A54

Gomez-Gonzalez J., Guelin M., 1974, Astronomy and Astrophysics, 32, 441

Good D. C., et al., 2021, Astrophysical Journal, 922, 43

Gould D. M., Lyne A. G., 1998, Monthly Notices of the Royal Astronomical Society, 301, 235

Guo Y. J., et al., 2021, Astronomy and Astrophysics, 654, A16

Hallinan G., et al., 2019, in Bulletin of the American Astronomical Society. p. 255 (arXiv:1907.07648), doi:10.48550/arXiv.1907.07648

Halpern J. P., Camilo F., Gotthelf E. V., Helfand D. J., Kramer M., Lyne A. G., Leighly K. M., Eracleous M., 2001, Astrophysical Journal Letters, 552, L125

Han J., Wang C., Xu J., Han J.-L., 2016, Research in Astronomy and Astrophysics, 16, 159

Han J., Wang C., Xu J., Han J., 2017, arXiv e-prints, p. arXiv:1703.05988

Han J. L., et al., 2021, Research in Astronomy and Astrophysics, 21, 107

Haskell B., Antonopoulou D., Barenghi C., 2020, Monthly Notices of the Royal Astronomical Society, 499, 161

Haslam C. G. T., Klein U., Salter C. J., Stoffel H., Wilson W. E., Cleary M. N., Cooke D. J., Thomasson P., 1981, Astronomy and Astrophysics, 100, 209

Haslam C. G. T., Salter C. J., Stoffel H., Wilson W. E., 1982, Astronomy and Astrophysics Supplement, 47, 1

Hessels J. W. T., Ransom S. M., Kaspi V. M., Roberts M. S. E., Champion D. J., Stappers B. W., 2008, in Bassa C., Wang Z., Cumming A., Kaspi V. M., eds, American Institute of Physics Conference Series Vol. 983, 40 Years of Pulsars: Millisecond Pulsars, Magnetars and More. pp 613–615 (arXiv:0710.1745), doi:10.1063/1.2900310

Hewish A., 1975, Science, 188, 1079

Hewish A., Bell S. J., Pilkington J. D. H., Scott P. F., Collins R. A., 1968, Nature, 217, 709

Hisano S., et al., 2022, Astrophysical Journal, 928, 161

Hobbs G., et al., 2004a, Monthly Notices of the Royal Astronomical Society, 352, 1439

Hobbs G., Lyne A. G., Kramer M., Martin C. E., Jordan C., 2004b, Monthly Notices of the Royal Astronomical Society, 353, 1311

Hobbs G. B., Edwards R. T., Manchester R. N., 2006, Monthly Notices of the Royal Astronomical Society, 369, 655

Hu H., Kramer M., Wex N., Champion D. J., Kehl M. S., 2020, Monthly Notices of the Royal Astronomical Society, 497, 3118

Hulse R. A., Taylor J. H., 1975, Astrophysical Journal Letters, 201, L55

Jacoby B. A., Bailes M., Ord S. M., Knight H. S., Hotan A. W., 2007, Astrophysical Journal, 656, 408

Jankowski F., van Straten W., Keane E. F., Bailes M., Barr E. D., Johnston S., Kerr M., 2018a, Monthly Notices of the Royal Astronomical Society, 473, 4436

Jankowski F., van Straten W., Keane E. F., Bailes M., Barr E. D., Johnston S., Kerr M., 2018b, Monthly Notices of the Royal Astronomical Society, 473, 4436

Jankowski F., et al., 2019, Monthly Notices of the Royal Astronomical Society, 484, 3691

Janssen G. H., Stappers B. W., Braun R., van Straten W., Edwards R. T., Rubio-Herrera E., van Leeuwen J., Weltevrede P., 2009, Astronomy and Astrophysics, 498, 223

Janssen G. H., Stappers B. W., Bassa C. G., Cognard I., Kramer M., Theureau G., 2010, Astronomy and Astrophysics, 514, A74

Jiang P., Peng B., Li D., Xu R., 2019, arXiv e-prints, p. arXiv:1903.07240

Johnston S., Karastergiou A., 2019, Monthly Notices of the Royal Astronomical Society, 485, 640

Johnston S., Kerr M., 2018, Monthly Notices of the Royal Astronomical Society, 474, 4629

Johnston S., Lyne A. G., Manchester R. N., Kniffen D. A., D'Amico N., Lim J., Ashworth M., 1992, Monthly Notices of the Royal Astronomical Society, 255, 401

Joshi B. C., et al., 2009, Monthly Notices of the Royal Astronomical Society, 398, 943

Kaplan D. L., 2022, PSS: Pulsar Survey Scraper, Astrophysics Source Code Library, record ascl:2210.001 (ascl:2210.001)

Kaplan D. L., et al., 2016, Astrophysical Journal, 826, 86

Kaplan D. L., et al., 2019, Astrophysical Journal, 884, 96

Karako-Argaman C., et al., 2015, Astrophysical Journal, 809, 67

Karako-Argaman C., et al., 2020, RRATtrap: Rotating Radio Transient identifier, Astrophysics Source Code Library, record ascl:2011.017 (ascl:2011.017)

Kawash A. M., et al., 2018, Astrophysical Journal, 857, 131

Keane E. F., et al., 2018, Monthly Notices of the Royal Astronomical Society, 473, 116

Keith M. J., et al., 2010a, Monthly Notices of the Royal Astronomical Society, 409, 619

Keith M. J., et al., 2010b, Monthly Notices of the Royal Astronomical Society, 409, 619

Kellermann K. I., Pauliny-Toth I. I. K., Williams P. J. S., 1969, Astrophysical Journal, 157, 1

Kiminki D. C., Kobulnicky H. A., Vargas Álvarez C. A., Alexander M. J., Lundquist M. J., 2015, Astrophysical Journal, 811, 85

Kirichenko A., et al., 2015, Astrophysical Journal, 802, 17

Koch-Miramond L., Ábrahám P., Fuchs Y., Bonnet-Bidaud J. M., Claret A., 2002, Astronomy and Astrophysics, 396, 877

Kondratiev V. I., et al., 2016, Astronomy and Astrophysics, 585, A128

Kramer M., Xilouris K. M., Lorimer D. R., Doroshenko O., Jessner A., Wielebinski R., Wolszczan A., Camilo F., 1998, Astrophysical Journal, 501, 270

Kramer M., Lange C., Lorimer D. R., Backer D. C., Xilouris K. M., Jessner A., Wielebinski R., 1999, Astrophysical Journal, 526, 957

Kramer M., et al., 2006, Science, 314, 97

Krishnakumar M. A., Mitra D., Naidu A., Joshi B. C., Manoharan P. K., 2015, Astrophysical Journal, 804, 23

Krishnakumar M. A., Joshi B. C., Manoharan P. K., 2017, Astrophysical Journal, 846, 104

Kuzmin A. D., Losovsky B. Y., 2001, Astronomy and Astrophysics, 368, 230

Lai X. Y., Yun C. A., Lu J. G., Lü G. L., Wang Z. J., Xu R. X., 2018, Monthly Notices of the Royal Astronomical Society, 476, 3303

Lange C., Camilo F., Wex N., Kramer M., Backer D. C., Lyne A. G., Doroshenko O., 2001, Monthly Notices of the Royal Astronomical Society, 326, 274

Lattimer J. M., 2021, Annual Review of Nuclear and Particle Science, 71, 433

Layek B., Godaba Venkata D., Yadav P., 2023, Physical Reviews D, 107, 023004

Lazarus P., et al., 2015, Astrophysical Journal, 812, 81

Lentati L., et al., 2015, Monthly Notices of the Royal Astronomical Society, 453, 2576

Levin L., et al., 2016, Astrophysical Journal, 818, 166

Lewandowska N., Demorest P., McLaughlin M., Kilian P., Hankins T., 2023, in American Astronomical Society Meeting Abstracts. p. 438.05

Lewandowski W., Wolszczan A., Feiler G., Konacki M., Sołtysiński T., 2004, Astrophysical Journal, 600, 905

Link B., Epstein R. I., van Riper K. A., 1992, Nature, 359, 616

Lommen A. N., Zepka A., Backer D. C., McLaughlin M., Cordes J. M., Arzoumanian Z., Xilouris K., 2000, Astrophysical Journal, 545, 1007

Lorimer D., 1994, PhD thesis, The University of Manchester

Lorimer D. R., 2018, Nature Astronomy, 2, 860

Lorimer D. R., Kramer M., 2004, Handbook of Pulsar Astronomy. Cambridge University Press

Lorimer D. R., Yates J. A., Lyne A. G., Gould D. M., 1995a, Monthly Notices of the Royal Astronomical Society, 273, 411

Lorimer D. R., et al., 1995b, Astrophysical Journal, 439, 933

Lorimer D. R., Lyne A. G., Camilo F., 1998, Astronomy and Astrophysics, 331, 1002

Lorimer D. R., et al., 2006, Monthly Notices of the Royal Astronomical Society, 372, 777

Lorimer D. R., et al., 2015, Monthly Notices of the Royal Astronomical Society, 450, 2185

Lower M. E., et al., 2020, Monthly Notices of the Royal Astronomical Society, 494, 228

Lower M. E., et al., 2021, Monthly Notices of the Royal Astronomical Society, 508, 3251

Lu R., Yue H., Lai X., Wang W., Zhang S., Xu R., 2023, Monthly Notices of the Royal Astronomical Society, 520, 4289

Luo J., et al., 2021, Astrophysical Journal, 911, 45

Lynch R. S., et al., 2013, Astrophysical Journal, 763, 81

Lynch R. S., et al., 2018a, in American Astronomical Society Meeting Abstracts #231. p. 243.13

Lynch R. S., et al., 2018b, Astrophysical Journal, 859, 93

Lyne A., Graham-Smith F., 2012, Pulsar Astronomy. Cambridge University Press

Lyne A. G., et al., 1998, Monthly Notices of the Royal Astronomical Society, 295, 743

Main R. A., et al., 2023, arXiv e-prints, p. arXiv:2306.13462

Manchester R. N., 2017, in Journal of Physics Conference Series. p. 012002 (arXiv:1801.04318), doi:10.1088/1742-6596/932/1/012002

Manchester R. N., Lyne A. G., Taylor J. H., Durdin J. M., Large M. I., Little A. G., 1978, Monthly Notices of the Royal Astronomical Society, 185, 409

Manchester R. N., et al., 1996, Monthly Notices of the Royal Astronomical Society, 279, 1235

Manchester R. N., et al., 2001, Monthly Notices of the Royal Astronomical Society, 328, 17

Manchester R. N., Hobbs G. B., Teoh A., Hobbs M., 2005a, Astronomical Journal, 129, 1993

Manchester R. N., Hobbs G. B., Teoh A., Hobbs M., 2005b, Astronomical Journal, 129, 1993

Manchester R. N., et al., 2013, PASA, 30, e017

Manchester R. N., Hobbs G. B., Teoh A., Hobbs M., 2016, VizieR Online Data Catalog, p. B/psr

Martinez J. G., et al., 2019, Astrophysical Journal, 881, 166

Mata Sánchez D., et al., 2023, Monthly Notices of the Royal Astronomical Society, 520, 2217

McCollough M., et al., 2022, in AAS/High Energy Astrophysics Division. p. 110.80

McEwen A. E., et al., 2020, Astrophysical Journal, 892, 76

McLaughlin M. A., et al., 2006, Nature, 439, 817

Melatos A., Millhouse M., 2023, Astrophysical Journal, 948, 106

Merryfield M., et al., 2023, Astronomical Journal, 165, 152

Miles M. T., et al., 2023, Monthly Notices of the Royal Astronomical Society, 519, 3976

Millhouse M., Melatos A., Howitt G., Carlin J. B., Dunn L., Ashton G., 2022, Monthly Notices of the Royal Astronomical Society, 511, 3304

Mohanty D. K., 1983, in Danziger J., Gorenstein P., eds, IAU Symposium Vol. 101, Supernova Remnants and their X-ray Emission. p. 503

Morello V., et al., 2019, Monthly Notices of the Royal Astronomical Society, 483, 3673

Murphy T., et al., 2017, PASA, 34, e020

Navarro J., Anderson S. B., Freire P. C., 2003, Astrophysical Journal, 594, 943

Nicastro L., Lyne A. G., Lorimer D. R., Harrison P. A., Bailes M., Skidmore B. D., 1995, Monthly Notices of the Royal Astronomical Society, 273, L68

Nice D. J., et al., 2013, Astrophysical Journal, 772, 50

Nordtvedt K., 1968, Physical Review, 170, 1186

Ocker S. K., Cordes J. M., Chatterjee S., 2021, Astrophysical Journal, 911, 102

Orellana R. B., De Biasi M. S., Paíz L. G., 2021, Monthly Notices of the Royal Astronomical Society, 502, 6080

Özel F., Freire P., 2016, Annual Review of Astronomy and Astrophysics, 54, 401

P. R. S., R. S. D., eds, 1984, Birth and evolution of neutron stars: Issues raised by millisecond pulsars

Pang P. T. H., Tews I., Coughlin M. W., Bulla M., Van Den Broeck C., Dietrich T., 2021, Astrophysical Journal, 922, 14

Parent E., et al., 2020, Astrophysical Journal, 904, 92

Parent E., et al., 2022, Astrophysical Journal, 924, 135

Park R. S., Folkner W. M., Williams J. G., Boggs D. H., 2021, Astronomical Journal, 161, 105

Parthasarathy A., et al., 2019, Monthly Notices of the Royal Astronomical Society, 489, 3810

Petroff E., Hessels J. W. T., Lorimer D. R., 2022, The Astronomy and Astrophysics Review, 30, 2

Phillips A. C., 1999, The Physics of Stars, 2nd Edition. Wiley

Piddington J. H., Minnett H. C., 1952, Australian Journal of Scientific Research A Physical Sciences, 5, 17

Pletsch H. J., et al., 2012, Astrophysical Journal, 744, 105

Polzin E. J., Breton R. P., Stappers B. W., Bhattacharyya B., Janssen G. H., Osłowski S., Roberts M. S. E., Sobey C., 2019, Monthly Notices of the Royal Astronomical Society, 490, 889

Posselt B., et al., 2023, Monthly Notices of the Royal Astronomical Society, 520, 4582

Qiao G., Manchester R. N., Lyne A. G., Gould D. M., 1995, Monthly Notices of the Royal Astronomical Society, 274, 572

Quintana A. L., Wright N. J., 2021, Monthly Notices of the Royal Astronomical Society, 508, 2370

Quintana A. L., Wright N. J., 2022, Monthly Notices of the Royal Astronomical Society, 515, 687

Raaijmakers G., et al., 2021, Astrophysical Journal Letters, 918, L29

Ransom S. M., 2001, PhD thesis, Harvard University

Ransom S., 2011, PRESTO: PulsaR Exploration and Search TOolkit, Astrophysics Source Code Library, record ascl:1107.017 (ascl:1107.017)

Ransom S. M., Cordes J. M., Eikenberry S. S., 2003, Astrophysical Journal, 589, 911

Ransom S. M., et al., 2011, Astrophysical Journal Letters, 727, L16

Rauw G., et al., 2015, Astrophysical Journal Supplement, 221, 1

Ray P. S., Thorsett S. E., Jenet F. A., van Kerkwijk M. H., Kulkarni S. R., Prince T. A., Sand hu J. S., Nice D. J., 1996, Astrophysical Journal, 470, 1103

Ray P. S., et al., 2011, The Astrophysical Journal Supplement Series, 194, 17

Reardon D. J., et al., 2016, Monthly Notices of the Royal Astronomical Society, 455, 1751

Reardon D. J., et al., 2023, Astrophysical Journal Letters, 951, L6

Ridley J. P., Crawford F., Lorimer D. R., Bailey S. R., Madden J. H., Anella R., Chennamangalam J., 2013, Monthly Notices of the Royal Astronomical Society, 433, 138

Rygl K. L. J., et al., 2012, Astronomy and Astrophysics, 539, A79

Sanidas S., et al., 2019, Astronomy and Astrophysics, 626, A104

Sayer R. W., Nice D. J., Taylor J. H., 1997, Astrophysical Journal, 474, 426

Sengar R., et al., 2023, Monthly Notices of the Royal Astronomical Society, 522, 1071

Shannon R. M., et al., 2013, Science, 342, 334

Shapiro I. I., 1966, Physical Review, 141, 1219

Shibazaki N., Murakami T., Shaham J., Nomoto K., 1989, Nature, 342, 656

Shklovskii I. S., 1970, Soviet Astronomy, 13, 562

Singha J., Joshi B. C., Bandyopadhyay D., Grover H., Desai S., Arumugam P., Banik S., 2022, Journal of Astrophysics and Astronomy, 43, 81

Spruit H., Phinney E. S., 1998, Nature, 393, 139

Stairs I. H., 2003, Living Reviews in Relativity, 6, 5

Stairs I. H., et al., 1999a, arXiv e-prints, pp astro–ph/9903290

Stairs I. H., Thorsett S. E., Camilo F., 1999b, Astrophysical Journal Supplement, 123, 627

Stairs I. H., Thorsett S. E., Arzoumanian Z., 2004, Physical Review Letters, 93, 141101

Stokes G. H., Taylor J. H., Welsberg J. M., Dewey R. J., 1985, Nature, 317, 787

Stokes G. H., Segelstein D. J., Taylor J. H., Dewey R. J., 1986, Astrophysical Journal, 311, 694

Stovall K., et al., 2014, Astrophysical Journal, 791, 67

Stovall K., et al., 2015, Astrophysical Journal, 808, 156

Surnis M. P., Joshi B. C., McLaughlin M. A., Krishnakumar M. A., Manoharan P. K., Naidu A., 2019, Astrophysical Journal, 870, 8

Suryanarayanan A., Paerels F., Leutenegger M., 2022, arXiv e-prints, p. arXiv:2212.04165

Swiggum J. K., Gentile P. A., 2018, Astronomical Journal, 156, 190

Swiggum J. K., et al., 2014, Astrophysical Journal, 787, 137

Swiggum J. K., et al., 2015, Astrophysical Journal, 805, 156

Swiggum J. K., et al., 2017, Astrophysical Journal, 847, 25

Swiggum J. K., et al., 2023, Astrophysical Journal, 944, 154

Tauris T. M., 2011, in Schmidtobreick L., Schreiber M. R., Tappert C., eds, Astronomical Society of the Pacific Conference Series Vol. 447, Evolution of Compact Binaries. p. 285 (arXiv:1106.0897), doi:10.48550/arXiv.1106.0897

Tauris T. M., Savonije G. J., 1999, Astronomy and Astrophysics, 350, 928

Tauris T. M., et al., 2017, Astrophysical Journal, 846, 170

Taylor J. H., Weisberg J. M., 1982, Astrophysical Journal, 253, 908

Taylor J. H., Wolszczan A., Damour T., Weisberg J. M., 1992, Nature, 355, 132

Taylor J. H., Manchester R. N., Lyne A. G., 1993, Astrophysical Journal Supplement, 88, 529

Thompson C., Duncan R. C., 1993, Astrophysical Journal, 408, 194

Titus N., et al., 2019, Monthly Notices of the Royal Astronomical Society, 487, 4332

Toscano M., Bailes M., Manchester R. N., Sand hu J. S., 1998, Astrophysical Journal, 506, 863

Trushkin S. A., Nizhelskij N. A., Tsybulev P. G., Zhekanis G. V., 2017, in Balega Y. Y., Kudryavtsev D. O., Romanyuk I. I., Yakunin I. A., eds, Astronomical Society of the Pacific Conference Series Vol. 510, Stars: From Collapse to Collapse. p. 492 (arXiv:1612.00634), doi:10.48550/arXiv.1612.00634

Turner J. E., et al., 2021, Astrophysical Journal, 917, 10

Tyul'bashev S. A., Tyul'bashev V. S., Oreshko V. V., Logvinenko S. V., 2016, Astronomy Reports, 60, 220

Verbiest J. P. W., et al., 2009, Monthly Notices of the Royal Astronomical Society, 400, 951

Vergely J. L., Lallement R., Cox N. L. J., 2022, Astronomy and Astrophysics, 664, A174

Wahl H. M., et al., 2022, Astrophysical Journal, 926, 168

Wex N., 1997, Astronomy and Astrophysics, 317, 976

Wolszczan A., Frail D. A., 1992, Nature, 355, 145

Wu Z., et al., 2023, Monthly Notices of the Royal Astronomical Society, 520, 5536

Xue M., et al., 2017, PASA, 34, e070

Yao J. M., Manchester R. N., Wang N., 2017, Astrophysical Journal, 835, 29

Yin D.-s., Gao Y.-p., Zhao S.-h., 2017, Chinese Astronomy and Astrophysics, 41, 430

Young O., Lam M., 2023, arXiv e-prints, p. arXiv:2306.06046

Yu Q.-Y., et al., 2020, Research in Astronomy and Astrophysics, 20, 091

Zhou S., Gügercinoğlu E., Yuan J., Ge M., Yu C., 2022a, Universe, 8, 641

Zhou Z.-R., Wang J.-B., Wang N., Yuan J.-P., Kou F.-F., Dang S.-J., 2022b, Research in Astronomy and Astrophysics, 22, 095008

Zubieta E., et al., 2023, Monthly Notices of the Royal Astronomical Society, 521, 4504

van Haarlem M. P., et al., 2013, Astronomy and Astrophysics, 556, A2

van Straten W., Demorest P., Oslowski S., 2012, Astronomical Research and Technology, 9, 237

van der Walt, S. J. Kristensen, L. E. Jørgensen, J. K. Calcutt, H. Manigand, S. el Akel, M. Garrod, R. T. Qiu, K. 2021, A&A, 655, A86

van der Wateren E., et al., 2023, Astronomy and Astrophysics, 669, A160

APPENDIX A
Chapter 2 Measurements and Profiles

In Table A.1 we list the measured quantities of DM, pulse width, S/N, S_{350}, and α. We include the references to papers from which measurements of flux density at other frequencies were taken to determine α in the table footnotes. Pulse profiles are shown in Figures A.1–A.12.

Table A.1. Pulsar Detections in the GBNCC Survey.

PSR[a]	PSR B	DM (pc/cm^3)	MJD	θ (deg)	W_{50} (ms)	W_{10} (ms)	S/N	S_{350} (mJy)	α	Refs.
J0014+4746*	B0011+47	30.2(3)	55538	0.227	109	175	29.6(5)	5.0(8)	−1.0(7)	1,2
J0025−19[B]	···	21.3(3)	58079	0.002	39	95	51.3(15)	3.8(7)	···	···
J0026+6320	···	244.7(8)	55198	0.196	23	48	16.6(9)	4.7(5)	−1.12(9)	3,4
J0030+0451	···	4.335(5)	58229	0.086	0.7	1	41.2(13)	6.8(14)	−2.4(5)	5,6,7
J0033+57	···	75.65(8)	55325	0.389	8	18	29.4(15)	9.1(12)	···	···
J0033+61	···	37.6(2)	55249	0.303	16	25	12.(2)	1.7(4)	···	···
J0034−0534	···	13.76(19)	57380	0.253	0.7	0.8	103.7(18)	36.(7)	†	···
J0034−0721*	B0031−07	10.9(2)	57387	0.277	62	106	184.(8)	28.(5)	−2.4(4)	8,9,10,2,11,12
J0034+69	···	80.01(14)	55169	0.024	1	2	22.(6)	2.5(7)	···	···
J0038−25[B]	···	5.7(6)	56774	0.007	6	23	70.9(6)	5.0(10)	···	···
J0040+5716	B0037+56	92.5(2)	55325	0.207	13	26	76.0(10)	5.7(8)	−1.59(17)	1,2
J0048+3412*	B0045+33	40.0(3)	56025	0.244	17	36	19.0(17)	2.0(5)	−2.65(4)	13,1,2
J0051+0423	···	13.93(9)	58229	0.174	11	34	31.3(15)	2.1(4)	−2.3(14)	1,14,12
J0053+69	···	116.7(2)	55169	0.017	13	30	32.5(7)	2.5(3)	···	···
J0055+5117*	B0052+51	43.8(5)	55405	0.286	16	73	16.3(7)	1.2(2)	−0.7(4)	1,2
J0056+4756	B0053+47	17.93(12)	55538	0.236	12	31	21.5(16)	2.5(4)	−2.0(2)	1,2
J0058+6125	···	128.3(16)	55249	0.226	7	17	19.3(6)	2.0(2)	···	···
J0059+50	···	66.8(2)	55531	0.000	38	49	27.1(10)	1.8(3)	···	···
J0100+69[L]	···	63.5‡	55163	0.255	11	59	13.(7)	2.1(12)	···	···
J0102+6537*	B0059+65	65.8(4)	55188	0.237	16	66	24.1(12)	2.6(3)	−0.7(7)	1,2
J0103+54*	···	55.49(9)	55353	0.359	6	13	11.5(18)	1.8(3)	···	···
J0104+64[B]	···	44.6(3)	55188	0.008	45	82	6.0(15)	0.69(19)	···	···
J0108+6608	B0105+65	30.4(3)	55180	0.053	73	142	71.5(9)	11.6(13)	−1.65(7)	1,2
J0108+6905*	B0105+68	61.1(2)	55169	0.185	11	65	17.5(18)	1.3(2)	−1.3(3)	1,2
J0110−22[B]	···	20.8(3)	56593	0.012	42	64	22.0(12)	1.1(2)	···	···
J0112+66*	···	111.6(11)	55188	0.007	32	86	17.5(5)	1.10(14)	···	···
J0117+5914	B0114+58	49.4(2)	55253	0.301	3	7	40.8(13)	9.4(11)	−2.35(6)	1,2
J0121+14[L]	···	17.8‡	58347	0.291	21	44	10(10)	1.4(11)	···	···
J0125−23[B]	···	9.59(3)	56718	0.000	0.7	1	37.1(17)	5.5(11)	···	···
J0125+62	···	118.0(4)	55200	0.003	17	60	10.8(12)	0.99(15)	···	···
J0134−2937	···	21.8(3)	56898	0.177	5	12	63.9(12)	6.0(12)	−0.2(10)	15,11,12
J0136+63	···	285.8(18)	55197	0.007	24	57	11.9(14)	1.7(2)	···	···
J0139+5621	···	102.4(4)	55325	0.302	35	63	7.0(8)	0.90(16)	−1.9(3)	1,16
J0139+5814*	B0136+57	73.84(7)	55254	0.153	5	9	175.9(18)	14.5(19)	−1.4(2)	1,2
J0141+6009*	B0138+59	34.7(3)	55250	0.245	34	97	128.(2)	26.(3)	−1.22(19)	8,1,2
J0141+63	···	272.8(18)	55197	0.006	2	4	6.(3)	1.1(6)	···	···
J0147+5922	B0144+59	40.08(5)	55253	0.315	6	9	33.4(7)	6.7(8)	−1.18(14)	1,2
J0151−0635*	B0148−06	25.5(3)	57387	0.049	58	79	47.4(16)	4.3(8)	−1.1(9)	6,2,11,12
J0152−1637	B0149−16	12.0(2)	57880	0.151	18	30	208.5(11)	11.(2)	−1.68(7)	8,6,2,11,12
J0156+3949	B0153+39	58.4(4)	55657	0.313	99	159	16.(2)	3.2(7)	−0.8(6)	1,2
J0157+6212	B0154+61	30.1(6)	55200	0.159	40	74	35.2(19)	3.6(4)	−0.3(3)	1,2
J0201+7005	···	21.0(3)	55163	0.326	11	49	6.1(17)	1.1(3)	···	···
J0212+5222	···	38.27(9)	55353	0.180	13	20	14.(2)	1.3(2)	−1.2(13)	1,17,18
J0214+5222	···	22.05(9)	55353	0.248	1	3	11.5(7)	2.4(3)	−2.8(6)	1,17
J0215+6218	···	84.65(14)	55200	0.278	41	105	14.7(9)	6.9(8)	−0.(2)	17,19
J0218+4232	···	61.23(2)	55624	0.255	1	1	48.(2)	28.(4)	†	···
J0231+7026	B0226+70	46.5(3)	55163	0.241	35	47	32.(4)	3.6(7)	−1.75(6)	1,2
J0242+62*	···	3.91(15)	55197	0.087	18	39	78.4(16)	9.6(11)	···	···
J0243+6027*	···	141.0(3)	55250	0.075	35	82	16.3(15)	2.3(3)	···	···
J0301+35[A]	···	57.43(14)	55984	0.147	5	11	12.2(14)	0.63(14)	···	···
J0323+3944	B0320+39	26.3(7)	55654	0.129	45	81	211.9(5)	11.2(18)	−1.87(16)	8,13,1,2
J0324+5239	···	115.3(8)	55352	0.243	13	21	10.(2)	1.7(5)	−1.558(6)	20,18
J0325+67*	···	64.9(3)	55171	0.007	14	26	25.3(11)	1.30(19)	···	···

Table A.1 (cont'd)

PSR[a]	PSR B	DM (pc/cm^3)	MJD	θ (deg)	W_{50} (ms)	W_{10} (ms)	S/N	S_{350} (mJy)	α	Refs.
J0332+5434*	B0329+54	26.76(18)	55348	0.451	7	19	610(10)	510(60)	−0.7(14)	8,2
J0335+4555	B0331+45	47.26(6)	55559	0.177	6	10	8.(7)	0.8(6)	−1.0(2)	1,2
J0335+6623	···	66.6(4)	55179	0.000	30	52	23.5(7)	1.4(2)	···	···
J0341+5711	···	101.0(4)	55279	0.150	43	75	26.(5)	2.6(6)	···	···
J0343+06[A]	···	46.0(2)	58228	0.266	32	65	9.4(14)	1.0(2)	···	···
J0343−3000	···	20.2(6)	56844	0.106	38	98	7.9(8)	0.38(13)	···	···
J0343+5312*	B0339+53	67.5(4)	55348	0.238	43	72	54.6(8)	6.6(8)	−2.0(10)	2
J0348+0432	···	40.46(15)	58233	0.311	2	5	8.(2)	1.8(6)	−1.0(2)	1,21
J0355+28[B]	···	48.68(9)	56277	0.001	8	17	14.5(10)	0.81(16)	···	···
J0357+5236	B0353+52	103.7(5)	55504	0.104	13	27	49.1(3)	9.8(11)	−1.32(19)	2
J0358+42*	···	46.27(5)	55629	0.002	10	15	23.9(14)	2.2(3)	···	···
J0358+5413*	B0355+54	57.12(4)	55343	0.208	3	9	110.7(5)	15.2(19)	−0.7(7)	8,1,2
J0358+66	···	62.27(2)	55179	0.001	2	4	10.(2)	0.8(2)	···	···
J0405+3347[B]	···	53.3(16)	56156	0.005	2	5	7.1(4)	0.42(7)	···	···
J0406+30[B]	···	49.37(2)	56277	0.008	0.2	0.6	26.1(2)	3.7(6)	···	···
J0406+6138*	B0402+61	65.32(15)	55237	0.092	19	32	157.5(7)	14.2(18)	−1.30(4)	1,2
J0408+552	···	63.76(19)	55343	0.418	47	88	23.(4)	15.(3)	···	···
J0410−31*	···	8.9(4)	56902	0.470	25	49	44.(3)	7.8(19)	···	···
J0413+58	···	57.0(17)	55263	0.435	21	55	8.(4)	4.(2)	···	···
J0414+31[B]	···	64.1(2)	56184	0.000	19	49	12.(3)	0.7(2)	···	···
J0415+6954	B0410+69	27.44(19)	55163	0.052	4	11	112.0(5)	6.0(9)	−1.7(5)	1,2
J0417+35	···	48.63(16)	55683	0.252	8	17	19.1(13)	1.6(2)	···	···
J0417+61	···	70.14(11)	55249	0.033	19	38	6.8(11)	0.82(17)	···	···
J0421−0345	···	44.3(5)	57154	0.191	27	47	53.6(7)	2.7(7)	−1.8(12)	15,22
J0426+4933	···	84.2(2)	55538	0.241	13	27	12.1(14)	1.4(2)	−1.4785(14)	1,18
J0448−2749*	···	26.22(11)	56809	0.251	6	18	14.6(13)	1.0(2)	0.2(19)	23,24,12
J0450−1248	B0447−12	37.0(11)	57122	0.262	18	30	107.7(7)	10.(2)	−1.64(19)	2,11,12
J0452−1759*	B0450−18	39.9(14)	58058	0.036	29	39	550(10)	43.(9)	−0.8(15)	2,11,12
J0454+5543*	B0450+55	14.59(8)	55343	0.154	10	30	190.(3)	24.(3)	−0.8(2)	8,1,2
J0458−0505*	···	47.8(4)	57379	0.162	17	39	26.(3)	1.2(3)	···	···
J0459−0210	···	21.0(2)	57662	0.271	15	75	29.1(10)	3.4(6)	−2.0(9)	1,15,12
J0502+4654	B0458+46	42.38(16)	55552	0.078	24	59	52.3(13)	8.5(10)	−1.2(2)	20,2
J0510+38	···	69.11(19)	55658	0.003	4	11	15.9(14)	2.5(3)	···	···
J0519+54	···	42.55(8)	55343	0.004	9	20	14.2(5)	1.22(17)	···	···
J0520−2553	···	33.77(6)	56776	0.144	2	13	55.9(5)	2.8(6)	−1.(4)	23,24,12
J0530−39[B]	···	48.5(2)	56998	0.012	33	42	22.9(8)	1.1(2)	···	···
J0533+0402*	···	83.9(2)	58251	0.319	16	32	42.3(4)	4.6(7)	−1.0(2)	1,14,11,12
J0534−13[B]	···	74.3(2)	57149	0.071	13	38	20.2(17)	1.0(2)	···	···
J0540+3207*	···	62.08(13)	56478	0.140	9	16	104.2(5)	6.7(10)	−1.98(5)	1,25
J0555+3948	···	36.1(2)	55650	0.323	26	52	15.3(15)	2.3(4)	···	···
J0557−2948	···	49.05(17)	56835	0.012	0.7	2	18.1(17)	0.9(2)	···	···
J0601−0527*	B0559−05	80.58(12)	57380	0.133	12	26	139.9(4)	12.(2)	−1.7(2)	2,26,11,12
J0608+00	···	48.4(2)	57755	0.079	17	30	20.(2)	1.1(2)	···	···
J0610−2100	···	60.7(3)	56592	0.100	0.6	0.8	17.3(7)	2.1(4)	···	···
J0610+37	···	39.09(11)	55682	0.451	12	25	19.6(6)	7.8(14)	···	···
J0611+1436	···	43.99(6)	58355	0.225	16	33	9.(3)	2.0(8)	···	···
J0612+3721	B0609+37	27.12(7)	55682	0.313	7	18	82.9(10)	12.(2)	0.0(7)	1,2
J0613−0200	···	38.77(3)	57791	0.289	0.3	0.7	29.(2)	8.8(17)	−1.60(16)	5,27,28,29
J0613+3731	···	18.78(15)	55682	0.213	10	27	15.(2)	1.6(3)	−2.7(6)	1,16
J0614−3329	···	37.04(3)	56957	0.192	0.4	0.6	18.6(10)	2.6(6)	···	···
J0614+83*	···	44.2(2)	55148	0.004	11	81	14.3(9)	1.0(2)	···	···
J0621+0336	···	72.53(6)	58355	0.190	4	7	49.8(6)	3.3(5)	−1.5(9)	1,30
J0624−0424*	B0621−04	70.9(2)	57154	0.162	24	78	51.9(10)	6.4(10)	−1.00(6)	1,2,26,12

Table A.1 (cont'd)

PSR[a]	PSR B	DM (pc/cm^3)	MJD	θ (deg)	W_{50} (ms)	W_{10} (ms)	S/N	S_{350} (mJy)	α	Refs.
J0627+0649	···	86.6(8)	58202	0.234	9	18	27.5(15)	3.4(5)	···	···
J0627+0706*	···	138.2‡	58202	0.186	7	31	60.1(11)	7.4(10)	−1.44(13)	1,31,32,26,11
J0630−0046	···	97.89(17)	57540	0.069	11	36	11.0(14)	1.6(5)	···	···
J0630−2834	B0628−28	34.4(3)	56777	0.058	72	143	349.(4)	39.(8)	−1.4(4)	8,9,10,2,26,11,12
J0636−23[B]	···	59.12(12)	56666	0.000	14	27	11.(2)	0.65(19)	···	···
J0636+5129	···	11.11(2)	55442	0.147	0.2	0.3	12.1(3)	1.5(2)	−1.1(2)	33,17
J0645+5158	···	18.24(9)	55366	0.135	0.3	0.6	36.8(6)	2.9(5)	−2.2(6)	1,17,34
J0645+80	···	49.71(16)	55146	0.011	32	52	30.5(10)	2.1(4)	0.(2)	1,17
J0648−27[B]	···	132.5(10)	56777	0.005	54	115	18.5(7)	0.75(15)	···	···
J0652−0142*	···	117.3(2)	57763	0.129	9	24	15.5(8)	1.3(2)	···	···
J0653+8051*	B0643+80	33.1(3)	55146	0.131	18	40	92.3(10)	4.5(8)	−1.2(4)	1,2
J0656−2228*	···	31.8(3)	56655	0.174	27	52	11.4(13)	0.85(17)	0.(2)	26
J0659+1414*	B0656+14	14.1(9)	58356	0.227	14	34	33.5(9)	3.9(7)	−0.52(5)	1,2,26,11
J0659−36[B]	···	83.37(16)	56987	0.013	13	35	7.1(10)	0.42(18)	···	···
J0700+6418	B0655+64	8.76(5)	55226	0.201	5	9	149.9(4)	12.(2)	−2.8(2)	8,1,2
J0709+05[A]	···	44.23(13)	58201	0.084	3	4	7.(2)	0.8(3)	···	···
J0719−2545*	···	254.4(2)	56771	0.157	83	163	26.7(4)	4.1(6)	···	···
J0721−2038	···	76.01(6)	58107	0.153	0.4	3	9.8(11)	2.1(4)	−1.7(2)	26
J0725−1635	···	99.02(19)	57854	0.115	7	14	16.7(8)	1.2(2)	−1.(5)	15,35
J0726−2612	···	69.4‡	56771	0.290	56	103	10.9(7)	1.2(2)	···	···
J0729−1448*	···	91.89(6)	57854	0.192	8	15	29.(2)	3.5(6)	−1.4(4)	26
J0729−1836*	B0727−18	61.34(13)	56993	0.080	6	30	98.9(10)	8.6(13)	−1.2(2)	2,26,11
J0733−2345	···	190.2(4)	56722	0.203	20	69	8.6(16)	0.79(19)	···	···
J0737−2202	···	95.59(8)	56663	0.160	11	28	19.7(12)	2.3(3)	···	···
AJ0737−3039A	···	48.9(9)	56902	0.307	1	4	68.7(7)	26.(4)	−1.59(17)	33,11,36,37
J0737+69*	···	15.5(17)	55173	0.008	60	154	67.(4)	2.2(4)	···	···
J0740+41	···	20.82(3)	55630	0.046	0.6	1	11.1(10)	2.0(4)	···	···
J0740+6620	···	14.95(2)	55189	0.133	0.2	0.9	42.3(7)	7.8(14)	···	···
J0742−2822	B0740−28	73.78(4)	56778	0.214	5	9	910(20)	130(20)	−1.1(5)	10,2,26,11
J0746+66*	···	27.7(15)	55189	0.010	5	20	10.(3)	0.7(2)	···	···
J0750+57*	···	26.7(3)	55290	0.007	13	104	18.9(3)	1.5(2)	−0.7(14)	1,17
J0754+3231*	B0751+32	39.8(3)	56278	0.218	13	104	41.0(5)	3.6(7)	−1.74(16)	13,1,2
J0758−1528	B0756−15	63.25(17)	57150	0.056	8	15	93.8(12)	3.8(7)	−1.1(8)	2,26,11
J0758−30[B]	···	86.4(2)	56784	0.000	27	49	27.2(12)	1.6(2)	···	···
J0804−3647*	···	187.6(5)	56969	0.239	37	76	26.4(5)	3.3(6)	···	···
J0808−3937	···	169.1(2)	56991	0.270	13	30	10.(2)	1.1(3)	···	···
J0812−3905	···	329.6(12)	56973	0.267	6	62	13.2(13)	3.0(5)	−1.4(14)	26
J0814+7429	B0809+74	5.8(3)	55171	0.118	47	93	143.6(13)	9.1(18)	−1.4(17)	8,20,2
J0815+4611[L]	···	11.09(11)	55508	0.227	13	20	35.(6)	2.5(7)	···	···
J0818−3049	···	118.9(2)	56779	0.229	46	63	22.(2)	2.8(5)	−1.5(4)	26
J0818−3232*	···	132.5(5)	56813	0.328	42	60	17.4(11)	2.0(3)	−1.1(18)	26
J0820−1350	B0818−13	41.0(3)	57096	0.128	22	38	610(20)	42.(9)	−1.4(2)	8,10,2,26,11
J0820−3826	···	195.5(3)	56971	0.110	8	16	14.(3)	2.2(6)	−1.7(4)	26
J0820−3921*	···	179.9(2)	56973	0.074	46	107	39.0(9)	8.1(11)	···	···
J0823+0159	B0820+02	23.9(2)	57688	0.179	22	37	170.0(17)	8.(2)	−1.3(3)	1,10,2,26
J0826+2637	B0823+26	19.53(13)	56529	0.067	7	16	376.(7)	31.(7)	−1.5(3)	8,13,1,2
J0828−3417*	B0826−34	51.5(4)	56902	0.362	112	913	138.2(14)	130(20)	···	···
J0835−3707	···	112.4(13)	56968	0.109	6	16	40(20)	3.2(17)	···	···
J0837+0610	B0834+06	12.8(3)	58079	0.191	23	36	400(10)	27.(6)	−2.7(2)	8,10,2,26
J0838−2621	···	116.9‡	56747	0.176	7	45	16.(2)	2.4(5)	···	···
J0846−3533*	B0844−35	94.2(2)	56936	0.164	16	95	75.2(8)	9.8(15)	−1.3(6)	38,26,11
J0849+8028	B0841+80	34.9(4)	55152	0.057	26	93	39.6(19)	2.0(4)	−1.12(5)	1,39
J0855−3331*	B0853−33	86.4(3)	56899	0.315	24	40	101.3(8)	12.0(19)	−2.14(9)	10,2,26,11

Table A.1 (cont'd)

PSR[a]	PSR B	DM (pc/cm^3)	MJD	θ (deg)	W_{50} (ms)	W_{10} (ms)	S/N	S_{350} (mJy)	α	Refs.
J0908−1739*	B0906−17	15.79(13)	57148	0.247	9	23	87.(3)	7.2(16)	−1.5(4)	8,2,26
J0912−3851	···	71.5(3)	56972	0.255	36	72	11.2(19)	1.6(4)	···	···
J0921+6254*	B0917+63	13.0(4)	55202	0.163	19	48	61.4(16)	3.4(6)	−1.04(15)	1,2
J0922+0638	B0919+06	27.29(11)	58002	0.220	11	24	248.8(11)	16.(4)	−1.6(6)	10,2,26,11
J0928+06	···	49.7(5)	58057	0.190	23	50	21.(4)	0.9(3)	···	···
J0930−2301*	···	78.4(4)	56663	0.085	12	60	27.9(9)	1.2(2)	···	···
J0931−1902	···	41.5(4)	56993	0.321	0.4	1	4.8(7)	1.6(4)	···	···
J0932−3217	···	102.1(4)	56785	0.197	22	54	31.3(12)	2.1(3)	···	···
J0943+41*	···	21.7(5)	55635	0.067	17	88	30.6(13)	1.2(2)	···	···
J0944−1354	B0942−13	12.43(14)	57095	0.351	7	13	85.1(5)	7.2(16)	−2.(5)	2,11
J0947+2740*	···	28.9(2)	56180	0.295	32	48	46.(2)	3.9(9)	−1.77(14)	1,31,40
J0952−3839*	B0950−38	163.5(3)	56973	0.165	36	85	70.8(13)	5.8(10)	−0.(4)	38,26
J1012−2337*	B1010−23	22.6(6)	56666	0.179	45	79	214.3(14)	10.(2)	−3.(2)	2
J1012+5307	···	9.022(5)	55351	0.242	0.7	1	39.(2)	8.(2)	−0.9(4)	5,1,41,27,34,42
J1018−1523[B]	···	17.17(2)	57098	0.004	2	5	8.(2)	0.49(16)	···	···
J1018−1642	B1016−16	48.8(4)	57127	0.277	28	57	96.0(3)	6.0(12)	−1.61(16)	2,26
J1024−0719	···	6.48(5)	57444	0.236	0.6	1	22.5(19)	5.7(13)	−1.7(2)	5,33,43,29,28,26
J1034−3224*	···	50.6(2)	56785	0.036	17	176	141.2(15)	14.(2)	−1.1(15)	15,26,11
J1038+0032	···	26.34(11)	57754	0.123	2	5	18.(3)	2.4(7)	−1.963(7)	33,36
J1041−1942*	B1039−19	33.9(3)	56998	0.116	41	80	126.7(7)	8.4(17)	−0.(4)	2,26
J1045−0436[B]	···	4.833(9)	57156	0.001	1	4	29.(2)	2.9(6)	···	···
J1046+0304	···	24.98(8)	57997	0.090	3	13	5.5(7)	0.25(6)	···	···
J1047−3032	···	52.28(8)	56777	0.116	13	26	80.5(4)	5.7(11)	−1.(3)	23,24,12
J1101+65*	···	19.2(9)	55227	0.007	37	69	23.3(13)	0.62(13)	···	···
J1110+58*	···	26.2(2)	55285	0.047	17	39	13.3(6)	0.66(13)	−0.(2)	1,17
J1115+5030*	B1112+50	9.1(4)	55367	0.260	22	44	141.5(5)	7.2(16)	−1.37(17)	8,1,2
J1116−2444	···	29.6(2)	56719	0.275	8	29	44.(2)	2.7(6)	···	···
J1120−24[B]	···	9.81(12)	56663	0.094	6	13	13.7(11)	0.45(11)	···	···
J1122−3546[B]	···	39.49(8)	56907	0.006	1.0	1	12.5(3)	1.7(3)	···	···
J1125+7819	···	11.22(4)	55168	0.203	0.4	1.0	52.2(4)	8.1(16)	···	···
J1126−27*	···	27.09(9)	56772	0.008	8	19	5.4(19)	0.29(12)	···	···
J1126−38	···	46.0(2)	56990	0.375	31	57	45.7(4)	10.(2)	···	···
J1134+24[G]	···	24.19(12)	56457	0.462	13	24	7.(3)	1.8(8)	···	···
J1141−3107*	···	30.82(13)	56780	0.311	18	29	44.9(16)	4.5(9)	−1.(5)	15,12
J1141−3322*	···	46.38(7)	56844	0.086	4	9	60.0(14)	2.6(5)	−1.(6)	23,24,26
J1154−19[B]	···	10.69(4)	56999	0.011	0.5	1	15.3(8)	1.4(3)	···	···
J1221−0633[B]	···	16.43(19)	57379	0.008	0.2	0.3	9.3(4)	0.98(19)	···	···
J1231−1411	···	8.072(3)	57096	0.243	0.4	0.8	9.1(3)	1.7(3)	−2.3(3)	33,44
J1234−3630*	···	59.29(14)	56929	0.219	9	16	45.9(8)	2.9(5)	···	···
J1235−02[L]	···	18.7(9)	57545	0.191	96	135	51.4(10)	3.6(6)	···	···
J1239+2453*	B1237+25	9.4(3)	56458	0.438	36	67	384.9(13)	80(20)	−0.87(4)	8,13,1,2,12
J1239+32[B]	···	16.85(4)	56054	0.021	0.4	1	20(20)	2.(2)	···	···
J1257−1027*	B1254−10	29.7(15)	57062	0.245	6	27	73.5(6)	7.7(14)	−1.6(4)	2
J1300+1240	B1257+12	10.15(6)	58356	0.058	0.8	1	32.3(18)	5.1(10)	−1.8(17)	5,1,45,46
J1308−23[B]	···	22.357(11)	56718	0.006	0.2	0.4	32.6(12)	3.3(6)	···	···
J1311−1228	B1309−12	36.21(11)	57091	0.287	6	13	117.3(7)	10.2(19)	−2.2(13)	2
J1317−0157[B]	···	29.39(3)	57542	0.007	0.3	0.5	14.(2)	1.7(4)	···	···
J1320−3512	···	15.52(11)	56962	0.044	24	60	13.0(4)	1.7(2)	···	···
J1320+67*	···	28.0(2)	55200	0.093	11	58	15.1(7)	0.89(17)	···	···
J1321+8323	B1322+83	13.37(17)	55166	0.252	21	40	86.0(6)	7.6(15)	−1.49(11)	1,2
J1327−0755	···	27.9(2)	57637	0.251	0.1	0.3	19.2(19)	2.3(5)	···	···
J1327+34[B]	···	4.193(16)	56052	0.007	1	2	68.3(9)	3.7(7)	···	···
J1332−3032*	···	14.81(16)	56845	0.146	29	109	69.4(8)	14.(2)	−2.7(9)	23,24

Table A.1 (cont'd)

PSR[a]	PSR B	DM (pc/cm^3)	MJD	θ (deg)	W_{50} (ms)	W_{10} (ms)	S/N	S_{350} (mJy)	α	Refs.
J1335−3642*	···	41.82(13)	56972	0.204	10	38	35.(2)	5.3(8)	···	···
J1336−2522*	···	37.39(12)	56751	0.093	13	26	42.6(12)	2.8(5)	···	···
J1358−2533	···	16.0(2)	56752	0.228	13	51	10.(6)	0.6(4)	···	···
J1400−1431	···	4.932(3)	57855	0.216	0.2	0.5	32.2(8)	5.0(9)	−1.(2)	47
J1411+2551	···	12.34(16)	56459	0.100	2	4	17.3(13)	1.1(2)	···	···
J1418−3921	···	60.2(2)	57063	0.214	22	58	103.0(4)	13.5(18)	−2.(5)	15,12
J1434+7257	···	12.61(16)	55196	0.371	1	3	11.(2)	2.1(6)	−2.5(2)	1,17
J1439+76*	···	22.3(2)	55196	0.024	6	31	9.7(11)	0.41(9)	···	···
J1455−3330	···	13.56(8)	56962	0.058	0.6	2	40.9(6)	8.7(12)	−1.5(6)	29
J1501−0046	···	22.3(11)	57509	0.244	11	16	23.9(15)	2.2(4)	···	···
J1505−25[B]	···	44.6(2)	56754	0.001	11	26	22.3(10)	1.12(18)	···	···
J1509+5531	B1508+55	19.61(19)	55349	0.181	11	27	630(20)	50(10)	−2.0(2)	8,20,2
J1515−32[B]	···	25.3(16)	56936	0.493	2	3	65.(2)	37.(5)	···	···
J1518−0627	···	27.7(2)	57998	0.205	8	41	11.(5)	1.1(6)	···	···
J1518−3950[ML]	···	102.4(12)	57538	0.265	8	42	17.3(9)	4.9(6)	···	···
J1518+4904	···	11.61(16)	55415	0.223	1	3	82.3(15)	7.7(15)	−1.09(13)	5,1,14,27,46,42
J1524−33	···	73.3(3)	56958	0.260	16	97	8.8(18)	2.0(5)	···	···
J1527−3931*	B1524−39	48.7(6)	57384	0.061	39	65	144.1(15)	12.4(15)	−1.8(2)	38,11
J1528−3146	···	18.19(15)	56936	0.125	1	5	17.(2)	2.7(5)	···	···
J1529−26[B]	···	44.5(2)	56755	0.499	20	30	20.4(7)	9.4(14)	···	···
J1529−3828	···	73.62[‡]	57129	0.101	0.8	1	6.(4)	1.3(9)	···	···
J1530−21[B]	···	38.05(13)	56588	0.000	12	28	11.8(8)	0.92(15)	···	···
J1532+2745*	B1530+27	14.6(2)	56457	0.208	18	46	108.1(4)	7.5(13)	−1.67(14)	13,1,2
J1536−30[B]	···	63.6(4)	56908	0.005	13	66	16.1(18)	1.7(3)	···	···
J1536−3602*	···	86.8(2)	57095	0.148	51	112	32.1(10)	5.2(6)	···	···
J1543−0620	B1540−06	18.3(18)	58082	0.253	9	20	150.6(14)	10.2(17)	−1.3(12)	8,2
J1544+4937	···	23.22(2)	55413	0.271	0.2	0.4	31.(2)	6.1(13)	−0.7651(12)	33,48
J1547−0944*	···	36.9(4)	58252	0.145	30	42	28.1(15)	1.7(3)	···	···
J1555−0515*	···	23.2(2)	58051	0.051	10	19	37.5(11)	1.4(2)	···	···
J1555−2341	B1552−23	51.95(13)	56718	0.189	13	31	67.8(7)	7.8(11)	−1.6(4)	2
J1555−3134*	B1552−31	73.11(13)	56936	0.379	13	32	53.9(15)	17.(2)	−1.0(3)	2,12
J1600−3053	···	52.312(3)	56933	0.338	0.3	1	7.(2)	6.3(19)	−0.8(3)	28
J1603−2531*	···	53.7(7)	56755	0.266	6	17	20.(3)	3.5(7)	···	···
J1603−2712*	B1600−27	46.2(2)	56779	0.136	20	35	161.8(12)	15.(2)	−1.5(14)	2
J1607−0032*	B1604−00	10.72(18)	57508	0.279	14	20	168.(2)	22.(3)	−2.2(3)	8,1,10,2,12
J1611−29[B]	···	83.033(3)	56907	0.006	0.5	1	22.(4)	3.5(8)	···	···
J1612−2408*	···	49.2(2)	56750	0.180	23	33	95.4(8)	8.8(11)	···	···
J1614−2230	···	34.49(3)	56663	0.215	0.3	0.6	19.5(18)	5.6(8)	···	···
J1614−23	···	52.4(13)	56747	0.148	1	2	13.5(12)	1.9(3)	···	···
J1614−3937	···	151.7(15)	58175	0.216	16	29	41.5(7)	10.9(10)	−2.0(7)	15,12
J1615−2940*	B1612−29	44.6(6)	56907	0.169	23	57	66.9(19)	5.5(7)	−1.(9)	2
J1622−3751	···	155.7(18)	57152	0.022	16	61	7.(2)	1.6(4)	···	···
J1623−0908	B1620−09	68.1(3)	58257	0.203	14	27	84.1(13)	6.5(10)	−1.6(3)	2
J1623−2631	B1620−26	62.85(4)	56776	0.218	1	2	29.(2)	9.3(12)	−2.1(2)	5,2,29,46,42
J1627+86	···	46.55(12)	55149	0.008	6	11	14.5(15)	0.62(13)	···	···
J1629+33[B]	···	35.0(3)	56089	0.002	42	59	17.0(3)	0.85(15)	···	···
J1629−3827[ML]	···	127.9(13)	57384	0.256	9	23	10.7(5)	2.3(2)	···	···
J1629+43	···	7.36(4)	55553	0.058	4	15	25.9(15)	1.9(3)	···	···
J1630+37	···	14.125(3)	56045	0.645	0.3	1	36.(2)	450(100)	···	···
J1632−1013	···	89.97(18)	58349	0.243	14	34	11.2(5)	1.6(2)	···	···
J1636−2614	···	92.72(13)	56776	0.299	6	13	23.5(13)	3.2(4)	···	···
J1638−35[B]	···	115.1(18)	57123	0.005	10	31	15.8(13)	2.6(4)	···	···
J1638−3815	···	240.2(18)	57155	0.113	10	44	6.8(12)	1.3(2)	···	···

Table A.1 (cont'd)

PSR[a]	PSR B	DM (pc/cm^3)	MJD	θ (deg)	W_{50} (ms)	W_{10} (ms)	S/N	S_{350} (mJy)	α	Refs.
J1641−2347*	···	28.1(2)	56752	0.088	46	68	19.8(14)	2.4(3)	···	···
J1643−10^{G}	···	75.850(16)	58349	0.186	3	8	9.(2)	2.3(8)	···	···
J1644−33^{B}	···	130.3(12)	56989	0.010	20	57	14.0(4)	3.6(3)	···	···
J1645−0317	B1642−03	35.71(11)	58054	0.131	4	8	1000(40)	110(20)	−2.0(11)	8,1,10,2,11,12
J1646−2142	···	29.735(6)	56588	0.231	0.8	1	7.(2)	3.9(11)	···	···
J1647−3607	···	228.5(5)	57123	0.338	2	9	4.(3)	1.6(13)	···	···
J1647+66*	···	22.7(4)	55202	0.006	23	54	55.(2)	2.8(4)	···	···
J1648−3256	···	128.5(18)	56989	0.259	11	20	27.8(7)	4.6(5)	−1.(5)	15,12
J1649+2533*	···	34.3(2)	56480	0.038	27	45	43.(2)	2.7(4)	−0.(2)	1,49
J1649+80	···	31.09(2)	55166	0.009	0.2	0.3	15.9(11)	1.6(3)	···	···
J1652−2404*	B1649−23	68.41‡	56754	0.277	39	58	83.1(8)	14.9(16)	−1.5(3)	2,12
J1652+2651*	···	40.8(2)	56459	0.126	27	48	176.(3)	12.(2)	0.5(6)	1,49,14
J1654−2636^{ML}	···	103.3(2)	56783	0.233	25	150	14.(2)	4.2(8)	···	···
J1654−2713	···	93.3(2)	56783	0.271	23	46	14.5(17)	3.3(5)	···	···
J1655−3048*	···	154.1(14)	56932	0.212	19	109	22.8(18)	10.6(13)	···	···
J1700−3312*	···	167.2(3)	56989	0.139	49	75	22.(2)	5.3(7)	−1.5(19)	15,26,11,12
J1700−3611*	···	233.9(3)	57129	0.159	34	56	14.(2)	3.2(6)	···	···
J1701−3130	···	131.4(7)	56933	0.142	20	28	10.(2)	3.1(8)	···	···
J1703−3241	B1700−32	110.3(3)	56962	0.258	50	64	169.7(14)	54.(4)	−1.(2)	2,26,11,12
J1705−3423	···	146.4(6)	57123	0.110	25	57	25.(6)	14.(3)	−1.3(2)	15,26,11,12
J1706+59	···	30.7(3)	55284	0.475	20	56	96.(2)	27.(4)	−0.(3)	1,17
J1708−3426*	···	188.7(17)	57127	0.200	88	129	16.(6)	12.(5)	−2.3(3)	15,26,11,12
J1710−2616*	···	110.0(2)	56776	0.126	46	95	20.(3)	5.1(9)	···	···
J1710+49	···	7.083(3)	55416	0.000	0.3	0.7	9.6(16)	1.2(3)	···	···
J1712−2715	···	91.78(6)	56783	0.086	38	63	21.6(4)	9.6(8)	···	···
J1720−0212*	B1718−02	66.92(12)	57655	0.216	66	84	93.4(16)	27.(3)	−1.3(6)	1,2
J1720−2446*	···	104.3(2)	56755	0.221	31	55	13.(3)	3.7(10)	···	···
J1720−2933	B1717−29	42.77(16)	56908	0.322	31	42	73.(2)	47.(4)	−2.24(3)	2,11,12
J1721−2457	···	48.23(3)	56755	0.190	0.6	0.9	8.(5)	4.(3)	···	···
J1722+35	···	22.1(2)	56072	0.133	20	51	8.1(16)	0.9(2)	···	···
J1722−3207	B1718−32	126.0(12)	56958	0.208	19	39	80.0(9)	49.(3)	−1.7(2)	2,26,11,12
J1722−3712	B1719−37	99.56(6)	57170	0.156	6	15	51.(5)	40.(4)	−1.66(17)	38,11,26
J1725−0732*	···	58.72(6)	58255	0.183	10	21	14.(4)	2.8(8)	···	···
J1727−2739*	···	146.0(3)	56783	0.376	35	49	8.7(10)	5.7(8)	−0.9(5)	26,12
J1728−0007	B1726−00	41.09‡	57999	0.416	11	28	21.(6)	9.(3)	−1.64(17)	1,2
J1729−2117	···	34.22(17)	56588	0.214	1	2	11.(2)	2.2(6)	···	···
J1730−2304	···	9.624(8)	56750	0.176	0.6	1	49.2(13)	23.(2)	−1.72(7)	5,33,50,29,26
J1733−01^{B}	···	61.98(7)	57535	0.004	9	16	8.(3)	0.9(3)	···	···
J1733−2228*	B1730−22	41.1(2)	56750	0.124	14	79	77.1(6)	25.(2)	−1.31(12)	2,12
J1734−0212	B1732−02	64.8(2)	57542	0.134	27	40	21.(2)	2.6(4)	···	···
J1734−2415	···	117.1(11)	56755	0.157	16	48	4.8(12)	1.4(3)	···	···
J1735−0243*	···	54.8(2)	57656	0.193	12	106	12.4(18)	3.3(6)	···	···
J1735−0724*	B1732−07	73.42(18)	58255	0.244	5	15	100.4(14)	18.(2)	−1.1(16)	2,12
J1736−2457*	···	169.4(6)	56755	0.217	109	170	12.(2)	4.7(12)	···	···
J1738−2330	···	96.6(13)	56750	0.401	39	61	4.(4)	6.(5)	···	···
J1738−3211*	B1735−32	50.09(19)	56962	0.106	26	44	11.(8)	20(10)	−0.7(3)	2,26,12
J1739−2903	B1736−29	138.4(8)	56902	0.130	17	40	7.(5)	12.(8)	−0.8(16)	2,11,26
J1740+27^{L}	···	35.6(2)	56297	0.115	18	36	29.(6)	1.7(4)	···	···
J1740−3015	B1737−30	152.1(15)	56909	0.291	20	74	7.5(6)	30.(3)	−1.00(3)	2,26
J1741−0840	B1738−08	74.7(5)	58348	0.299	78	116	70(20)	24.(6)	−2.(2)	2
J1741−21^{B}	···	150.7(6)	56591	0.010	81	181	9.(4)	2.1(10)	···	···
J1741−2733*	···	147.4(2)	56783	0.084	60	90	27.(2)	16.6(18)	−1.595(14)	26,12
J1741+2758*	···	28.9(3)	56297	0.180	30	48	41.(3)	2.7(5)	−1.77(14)	13,1,49

Table A.1 (cont'd)

PSR[a]	PSR B	DM (pc/cm^3)	MJD	θ (deg)	W_{50} (ms)	W_{10} (ms)	S/N	S_{350} (mJy)	α	Refs.
J1741−3927	B1737−39	158.2(13)	57538	0.265	18	47	59.1(11)	27.(2)	−1.3(4)	38,51,26,11,12
J1742−0203[B]	···	81.89(3)	57542	0.003	4	10	9.(3)	1.7(6)	···	···
J1742−3957	···	220.(7)	57538	0.301	60	125	7.8(7)	4.8(6)	···	···
J1743−0339*	B1740−03	30.11(11)	58054	0.357	11	20	18.(3)	5.8(13)	−1.53(16)	2
J1743−3150	B1740−31	192.2(6)	56962	0.310	113	303	14.(2)	45.(8)	−1.(2)	2,26,11,12
J1744−2335*	···	96.4(4)	56746	0.258	25	51	30(20)	11.(8)	−3.5(2)	23,24
J1745−0129*	···	89.3(2)	57535	0.124	15	50	10.(5)	1.8(9)	···	···
J1745−3040*	B1742−30	88.01(9)	56930	0.299	7	25	61.4(15)	150(10)	−1.2(2)	2,11,26
J1745−3812	···	163.6(18)	57213	0.146	21	62	0(20)	1.(5)	···	···
J1746+2245*	···	49.2(8)	56481	0.321	28	129	11.7(18)	1.5(3)	−1.304(3)	20,52
J1746+2540*	···	51.3(2)	56459	0.196	27	47	15.(2)	1.2(2)	−2.06(11)	1,49
J1750−3503	···	190.5(17)	57151	0.167	87	159	25.2(9)	17.0(15)	−2.(3)	15,35
J1752+2359*	···	36.01(15)	56480	0.404	6	15	13.(2)	2.6(7)	−0.81(19)	1,49
J1752−2806	B1749−28	50.37(14)	56900	0.245	7	13	1050(50)	930(80)	−1.85(5)	8,9,10,2,26,11,12
J1753−38*	···	167.6(17)	57384	0.093	8	21	50(30)	7.(4)	···	···
J1754−3443	···	188.7(9)	57151	0.276	28	52	16.1(17)	10.1(13)	···	···
J1754−3510	···	81.23(11)	57151	0.239	9	26	10.(2)	3.8(10)	···	···
J1754+5201	B1753+52	35.5(6)	55384	0.259	19	149	22.(2)	2.4(4)	−0.0(4)	1,2
J1755−0903	···	63.67(4)	58349	0.165	6	20	17.7(15)	6.4(7)	···	···
J1755−2725	···	115.1(6)	56810	0.205	9	27	6.0(16)	6.8(19)	···	···
J1758+3030*	···	35.0(2)	56178	0.164	22	41	107.(4)	7.4(13)	−1.5(4)	13,1,14
J1759−1029	···	115.4(6)	58355	0.347	185	329	11.7(17)	11.1(19)	···	···
J1759−2205	B1756−22	177.0(11)	56663	0.249	9	28	25.(6)	27.(7)	−2.01(18)	2,11,35,26
J1759−2922	···	79.42(14)	56902	0.286	9	17	32.(6)	14.(2)	−2.4(7)	23,24,35
J1759−3107*	···	128.3(2)	56932	0.177	25	61	17.(4)	5.7(15)	−1.4(6)	26,35
J1800−0125	···	51.0(2)	57535	0.301	25	41	10.(2)	3.3(9)	···	···
J1800+5034	···	22.64(14)	55384	0.004	13	20	43.(2)	2.0(3)	···	···
J1801−0357*	B1758−03	120.2(2)	58087	0.234	10	25	63.5(5)	11.7(11)	−2.3(14)	2
J1801−2920*	B1758−29	125.4(2)	56903	0.084	37	71	71.(2)	28.(2)	−1.90(16)	53,26,11,12
J1802+0128	···	101.4(14)	57854	0.205	29	54	5.(3)	2.0(13)	···	···
J1803−3329	···	170.9[‡]	56989	0.234	15	57	6.1(16)	2.8(8)	···	···
J1804−2717	···	24.66(9)	56783	0.102	0.8	2	14.(2)	11.(2)	−1.(4)	29,46
J1804−28	···	213.0(3)	56810	0.270	17	67	7.(2)	4.5(14)	···	···
J1805+0306	B1802+03	80.95(5)	57692	0.493	3	14	8.(5)	8.(4)	−1.33(3)	1,54
J1805−0619	···	147.1(11)	58254	0.146	15	32	7.(5)	2.1(15)	···	···
J1806+2819	···	18.69(6)	56254	0.180	2	2	21.8(17)	3.9(7)	···	···
J1807−0847	B1804−08	112.3(4)	58349	0.225	5	17	68.5(9)	32.(2)	−0.6(12)	2,26,11,12
J1807−2715	B1804−27	313.2(2)	56782	0.274	29	74	24.(3)	19.(3)	−2.5(3)	55,2,11,35
J1808+00	···	149.2(19)	57877	0.358	19	34	8.(4)	5.(2)	···	···
J1808−0813*	···	151.6(2)	58258	0.215	28	67	30.(3)	14.(2)	−2.2(3)	15,26,11,12
J1808−3249*	···	147.3(9)	56966	0.209	6	25	12.(3)	4.7(13)	···	···
J1809−0119	···	138.3(19)	57511	0.203	34	49	9.(2)	2.5(6)	···	···
J1809−3547	···	192.2(2)	57151	0.305	108	191	18.8(19)	14.(2)	···	···
J1811−0154*	···	148.1(2)	57535	0.248	26	54	10.(3)	3.4(11)	···	···
J1811−2439	···	167.2(17)	56773	0.251	19	41	19.(2)	13.(2)	···	···
J1812+0226	B1810+02	104.1(2)	57692	0.232	15	25	25.(3)	5.1(10)	−2.0(3)	2
J1812−3039	···	141.4(15)	56931	0.206	12	38	6.(2)	2.0(6)	···	···
J1813+4013	B1811+40	41.4(2)	55845	0.311	22	36	121.8(19)	12.(2)	−1.64(14)	1,2,56
J1814−0521	···	130.6(2)	58233	0.415	23	66	7.(2)	8.(3)	···	···
J1815+55	···	58.86(11)	55346	0.006	10	18	11.(7)	0.6(4)	···	···
J1816−0755	···	117.9(5)	58258	0.037	7	12	18.4(4)	5.0(5)	···	···
J1816−2650*	B1813−26	128.3(15)	56782	0.317	34	73	31.1(16)	24.(2)	−1.50(7)	2,11,12
J1816+4510	···	38.88(3)	55526	0.274	0.3	1.0	34.(4)	10.(2)	−3.5(3)	33,17

Table A.1 (cont'd)

PSR[a]	PSR B	DM (pc/cm^3)	MJD	θ (deg)	W_{50} (ms)	W_{10} (ms)	S/N	S_{350} (mJy)	α	Refs.
J1817−3618*	B1813−36	94.1(9)	57152	0.125	6	15	96.(2)	14.4(15)	−1.2(4)	38,57,26,11,12
J1817−3837	···	102.7(9)	57383	0.062	9	17	45.(2)	5.6(6)	−1.1(8)	23,26,12
J1819−37[B]	···	68.2(16)	57170	0.003	8	38	24.1(12)	4.2(5)	···	···
J1820−0427	B1818−04	84.37(15)	58082	0.155	10	29	118.9(11)	29.(2)	−1.(2)	1,10,2,11,12
J1820−0509*	···	102.4(8)	58233	0.212	10	22	18.(3)	7.5(16)	···	···
J1821+0155	···	51.75[‡]	57695	0.123	0.5	1	9.(2)	1.8(4)	···	···
J1821+41*	···	40.6(3)	55689	0.000	9	43	18.4(11)	0.89(19)	···	···
J1822+02[B]	···	103.8(3)	57665	0.000	62	93	14.9(5)	3.5(5)	···	···
J1822−2256*	B1819−22	121.4(4)	56750	0.278	87	128	51.8(18)	28.(2)	−1.44(5)	2,26,11,12
J1823−0154*	···	135.8(19)	57535	0.311	11	25	17.(5)	6.(2)	−2.2(7)	15,11,35
AJ1823−3021A	B1820−30A	86.88(5)	56908	0.234	0.9	1	27.(3)	18.(3)	−2.5(6)	29,58
BJ1823−3021B*	B1820−30B	86.88(9)	56908	0.232	5	13	16.(2)	3.3(6)	−2.4(3)	2,58
J1823−3106	B1820−31	50.24(7)	56931	0.092	5	12	136.3(16)	19.4(19)	−1.3(3)	10,2,26,11,12
J1824−0127*	···	63.00(2)	57535	0.125	16	59	38.(2)	7.6(9)	···	···
J1824−2328*	···	195.3(2)	56752	0.184	39	96	18.(2)	6.0(11)	···	···
J1825+0004	B1822+00	56.7(2)	57997	0.270	10	26	30.(3)	7.7(10)	−1.4(2)	1,2
J1825−0935	B1822−09	19.29(19)	58347	0.123	15	32	82.(2)	48.(3)	−2.2(9)	8,10,2,11,12
J1825−31	···	93.3(10)	56933	0.214	47	163	4.(5)	1.5(16)	···	···
J1829+0000	···	116.8(5)	57507	0.184	8	20	13.(2)	5.0(11)	···	···
J1829+25[B]	···	74.0(7)	56458	0.003	33	57	17.7(17)	0.82(15)	···	···
J1831−0823	···	246.4(15)	58347	0.119	13	54	5.7(8)	3.7(6)	−1.2(8)	26,12
J1832−0827	B1829−08	303.7(16)	58347	0.185	49	113	12.(3)	16.(5)	−0.92(13)	2,11,26
J1833−0338	B1831−03	234.8(17)	57999	0.236	46	115	71.(5)	62.(6)	−2.7(7)	2,26,11,35
J1834−0010	B1831−00	88.36(13)	57506	0.212	29	46	17.(5)	7.(2)	−2.58(16)	1,2,35
J1834−0426*	B1831−04	79.4(7)	58055	0.178	18	83	111.(2)	150(10)	−2.0(3)	1,2,11,35
J1835−1020	···	115.9(7)	58355	0.040	10	37	10(10)	7.(9)	−0.86(3)	56,12,26
J1836−1008	B1834−10	315.8(14)	58355	0.236	49	192	16.(3)	36.(7)	−2.1(2)	2,11,12,26
J1836+51[B]	···	44.4(2)	55385	0.000	18	35	5.(6)	0.4(4)	···	···
J1837−0045	···	87.11(15)	57506	0.202	16	35	17.5(6)	5.5(4)	−1.(6)	15,12
J1838−1046	···	209.3(3)	58355	0.272	17	54	10.(2)	6.1(14)	···	···
J1839−0627	···	92.49(12)	58255	0.131	18	28	13.(5)	10.(4)	···	···
J1840−0840	···	285.2(13)	58347	0.386	243	608	9.(4)	17.(8)	···	···
J1840+5640*	B1839+56	26.7(4)	55330	0.158	25	56	310(20)	23.(3)	−1.23(8)	8,1,2
J1842+0257*	···	146.0(7)	57665	0.335	63	120	17.(4)	10.(3)	···	···
J1842−39[B]	···	47.6(9)	57384	0.013	17	56	23.(8)	3.9(14)	···	···
J1843−0000	···	101.8(2)	57507	0.152	58	179	13.2(8)	10.1(9)	−0.5(7)	26,11,12
J1844+00	···	346.6(11)	57877	0.002	43	139	21.(3)	18.(3)	···	···
J1844−0433*	B1841−04	123.0(2)	58107	0.120	42	92	23.(2)	14.(2)	−1.7(2)	2,26,35
2J1846−07492	···	190.8(2)	58204	0.415	18	42	8.(3)	14.(6)	···	···
J1847−0402	B1844−04	142.0(15)	58055	0.088	33	84	80(10)	55.(8)	−2.11(15)	2,11,26
J1848−0023	···	34.9(2)	57507	0.165	8	31	7.(4)	4.(2)	···	···
J1848−0123	B1845−01	159.1(17)	57511	0.140	83	0.0	34.(3)	50.(6)	−1.2(3)	2,26,11,12
J1849−0317	···	40.0(17)	57452	0.256	15	40	15.(5)	14.(5)	···	···
J1849−0614	···	118.2(2)	58087	0.169	17	35	14.(5)	8.(3)	···	···
J1849−0636	B1846−06	148.3(3)	58204	0.225	29	77	46.(4)	31.(5)	−2.319(12)	2,26,11,35
J1849+2423	···	62.53(7)	56276	0.152	16	26	11.(6)	1.7(10)	−1.54(19)	1,52
J1850+0026	···	201.2(2)	57997	0.182	68	182	8.6(8)	9.5(11)	···	···
J1851−0053	···	23.9(3)	57510	0.274	23	42	19.(4)	11.(2)	−1.56(17)	1,12
J1852−2610	···	56.81(8)	56777	0.200	6	25	94.(7)	19.(2)	−1.8(7)	15,26,12
J1854+36[A]	···	59.8[‡]	56046	0.146	48	140	11.(4)	1.6(7)	···	···
J1855−0941	···	153.6(8)	58252	0.124	32	51	14.(2)	8.0(18)	···	···
J1856+0113	B1853+01	96.47(6)	57818	0.170	4	10	8.(2)	3.6(9)	−2.(5)	2,35
J1856−0526	···	131.8(9)	58087	0.245	16	41	13.(3)	9.(2)	···	···

Table A.1 (cont'd)

PSR[a]	PSR B	DM (pc/cm^3)	MJD	θ (deg)	W_{50} (ms)	W_{10} (ms)	S/N	S_{350} (mJy)	α	Refs.
J1857+0057	B1854+00	82.54(9)	57877	0.154	33	42	15.(2)	11.(2)	−1.4(7)	59,35
J1857−1027	···	107.3(9)	58355	0.140	116	257	48.(3)	11.6(14)	···	···
J1859+00	···	423.0(14)	57877	0.210	69	109	23.(3)	19.(3)	···	···
J1859+76	···	47.0(3)	55177	0.003	32	50	15.(3)	0.7(2)	···	···
J1900−2600*	B1857−26	37.92(15)	56777	0.118	13	69	521.2(5)	100(10)	†	···
J1900−0933	···	162.6(3)	58252	0.049	104	36	10(10)	2.(3)	···	···
J1900+30*	···	71.91(15)	56085	0.088	12	19	31.9(17)	2.0(3)	···	···
J1901+0156	B1859+01	105.3(7)	57692	0.276	3	8	42.5(8)	21.(2)	−2.976(19)	1,2,35
J1901−04[B]	···	106.5(7)	57544	0.016	72	352	13.(4)	6.(2)	···	···
J1901−0906	···	72.4(4)	58252	0.121	14	73	36.(2)	8.2(12)	−1.1(8)	23,24,26,11,12
J1902−1036	···	96.2(2)	58355	0.215	11	44	10.(2)	2.5(6)	···	···
J1903+0135*	B1900+01	245.0(18)	57695	0.254	23	70	73.5(15)	45.(4)	−1.6(3)	2,26,11,35
J1903−0258	···	114.1(7)	57452	0.225	11	33	7.(5)	4.(3)	···	···
J1903−0632*	B1900−06	195.7(11)	58204	0.433	18	48	25.(2)	29.(4)	−2.3(2)	2,26,11
J1903−0848	···	66.6(2)	58227	0.380	16	35	8.(6)	4.(3)	···	···
J1903+2225	···	110.8(16)	56457	0.177	7	52	5.(4)	0.9(8)	···	···
J1904+0004	···	233.2(3)	57877	0.028	11	19	20.8(10)	8.1(9)	−1.3(6)	15,26,12
J1904+33[B]	···	81.04(17)	56053	0.001	15	33	12.8(16)	1.1(2)	···	···
J1905−0056*	B1902−01	228.9(16)	57510	0.240	12	27	42.5(4)	12.7(12)	−2.0(3)	2,26,12
J1907+4002*	B1905+39	30.9(3)	55846	0.081	62	77	222.(2)	15.(2)	−0.7(6)	13,1,2
J1907+57[B]	···	54.63(19)	55330	0.002	8	25	20.(3)	1.6(3)	···	···
J1908+2351*	···	102.2(9)	56278	0.193	7	16	7.4(5)	0.81(11)	−0.(2)	20,49
J1909−3744	···	10.392(3)	57170	0.185	0.1	0.2	32.(4)	6.5(13)	−1.0(5)	26,11
J1909+0007*	B1907+00	112.7(2)	57877	0.405	8	18	39.8(9)	14.7(19)	−1.5(4)	1,2,11,35
J1909+0254	B1907+02	171.7(2)	57666	0.026	12	31	116.(6)	24.(2)	−2.1(6)	1,2,11,35
J1910+0225	···	209.0[‡]	57692	0.111	12	50	7.(4)	4.(2)	···	···
J1910−0309	B1907−03	205.4(13)	57452	0.272	7	20	81.(2)	24.(2)	−1.7(9)	1,2,11,35
J1911−1114	···	30.97(3)	58355	0.217	0.3	0.6	45.(3)	16.(2)	−2.0(2)	5,33,27,29,46
J1912+2104*	B1910+20	88.5(5)	56460	0.217	15	93	28.(2)	4.6(7)	−1.2(6)	20,2
J1912+2525	···	37.91(16)	56223	0.321	8	17	14.5(19)	2.0(3)	−2.79(4)	1,61
J1913−0440	B1911−04	89.3(2)	57544	0.244	7	15	146.0(16)	21.(2)	−1.4(6)	1,10,2,26,11,12
J1913+3732	···	72.1(2)	56017	0.191	12	30	64.(5)	4.4(8)	−1.6(5)	20,18
J1914+0219	···	236.0(11)	57666	0.275	13	37	13.8(12)	7.5(10)	···	···
J1915+0227	···	191.9(8)	57666	0.083	8	28	33.(3)	13.5(18)	···	···
J1916+32[L]	···	83.3(2)	56075	0.223	19	34	10.(9)	1.1(11)	···	···
J1917+2224*	B1915+22	134.5(11)	56297	0.230	21	38	25.(2)	5.0(7)	−1.85(4)	1,54,62
J1917−30[B]	···	38.1(3)	56902	0.181	35	60	32.7(13)	3.9(5)	···	···
J1918−0642	···	26.58(7)	57997	0.321	0.7	2	13.2(11)	10.2(14)	−1.88(2)	33,63
J1918−1052	···	62.7(2)	58255	0.211	12	20	21.(2)	2.9(5)	···	···
J1919+0021*	B1917+00	90.3(3)	57877	0.174	24	47	75.1(17)	14.2(15)	−1.89(19)	1,2,11
J1920+2650*	B1918+26	27.7(2)	56159	0.148	13	23	113.(2)	10.9(14)	−1.6(10)	1,2
J1921−05B[B]	···	80.7(5)	58087	0.000	27	96	20(10)	2.3(15)	···	···
J1921−05A	···	97.5(2)	58087	0.216	20	32	9.6(19)	1.8(4)	···	···
J1921+1948	B1918+19	154.1(2)	56480	0.561	29	80	10.(4)	17.(8)	−2.3(3)	2
J1921+2153	B1919+21	12.4(3)	56457	0.088	30	46	249.2(13)	25.(3)	−2.(4)	8,13,20,10,2,12
J1921+42	···	53.18(15)	55633	0.492	7	26	85.4(10)	32.(5)	···	···
J1922+2018	B1920+20	201.6(3)	56480	0.338	56	79	8.(4)	2.8(14)	−2.(3)	2
J1922+2110*	B1920+21	216.9(2)	56459	0.267	13	41	89.(2)	15.1(17)	−1.5(15)	1,2
J1922+58	···	53.74(13)	55330	0.017	13	20	16.(2)	0.9(2)	−1.(3)	1,17
J1923+2515	···	18.85(3)	56180	0.170	0.4	0.7	19.7(6)	4.5(6)	−1.96(4)	33,21,34
J1927+2234	B1925+22	186.5(3)	56296	0.296	28	86	13.(6)	3.0(15)	···	···
J1928+28[B]	···	79.2(2)	56107	0.005	43	55	13.(2)	1.2(2)	···	···
J1929+00	···	42.95(7)	57877	0.049	18	53	24.1(7)	3.3(3)	···	···

Table A.1 (cont'd)

PSR[a]	PSR B	DM (pc/cm^3)	MJD	θ (deg)	W_{50} (ms)	W_{10} (ms)	S/N	S_{350} (mJy)	α	Refs.
J1929+3817	···	93.2(2)	55851	0.122	26	84	34.0(14)	4.0(6)	···	···
J1929+62*	···	67.7(3)	56657	0.071	24	47	13.6(10)	0.66(12)	−0.7(18)	1,17
J1929+66^{B}	···	59.5(2)	55178	0.010	13	38	8.2(7)	0.50(9)	···	···
J1930−01^{G}	···	36.45(15)	57535	0.492	19	40	48.1(4)	48.(5)	···	···
J1931+30*	···	53.03(15)	56082	0.317	8	21	9.(7)	2.0(17)	···	···
J1932+2020	B1929+20	211.3(6)	56477	0.081	16	43	63.5(18)	19.4(18)	−1.(3)	2
J1932+2220	B1930+22	218.9(3)	56297	0.137	2	6	38.(2)	5.2(6)	−1.2(3)	2
J1932−3655*	···	60.12(14)	57155	0.319	8	31	9.2(11)	1.7(3)	−1.(2)	23,26,12
J1935+52*	···	71.26(14)	55363	0.006	21	44	18.9(15)	1.7(2)	···	···
J1937+2544*	B1935+25	53.26(5)	56180	0.227	6	14	55.5(5)	15.6(16)	−0.9(8)	1,2,12
J1937+2950	···	113.6(4)	56082	0.101	35	119	28.(2)	4.5(7)	−2.9(10)	20,64
J1939+66	···	41.24(8)	55179	0.010	0.5	1	18.9(16)	1.3(2)	···	···
J1939+2134	B1937+21	71.02(2)	56459	0.234	0.3	0.8	34.3(4)	36.(3)	−1.1(5)	33,65,27,28
J1939+2449*	B1937+24	143.2(16)	56224	0.334	23	33	22.(4)	7.4(17)	···	···
J1940−2403*	···	65.4(4)	56752	0.324	40	70	60.(2)	8.6(13)	···	···
J1940−24^{B}	···	53.4(3)	56773	0.019	2	3	60.(2)	4.9(7)	···	···
J1941+0121	···	51.87(5)	57755	0.151	21	29	19.9(11)	5.6(7)	−1.68(5)	1,60
J1941+0237^{HL}	···	87.2(3)	57693	0.311	47	59	23.9(13)	7.0(11)	···	···
J1941−2602*	B1937−26	50.03(14)	56777	0.198	4	13	67.(2)	5.6(8)	−1.1(9)	2,26,11,12
J1941+43*	···	79.4(2)	55633	0.002	15	29	20.4(13)	1.4(2)	···	···
J1942+81*	···	40.19(5)	55128	0.005	2	5	12.8(6)	0.52(15)	···	···
J1943−1237	B1940−12	29.0(2)	58349	0.346	12	23	89.2(3)	14.(2)	−2.16(11)	10,2,11,12
J1945−0040*	B1942−00	59.7(2)	57507	0.138	28	69	98.(3)	17.(2)	−1.7(2)	1,2
J1946−09^{B}	···	50.63(2)	58055	0.006	4	8	6.(2)	0.9(4)	···	···
J1946−1312*	···	63.04(12)	58348	0.155	9	23	17.0(5)	1.8(3)	···	···
J1946+2244	B1944+22	141.5(3)	56296	0.228	17	50	10.1(9)	1.8(2)	−2.0(14)	66,67
J1946−2913*	B1943−29	44.3(2)	56901	0.254	8	25	88.(2)	7.7(11)	−1.8(7)	2,26,11,12
J1948−27^{B}	···	57.85(8)	56783	0.007	6	10	14.(2)	0.75(16)	···	···
J1948+3540*	B1946+35	129.1(18)	56044	0.092	29	89	98.5(4)	17.(2)	−1.(3)	20,2
J1949−2524*	B1946−25	23.0(2)	56777	0.225	12	24	75.(2)	5.4(8)	−1.7(4)	2,11
J1949+34^{B}	···	228.2(14)	56052	0.006	17	53	15.5(16)	3.3(4)	···	···
J1952+3252	B1951+32	45.17(15)	56073	0.085	3	7	32.8(8)	10.7(10)	−1.83(13)	1,2
J1953+2732*	···	194.2(3)	56157	0.218	33	43	9.4(14)	1.3(2)	···	···
J1953+67	···	57.14(8)	55178	0.007	0.5	0.8	16.(4)	1.3(4)	···	···
J1954+2923*	B1952+29	7.95(11)	56089	0.245	7	30	46.9(18)	14.1(14)	−1.5(11)	1,2
J1954+3852	···	65.36(9)	55852	0.234	4	9	11.(2)	11.(2)	···	···
J1954+43*	···	129.6(3)	55633	0.002	100	135	19.(8)	3.0(13)	···	···
J1955+2908	B1953+29	104.5(6)	56107	0.191	0.6	1	39.6(10)	20.(2)	−1.2(3)	33,68,46
J1955+5059*	B1953+50	31.98[‡]	55420	0.314	7	15	164.(2)	20.(2)	−1.22(7)	1,2
J1957+2831*	···	138.8(7)	56107	0.013	8	18	14.0(4)	2.0(2)	−0.4(2)	19
J1959+2048	B1957+20	29.11(2)	56477	0.230	0.4	0.8	32.0(9)	16.(2)	−2.29(18)	33,69,46
J2000+29^{B}	···	132.3(7)	56089	0.005	23	87	15.(2)	1.4(3)	···	···
J2001+42	···	54.92(18)	55633	0.005	10	19	18.5(15)	1.6(2)	···	···
J2002+30	···	187.8(18)	56081	0.228	25	79	8.3(10)	3.5(5)	···	···
J2002+3217*	B2000+32	142.0(18)	56073	0.103	17	44	20.8(17)	3.9(4)	−1.1(2)	2
J2002+4050*	B2000+40	130.9(2)	55691	0.371	30	71	60.7(14)	36.(3)	†	···
J2004+3137	B2002+31	234.8(5)	56075	0.131	22	51	107.(5)	13.6(17)	−1.5(10)	2
J2005−0020*	···	36.0(5)	57507	0.203	56	78	37.(3)	4.2(8)	−1.4(4)	1,15,12
J2006−0807*	B2003−08	32.45(15)	57877	0.182	30	113	138.7(18)	31.(5)	−1.3(2)	2,26,11,12
J2006+22^{L}	···	127.3(4)	56459	0.363	53	71	6.(5)	1.5(13)	···	···
J2008+2513	···	60.29(15)	56224	0.224	12	31	13.(2)	2.0(4)	−1.6(5)	1,61
J2010−1323	···	22.16(5)	58347	0.262	0.3	0.6	16.0(12)	2.9(5)	−0.4(2)	26,70
J2010+2845	···	112.3(14)	56089	0.188	7	23	31.6(10)	4.5(5)	···	···

Table A.1 (cont'd)

PSR[a]	PSR B	DM (pc/cm^3)	MJD	θ (deg)	W_{50} (ms)	W_{10} (ms)	S/N	S_{350} (mJy)	α	Refs.
J2012−2029	···	37.67(14)	58386	0.397	18	33	17.(5)	4.9(19)	···	···
J2013−0649	···	63.29(14)	57661	0.220	9	21	31.0(14)	2.7(4)	···	···
J2013+3058*	···	148.7(7)	56080	0.050	3	7	18.5(6)	1.7(2)	···	···
J2013+3845	B2011+38	238.2(5)	55852	0.148	27	50	44.1(9)	20.2(18)	−1.00(7)	2
J2015+2524*	···	10.9(5)	56180	0.066	51	97	10.(2)	0.9(2)	···	···
J2016+1948	···	33.76(16)	56480	0.445	1	2	13.3(12)	4.0(7)	−1.947(5)	1,71
J2017−0414[B]	···	30.85(16)	57384	0.008	1	2	10.(2)	0.9(2)	···	···
J2017+2043	···	60.43(13)	56460	0.313	5	24	20.5(3)	3.2(4)	−1.8(10)	1,71
J2017−2737[B]	···	25.38(5)	56783	0.017	12	62	15.9(15)	3.0(5)	···	···
J2017+59	···	60.1(14)	55263	0.003	19	69	12.5(7)	1.7(2)	···	···
J2018+2839	B2016+28	14.19(14)	56089	0.154	16	24	590(20)	100(10)	−0.7(7)	8,13,1,10,2
J2019+2425	···	17.2[‡]	56254	0.216	0.4	0.9	14.(4)	4.1(14)	···	···
J2019+72[B]	···	34.88(8)	55178	0.006	20	55	10.4(11)	1.7(3)	···	···
J2022+2534[B]	···	53.66(2)	56180	0.009	0.5	1	16.4(6)	6.8(9)	···	···
J2022+2854*	B2020+28	24.66(8)	56089	0.059	7	19	550.3(12)	84.(9)	−0.78(19)	8,1,10,2,72
J2022+5154*	B2021+51	22.54(13)	55383	0.198	9	31	120(10)	17.(2)	−0.0(16)	1,2
J2023+5037	B2022+50	32.98(9)	55440	0.245	6	22	38.(2)	6.3(8)	−1.2(2)	1,2
J2027+4557	···	229.7(2)	55508	0.064	41	120	32.1(14)	7.8(8)	−1.3(10)	64,17
J2027+74	···	11.42(13)	55149	0.008	29	87	25.3(17)	3.0(5)	···	···
J2029+3744*	B2027+37	190.9(3)	55982	0.158	25	50	69.7(6)	17.0(14)	−2.25(17)	1,2
J2030+2228	B2028+22	71.93(16)	56297	0.214	13	29	44.(3)	4.3(7)	−0.72(18)	1,55
J2030+55*	···	59.43(14)	55362	0.149	19	35	13.0(12)	1.3(2)	···	···
J2033+0042*	···	37.5(12)	57753	0.307	113	192	51.7(8)	9.1(17)	−0.6(8)	1,11
J2033−1938*	···	23.3(3)	58232	0.099	10	48	26.(3)	1.9(5)	···	···
J2036+2835	···	84.3(3)	56089	0.202	25	35	37.5(10)	2.9(4)	−1.5(6)	1,18
J2037+1942*	B2034+19	36.6(5)	56480	0.453	20	46	30.9(13)	5.6(10)	−1.(2)	1,54
J2037+3621*	B2035+36	93.56(15)	56025	0.200	26	48	43.(4)	10.0(14)	−1.8(5)	2
J2038+35	···	57.91(4)	56046	0.298	5	11	6.0(18)	1.7(6)	···	···
J2038−3816	···	34.0(4)	57170	0.210	29	51	39.7(15)	2.9(5)	−2.(7)	23,26,12
J2038+5319	B2036+53	160.6(3)	55362	0.222	27	54	16.8(13)	1.9(2)	−1.5(3)	20,2
J2039−3616[B]	···	23.96(3)	57151	0.006	0.3	0.5	10.0(15)	1.3(3)	···	···
J2040−21[B]	···	23.87(14)	56655	0.009	22	29	52.6(4)	3.0(5)	···	···
J2043+2740	···	21.02(2)	56110	0.193	2	5	82.5(7)	10.2(13)	−2.(2)	1,40
J2043+7045	···	57.64(15)	55160	0.346	37	23	21.4(17)	3.6(6)	···	···
J2044+28[B]	···	90.3(4)	56089	0.005	31	58	15.1(12)	1.07(16)	···	···
J2044+4614	···	311.3(3)	55508	0.336	104	211	11.2(8)	6.9(8)	···	···
J2046−0421	B2043−04	35.9(3)	57384	0.369	22	39	93.(3)	13.(2)	−1.3(3)	1,10,2,11,26
J2046+5708	B2045+56	101.6(12)	55325	0.165	12	29	22.(4)	2.5(5)	−1.7(3)	1,2
J2048−1616*	B2045−16	11.4(5)	58118	0.260	57	105	377.8(9)	52.(9)	−1.8(10)	9,10,2,26,11,12
J2048+2255	···	70.46(7)	56297	0.248	6	18	11.(9)	1.4(13)	−0.6(2)	20,71
J2051−0827	···	20.72(4)	57656	0.314	0.3	0.7	28.1(9)	7.6(15)	−1.60(14)	5,33,27,29,26,46,42
J2054−39[B]	···	24.8(2)	57214	0.000	8	36	30.9(19)	1.5(3)	···	···
J2055+2209	B2053+21	36.1(2)	56459	0.182	9	24	107.8(5)	9.3(14)	−1.10(3)	1,2
J2055+3630	B2053+36	97.34(5)	56025	0.267	6	19	65.5(19)	14.0(18)	−1.5(9)	1,2
J2102+38*	···	86.2(3)	55982	0.345	37	65	15.(2)	3.5(6)	···	···
J2105+28	···	62.48(14)	56156	0.041	7	11	12.(2)	0.65(16)	···	···
J2108−3429*	···	30.1(3)	57015	0.150	15	32	48.0(5)	2.3(4)	−1.(3)	23,26,12
J2108+4441*	B2106+44	139.8(17)	55626	0.286	30	67	80.7(11)	28.(3)	−0.8(6)	1,2
J2111+2106*	···	59.1(10)	56477	0.047	40	87	48.(3)	2.0(3)	−0.71(4)	20,60
J2113+2754*	B2110+27	25.1(3)	56156	0.227	13	25	98.0(12)	5.7(10)	−1.73(15)	8,13,1,2
J2113+4644*	B2111+46	141.3(2)	55557	0.180	31	118	403.8(18)	170(20)	−1.5(5)	1,2
J2113+67*	···	54.98(14)	56655	0.047	8	27	10(20)	0.6(15)	−1.487(7)	1,17
J2123+36[L]	···	108.2(3)	56025	0.056	21	39	20.2(6)	1.27(19)	···	···

Table A.1 (cont'd)

PSR[a]	PSR B	DM (pc/cm^3)	MJD	θ (deg)	W_{50} (ms)	W_{10} (ms)	S/N	S_{350} (mJy)	α	Refs.
J2122+54	···	31.78(3)	55348	0.003	2	6	10.4(7)	1.21(15)	···	···
J2124−3358	···	4.595(5)	56967	0.197	0.9	3	15.2(6)	7.5(14)	−1.4(3)	29,28
J2129−0429	···	16.88(7)	57214	0.191	1	5	44.(2)	30.(5)	···	···
J2131−31^{B}	···	31.5(13)	56932	0.015	53	98	26.(2)	1.0(2)	···	···
J2136−1606*	···	18.5(3)	57875	0.123	19	36	42.0(9)	2.1(4)	···	···
J2137+64*	···	106.0(4)	55196	0.017	19	53	14.2(9)	0.90(14)	···	···
J2138+4911	···	168.4(17)	55524	0.103	26	59	53.3(7)	7.9(9)	···	···
J2139+00	···	31.18(8)	57696	0.323	14	31	24.0(14)	4.6(9)	···	···
J2139+2242*	···	44.1(2)	56298	0.096	40	62	217.9(14)	15.(2)	−0.2(2)	13,1,14
J2144−3933*	···	3.(2)	57152	0.260	50	107	65.(3)	2.8(6)	−2.(2)	15,11,22
J2145−0750	···	9.005(6)	57445	0.157	1	3	316.(2)	100(20)	−1.41(11)	5,33,10,27,26,11,29
J2145+21^{B}	···	44.1(3)	56459	0.009	24	44	10(20)	0.6(10)	···	···
J2148−34^{B}	···	13.9(2)	56967	0.008	20	35	16.7(5)	0.84(17)	···	···
J2149+6329*	B2148+63	129.6(9)	55229	0.127	18	34	154.5(4)	21.(2)	−1.0(8)	1,2
J2150−03^{B}	···	20.67(3)	57170	0.006	0.2	0.5	15.(3)	1.5(4)	···	···
J2150+5247	B2148+52	148.9(8)	55362	0.074	10	23	64.1(4)	7.9(9)	−0.9(4)	1,2
J2151+2315	···	20.6(9)	56297	0.248	17	49	8.2(13)	1.0(2)	···	···
J2154−2812*	···	32.9(3)	56838	0.309	9	22	28.3(9)	1.6(3)	···	···
J2155+2813*	···	78.1(4)	56156	0.252	26	41	15.4(14)	1.0(2)	−0.8(12)	1,49
J2155−3118	B2152−31	14.8(2)	56932	0.268	15	37	152.8(12)	10.(2)	−1.8(5)	2,11,12
J2156+2618	···	48.33(12)	56159	0.304	8	17	17.(2)	1.8(4)	−1.0(4)	1,61
J2157+4017*	B2154+40	71.1(3)	55847	0.072	67	124	206.6(11)	20.(2)	−0.7(5)	13,1,2
J2158−27^{B}	···	22.15(12)	56837	0.498	13	25	30.(3)	9.(2)	···	···
J2202+21^{A}	···	17.6(3)	56477	0.241	22	31	9.(3)	0.5(2)	···	···
J2203+50	···	76.98(19)	55504	0.949	29	72	10.(4)	1010(500)	···	···
J2205+1444	···	36.7(2)	58355	0.215	8	57	17.3(8)	1.8(3)	−1.355(2)	1,61
J2206+6151	···	168.8(8)	55199	0.220	24	49	10.1(10)	2.8(4)	−0.(5)	17,18
J2207−15^{B}	···	27.5(19)	57789	0.004	25	40	13.1(12)	0.76(17)	···	···
J2207+40	···	11.33(16)	55657	0.057	28	61	23.5(4)	2.5(3)	···	···
J2208+5500*	···	104.6(2)	55348	0.245	14	29	54.0(8)	6.7(8)	−1.2(5)	1,3
J2210+21^{L}	···	46.5(4)	56477	0.090	21	41	44.8(18)	1.9(3)	···	···
J2210+57	···	192.1(5)	55325	0.021	63	154	9.0(7)	1.28(17)	···	···
J2212+2933*	B2210+29	74.5(2)	56086	0.067	52	64	50.9(14)	3.6(6)	−1.0(2)	1,2
J2214+3000	···	22.56(3)	56086	0.243	0.2	0.8	8.4(9)	1.9(4)	−0.9(8)	33,44,34
J2217+5733*	···	130.49(9)	55327	0.176	43	99	26.6(8)	5.2(5)	−1.6(7)	3,17
J2219+4754*	B2217+47	43.49(13)	55554	0.285	7	15	650(30)	90(10)	−2.44(11)	8,1,2,73
J2222−0137	···	3.265(13)	57541	0.276	0.8	1	25.(3)	3.4(9)	−0.90(8)	1,26,11
J2222+2923*	···	49.44(7)	56086	0.240	5	21	18.7(10)	2.1(3)	···	···
J2222+5602*	···	163.3(3)	55348	0.394	42	122	9.5(8)	4.3(6)	···	···
J2225+6535*	B2224+65	36.22(17)	55196	0.216	22	78	76.(3)	19.(2)	−1.76(5)	1,2
J2227+30*	···	20.0(2)	56080	0.287	24	32	43.(2)	4.4(9)	−1.7(3)	1,74
J2229+64	···	193.8(4)	55196	0.005	51	74	13.2(15)	1.1(2)	···	···
J2229+2643	···	22.72(3)	56159	0.241	0.5	0.7	33.8(9)	7.7(14)	−1.4(4)	5,75,46
J2229+6114	···	205.1(13)	55249	0.129	8	17	20.3(17)	8.2(11)	−1.(5)	17,76
J2229+6205*	B2227+61	124.5(11)	55199	0.173	26	35	100.5(14)	17.4(19)	−2.0(5)	1,2
J2234+2114*	···	35.5(3)	56480	0.283	33	189	27.(2)	5.0(10)	−1.7(2)	13,1,61
J2238+6021*	···	185.3(7)	55250	0.158	25	56	46.(7)	4.3(9)	···	···
J2242+6950*	B2241+69	40.4(4)	55164	0.189	20	51	22.(2)	1.8(3)	−1.6(3)	1,2
J2243+69*	···	67.8(2)	55164	0.055	45	12	12.3(12)	1.13(19)	···	···
J2244+63	···	92.15(11)	55198	0.590	16	23	11.(6)	15.(8)	···	···
J2248−0101	···	29.1(12)	57510	0.264	13	21	58.3(6)	5.5(11)	−1.(2)	1,15,12
J2251+24^{A}	···	34.6(3)	56295	0.130	19	84	8.(6)	0.7(6)	···	···
J2253+1516*	···	29.0(2)	58349	0.494	7	30	13.0(15)	6.0(13)	−1.7(9)	1,61

Here we list pulsars for which we have measured DM to have changed from previous measurements by $\geq 3\sigma$. We also include all pulsar profiles analyzed in Chapter 2.

Table A.1 (cont'd)

PSR[a]	PSR B	DM (pc/cm^3)	MJD	θ (deg)	W_{50} (ms)	W_{10} (ms)	S/N	S_{350} (mJy)	α	Refs.
J2256−1024	···	13.774(2)	57151	0.286	0.2	0.4	62.(3)	17.(3)	···	···
J2257−16^{B}	···	52.66(12)	57998	0.005	5	10	15.(4)	0.6(2)	···	···
J2257+5909	B2255+58	151.1(9)	55259	0.099	8	24	127.0(3)	95.(6)	−1.1(8)	1,2
J2302+4442	···	13.72(5)	55562	0.106	0.3	1	21.(8)	5.(2)	−0.2(12)	33,17,77
J2302+6028	···	156.7(3)	55250	0.109	20	35	99.6(11)	15.1(14)	−1.7667(19)	1,14
J2305+3100*	B2303+30	49.5(4)	56080	0.014	19	42	93.(3)	6.0(14)	−1.2(5)	8,1,2
J2305+4707	B2303+46	60.5(2)	55557	0.368	19	60	5.0(17)	1.3(5)	−1.65(16)	1,2
J2307+2225	···	6.74(13)	56459	0.290	10	24	15.(2)	1.4(3)	1.(2)	20,61
J2308+5547*	B2306+55	46.48(12)	55328	0.250	28	34	152.4(9)	61.(5)	−1.9(8)	1,2
J2313+4253*	B2310+42	17.31(9)	55625	0.153	8	15	208.3(6)	15.(2)	−0.7(14)	1,2
J2315+58	···	73.1(2)	55327	0.000	38	53	37.(6)	11.(2)	···	···
J2316+69*	···	71.3(2)	55164	0.011	17	32	11.(6)	0.8(4)	···	···
J2317+1439	···	21.9(3)	58350	0.259	0.4	0.7	30.(3)	6.7(15)	−1.0(3)	5,33,78,46
J2317+2149	B2315+21	20.8(3)	56477	0.068	23	41	349.5(17)	14.(2)	−1.48(5)	13,1,2
J2319+6411	···	246.1(5)	55198	0.321	38	77	32.(3)	23.(3)	···	···
J2321+6024*	B2319+60	94.0(5)	55250	0.171	111	184	117.(3)	109.(8)	−0.4(17)	1,2
J2322+2057	···	13.38(4)	56481	0.279	0.3	0.6	10(10)	1.3(17)	···	···
J2325−0530*	···	14.9(2)	57380	0.109	13	25	29.1(7)	1.3(2)	···	···
J2325+6316*	B2323+63	197.5(3)	55198	0.202	137	162	102.7(7)	22.(2)	−0.2(11)	1,2
J2326+6113*	B2324+60	122.5(6)	55235	0.108	15	22	74.(3)	13.4(15)	−0.6(2)	1,2
J2326+6141	···	34.5(2)	55199	0.780	26	46	17.(6)	200(80)	···	···
J2327+62^{B}	···	193.4(6)	55199	0.000	4	25	9.4(17)	1.6(3)	···	···
J2329+47^{L}	···	43.94(18)	55557	0.168	9	16	10(10)	0.6(5)	···	···
J2330−2005*	B2327−20	8.5(4)	58106	0.224	24	44	248.5(7)	13.(2)	−1.4(7)	8,2,11,12
J2333+6145	···	125.0‡	55199	0.185	23	97	6.(3)	1.9(10)	···	···
J2337+6151*	B2334+61	58.19(12)	55199	0.328	14	34	22.4(14)	6.9(8)	−1.29(13)	1,2
J2343+6221*	···	116.6(4)	55199	0.122	56	98	14.(2)	1.9(3)	···	···
J2346−0609*	···	22.5(3)	57384	0.189	10	73	105.5(14)	7.6(16)	−1.1(5)	15,11,12
J2347+02^{A}	···	15.0(3)	57666	0.056	25	40	22.6(19)	1.2(3)	···	···
J2352+65	···	152.7(3)	55197	0.271	32	118	7.3(6)	2.3(3)	···	···
J2353−22^{B}	···	9.92(14)	56666	0.015	9	21	32.(2)	1.4(2)	···	···
J2351+8533	···	38.2(2)	55082	0.011	17	33	16.4(4)	0.71(13)	0.(9)	1,17
J2354+6155*	B2351+61	94.7(2)	55199	0.344	10	29	19.3(6)	5.9(6)	−0.0(6)	1,2
J2356+22^{B}	···	22.9(4)	56480	0.000	68	124	20.(2)	1.1(2)	···	···

[a]Asterisks indicate pulsars with confirmed nulling or mode-changing during the observations. Letter superscripts indicate pulsars from survey discovery data: A corresponds to AODrift, ML to HTRU-mid and -lo lat, HL to HTRU-hi lat, S to SUPERB, G to GBT350, L to LOTAAS, and B to GBNCC.

†Single daggers in the α column correspond to pulsars with broken powerlaw spectral indices, which are reported in Table 2.2.

‡Double daggers indicate DM values that could not be improved by searching, and so come directly from the ATNF catalog.

◇PSR J2315+58 was found in a GBNCC beam that was $>3\sigma$ from the pulsar's published position, resulting in unbelievable flux density measurements. This is likely due to an error in the published position. So, we measure flux in the beam in which it was detected, and assume that the angular offset to the pulsar is zero.

References. — 1: Sanidas et al. (2019), 2: Lorimer et al. (1995a), 3: Surnis et al. (2019), 4: Joshi et al. (2009), 5: Kuzmin & Losovsky (2001), 6: Frail et al. (2016), 7: Lommen et al. (2000), 8: Stovall et al. (2015), 9: Bell et al. (2016), 10: Xue et al. (2017), 11: Jankowski et al. (2019), 12: Johnston & Kerr (2018), 13: Tyul'bashev et al. (2016), 14: Sayer et al. (1997), 15: Manchester et al. (1996), 16: Coenen et al. (2014), 17: Stovall et al. (2014), 18: Barr et al. (2013), 19: Lorimer et al. (1998), 20: Bilous et al. (2016), 21: Lynch et al. (2013), 22: Lorimer (1994), 23: Lyne et al. (1998), 24: Gould & Lyne (1998), 25: Nice et al. (2013), 26: Jankowski et al. (2018b), 27: Stairs et al. (1999b), 28: Manchester et al. (2013), 29: Toscano et al. (1998), 30: Burgay et al. (2013), 31: Brinkman et al. (2018), 32: Chandler (2003), 33: Kondratiev et al. (2016), 34: Levin et al. (2016), 35: Hobbs et al. (2004a), 36: Burgay et al. (2006), 37: Chatterjee et al. (2005), 38: Taylor et al. (1993), 39: Dewey et al. (1985b), 40: Ray et al. (1996), 41: Nicastro et al. (1995), 42: Kramer et al. (1999), 43: Bailes et al. (1997), 44: Ransom et al. (2011), 45: Wolszczan & Frail (1992), 46: Kramer et al. (1998), 47: Swiggum et al. (2017), 48: Bhattacharyya et al. (2013), 49: Lewandowski et al. (2004), 50: Lorimer et al. (1995b), 51: Costa et al. (1991), 52: Champion et al. (2005), 53: Johnston et al. (1992), 54: Stokes et al. (1986), 55: Ashworth & Lyne (1981), 56: Dembska et al. (2014), 57: Qiao et al. (1995), 58: Biggs et al. (1994), 59: Mohanty (1983), 60: Boyles et al. (2013), 61: Camilo & Nice (1995), 62: Han et al. (2016), 63: Janssen et al. (2010), 64: Janssen et al. (2009), 65: Foster et al. (1991), 66: Hulse & Taylor (1975), 67: Lazarus et al. (2015), 68: P. & R. (1984), 69: Fruchter et al. (1990), 70: Jacoby et al. (2007), 71: Navarro et al. (2003), 72: Gomez-Gonzalez & Guelin (1974), 73: Fomalont et al. (1992), 74: Camilo et al. (1996b), 75: Camilo (1995), 76: Halpern et al. (2001), 77: Cognard et al. (2011), 78: Camilo et al. (1996a)

Table A.2. Pulsars with $\geq 3\sigma$ DM changes.

Name	DM_{cat} [a] ($pc\,cm^{-3}$)	DM_{search} [b] ($pc\,cm^{-3}$)	Period (s)
J0026+6320	245.06(6)	244.70(8)	0.318
J0218+4232	61.252(5)	61.230(2)	0.002
J0502+4654	41.83(2)	42.38(16)	0.639
J0610−2100	60.6662(17)	60.700(3)	0.004
J0610+37	27.1549(3)	39.09(11)	0.444
J0740+6620	14.9617(2)	14.950(2)	0.003
J0818−3049	133.7(2)	118.9(2)	0.764
J1125+7819	11.73(15)	11.220(4)	0.004
J1231−1411	8.090(1)	8.072(3)	0.004
J1320−3512	16.42(1)	15.52(11)	0.458
J1327−0755	27.91215(6)	27.900(2)	0.003
J1358−2533	31.27(1)	16.0(2)	0.913
J1600−3053	52.3299(2)	52.312(3)	0.004
J1614−2230	34.9179(3)	34.490(3)	0.003
J1614−3937	152.44(2)	151.7(15)	0.407
J1622−3751	153.8(5)	155.7(18)	0.731
J1647−3607	224(1)	228.50(5)	0.212
J1654−2713	92.31(12)	93.3(2)	0.792
J1701−3130	130.73(6)	131.40(7)	0.291
J1708−3426	190.7(3)	188.7(17)	0.692
J1712−2715	92.64(13)	91.78(6)	0.255
J1721−2457	47.758(19)	48.230(3)	0.003
J1722+35	23.83(6)	22.1(2)	0.822
J1729−2117	34.49(4)	34.22(17)	0.066
J1734−2415	126.3(7)	117.1(11)	0.613
J1742−3957	186(8)	220.(7)	1.016
J1745−3040	88.373(4)	88.01(9)	0.367
J1745−3812	160.8(4)	163.6(18)	0.698
J1750−3503	189.35(2)	190.5(17)	0.684
J1754−3510	82.3(3)	81.23(11)	0.393
J1800−0125	50.0(2)	51.0(2)	0.783
J1802+0128	97.97(12)	101.4(14)	0.554
J1805−0619	146.22(9)	147.1(11)	0.455

Table A.2 (cont'd)

Name	DM_{cat} [a] ($pc\,cm^{-3}$)	DM_{search} [b] ($pc\,cm^{-3}$)	Period (s)
J1809−3547	193.84(7)	192.2(2)	0.860
J1811−2439	172.0(5)	167.2(17)	0.416
J1824−0127	58.0(15)	63.00(2)	2.499
J1824−2328	185(3)	195.3(2)	1.506
J1829+0000	114.0(4)	116.80(5)	0.199
J1832−0827	300.869(1)	303.7(16)	0.647
J1836−1008	316.98(3)	315.8(14)	0.563
J1839−0627	88.5(7)	92.49(12)	0.485
J1844+00	345.5(2)	346.6(11)	0.461
J1848−0023	30.6(1)	34.9(2)	0.538
J1849+2423	62.2677(16)	62.53(7)	0.276
J1855−0941	151.99(14)	153.60(8)	0.345
J1856−0526	130.5(4)	131.8(9)	0.370
J1903+2225	109.20(3)	110.8(16)	0.651
J1904+0004	233.61(4)	233.20(3)	0.140
J1908+2351	101.695(15)	102.2(9)	0.378
J1914+0219	233.8(4)	236.0(11)	0.458
J1918−0642	26.46(3)	26.580(7)	0.008
J1922+2018	203.31(1)	201.6(3)	1.173
J1935+52	71.9(1)	71.26(14)	0.568
J1940−2403	63.3(1)	65.4(4)	1.855
J1952+3252	45.006(19)	45.17(15)	0.040
J2016+1948	33.8148(16)	33.76(16)	0.065
J2044+4614	315.4(4)	311.3(3)	1.393
J2048+2255	70.684(2)	70.46(7)	0.284
J2151+2315	23.6(2)	20.6(9)	0.594
J2207+40	11.837(9)	11.33(16)	0.637
J2210+57	189.43(6)	192.1(5)	2.057
J2214+3000	22.545(2)	22.560(3)	0.003
J2229+6114	204.97(2)	205.10(13)	0.052
J2305+4707	62.067(3)	60.5(2)	1.066

[a]DM value from ATNF catalog.

[b]DM value from our search.

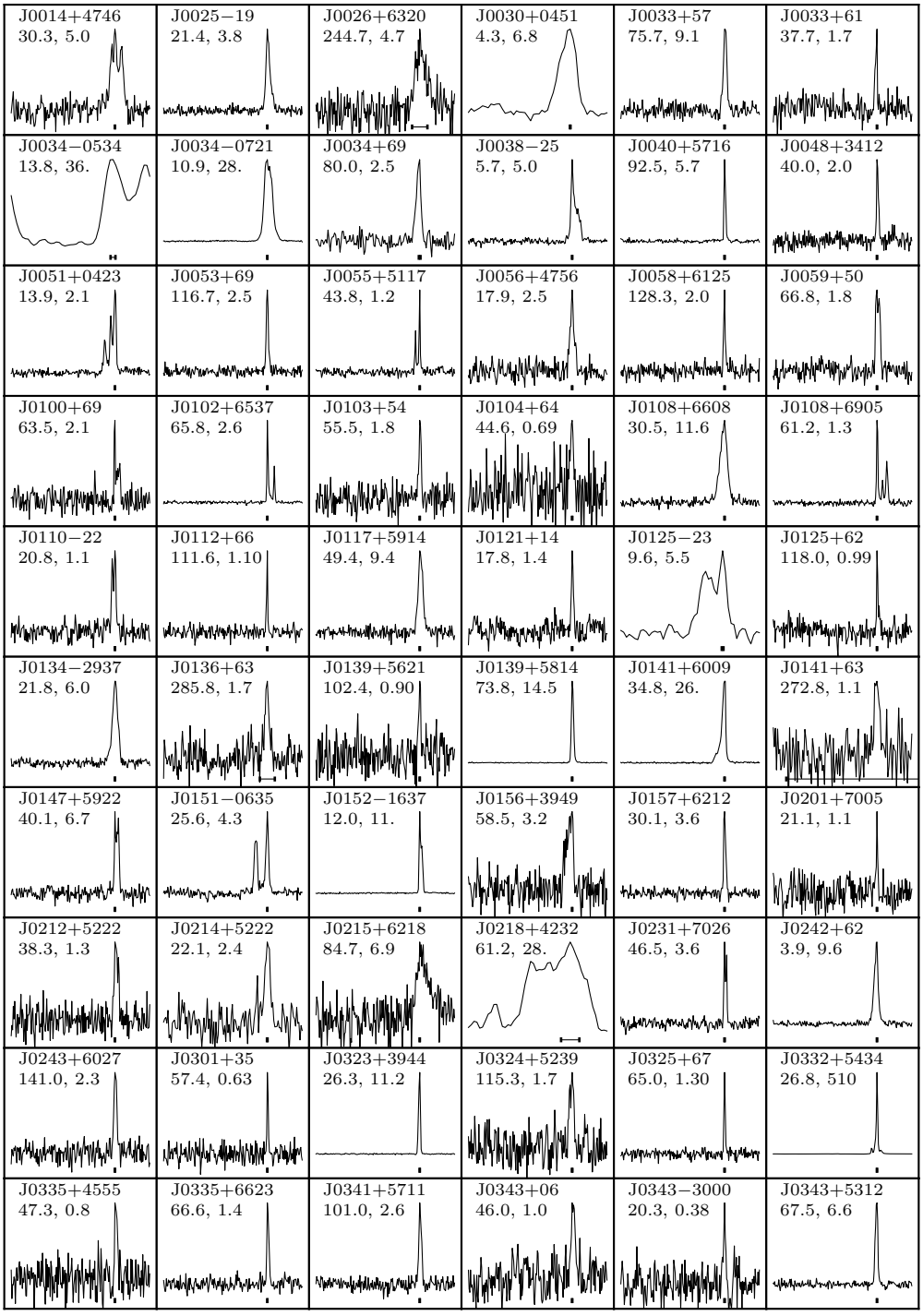

Figure A.1 Pulse profiles for all detections. Text in each plot gives the pulsar name, dispersion measure in pc cm^{-3}, and flux density in mJy. Centered beneath the profiles' peaks are error bars corresponding to the expected dispersive smearing of the pulse.

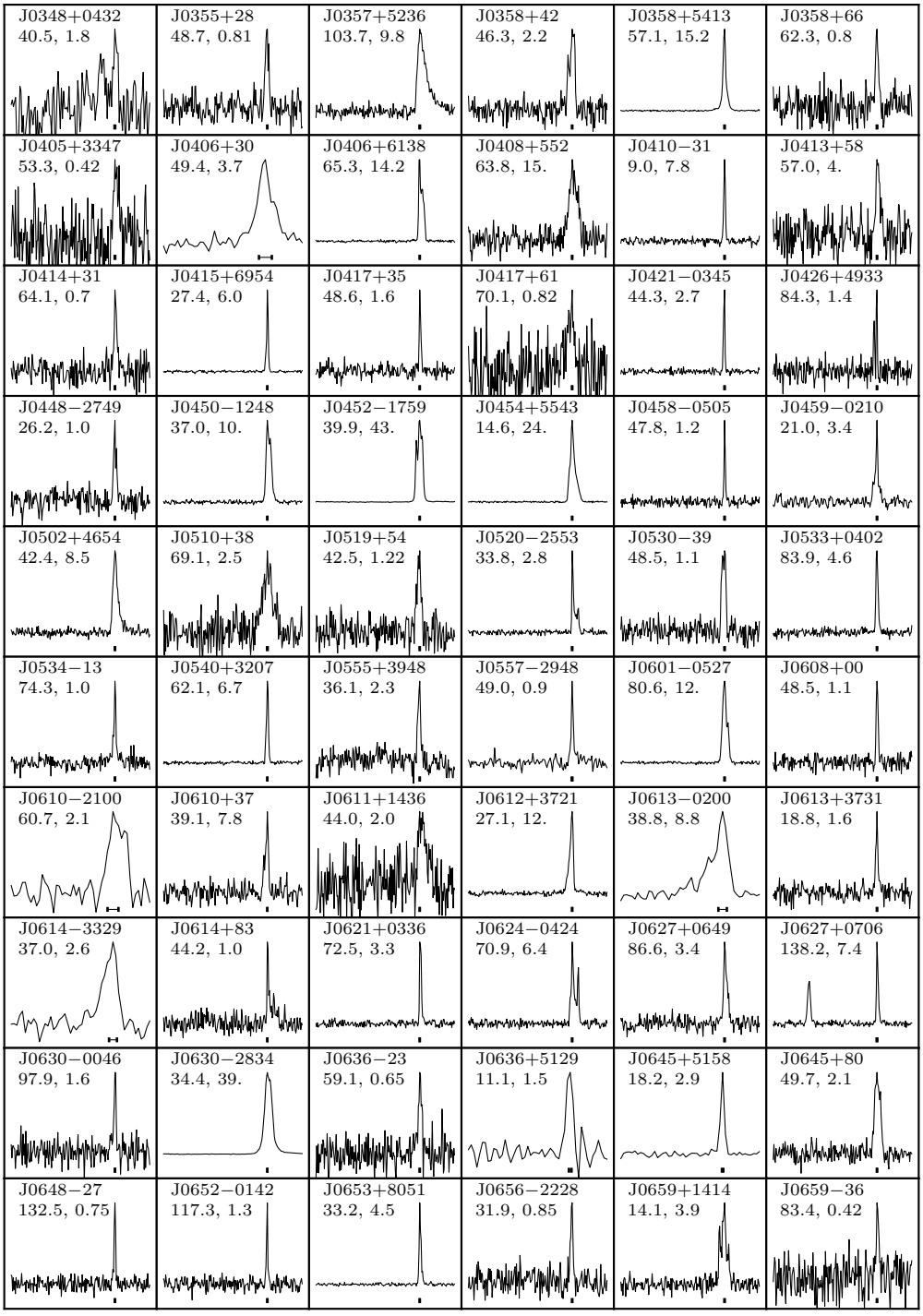

Figure A.2 Profile plots (continued). See Figure A.1 for details.

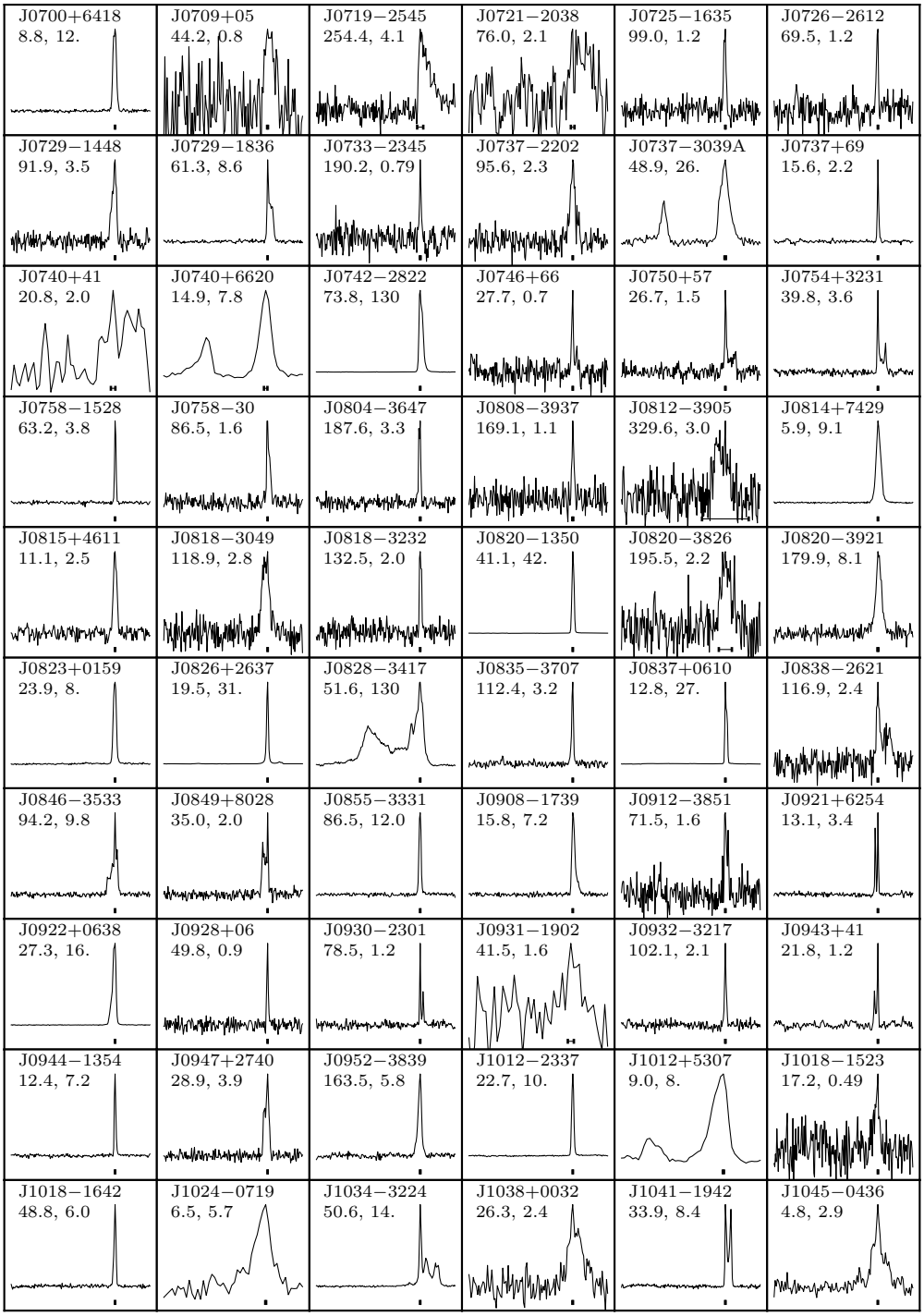

Figure A.3 Profile plots (continued). See Figure A.1 for details.

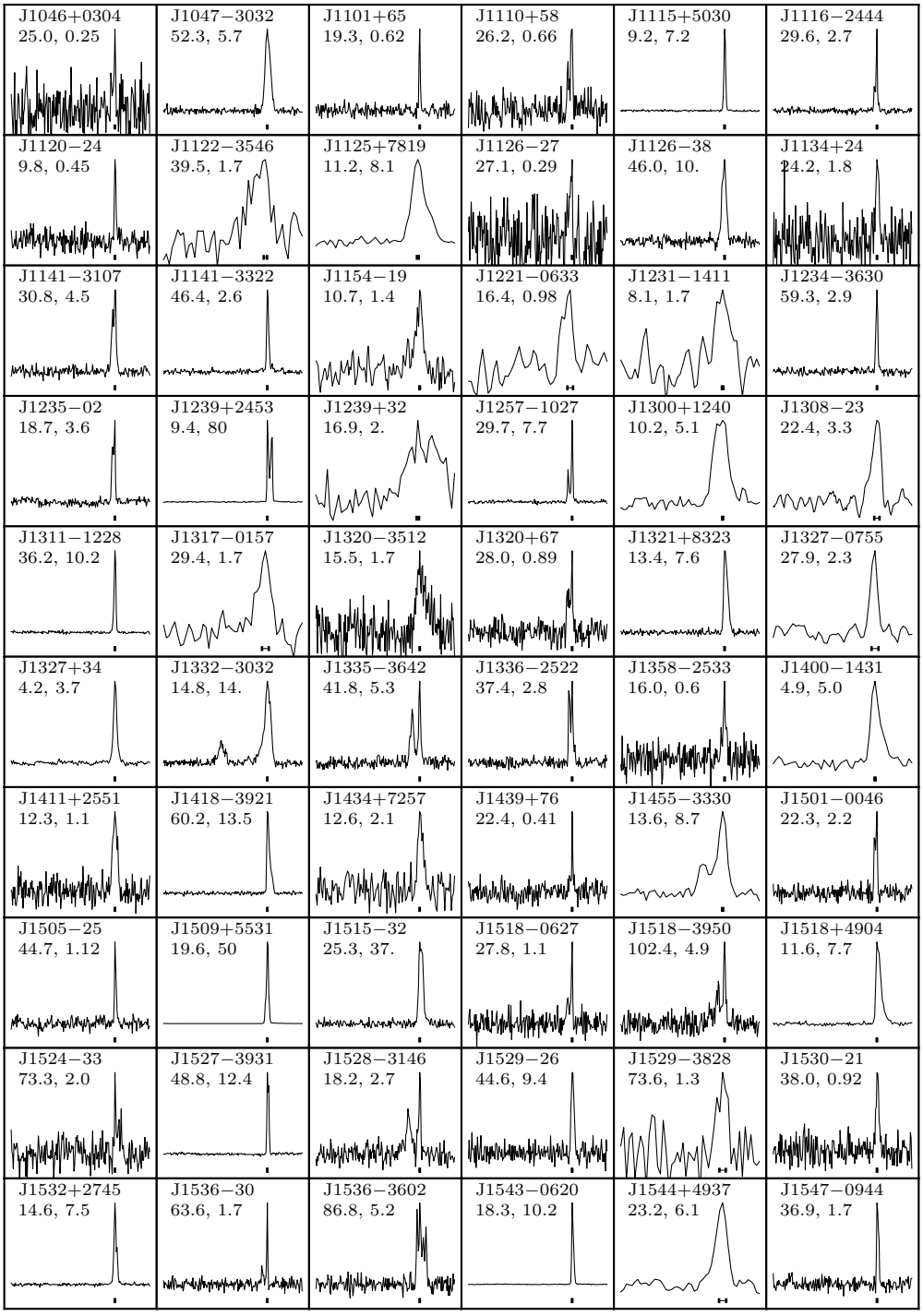

Figure A.4 Profile plots (continued). See Figure A.1 for details.

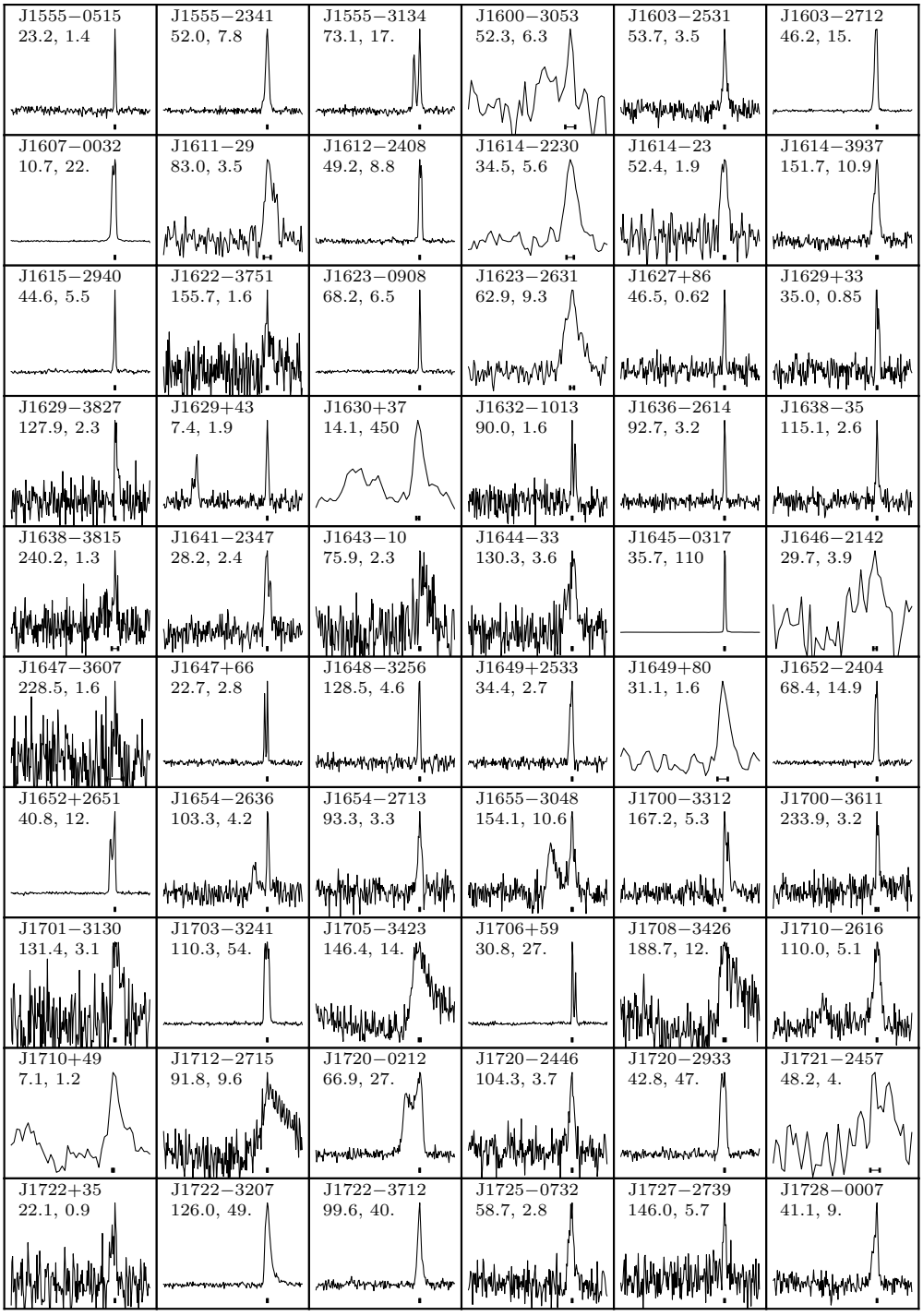

Figure A.5 Profile plots (continued). See Figure A.1 for details.

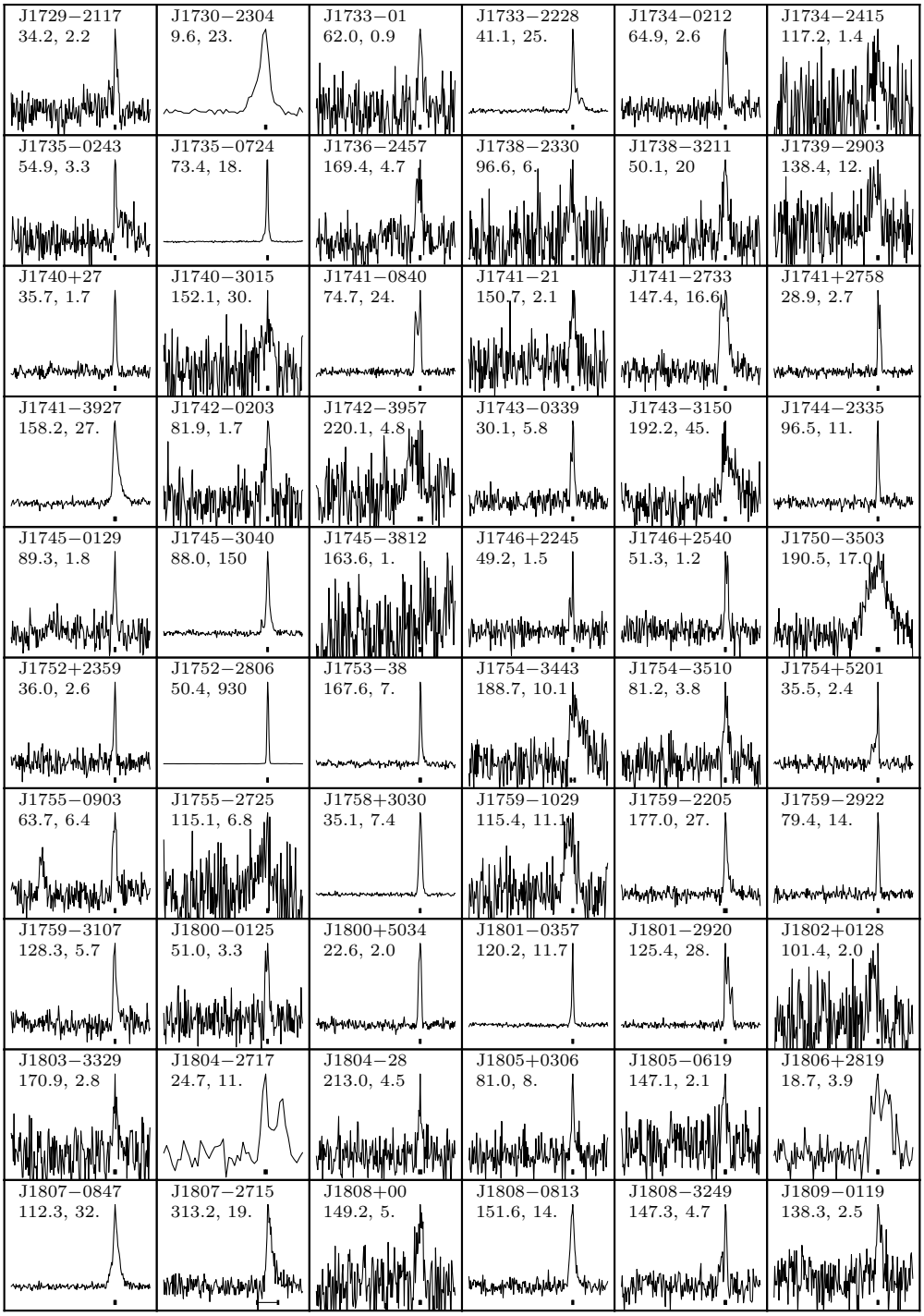

Figure A.6 Profile plots (continued). See Figure A.1 for details.

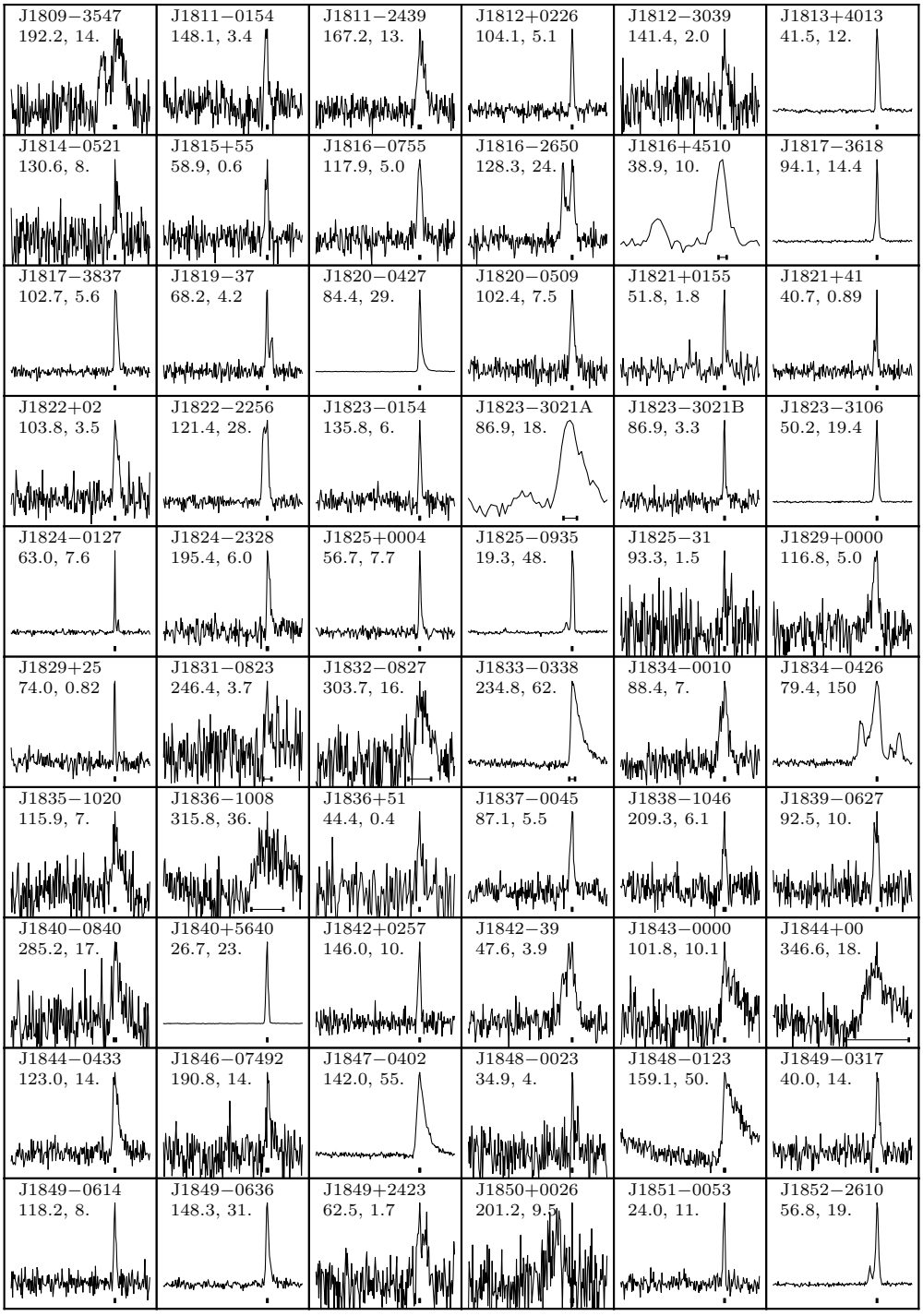

Figure A.7 Profile plots (continued). See Figure A.1 for details.

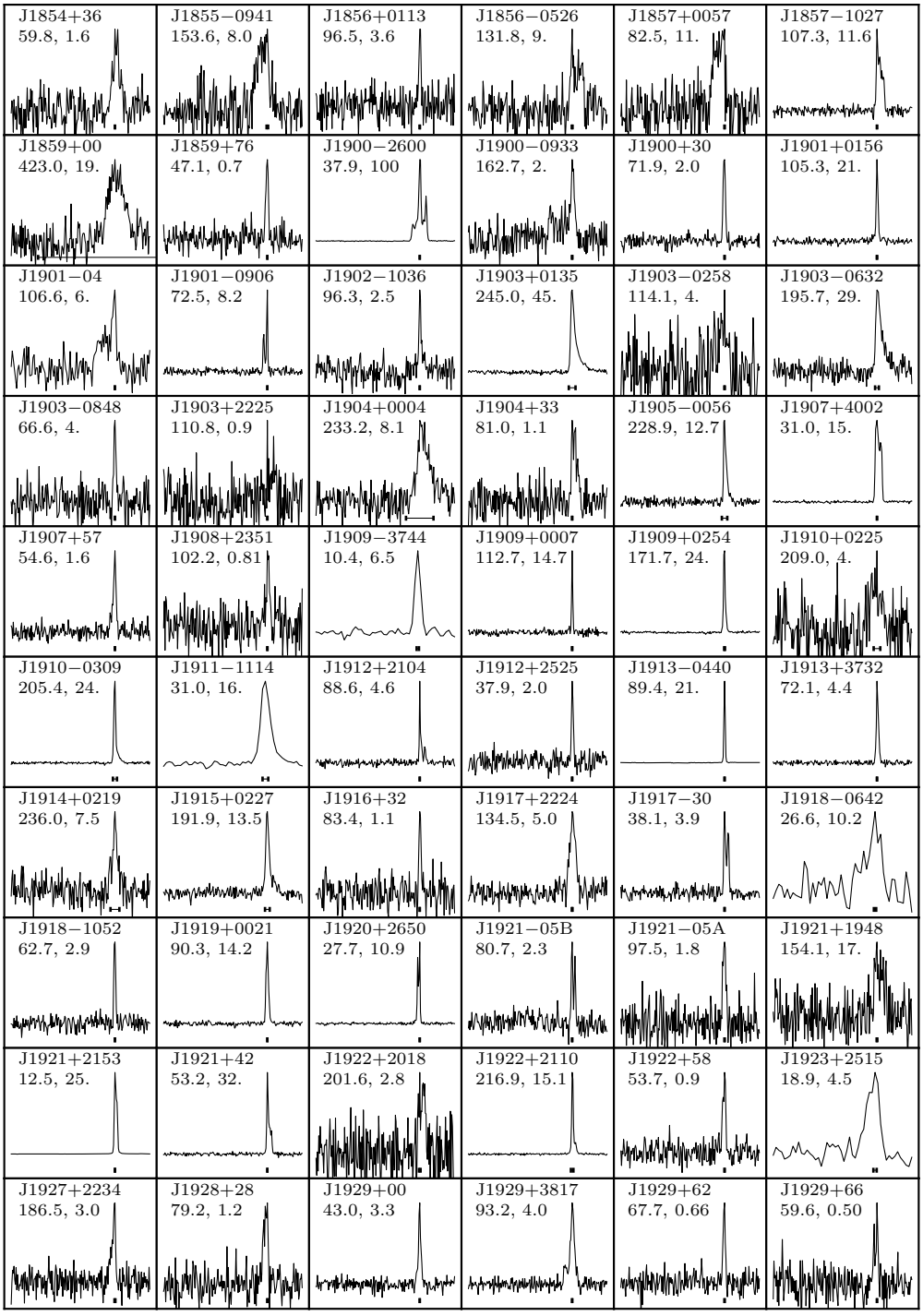

Figure A.8 Profile plots (continued). See Figure A.1 for details.

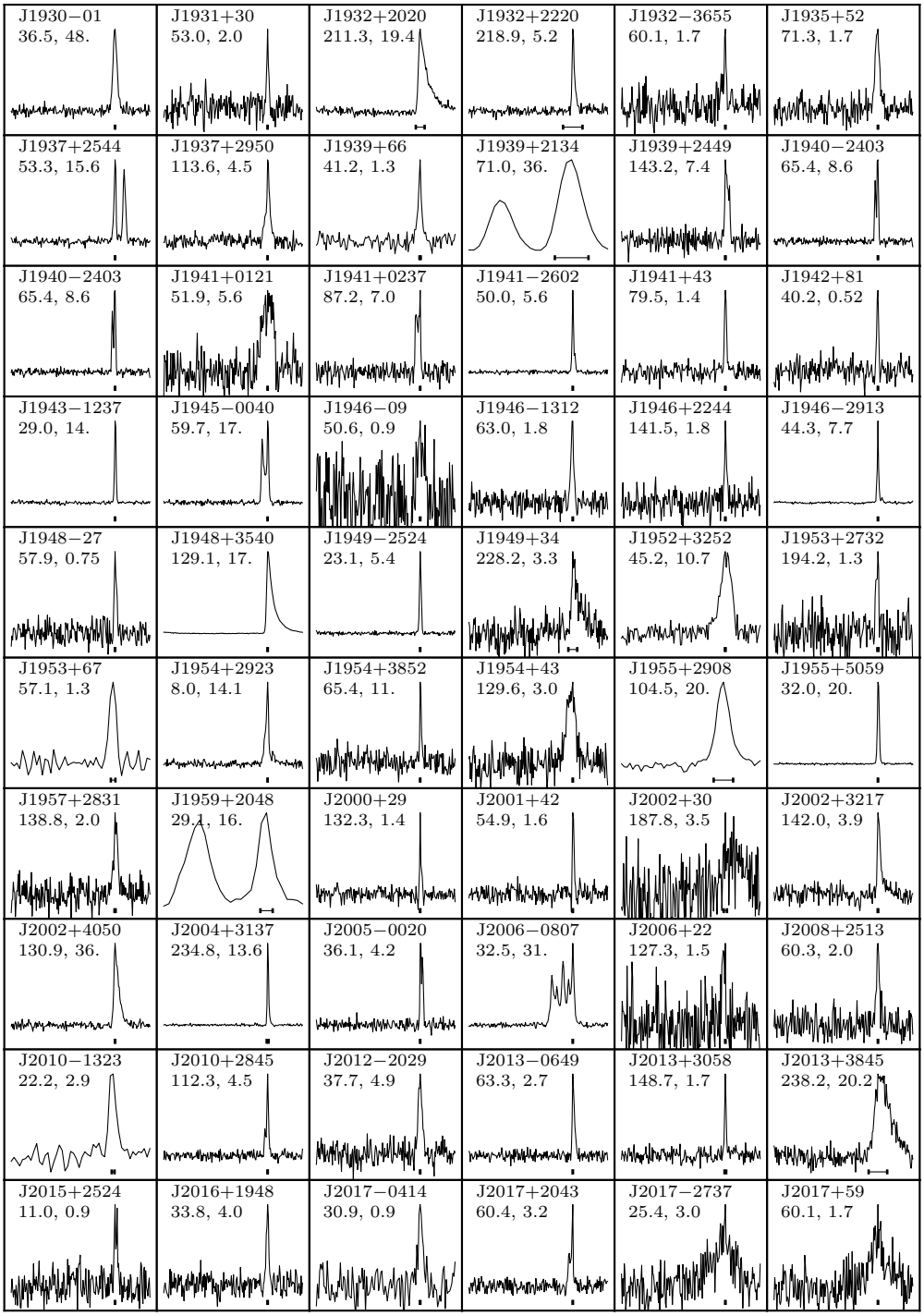

Figure A.9 Profile plots (continued). See Figure A.1 for details.

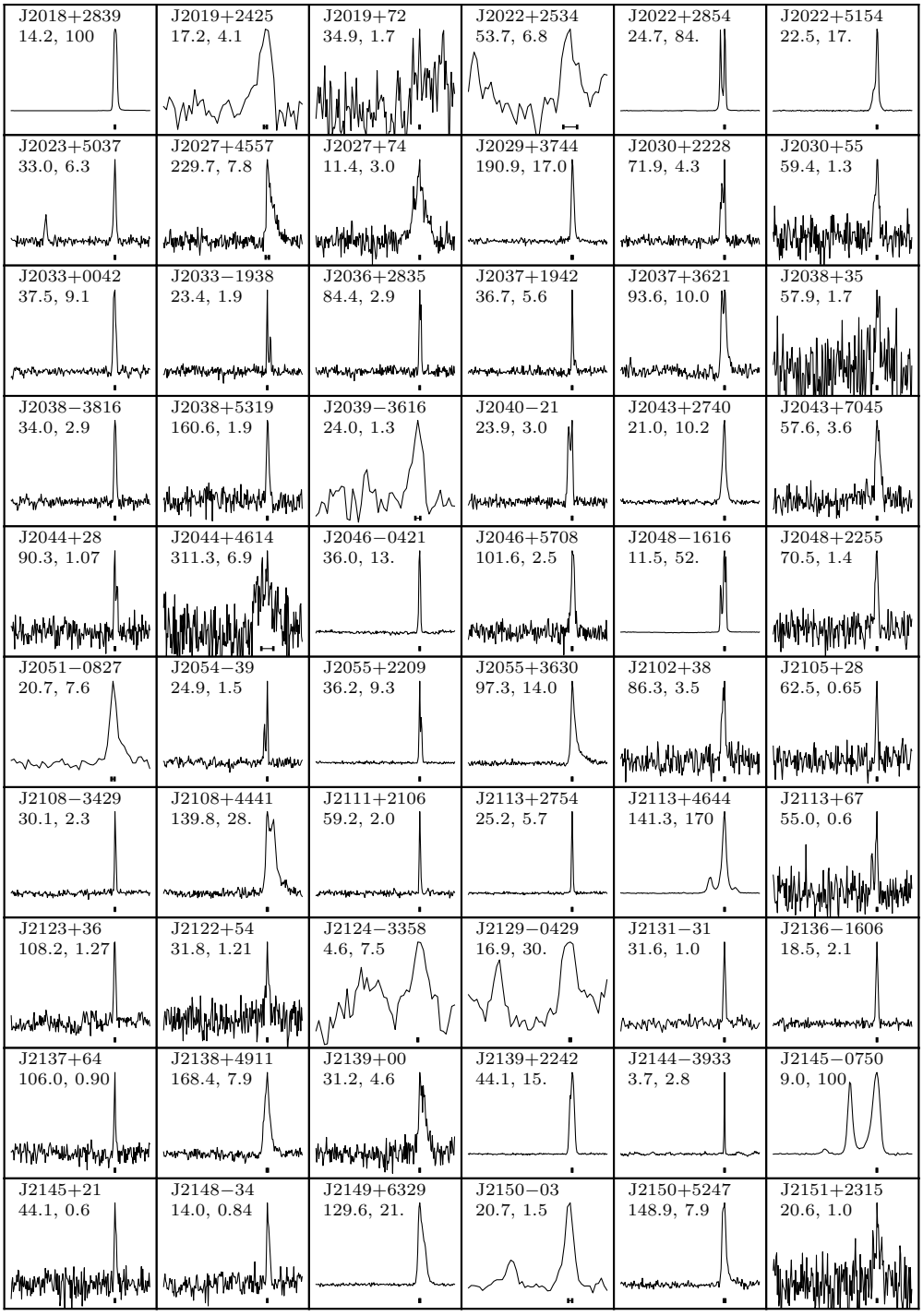

Figure A.10 Profile plots (continued). See Figure A.1 for details.

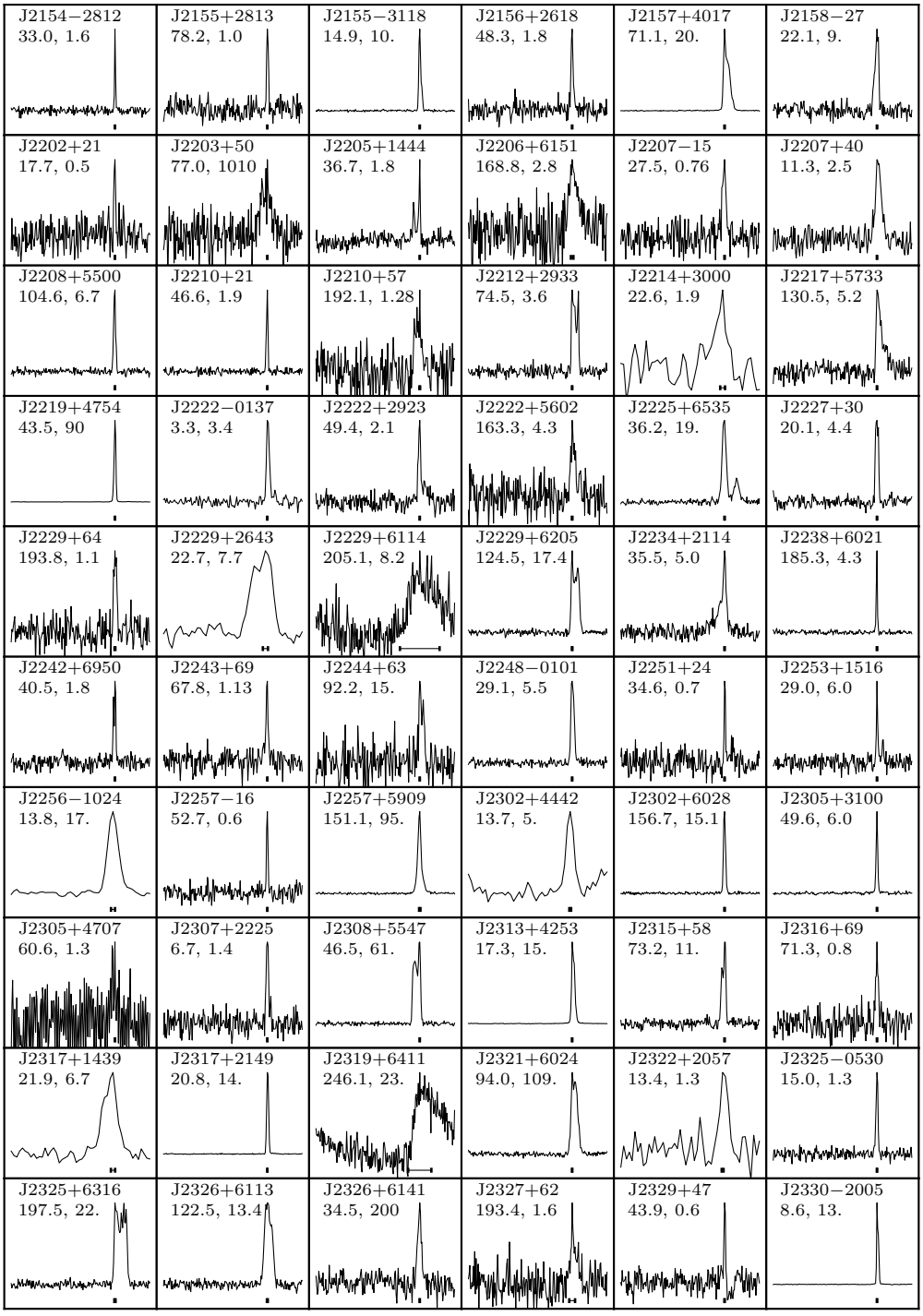

Figure A.11 Profile plots (continued). See Figure A.1 for details.

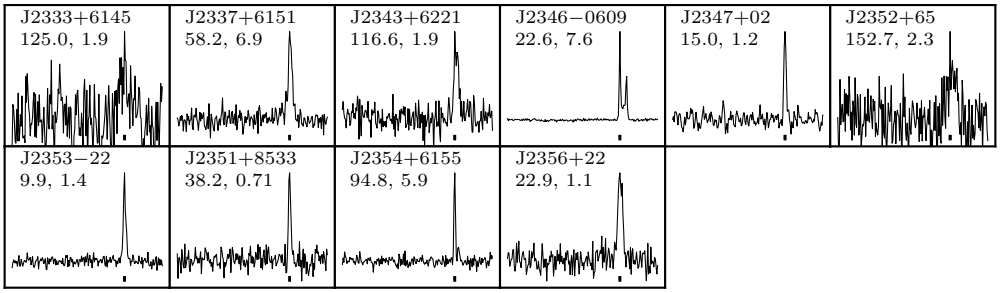

Figure A.12 Profile plots (continued). See Figure A.1 for details.

APPENDIX B
Chapter 4 Timing Residuals

We include all residuals for pulsars timed in Chapter 4.

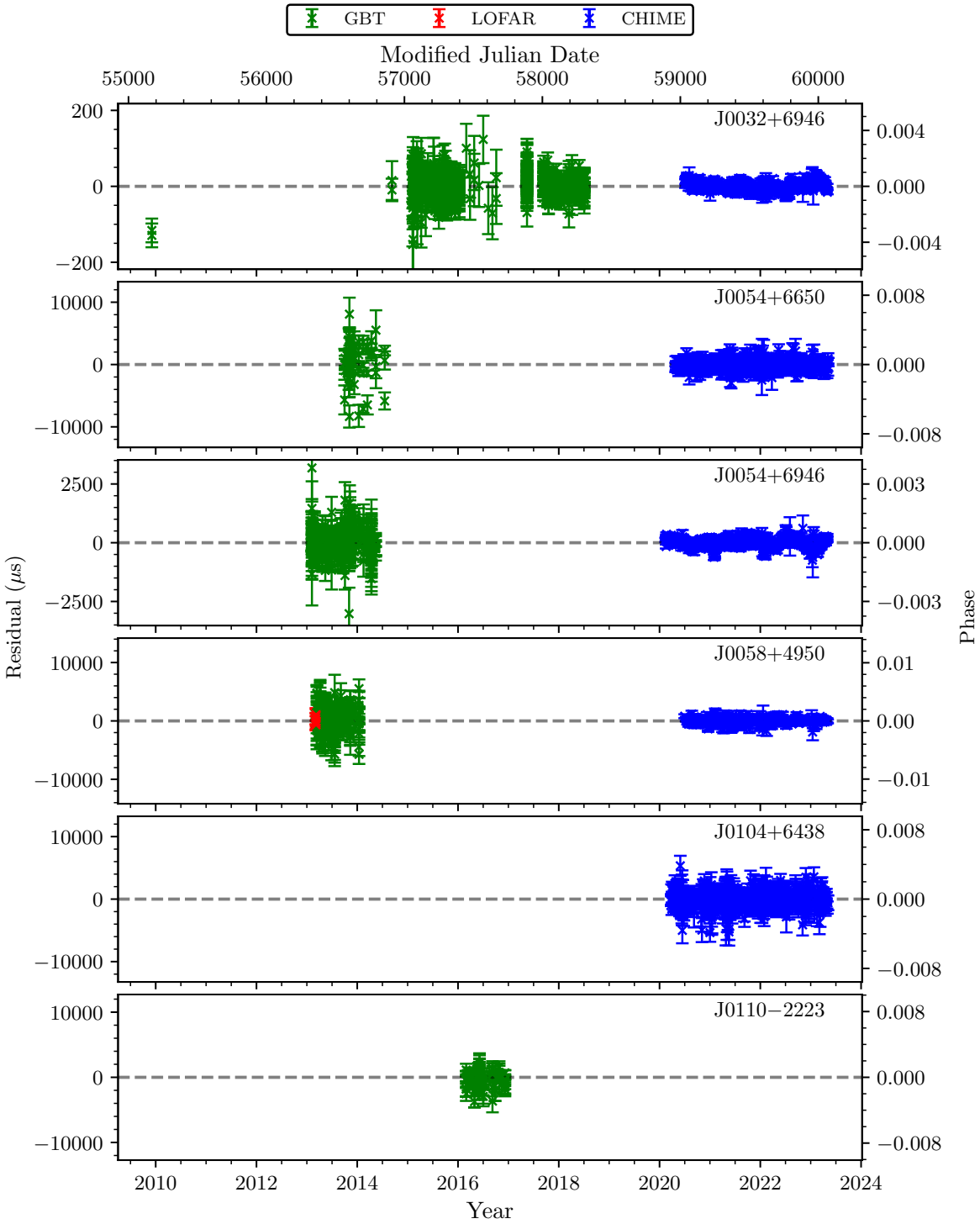

Figure B.1 Timing residuals for sources in this study. TOAs are colored by their observatory: blue corresponds to CHIME, green to GBT, red to LOFAR, and yellow to Arecibo.

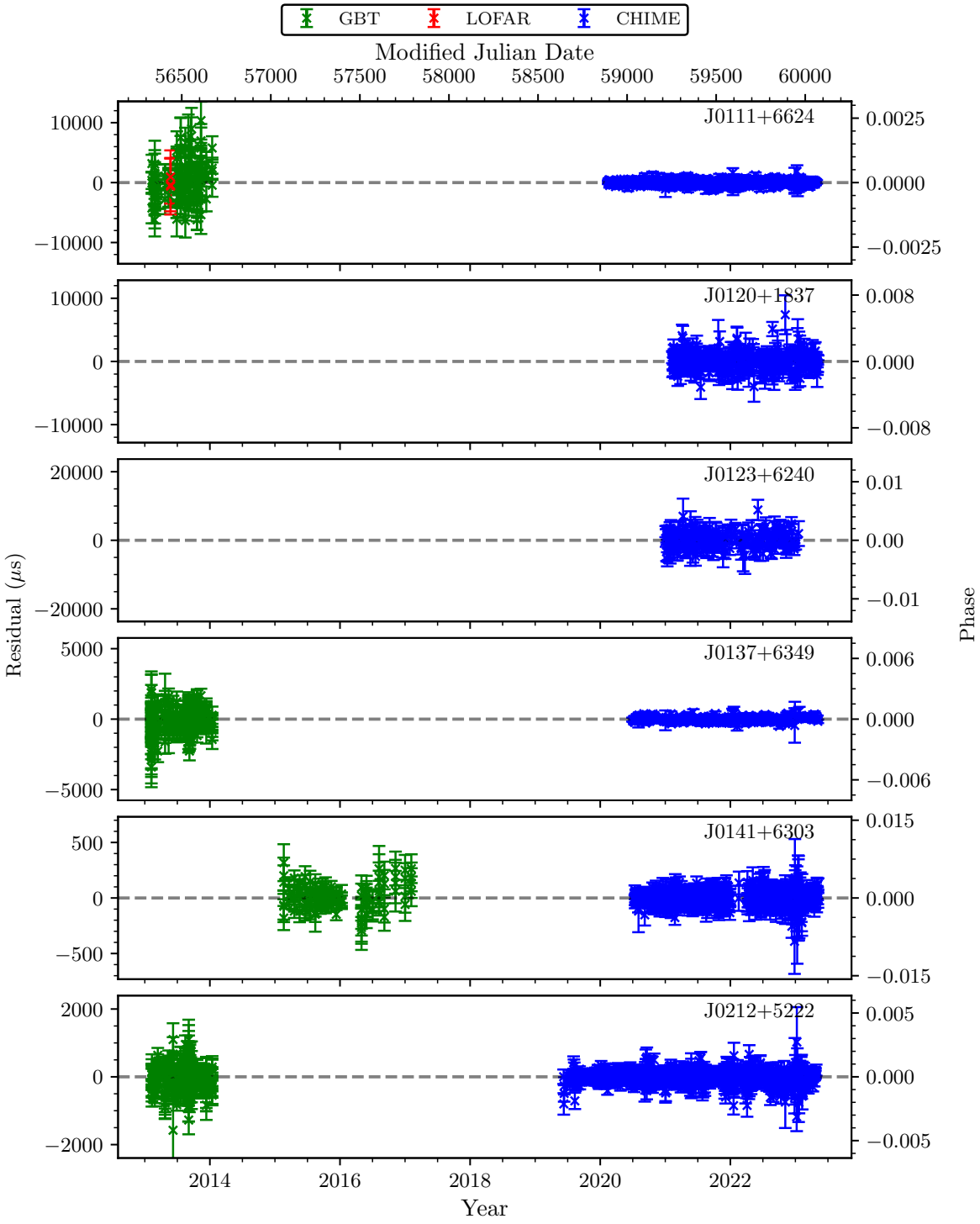

Figure B.2 Timing residuals (continued). See Figure B.1 for details.

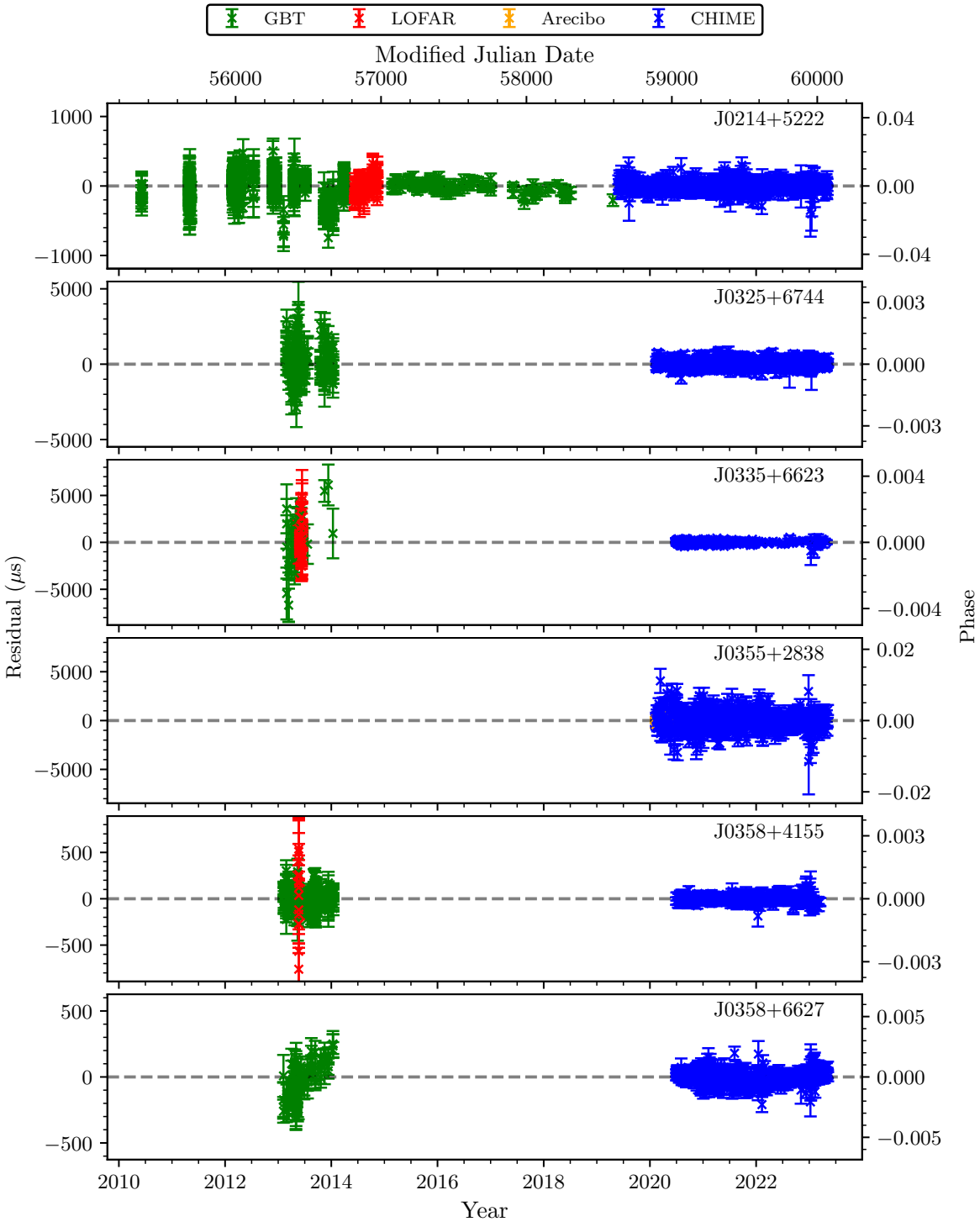

Figure B.3 Timing residuals (continued). See Figure B.1 for details.

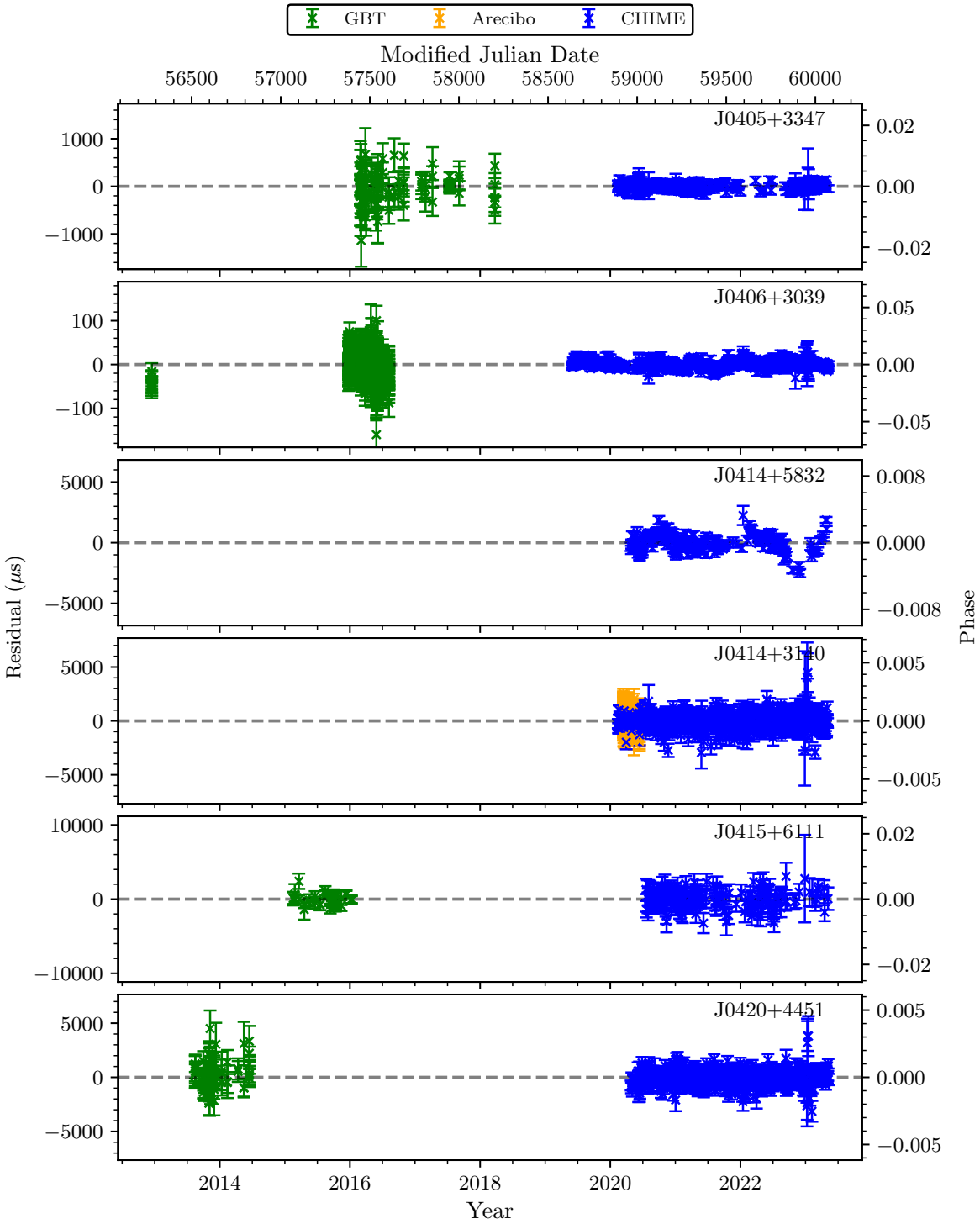

Figure B.4 Timing residuals (continued). See Figure B.1 for details.

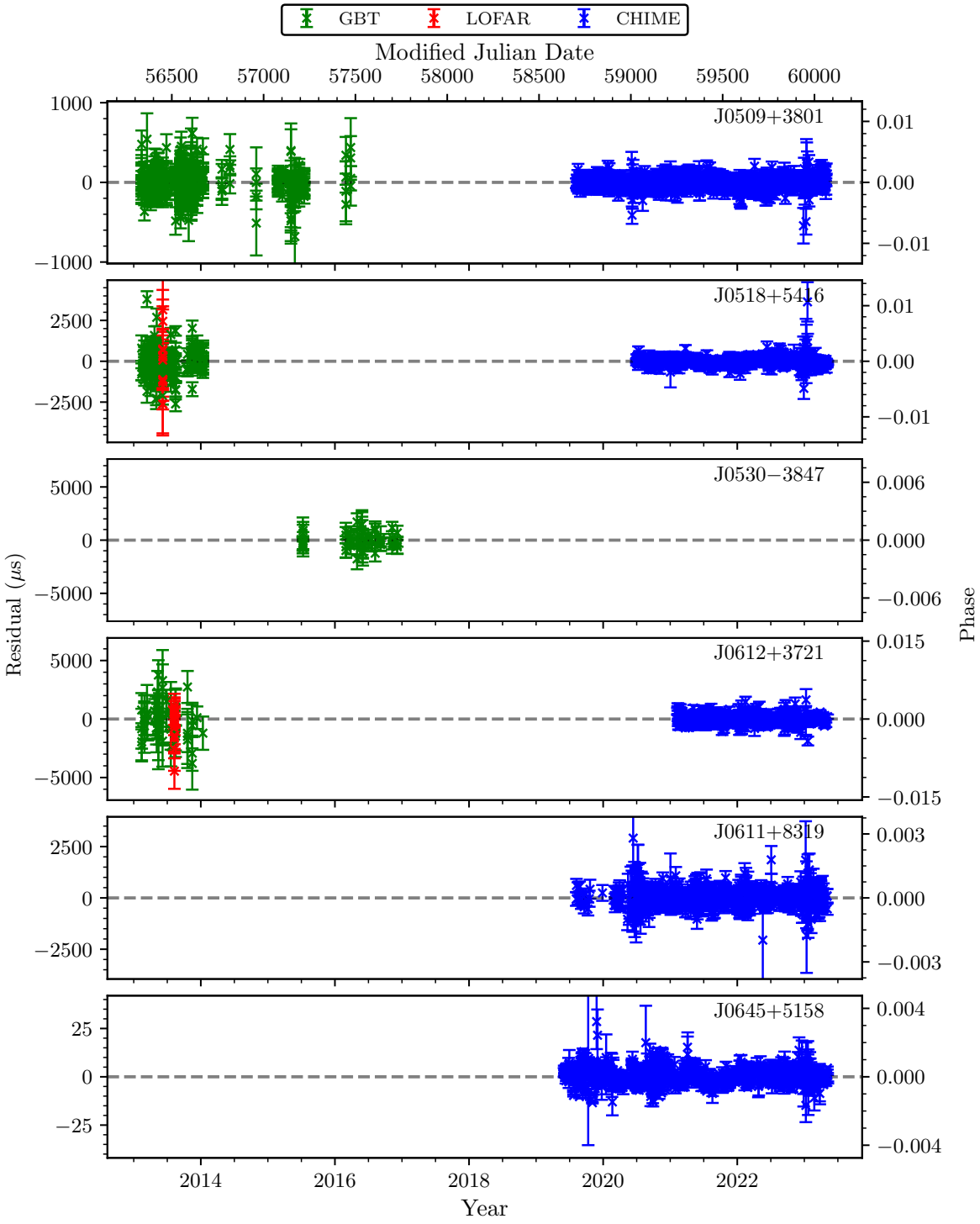

Figure B.5 Timing residuals (continued). See Figure B.1 for details.

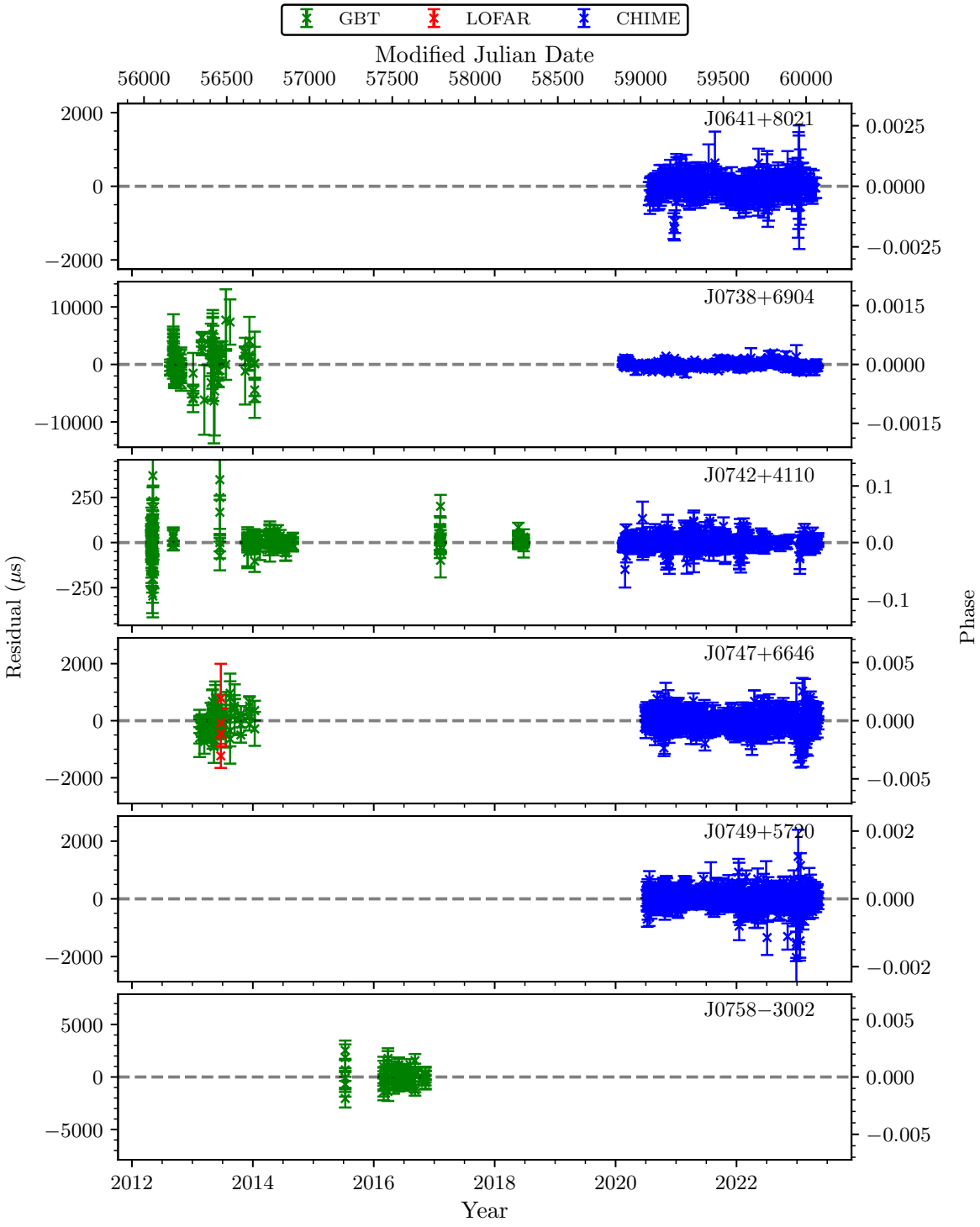

Figure B.6 Timing residuals (continued). See Figure B.1 for details.

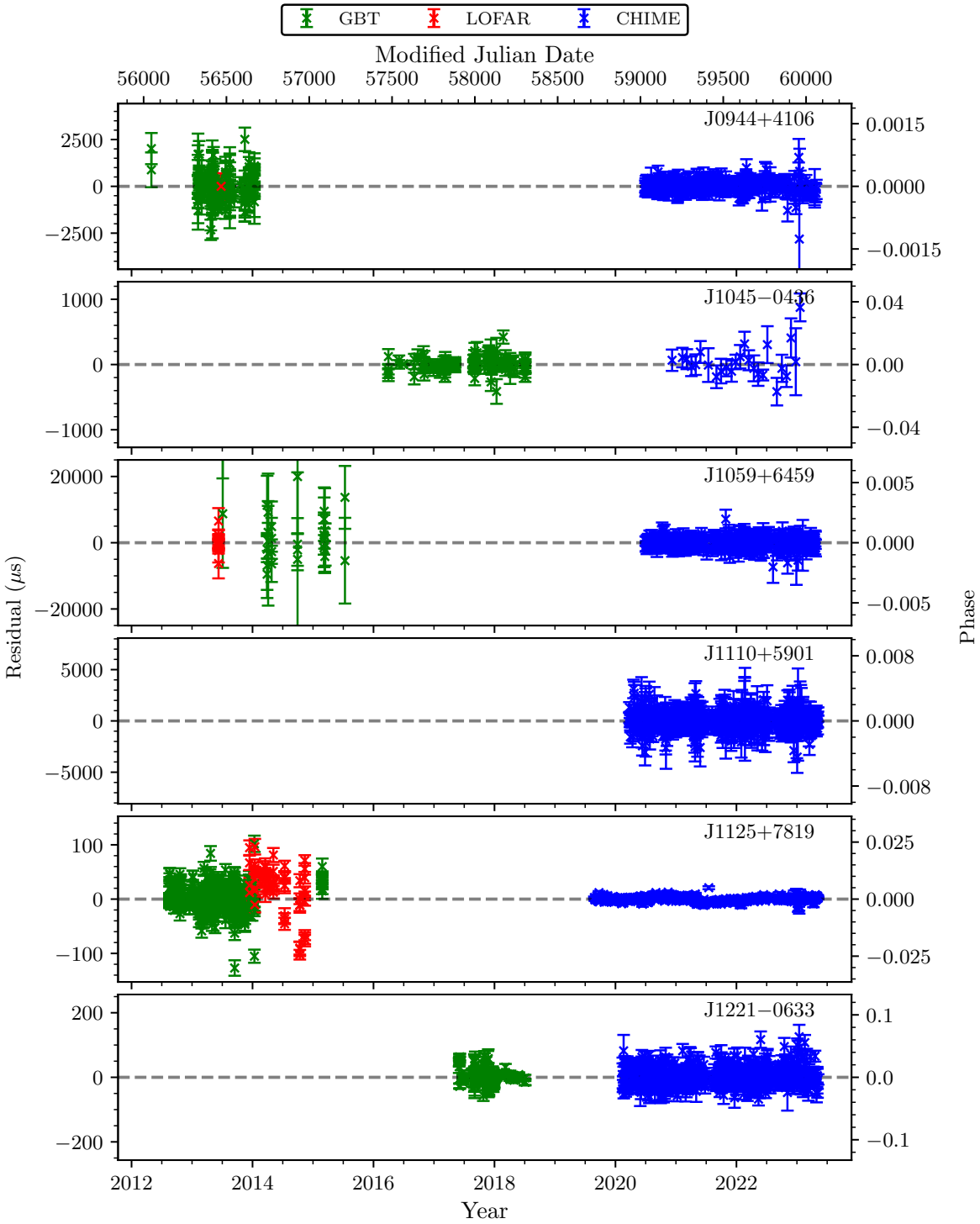

Figure B.7 Timing residuals (continued). See Figure B.1 for details.

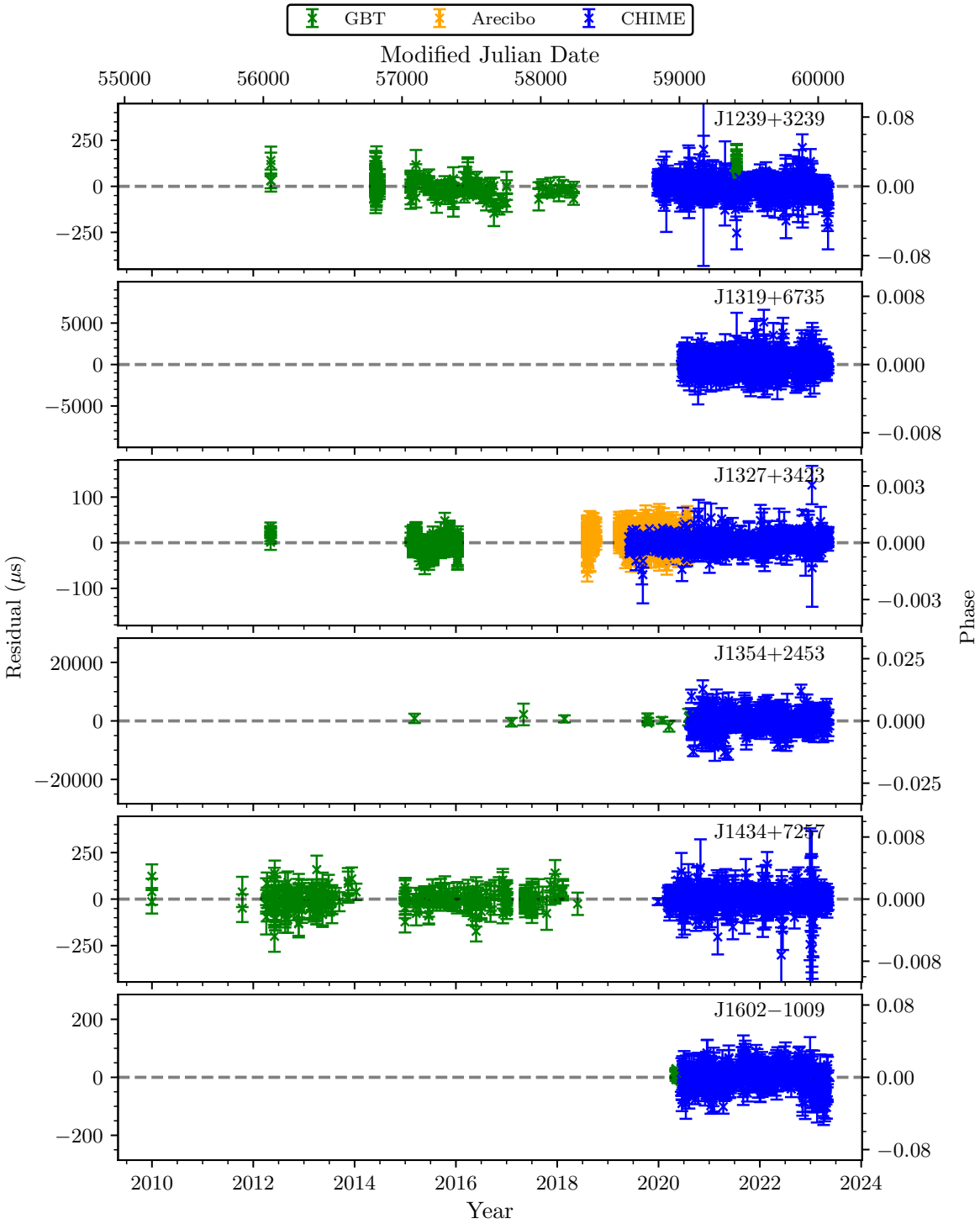

Figure B.8 Timing residuals (continued). See Figure B.1 for details.

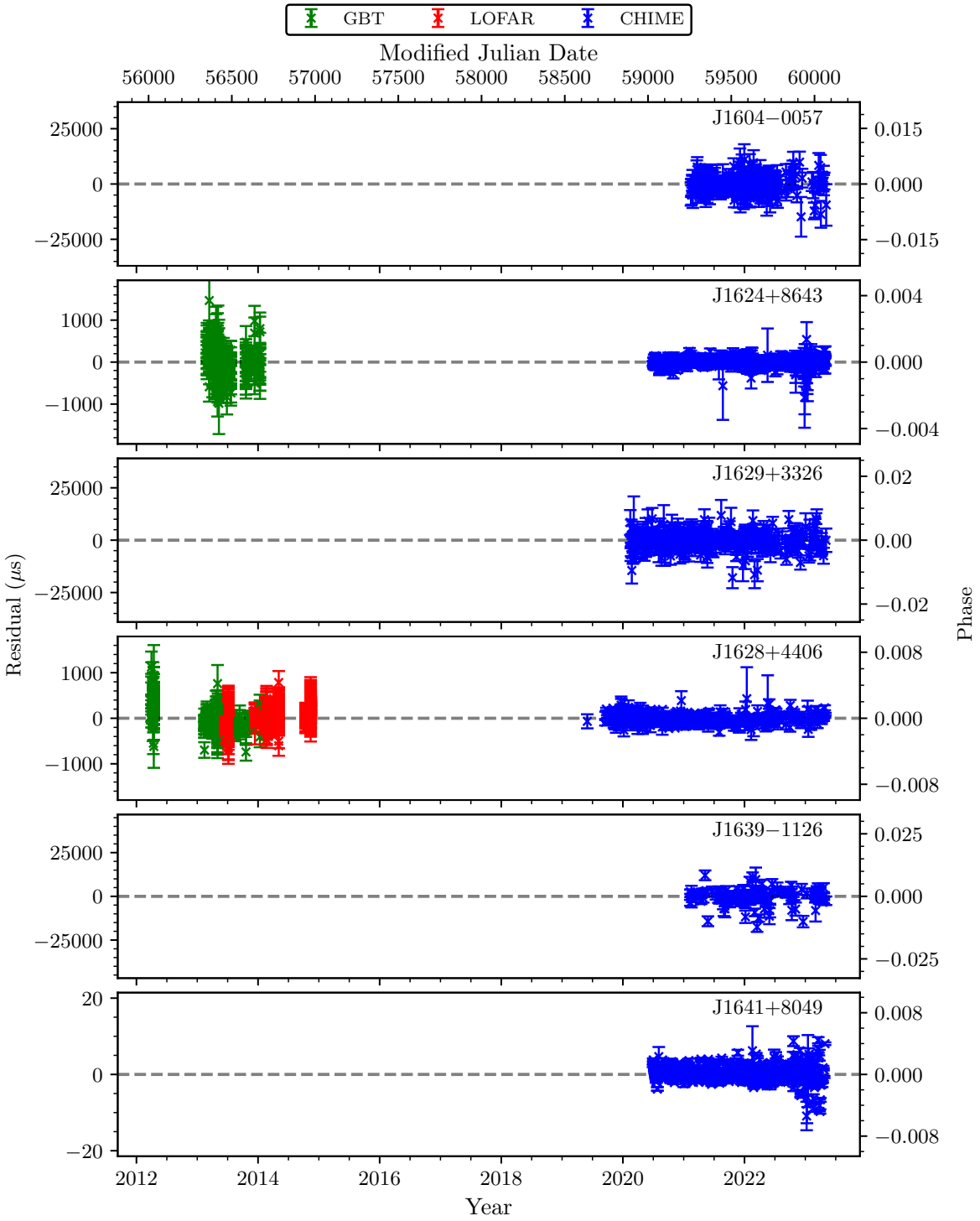

Figure B.9 Timing residuals (continued). See Figure B.1 for details.

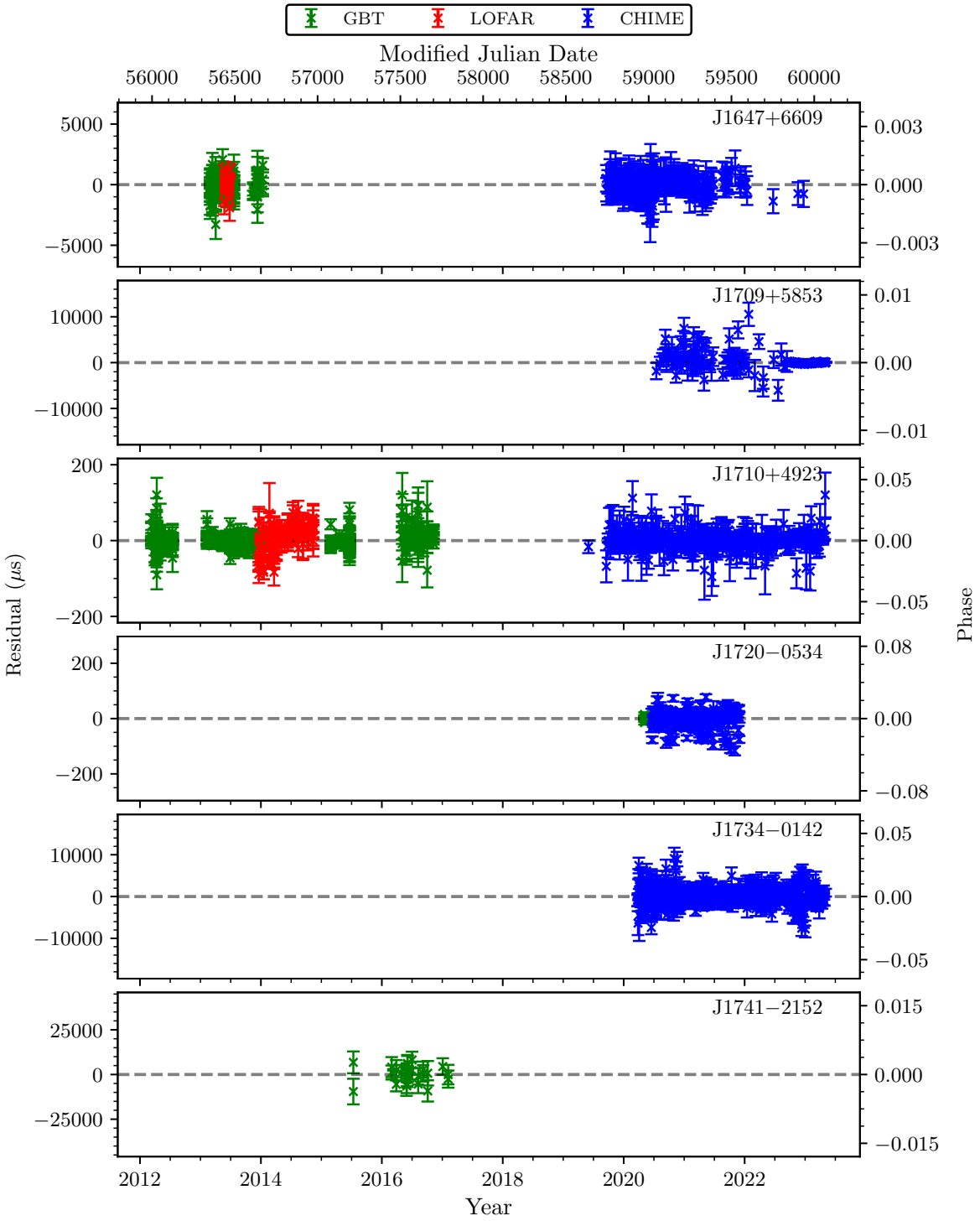

Figure B.10 Timing residuals (continued). See Figure B.1 for details.

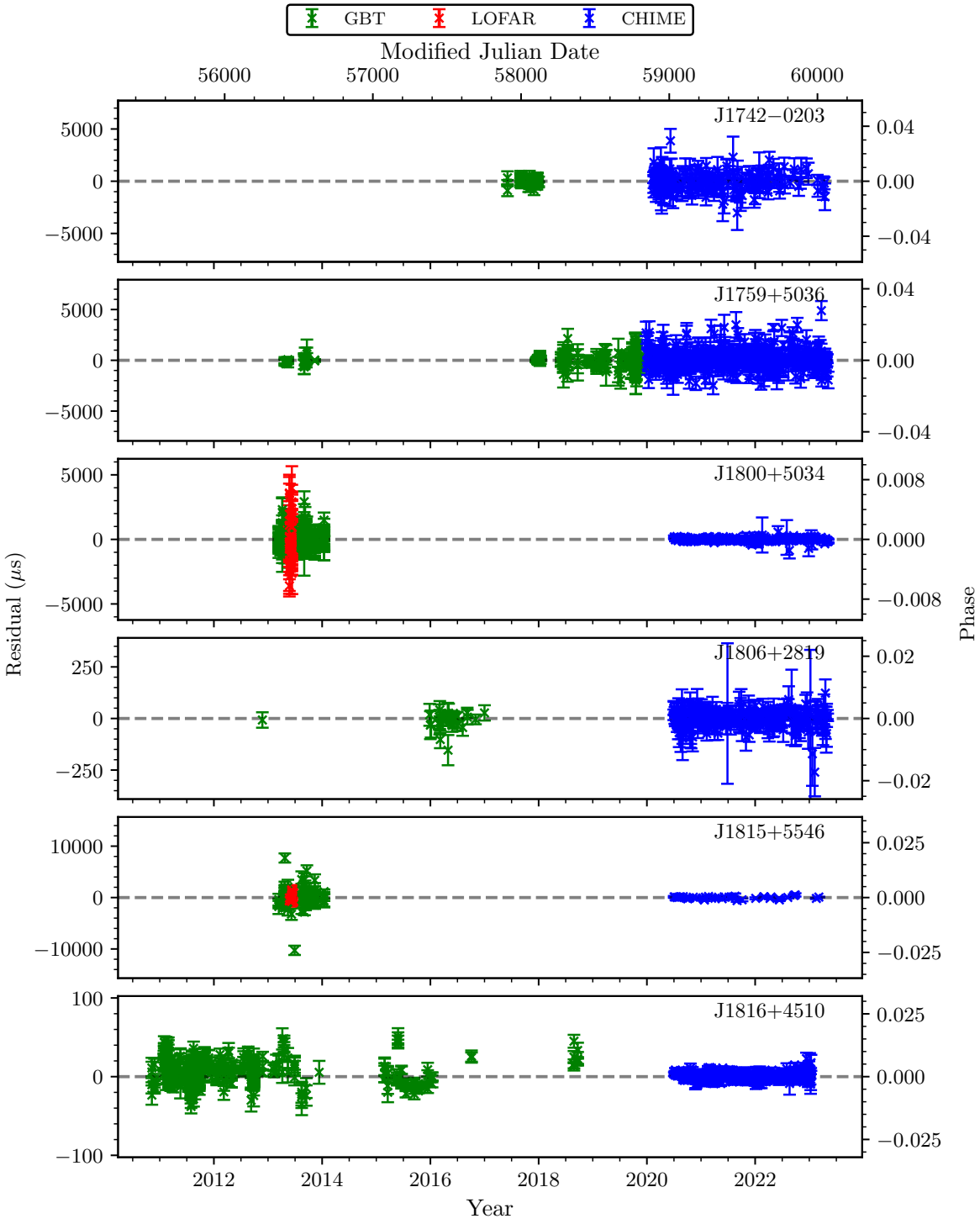

Figure B.11 Timing residuals (continued). See Figure B.1 for details.

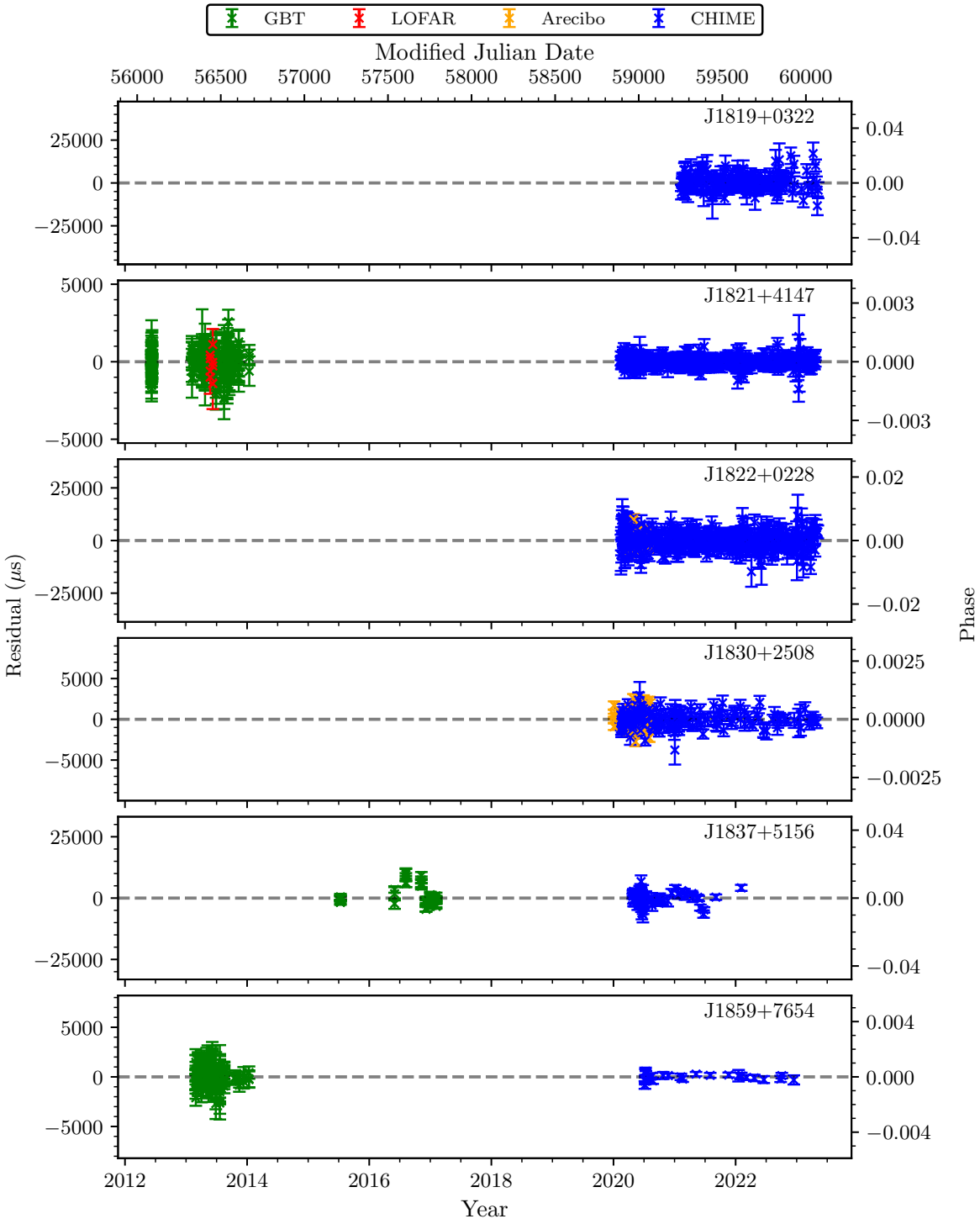

Figure B.12 Timing residuals (continued). See Figure B.1 for details.

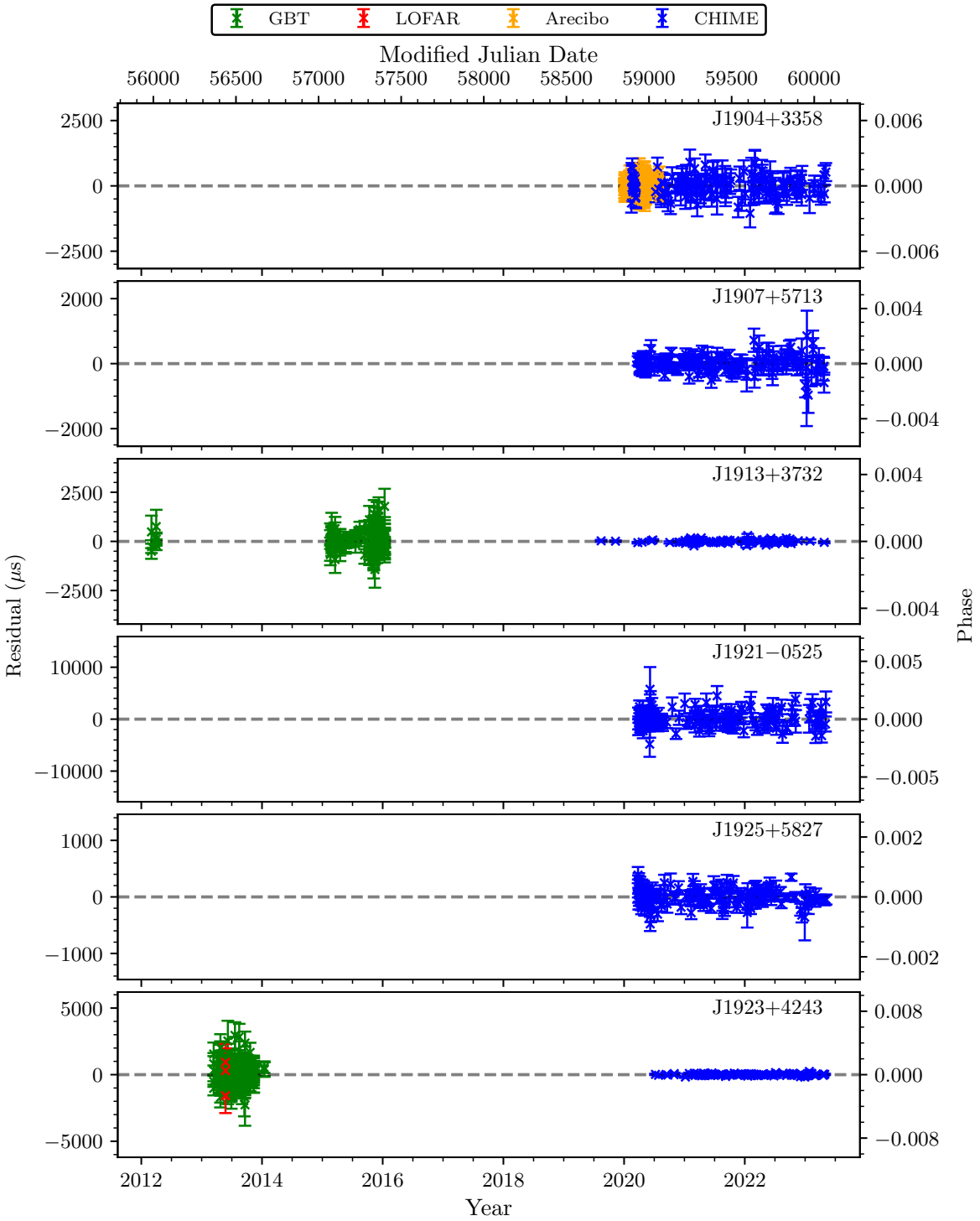

Figure B.13 Timing residuals (continued). See Figure B.1 for details.

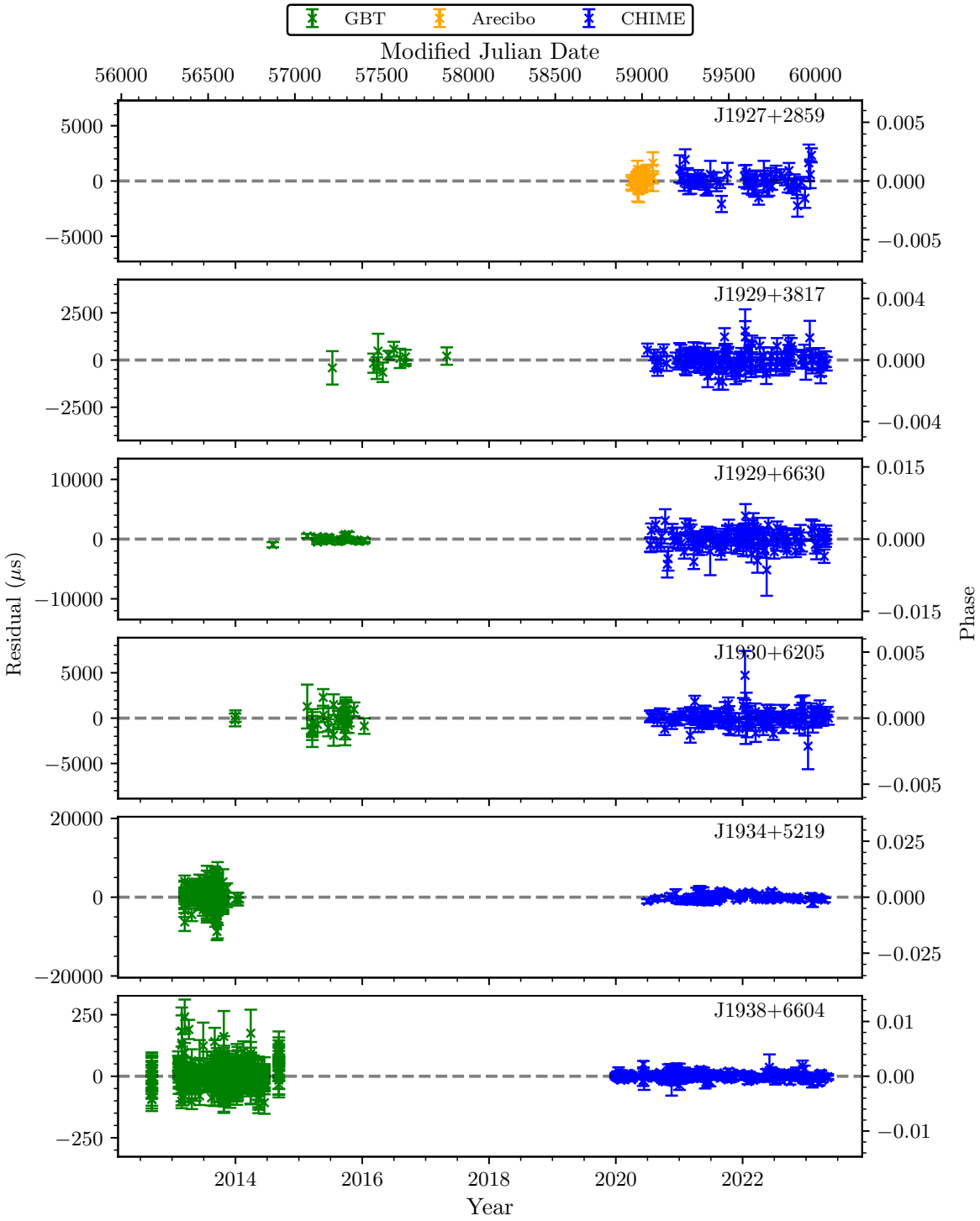

Figure B.14 Timing residuals (continued). See Figure B.1 for details.

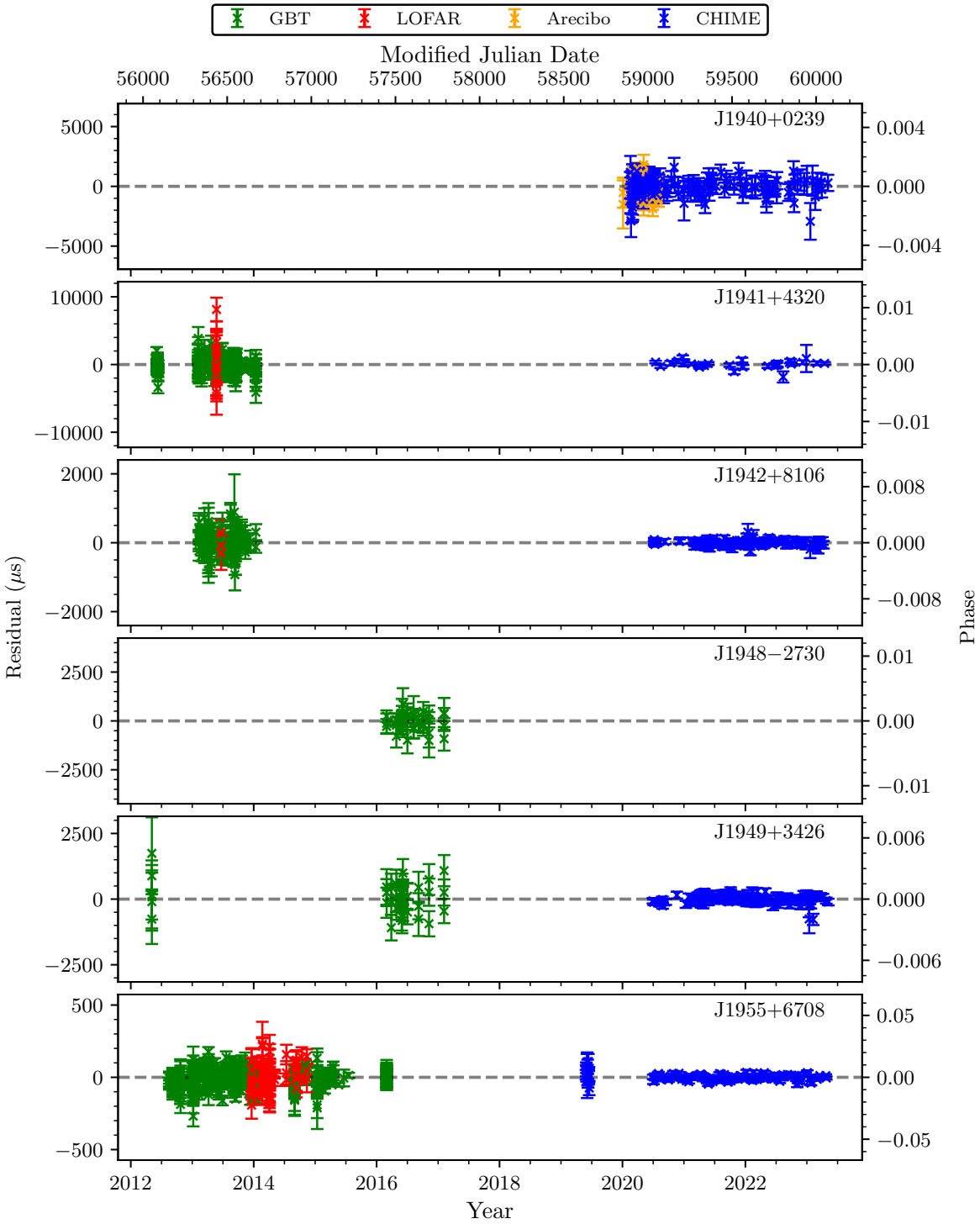

Figure B.15 Timing residuals (continued). See Figure B.1 for details.

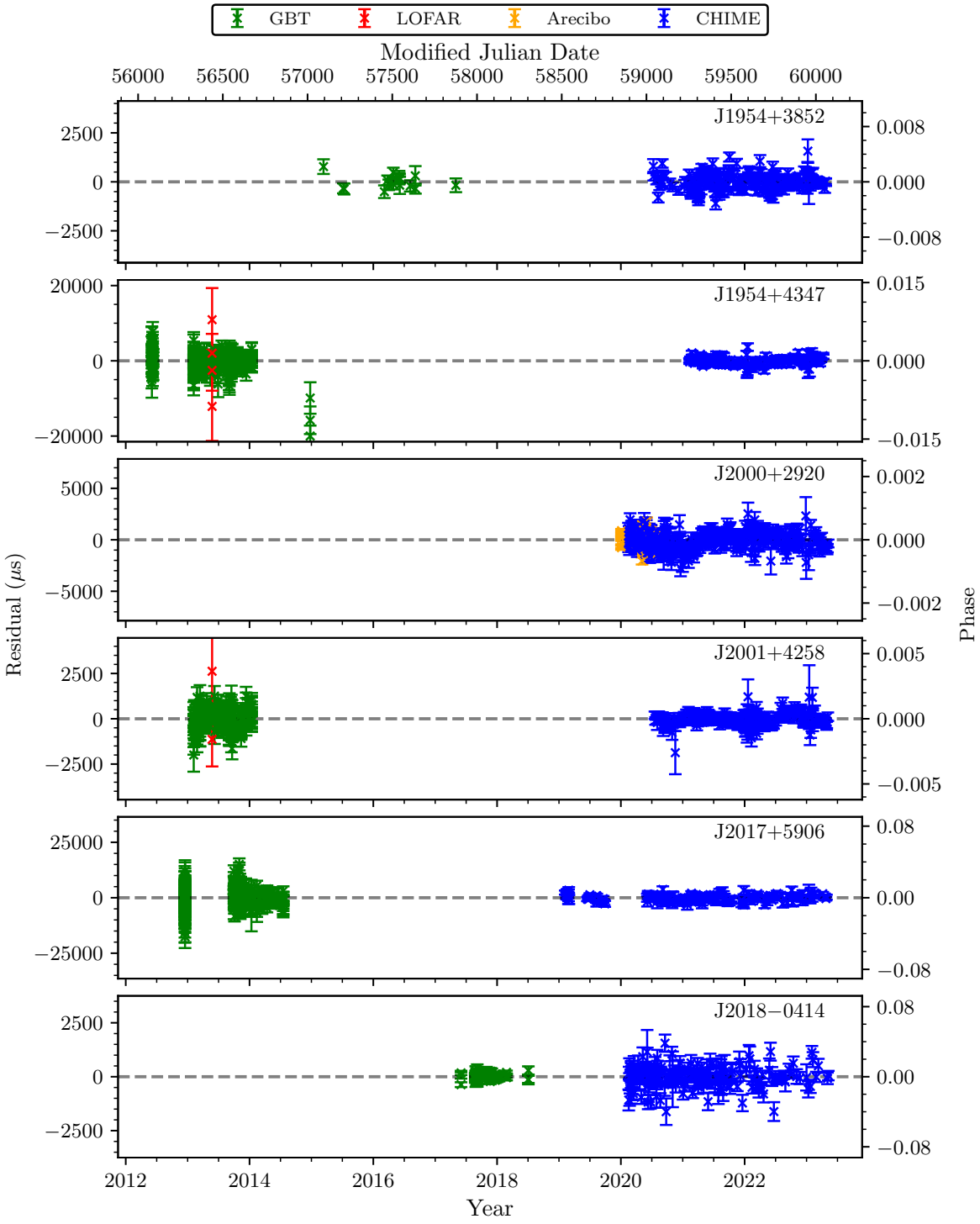

Figure B.16 Timing residuals (continued). See Figure B.1 for details.

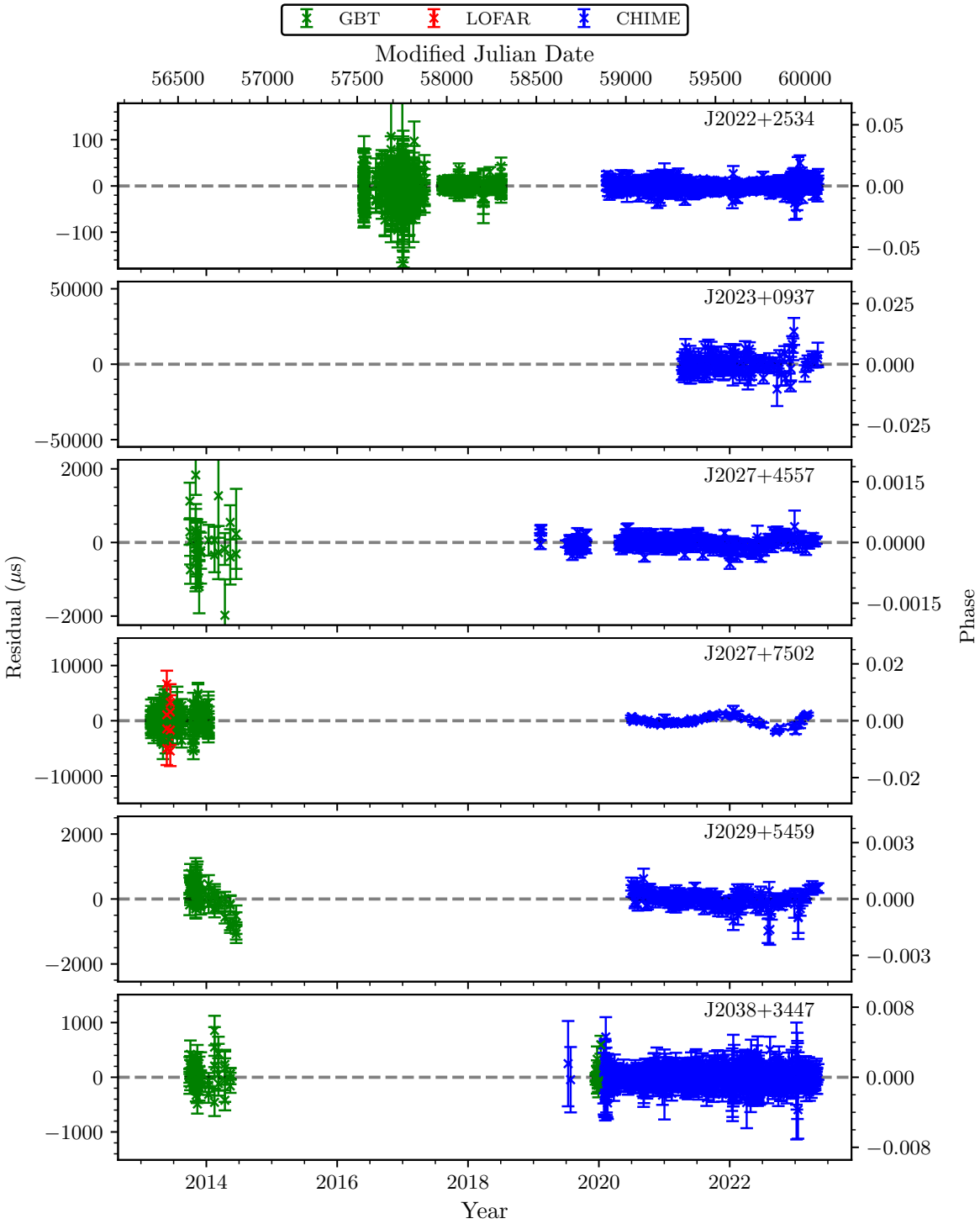

Figure B.17 Timing residuals (continued). See Figure B.1 for details.

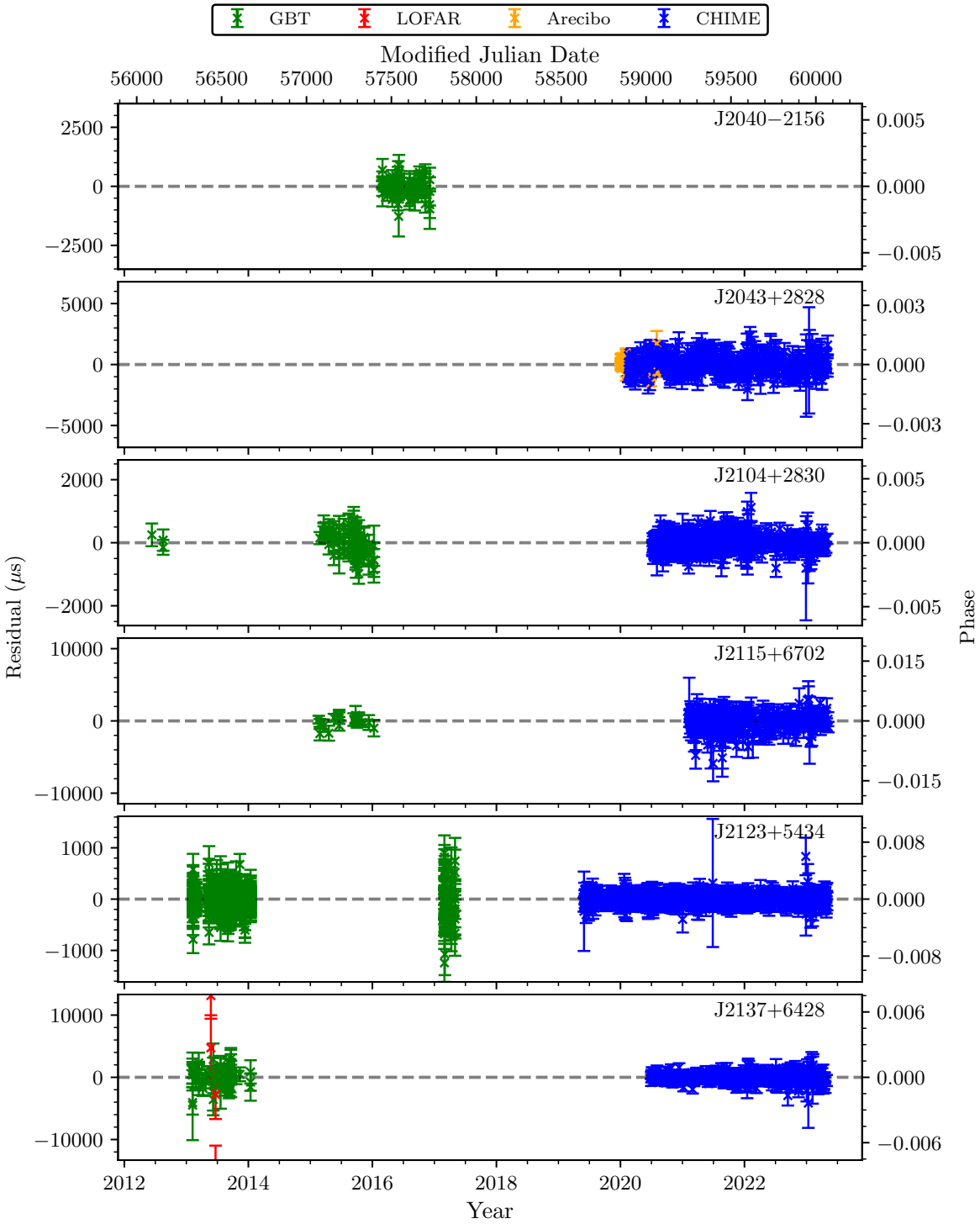

Figure B.18 Timing residuals (continued). See Figure B.1 for details.

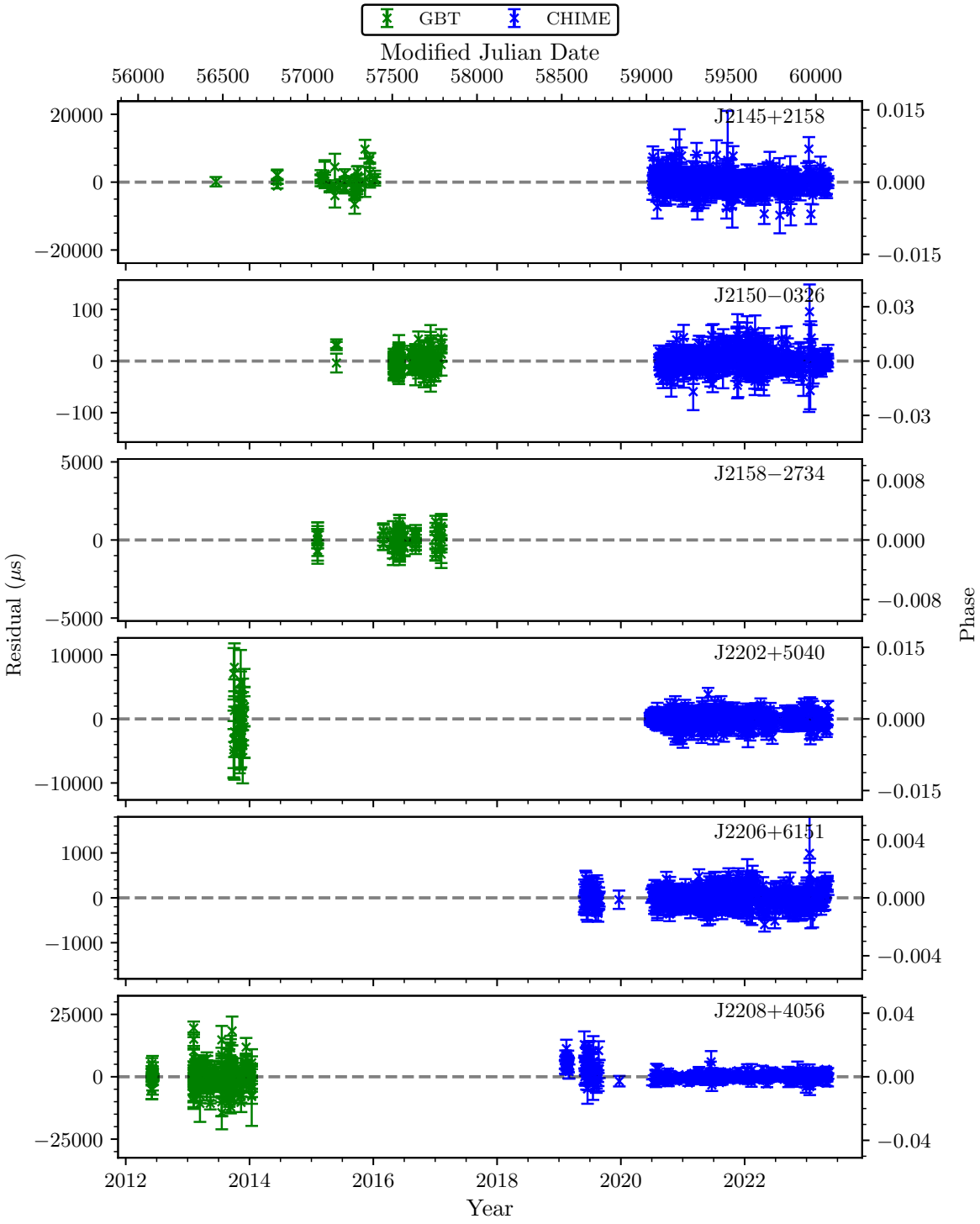

Figure B.19 Timing residuals (continued). See Figure B.1 for details.

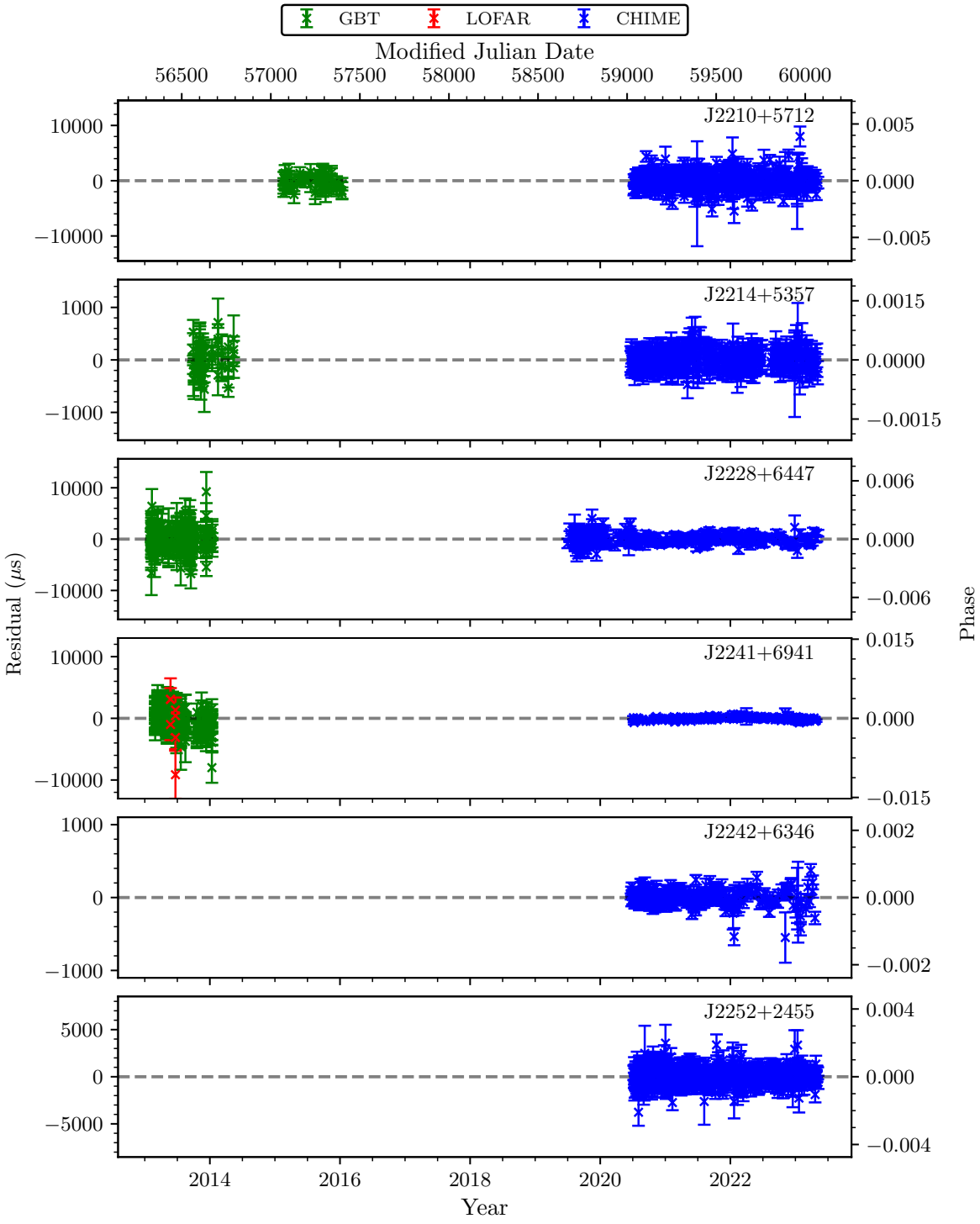

Figure B.20 Timing residuals (continued). See Figure B.1 for details.

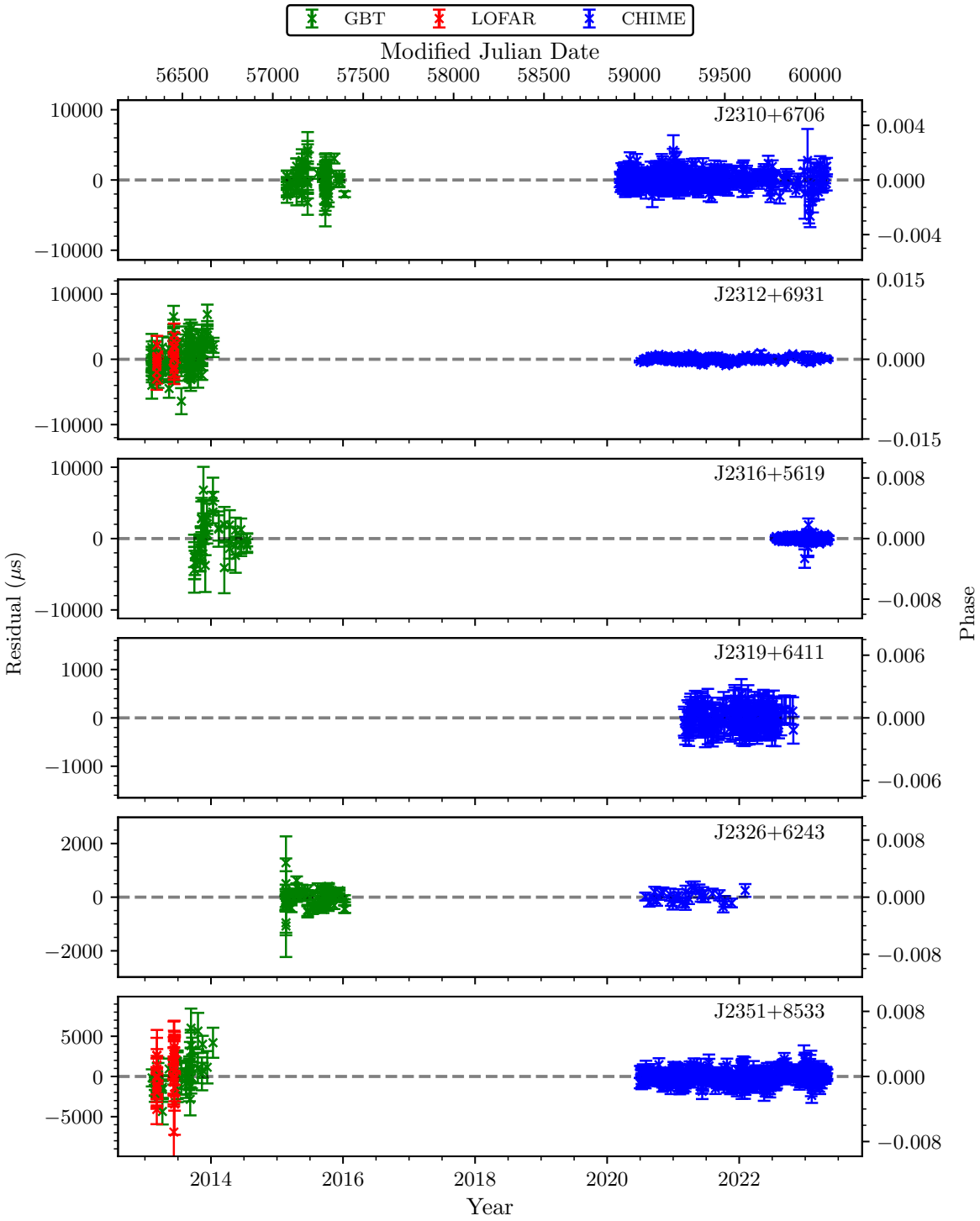

Figure B.21 Timing residuals (continued). See Figure B.1 for details.

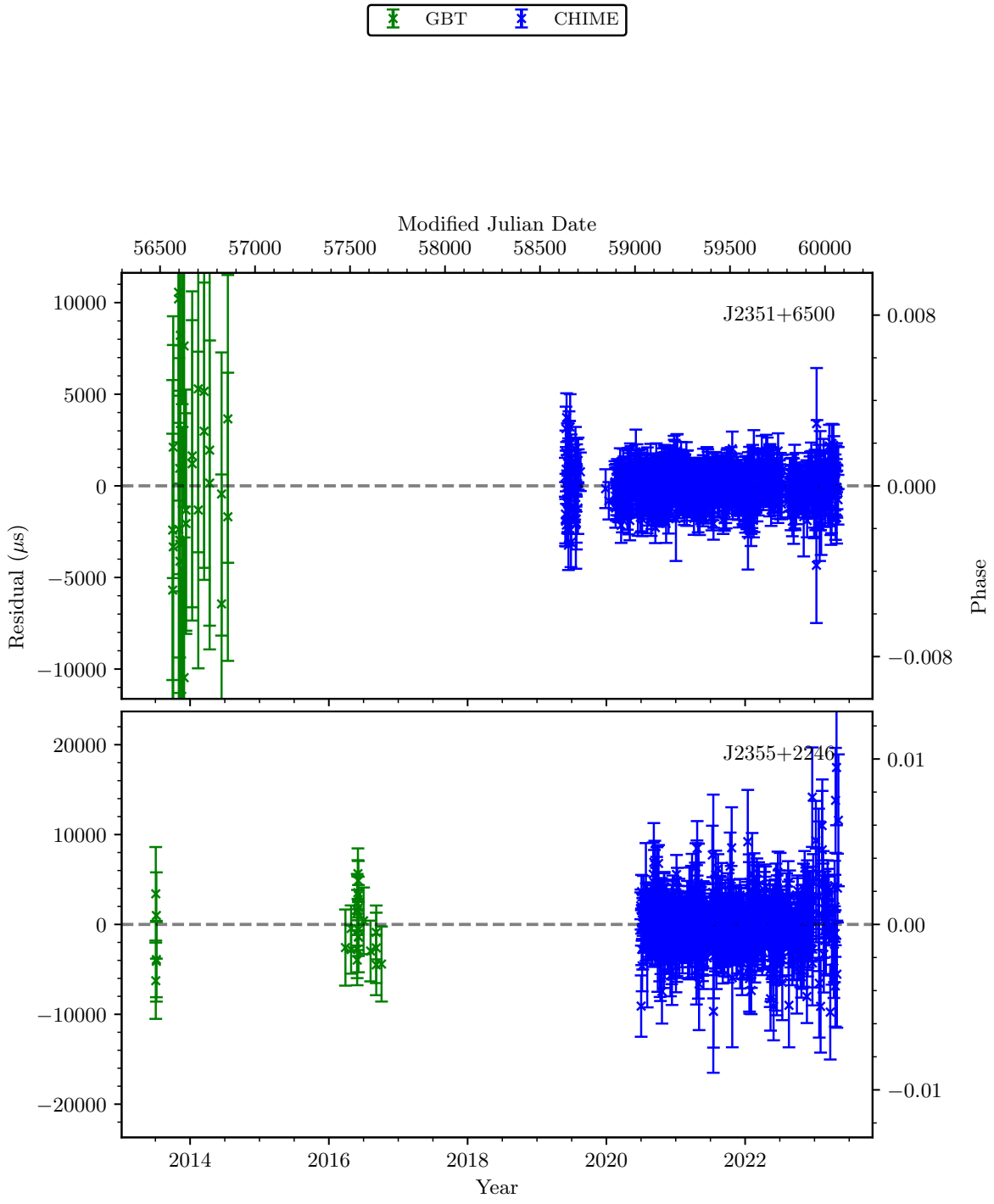

Figure B.22 Timing residuals (continued). See Figure B.1 for details.